Reaction-diffusion-advection models for collagenous cap formation in atherosclerotic plaques

Jong Hyun Won

A thesis submitted in fulfillment
of the requirements of the degree of
Master of Philosophy

Faculty of Science
School of Mathematics and Statistics
The University of Sydney

February 2024

Declaration

I hereby declare that this submission is my own work and that, to the best of my knowledge and belief, it contains no material previously published or written by another person nor material which to a substantial extent has been accepted for the award of any other degree or diploma of the University or other institute of higher learning, except where due acknowledgement has been made in the text.

Jong Hyun Won

29 February 2024

Acknowledgements

This thesis would not have been possible without the diligent, genial and patient supervision of my supervisor Mary Myerscough. Without her feedback and support, my journey would have been far more difficult. I thank her for being a continual inspiration as my supervisor during this Masters and also my Honours. I thank my former co-supervisor Michael Watson, whose research provided the inspiration for much of this thesis, for his opinions and guidance on the myriad of issues I faced. Special thanks go to Charlie Macaskill, who provided invaluable assistance and advice; I wish him the best of health. I also thank Ishraq Ahmed, who took the time to provide another helpful pair of eyes on things.

I am eternally grateful to Sana, who has been an unwavering source of love, inspiration and support. Thank you for your patience and for providing a light to look forward to during all the long nights and difficult times. Finally, thank you to my family and friends for your continued support.

Contents

Chapter 1

Introduction

1.1 Motivation

Atherosclerosis is the most common form of cardiovascular disease, with cardiovascular disease being the primary cause of heart disease and stroke [3,4]. Atherosclerosis is characterised by the chronic inflammation of the artery wall within the intima, which is the innermost wall of the artery. The origin of the term "atherosclerosis" are the Greek words "athero", "sclerosis" and "osis". "Athero" means gruel or paste, "sclerosis" means hardness, and "osis" is a Greek suffix that describes a diseased condition [1]. The term therefore describes the accumulation of lesions and the thickening of the intimal layer of arteries. It is characterised by the formation of plaques on the artery wall. These plaques contain lipids, cells, debris and scar tissue.

Plaque formation begins when cholesterol-carrying low density lipoproteins (LDL) enter the intima through the endothelium [23, 38]. These lipoproteins are then modified to become modified LDL (modLDL) [4, 33]. The presence of modLDL triggers an inflammatory response, initiating immune cells (monocytes) to enter the intima from the bloodstream [4, 31]. Monocytes differentiate into macrophages, which accumulate within the intima [4]. These macrophages consume modLDLs [4, 6, 29] and convert to lipid-bearing foam cells [4], forming a plaque. Over time however, foam cells undergo death and decay. This leads to cellular debris and necrotic tissue amassing in a necrotic lesion core within the plaque, which in turn stimulates further inflammation and monocyte recruitment [3]. If the cell death becomes uncontrolled, the necrotic lesion core grows and the plaque becomes less stable. As plaques grow, they acquire a cap of vascular smooth muscle cells (SMCs) [3]. If this cap is thick, it may stabilise the plaque. The growth of these lesions however may reduce blood flow in the lumen by more than fifty percent and cause angina [4]. If the cap is thin or is disrupted, the plaque may rupture, releasing cellular debris that create blood clots [4, 33, 35]. The blood clots may block arteries and cause heart attacks or strokes.

Research has been undertaken to understand the mechanisms and pathogenesis of atherosclerosis, though it is highly complex and not fully understood. Because experimental studies are complicated and resource-intensive, mathematical modelling is a way of exploring and hypothesising about the mechanisms of atherosclerosis. A number of mathematical models have been created to analyse the mechanisms involved. These models include reaction-diffusion equations, multiphase equations, and population-structured models. As new experimental and modelling results are published, these models too change over time.

The complexity of atherosclerosis means that simple and adaptable mathematical models that capture only the most important processes may provide an easier and more computationally efficient tool for analysing mechanisms of plaque formation, compared to more specialised and complex models. Such mathematical models may still be able to reflect the key results observed in more complex models without requiring the same level of analytical and numerical complexity. One example of this is reaction-diffusion equation models, which have been utilised by a number of studies to model plaque dynamics [10, 11, 37].

1.2 Research questions and objectives

In this thesis, we aim to address the following key research questions. We ask if we can replace the multiphase model of Watson *et al.* (2018) [44] by a reaction-diffusion model. Our motivation is to understand if we can create a reaction-diffusion framework that simply models key stages of atherosclerotic plaque dynamics while retaining experimental validity and avoiding the complexity of the multiphase model. We compare our model dynamics and results with those observed in Watson *et al.* (2018) [44]. If the reaction-diffusion model is simpler and produces qualitatively similar results, we will be able to conclude that the reaction-diffusion model could be a more useful model than the multiphase model.

We then ask if this base reaction-diffusion model can be extended to produce models that include more factors involved in plaque growth and results that are in qualitative agreement with experimental observations. We analyse four reference models that focus on different stages of plaque growth: the multiphase model of Watson *et al.* (2020) [45] and the reaction-diffusion models of Chalmers *et al.* (2015, 2017) [10,11] and Ougrinovskaia (2011) [37]. Their unique assumptions and equations that reflect up-to-date understandings of plaque dynamics are simplified and incorporated into submodels that we use to represent different stages of plaque formation. If we are able to present models that produce results that qualitatively agree with those of the reference models, we will have extended the reaction-diffusion framework to simply describe the general progression of plaque growth. Our focus will be on the numerical results of the models. This means that while we will describe general plaque dynamics explained in Chapter 2, our comparison of model results with experimental data and the broader biological literature will be in the form of adopting the assumptions of up-to-date reference models.

To meet our thesis aims, our reaction-diffusion model framework must achieve the following. First, the model must describe the key stages of atherosclerotic plaque formation and demonstrate biological behaviours that reflect current understandings of the mechanisms of atherosclerosis. Second, the model must be extendable to include more equations and variables without adding unnecessary additional complexity.

1.3 Thesis outline

We create reaction-diffusion models that represent the key stages of atherosclerotic plaque formation. We begin in Chapter 2 by discussing the biology behind atherosclerosis and the formation of atherosclerotic plaques. In Chapter 3 we review existing models of atherosclerosis and discuss the different ways in which specific stages of atherosclerosis are modelled.

An initial two-species reaction-diffusion model for the migration of SMCs in mid-stage atherosclerotic plaques is presented in Chapter 4. Our aim with this model is to present a simpler alternative to the multiphase model of Watson *et al.* (2018) [44]. We consider two model variables: SMC density and platelet-derived growth factor (PDGF) concentration. This reaction-diffusion model is used as a base submodel in Chapters 5 and 6.

In Chapter 5 we extend the reaction-diffusion model from Chapter 4 to model the synthesis of collagen. We introduce equations for extracellular matrix (ECM) density and transforming growth factor-β (TGF-β) concentration, and investigate the effect of SMCs on fibrous cap formation dynamics.

The base submodel is also extended in Chapter 6 to model the lesions in their entirety from initiation. We consider the migration of modLDL and macrophages and their interactions with SMCs and PDGF in the intima by introducing model variables of macrophage density and modLDL concentration. Because the migration of modLDL and macrophages occurs on a smaller timescale than SMCs, we explore the reaction-diffusion model's ability to accommodate equations that have varying timescales.

The submodels presented in Chapters 4, 5 and 6 are synthesised in Chapter 7 to present a multi-stage model of fibrous cap formation. We analyse which factors are important to fibrous cap dynamics.

Chapter 8 extends the reaction-diffusion model of Chapter 7 by describing necrotic core formation to provide a full model of atherosclerotic plaque formation. We observe the dynamics of the necrotic core, and analyse the factors that affect plaque stability.

We conclude the thesis in Chapter 9 by discussing reviewing our model results. We compare our model with some relevant reference models and present some future directions for our work.

Chapter 2

Atherosclerosis and atherosclerotic plaque formation

This chapter outlines the biology of atherosclerosis, its mechanisms and pathogenesis. It is separated into five sections. The first section describes the structure of the artery and affected regions of plaque formation. The remaining four sections describe the four main stages of atherosclerotic plaque formation: lesion initiation, SMC migration, collagen synthesis and necrotic core formation. These stages are not distinct nor strictly chronological.

2.1 Artery structure

The artery wall (shown in Figure 2.1) consists of three main layers: the intima, the media, and the adventitia. The intima is the innermost layer and is separated from the media by an internal elastic lamina. The media is the middle layer and is comprised of SMCs. The adventitia is the outer layer and consists of connective tissues interspersed with fibroblasts and SMCs [33]. The lumen is the hollow space enclosed by the artery walls, which carries the bloodflow.

The intima is covered by a monolayer of endothelial cells on the luminal side and supported by the internal elastic lamina on the peripheral side. The endothelial cells form the endothelium and act as a selectively permeable barrier between the intima and the bloodflow in the lumen [33]. The endothelium therefore controls transport between the artery wall and the bloodstream, such as the migration of SMCs from the bloodstream into the intima [1].

The endothelial cells are subject to a number of forces including fluid shear stress. Because cells are sensitive to changes in fluid shear stress, regions of changing shear flow exhibit different properties. Regions of high shear flow show endothelial cells deforming and elongating in the direction of blood flow to form a smooth endothelium. Regions of low shear flow however often occur in regions of arterial branching or curvature, and endothelial cells in these regions exhibit no specific orientation [4, 33]. The endothelium is weakened in these regions and shows increased permeability to larger molecules and small particles such as LDL. Plaque formation is more likely to occur in these regions of low share flow [4, 33].

The internal elastic lamina separates the intima from the media. Like the endothelium, it selectively allows the migration of cells into the intima from the media.

The media is composed of SMCs and ECM. It is separated from the adventitia by

another elastic layer known as the external elastic lamina. The vascular SMCs in the media, when subject to certain stimuli, migrate from the media into the intima through the internal elastic lamina [4].

The adventitia contains connective tissue, nerve fibers, lymphatic vessels, and smaller blood vessels that allow transport to and from the outer artery wall. It serves a number of functions, including connecting the artery wall to the central nervous system and facilitating transport to and from the outer artery wall [1]. Immune cells such as macrophages, which are observed in the fibrous cap in the intima, have been observed in the adventitia of advanced lesions [3]. There is limited evidence that adventitial cells migrate towards the intima (in the context of native atherosclerosis) [18], and no report of accumulation of adventitial macrophages in early human atherosclerosis [46].

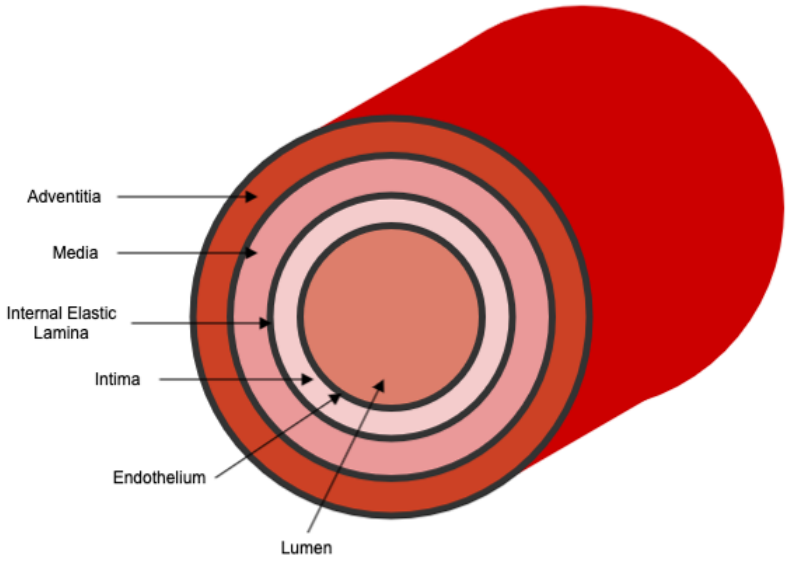

Figure 2.1: A simplified representation of a cross-section through the artery wall.

2.2 Lesion initiation

The process of lesion initiation is represented in Figure 2.2. Atherosclerosis is initiated by the deposition of lipids in the intima. This may be caused by disruptions in blood flow, which change the alignment of the endothelial cells. In regions of low shear flow, junctions between endothelial cells become loose and their permeability increases [4, 33]. Molecules can therefore pass through these loose junctions, including LDLs which are a type of lipoprotein that consist of a lipid centre containing cholesterol [42]. LDLs do not generally pass through firm endothelial junctions, but are able to pass through loose junctions via endocytosis [23,38]. Lipoproteins passing through the intima may become trapped in the intima and accumulate, which promotes the uptake of plasma LDL and triglyceride-rich lipoproteins by the endothelial cells [4]. The accumulation of lipoproteins triggers changes to both lipoproteins and

endothelial cells. Accumulated lipoproteins in the intima become modified, undergoing oxidation which produces inflammatory species [4, 33]. Endothelial cells, in response to the oxidation of LDLs, express adhesion molecules and chemotactic proteins such as P-selectin, E-selectin, VCAM1, and ICAM1 that promote the adhesion of monocytes and other leukocytes [4, 31]. The presence of oxidised LDLs in the intima has also been shown to up-regulate these adhesion molecules [38].

The expression of adhesion molecules by endothelial cells triggers the recruitment of leukocytes including monocytes. Activated endothelial cells produce the monocyte chemokine protein Monocyte Chemoattractant Protein 1 (MCP-1), which stimulates monocytes to enter the intima [16, 31, 36]. Oxidised LDLs also cause MCP-1 to be expressed by SMCs [38]. Upon entering the intima, monocytes differentiate into macrophages in response to locally produced M-CSF and other cytokines [4]. Macrophages accumulate in the intima and uptake modLDL at a greater rate than they uptake native LDLs [4, 6, 29]. As covered in the later section on necrotic core formation 2.5, this process of modLDL uptake results in the conversion of macrophages to foam cells.

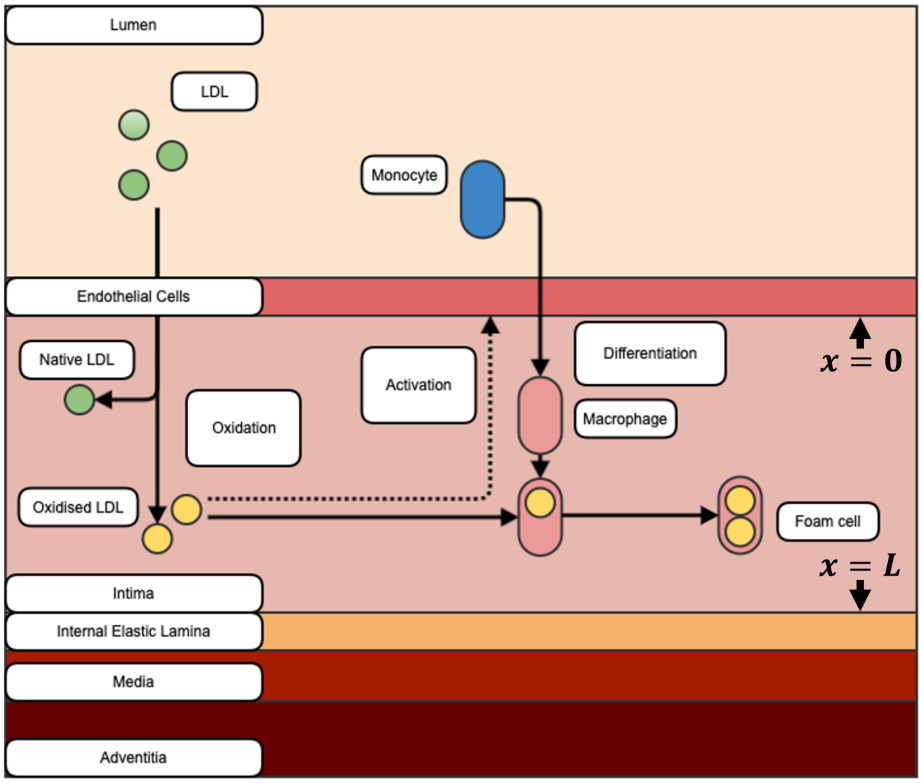

Figure 2.2: A simplified representation of the initiation of lesions and formation of foam cells. LDLs enter the intima past the endothelial cells. The LDLs oxidise and activate the recruitment of monocytes. Monocytes undergo differentiation into macrophages upon entering the intima. ModLDL are uptaken by macrophages to form foam cells.

This initial stage of lesion initiation is therefore characterised by the accumulation of modLDL and macrophages, and foam cells as atherosclerosis progresses, within the intima.

2.3 Smooth muscle cell migration

The accumulation of modLDL and macrophages within the intima produces inflammatory mediators and cytokines. Macrophages for example express growth factors such as Transforming Growth Factors α and β (TGF-α and β) as well as platelet-derived growth factor BB (PDGF-BB) [28, 46]. They also express other cytokines such as Interleukin-10 (IL-10) and vascular cell adhesion molecule 1 (VCAM1) [3,28]. In healthy arteries, SMCs are located mostly in the media and exhibit a differentiated (quiescent) phenotype. Quiescent SMCs exhibit a low rate of proliferation and migration, and express contractile proteins [25]. SMCs exhibit phenotypic plasticity, meaning that they are able to transform their phenotype [4, 25, 26]. In response to cytokines such as PDGF-BB, SMCs in the media transform to a proliferative stage and adopt a synthetic (de-differentiated) phenotype. Synthetic SMCs have higher expression of ECM components and ECM-remodelling enzymes, are more proliferative and can migrate into the intima from the surrounding media through the internal elastic lamina [4]. Figure 2.3 shows the effect of cytokines and growth factors on SMCs in the media and the migration of de-differentiated SMCs into the intima.

In the intima, de-differentiated SMCs undergo clonal expansion. SMCs that dominate the fibrous cap in the intima have been found to express genes associated with differentiated SMCs, suggesting that de-differentiated SMCs can switch their phenotype back to a quiescent one [25, 28]. Growth factors such as PDGF-BB drive SMC dedifferentiation, proliferation, and migration [28]. PDGF-BB in particular acts as a chemoattractant for SMCs [39], and SMCs are understood to migrate along a gradient of PDGF-BB that increases from the media to the endothelium [36]. SMCs are however affected by the production of cytokines such as interferon-γ (IFN-γ) by oxidised lipoproteins and a change of macrophage phenotype, which promote apoptosis and cause a decrease in SMC expansion rates [36].

As SMCs accumulate in the intima, this leads to an expansion of the intima (known as diffuse intimal thickening) which is thought to predispose the artery for plaque development [3]. The accumulation of SMCs and subsequent diffuse intimal thickening is part of the pathological intimal thickening stage of atherosclerosis. In the pathological intimal thickening stage, extracellular lipid pools are formed from the accumulation of modLDL in the intima. These pools form within a layer of SMCs and ECM [3].

As de-differentiated SMCs proliferate and migrate into the intima, they secrete ECM proteins. This remodels the intimal ECM, which consists mainly collagen, into a protective fibrous cap [3, 4, 25]. The mechanism of the synthesis of new collagen is explained in the next section 2.4.

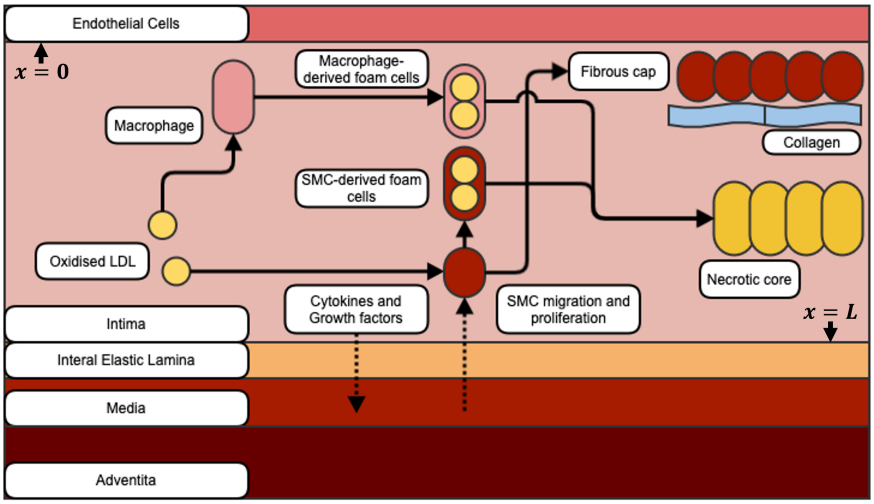

Figure 2.3: A simplified representation of the formation of a fibrous cap and necrotic core. In response to growth factors and cytokines, SMCs migrate into the intima. SMCs synthesise ECM to produce a fibrous cap. Both macrophages and SMCs uptake modLDL to create foam cells. These foam cells contribute to the creation of a necrotic core.

2.4 Collagen synthesis

The remodelling of the intimal ECM involves the replacement of existing intima ECM with new ECM comprised of synthesised and deposited collagen. SMCs in the intima deposit types I and III collagen, elastin and fibronectin, and synthesise ECM molecules including type VIII collagen, osteopontin and tenascin [2]. The synthesis of collagen by SMCs is affected by signalling pathways such as TGF-β, PDGF, and myocardin-related transcription factor B (MRTF-B). TGF-β is secreted by endothelial cells and expressed by macrophages [38], and promotes intimal growth and stimulates SMC synthesis of collagen [22,34]. This was observed when increased TGF-β expression in rats exhibited increased extracellular matrix deposition and SMC nuclei prevalence in intimal lesions [40]. On the other hand, TGF-β has also been observed to promote the SMC contractile phenotype, potentially leading to phenotype switching [3].

The synthesized ECM creates a fibrous cap, which is mainly composed of collagen-rich (mostly type I and III) fibre tissues, SMC, macrophages and T lymphocytes [38]. As seen in Figure 2.3, this fibrous cap lies on top of the ECM. This fibrous cap forms the atherosclerotic plaque and over time undergoes calcification, marking the transformation of the pathological intimal thickening to fibroatheromas [4]. Fibroatheromas are necrotic cores (also known as atheromas) that are encapsulated by a fibrous cap in the intima. Necrotic cores are comprised of extracellular lipid pools and dead SMCs and macrophages. The formation of these cores is described further in the next section 2.5. As fibroatheromas develop, the calcification of the plaque and continued proliferation of SMCs leads to the increased thickening of the intima [4].

The stability of this plaque is influenced by the integrity of the fibrous cap.

A number of factors degrade the fibrous cap. These include the effect of the necrotic core, and macrophages. Macrophages, and other inflammatory cells, secrete matrix metalloproteinase (MMP) which contribute to the lysis (cell breakdown) of extracellular matrix (in particular MMP-165) [3, 24, 38]. MMPs are also expressed by endothelial cells and SMCs. Cytokines such as IFN-γ and IL-1β, which are increasingly expressed during inflammation, blunt collagen synthesis by SMC and drive apoptosis [28]. The effect of the necrotic core on the fibrous cap is explained in Section 2.5. These factors may degrade the fibrous cap, leaving it vulnerable to rupture and thrombosis [4, 33, 35]. Vulnerable plaques generally have thin fibrous caps and increased numbers of inflammatory cells [33], while ruptures frequently occur at the lesion edges where foam cell density is greatest. Inflammation is therefore believed to influence the degradation of the fibrous cap and the breakdown of the integrity of the plaque.

2.5 Necrotic core formation

As modLDL and macrophages accumulate within the intima, macrophages ingest modLDL to remove them from the intima [5]. Macrophages uptake modLDL through phagocytosis and become lipid-laden [4]. These lipid-rich macrophages are termed "foam cells". Macrophages do not only ingest modLDL; they can produce cytotoxic substances such as tumor necrosis factors (TNF), growth factors, precoagulation substances (including tissue factors), and free radicals [38]. These substances can cause damage to the endothelium and increase LDL oxidation. The production of inflammatory species is therefore increased, leading to further SMC recruitment.

While SMCs contribute to the creation of the fibrous collagen cap as described in Section 2.4, some SMCs also create foam cells. The proportion of SMCs that migrate into intima undergo clonal expansion and redifferentiate into contractile SMCs. These SMCs can then undergo trans-differentiation into macrophage-like cells, which can uptake modLDL to create foam cells [4]. This phenotype-switching has been linked to SMC apoptosis (rapid programmed cell death) and free cholesterol in the tissue [3]. In animal models, up to 50% of foam cells are estimated to be SMC-derived [3]. The retention of foam cells is mediated by a number of factors, including the expression of adhesion molecules such as intercellular adhesion molecule-1 (ICAM-1), vascular cell adhesion molecule (VCAM-1) and fractalkine (CX3CL1) [17].

The plaque grows as the atheroma and fibrous cap develop. Over time, the foam cells in the atheroma undergo necrosis (non-programmed form of cell death characterized by catastrophic loss of plasma membrane integrity and leakage of cell contents) and apoptosis, leading to the accumulation of cell debris and cholesterol in the centre of the plaque [3]. This forms a necrotic core in the plaque, as shown in Figure 2.3. As the fibroatheroma develops and calcification increases, the plaque matures and bulges into the artery wall [3, 4]. The necrotic core develops below the fibrous cap,

which raises the risk of the rupture and release of the cell debris and cholesterol into the bloodstream [4, 33, 35].

Plaque rupture occurs when the fibrous cap thins and the integrity of the plaque breaks down. The exposure of collagen and lipids to the bloodstream contributes to the accumulation and adhesion of platelets and formation of blood clots (thrombus), which may suddenly block the bloodstream [38]. This may cause a stroke or myocardial infarction.

Chapter 3

Review of existing mathematical models

In this chapter, we review some of the mathematical models that describe various mechanisms of atherosclerosis. We explore the different aspects of atherosclerosis that are the focus of these models, and the different model types used. The models that we are interested in are those for specific stages of atherosclerosis and the dynamics of cells and particles inside the artery wall, rather than those that model forces such as fluid flow, wall shear stress or cell transport. These models are separated below into two general cases: models of inflammation, and models of plaque formation.

Models of inflammation focus on the inflammatory and immunological processes of atherosclerosis, rather than the direct mechanisms of cap formation. These processes include LDL oxidation and macrophage recruitment. These models may directly describe the early stages of lesion core formation such as the conversion of macrophages to foam cells.

Models of plaque formation focus on the creation of morphological features of the atherosclerotic plaque, including the fibrous cap and necrotic core. These models may also include the earlier stages of inflammation but focus on stages after lesion initiation, such as SMC migration, ECM creation, and the accumulation of foam cells and debris.

3.1 Models of inflammation

As described in Section 2.2, the oxidation of accumulated lipoproteins in the intima produces inflammatory species. This triggers the expression of adhesion molecules by the endothelial cells, which then promote the adhesion of monocytes. These monocytes differentiate into macrophages in the intima. Macrophages accumulating in the intima consume modLDL which results in the conversion of macrophages to foam cells. These processes form the lesion initiation stage of atherosclerosis. A number of models model this early stage [9, 14, 30].

An ordinary differential equation (ODE) model which focuses on LDL oxidation is presented in Cobbold *et al.* (2002) [14]. The model distinguishes six types of LDL and models the process of LDL modification and high density lipoproteins (HDL) oxidation. LDL are assumed to be oxidised by a free radical and undergo Vitamin E and lipid oxidation. HDLs are modelled as inhibiting LDL oxidation and a modulating force on inflammation. As an ODE model dependent only on time,

the model does not model spatial changes in the different species of LDL on the artery wall.

Another ODE model that separates LDL into classes is presented in Thon *et al.* (2018) [43]. This model is a combination of three submodels which reflect various in vitro experiments. LDL is distinguished into native LDL and modLDL, with only modLDL being assumed to stimulate inflammation. The first submodel describes the modification of LDL and its uptake due to phagocytosis by macrophages. The second submodel focuses on HDL inhibition of LDL modification, and the third submodel addresses the ingestion of modLDL by macrophages and the esterification of free cholesterol within macrophages. While this model presents a comprehensive description of LDL and macrophage dynamics, its level of detail and the eight ODEs in the combined model make it complex and difficult to easily extend to include other processes.

Khatib *et al.* (2007) [30] proposes a one-dimensional reaction-diffusion model with two species: immune cells (monocytes, macrophages) and cytokines secreted by the immune cells. Oxidised LDLs, which are assumed to be generated within the intima, are not modelled explicitly and instead form the boundary condition which models macrophages migration across the luminal boundary with oxidised LDLs acting as a macrophage chemoattractant. There is no model mechanism for the removal of LDL, and oxidised LDL are assumed to accumulate infinitely. Macrophages are assumed to undergo recruitment from the lumen, which is promoted by pro-inflammatory cytokines. This rate of recruitment is assumed to become saturated at high cytokine densities. The accumulation of macrophages, and the propagation of inflammation within the intima, is described as a traveling wave and is presented as dependent on oxidised LDL concentration. There are no foam cell species in the model as the dynamics of macrophages are assumed to be similar to that of foam cells.

A subsequent one-dimensional reaction-diffusion model by Younes *et al.* (2021) [47] builds on the model of Khatib *et al.* (2007) to include oxidised LDL as a model species. LDL enter the intima from the lumen, where they are assumed to undergo oxidation and phagocytosis by pro-inflammatory macrophages. The model does not distinguish between macrophages and monocytes, but extends the scope of the model from Khatib *et al.* (2007) to include the mechanisms of foam cell production. Foam cell production is modelled by the uptake of modLDL by macrophages. It is assumed that all macrophages that uptake modLDL differentiate into foam cells. This means that oxidised LDL concentration affects both inflammation and the rate of foam cell production. The work of Khatib *et al.* (2007) and Younes *et al.* (2021) therefore demonstrate the ability of reaction-diffusion models to be extended to include new model species.

Reaction-diffusion models are therefore used by a number of research papers to model the early stages of lesion initiation [10,11,30,37,47]. The model presented by Chalmers *et al.* (2015) [11] explores the mechanisms of early atherosclerosis by presenting equations for modLDL, chemoattractants, cytokines, macrophages/monocytes, and foam cells. Macrophage chemotaxis is a key feature of this model, with macrophages moving chemotactically up the gradients of both modLDL and chemoattractants such as MCP-1. ModLDL stimulates macrophage ingress into the intima and foam

cell and chemoattractant production. As with the previous two models [30, 47], all macrophages that uptake modLDL differentiate into foam cells. Foam cells are modelled as having no spatial movement. This model framework is extended in Chalmers *et al.* (2017) [10] to include equations for HDL and their modulating effect on cholesterol in foam cells. We note that these models correctly predict that the rate of accumulation of foam cells is proportional to the influx of modLDL, and also offer some hypotheses on HDL dynamics that have not been observed in experiments on real lesions. The terms and assumptions that reflect up-to-date general lesion dynamics and the reaction-diffusion framework make the models useful references for our research model. Further details of these models are explored in later chapters (6.2 and 8.1.1).

Other research papers employ submodels, which are part of a larger framework model, to model stages of inflammation. An example is Ougrinovskaia (2011) [37], which presents a reaction-diffusion model with submodels that describe different stages of atherosclerosis. One submodel incorporates three main lesion constituents: modLDL, macrophages/monocytes and macrophage chemoattractants. The equations for these species model the early lesion initiation stage and ignore the conversion of macrophages to foam cells. The uptake of modLDL by macrophages is still described, and macrophages are assumed to move chemotactically up the gradient of macrophage chemoattractants but not modLDL. A submodel described later in the thesis examines the early lipid core formation stage by introducing equations for foam cells and the early extra-cellular lipid pool core. This submodel builds on the earlier submodel that modelled lesion initiation. The assumption that all macrophages that uptake modLDL differentiate into foam cells is continued, but foam cells are additionally assumed to undergo spatial motion. Foam cells diffuse and are displaced by other cells. These later submodels therefore retain the dynamics presented in earlier submodels while introducing the dynamics of different stages of atherosclerosis. This model is explored in depth in later chapters (4.1.2, 6.1 and 8.1.2).

3.2 Models of plaque formation

Some models that describe the early lesion initiation stage of atherosclerosis also include the later stage of necrotic core formation, which forms part of later stage plaques. A model that is different to the spatially structured ODE and reaction-diffusion models presented in Section 3.1 is that proposed by Ford *et al.* (2019) [19]. The model does not include spatial dependence but the cell populations are structured according to intra-cellular lipid load. The focus of the model is the dynamics within the plaque rather than spatial patterns. The plaque is assumed to be comprised of live, apoptotic and necrotic macrophages with internalised lipid content. The model equations distinguish between live and apoptotic macrophages within the plaque, and the rate of production of necrotic macrophages is modelled by a live macrophage cell death term. Macrophages are assumed to enter the plaque through the endothelium, and migrate out of the artery. Within the plaque, macrophages undergo apoptosis, phagocytosis of necrotic cells, efferocytosis (the phagocytosis of

apoptotic cells), recruitment and necrosis. Rather than modelling the density or total number of foam cells, the development of the necrotic core is modelled by the total lipid load of necrotic macrophages in the plaque. This model is extended by Chambers *et al.* (2023) [12] to account for local macrophage proliferation. Additional terms are added to the macrophage population equation which describe the rate of proliferation of macrophages by cell division into two daughter cells and how extra lipid is added to the macrophage population via cell proliferation. This is a unique way of modelling necrotic core development that is an alternative to the spatially dependent framework that our thesis focuses on.

Another type of model is a multiphase model [7, 32, 44, 45]. Multiphase models consider various species such as SMCs and macrophages as separate distinct phases by defining equations for each phase. Each phase generally has continuity equations that describe various thermodynamic quantities, such as the conservation of mass and momentum. The paper by Watson *et al.* (2018) [44] models the migration of SMCs into the intima by proposing a model with two phases: matrix-synthesising SMCs and a generic non-SMC phase (comprising of all other cells and tissues). A non-volume-occupying species representing PDGF is modelled as being present only in the generic non-SMC phase. The two phases are represented by their volume fractions, and it is assumed that the remodelling of ECM and the distribution of the deposited matrix is reflected by the SMC profile. Each phase is mass balanced, and both phases are assumed to have the same constant total density. The two phases are assumed to satisfy a no-voids condition so that the intima tissue is incompressible and continuous. The model equation of the SMC phase assumes that SMCs migrate chemotactically through the intima at a rate determined by a function that decreases as the local PDGF concentration decreases. This chemotactic motion is modelled as a mechanism of stress relief in the SMC phase. The stress is due to interphase force exerted by the SMC phase on the non-SMC phase, and is therefore balanced by an equal and opposite interphase force exerted by the non-SMC phase on the SMC phase.

Watson *et al.* (2020) [45] extends the model in Watson *et al.* (2018) to include an immobile ECM phase and another non-volume-occupying species representing TGF-β. This model explicitly describes the mechanisms of the synthesis of a fibrous cap through the model equation for ECM volume fraction in the intima. TGF-β is assumed to stimulate ECM remodelling and matrix deposition, and SMCs are assumed to degrade the ECM by the expression of MMPs. This method provides a detailed insight into the mechanisms of SMC migration and the formation of a fibrous cap as physical forces. It is complex however, and the subsequent introduction of new phases and species requires mass and momentum balancing. Further detail on these models is provided in later chapters (4.1.1, 5.1). We note however that the analysis of TGF-β and MMPs and their effects on cap dynamics reflect results from recent studies [13, 27]. We aim to reflect this analysis in our reaction-diffusion models to present up-to-date understandings of plaque dynamics.

Friedman *et al.* (2015) [20] presents a reaction-diffusion model that models a number of mechanisms of plaque formation, including the migration of SMCs and the synthesis of ECM. It proposes fourteen variables which include LDL, MCP-1, MMPs, SMCs, foam cells, macrophages, PDGF, ECM and T cells. The large number of

variables and respective model equations allows the model to represent a wide range of processes. SMCs are assumed to be attracted into the intima from the media by PDGF and MCP-1, and to undergo chemotaxis by MCP-1 and PDGF and haptotaxis by ECM. Macrophages are assumed to migrate chemotactically up the MCP-1 gradient and uptake oxidised LDLs to convert into foam cells. The models are solved numerically in two dimensions using the finite element method where the domain is represented by a mesh of closed triangles, with each triangle having a defined polygonal boundary. This allows a two-dimensional simulation of the cross-section of an artery with a growing plaque.

We return to the reaction-diffusion framework model of Ougrinovskaia (2011) [37], which also models the formation of a fibrous cap and necrotic core. As explained in Section 3.1, the reaction-diffusion framework model is comprised of submodels that model individual stages of atherosclerosis. The complete reaction-diffusion model is comprised of five submodels that focus on the following stages: lesion initiation, early lipid core formation, SMC migration, fibrous cap formation, and atheroma formation. As outlined in the earlier section 3.1, submodels are able to build on earlier submodels. The model equation for SMCs in the SMC migration submodel describes SMC migration and proliferation in the intima. In the atheroma formation submodel, coupling between the macrophage density and SMC population is introduced to the model equation for SMCs to describe immune cell induced apoptosis of SMCs. We note that there are no mass and momentum balancing concerns when introducing coupling into reaction-diffusion equations. This relative simplicity in introducing coupling and expanding model equations is an advantage of the reaction-diffusion framework employed in this model. We compare this model to the more recent multiphase model of Watson *et al.* (2018) [44] in the next chapter 4.

Our thesis aim is to create a reaction-diffusion framework that can be extended to simply model key stages of atherosclerotic plaque dynamics while retaining experimental validity. We are therefore interested in models that can serve as references. We focus on five models described above: the multiphase models of Watson *et al.* (2018, 2020) and the reaction-diffusion models of Chalmers *et al.* (2015, 2017) and Ougrinovskaia (2011). The multiphase models of Watson *et al.* (2018, 2020) are recent works from our research group and their results reflect up-to-date experimental observations on SMC, PDGF and ECM dynamics. As noted before, multiphase models can be mathematically and computationally complex. Our interest in these models is to produce qualitatively similar results while using a simpler reaction-diffusion framework. The reaction-diffusion models of Chalmers *et al.* (2015, 2017) [10,11] focus on the early stages of plaque formation, including modLDL and macrophage dynamics. They also present results that reflect up-to-date experimental observations which allow our models to reflect current experimental data and the broader biological literature. These models are reaction-diffusion models and therefore provide useful references to our thesis reaction-diffusion framework. The reaction-diffusion model of Ougrinovskaia (2011) is comprised of submodels that model individual stages of atherosclerosis. We recall that an objective of our thesis is that our model must be extendable to include more equations and variables without adding additional complexity. This model is therefore a useful reference in analysing how the various submodels are married together.

Chapter 4

Creating the base model by modelling smooth muscle cell and platelet-derived growth factor characteristics

In this chapter, our aim is to create a two species reaction-diffusion model that models the SMC migration stage of atherosclerosis. The purpose of beginning with a two species model is to establish a reaction-diffusion framework that can be extended in subsequent chapters to model other stages of atherosclerosis. Because we intend to present a complete reaction-diffusion model that incorporates a number of stages of atherosclerosis, including those that are mature, it is important to create a biologically and mathematically sound submodel before extending it.

We detail two models created in our research group that model the SMC migration stage of atherosclerosis: Watson *et al.* (2018) [44], and Ougrinovskaia (2011) [37]. The approach to modelling differs between the two models, with the former model being a multiphase model and the latter being a reaction-diffusion model (as outlined in the previous chapter 3). The assumptions of the model proposed in Watson *et al.* (2018) reflect more recent understandings in research, but multiphase models involve some complexity due to the physical forces that must be accounted for in each phase. The submodel approach of Ougrinovskaia (2011) provides a simpler reaction-diffusion framework which we aim to use but modify with more biologically relevant assumptions and terms. We therefore compare the two models to analyse the assumptions and terms used to describe the key dynamics of SMC migration into the intima.

4.1 Two models: Watson *et al.* (2018); Ougrinovskaia (2011)

Watson *et al.* (2018) models the preliminary stages of atherosclerotic plaque formation by modelling different dynamics as multiphase equations. For example, SMCs are treated as a phase and non-SMC cells are treated as another distinct phase. These phases are governed by mass balance and momentum balance conditions and are generally also subject to conditions such as no voids conditions. These conditions impose volume filling and mass and volume distribution in a system, allowing the model to capture all dynamics in a closed system.

On the other hand Ougrinovskaia (2011) models the preliminary stages of atherosclerotic plaque formation as reaction-diffusion equations. Each relevant cell and growth factor is modelled by a partial differential equation and is not treated as a phase. This means that the formulation of the system is simpler, as there is no need for mass or momentum balances.

4.1.1 Multiphase SMC and PDGF model (Watson *et al.* (2018))

Watson *et al.* (2018) models the interaction between SMCs and PDGF with a multiphase approach. This model represents two phases: SMCs; and all other cells and tissues. SMCs are represented as a volume fraction denoted by $s(x,t)$ and all other cells and tissues are represented as a volume fraction denoted by $w(x,t)$. SMC dynamics are described by an elliptic parabolic PDE for SMC volume fraction. PDGF is treated as volume free and its dynamics are described by a reaction-diffusion equation for PDGF concentration.

The model accounts for early stage SMC migration and proliferation as a result of PDGF expression at the endothelium. Its two phase formulation addresses volume filling and exclusion in the intima. The model does not explicitly describe lesion cap formation but focuses instead on accurately describing SMC migration and proliferation. Due to fibrous collagen cap synthesis by SMCs, the multiphase approach is intended to indirectly address fibrous collagen cap stability.

The multiphase approach requires the two phases to be mass and momentum balanced. The model further assumes a no voids condition such that $s + w = 1$. Denoting SMC volume fraction as $s(x,t)$, all other cell and tissue volume fraction as $w(x,t)$, and PDGF concentration as $g(x,t)$, mass balance is applied to each phase:

$$\frac{\partial s}{\partial t} = \frac{\partial}{\partial x}\left(\nu_s s\right) = S_s(g,s,w), \tag{4.1}$$

$$\frac{\partial w}{\partial t} = \frac{\partial}{\partial x}\left(\nu_w w\right) = -S_s(g,s,w). \tag{4.2}$$

It is assumed that both phases have the same constant density. Where the rate of SMC production is denoted by S_s, mass transfers from the SMC phase to the other cell and tissue phase as SMCs degrades.

For momentum balancing, it is assumed that inertial effects are negligible and there are no external forces acting on the system. Where τ_s and τ_w represent the SMC and other cell and tissue phase stress terms, and F_{sw} denotes the force exerted by the SMC phase on the other cell and tissue phase, the momentum balance equations

become:

$$\frac{\partial}{\partial x}(\tau_s s) = F_{sw}, \tag{4.3}$$

$$\frac{\partial}{\partial x}(\tau_w w) = -F_{sw}. \tag{4.4}$$

We do not extensively describe the model simplification taken in Watson *et al.* (2018). We can understand however that increasing the number of phases in this system requires additional mass and momentum balancing, which potentially introduces more complexity. We note that the equations (4.1), (4.2), (4.3) and (4.4) produce the non-dimensionalised model equations for SMC and PDGF dynamics:

$$\frac{\partial s}{\partial t} = \frac{\partial}{\partial x}\left[(1-s)\frac{\partial}{\partial x}(s\Lambda)\right] + rs(1-s)\left(1 + \frac{Ag}{g_s + g}\right) - \beta_s s, \tag{4.5}$$

$$\frac{\partial}{\partial x}\left[(1-s)\frac{\partial g}{\partial x}\right] = \eta_g g s(1-s) + \beta_g g(1-s). \tag{4.6}$$

The first term on the right hand side of the first equation (4.5) represents the mass balance of both phases. Expanding this term gives the effective nonlinear diffusion and chemotaxis coefficients of SMCs which are proportional to a number of parameters. Firstly, the definition of the two phases and no voids condition means that both the diffusion and chemotaxis coefficient are proportional to the non-SMC phase. It is therefore assumed that the non-SMC phase influences SMC migration in the intima. The function $\Lambda(g)$ represents the assumption that SMC motility is nonlinear and influenced by local PDGF concentration g. Expanding the term via the chain rule results in SMC motility being dependent on both local PDGF concentration and its gradient. The second and third source terms describe SMC proliferation and decay respectively. Proliferation is assumed to be logistic with respect to s, where r represents a rescaled mitosis rate, A_g represents the maximum possible PDGF-stimulated increase in mitosis rate, and g_s represents the half-maximal kinetic constant. It is also assumed to be proportional to both local SMC and the non-SMC volume fractions. Decay is assumed to be linearly proportional to local SMC volume fraction and decay rate β_s.

The second equation assumes that the characteristic timescale of PDGF diffusion is significantly shorter than SMC migration. This means that PDGF is treated as being at steady state within the intima. It also means that there is no advective transport of PDGF within the non-SMC phase. The two terms on the right hand side of the equation represent the dynamics of PDGF in the intima steady state: SMC uptake and chemical decay. There are no source terms, and instead PDGF is introduced at the endothelial boundary.

The boundaries are defined as the endothelial layer at $x = 0$, and the medial layer at $x = L$ where L is the length of the region between the two layers. The domain is defined on a one-dimensional domain $x \in [0, L]$ where $L = 1$. The boundary

conditions are:

$$\begin{aligned} &\frac{\partial}{\partial x}(s\Lambda)\Big|_{x=0} = 0, \quad \frac{\partial}{\partial x}(s\Lambda)\Big|_{x=1} = \frac{d\Lambda}{dg}s^*\frac{\partial g}{\partial x}, \text{ where } \Lambda(g) = \frac{\chi}{1+(\kappa g)^n}, \\ &\frac{\partial g}{\partial x}\Big|_{x=0} = -\alpha_g, \quad \frac{\partial g}{\partial x}\Big|_{x=1} = \sigma_g(g^* - g), \end{aligned} \tag{4.7}$$

with initial condition

$$m(x,0) = s_i, \tag{4.8}$$

where s_i represents a small, uniform initial SMC population such that $0 < s_i \ll 1$. This initial SMC population is required as the velocity of the SMC phase ν_s observed in (4.1) creates a singularity when $s_i = 0$. At the medial boundary, s^* and g^* respectively denote some constant notional medial SMC volume fraction and PDGF concentration such that $s^* < 1$ and $g^* < 1$.

At $x = 0$, there is zero flux for SMCs following the assumption that SMCs neither enter the intima via the lumen nor exit via the endothelium. For PDGF, there is an inward flux representing PDGF entering from the lumen.

At $x = 1$, it is assumed that SMC migration is entirely chemotactic and dependent on the local PDGF gradient as well as the local SMC fraction volume. Passive diffusion is negligible, meaning that the contribution proportional to $\frac{\partial s}{\partial x}$ is zero. For PDGF, the gradient at this boundary is set as negative to represent SMCs migrating across the medial boundary by chemotaxis.

4.1.2 Reaction-diffusion model (Ougrinovskaia (2011))

The reaction-diffusion model of Ougrinovskaia (2011) shares a number of similarities with Watson *et al.* (2018). It explores the dynamics behind cap formation, focusing on the intermediate stages of atherosclerotic lesion formation. The domain of the model systems is also a one dimensional slice of the intima with $x = 0$ at the endothelial boundary and $x = L$ the media boundary where L is the length of the domain. Unlike the multiphase model of Watson *et al.* (2018), the partial differential equation model individually accounts for a number of mechanisms rather than treating them as phases. We focus on the model that explores the dynamics of modLDL, macrophages, macrophage chemoattractant MCP-1, SMCs and PDGF. This means that where non-SMC cells and tissue are treated as a volume-filling phase w such that $w = 1 - s$, the system includes equations for LDLs, macrophages and macrophage chemoattractants. Further developments of the model, explored in later stages of the thesis, include more mechanics such ECM and foam cells.

LDLs enter the intima where they oxidise to become modLDL; the model assumes that this occurs fast enough to directly describe modLDLs influx σ_l at the $x = 0$ boundary. ModLDLs diffuse through the domain with respect to diffusion coefficient D_l. They are assumed to be uptaken by both macrophages and foam cells (denoted by $N(x,t)$) at a rate proportional to the function $T_l(l)$ and to undergo linear decay with respect to the degradation term d_l.

Macrophages also enter the intima, represented as an influx σ_m at the $x = 0$ boundary. Motility is described as being driven by diffusion and chemotaxis, with macrophages diffusing through the domain with respect to diffusion coefficient D_m. They move chemotactically along the gradient of MCP-1 with respect to chemotaxis coefficient χ_m. As macrophages uptake modLDLs as described above, they are assumed to convert to foam cells at a rate proportional to the function $T_m(l)$. They also undergo aptosis and necrosis, which are represented as a linear decay term d_m.

Rather than migrating into the intima from the lumen, macrophage chemoattractants such as MCP-1 are mainly produced by endothelial cells. This is described in two forms: firstly as an influx σ_p at the $x = 0$ boundary, and also as a source term S_p. Macrophage chemoattractants diffuse through the domain with respect to diffusion coefficient D_p. They are assumed to decay linearly with respect to with respect to the decay term d_p.

Smooth muscle cells are assumed to migrate from the media into the lumen which is described as an influx σ_s at the $x = 1$ boundary. Unlike the flux conditions of equations (4.7), this influx is constant and independent of chemoattractant gradient. The flux terms are also different: while SMCs are described as diffusing through the intima with respect to diffusion coefficient D_s and moving chemotactically along the gradient of PDGF with respect to chemotaxis coefficient χ_s, they are also assumed to undergo haptotaxis along the ECM. This haptotactic flux is described with respect to haptotaxis coefficient h_s. The source term is similar to that of equation (4.5), proportional to logistic growth described by $S_s(g)$ and mitosis. While SMCs are assumed to undergo linear decay with respect to decay term d_s, the model goes further to describe SMC apoptosis in response to increased cytokines. This is represented as proportional to a decay term d_{sm}.

The differences in flux boundary conditions continue with PDGF. The model assumes zero flux conditions at both boundaries, with only a source term S_g due to PDGF elaboration by macrophages. PDGF is assumed to undergo diffusion with respect to diffusion coefficient D_s and to decay linearly proportional to a decay term d_g.

The domain is defined on a one-dimensional domain $x \in [0, L]$ where $L = 1$ and time is denoted as t. Setting LDL concentration as $l(x,t)$, macrophage density as $m(x,t)$, macrophage chemoattractant concentration as $p(x,t)$, collagen concentration as $x(c,t)$, PDGF concentration as $g(x,t)$ and SMC density as $s(x,t)$, the system

of equations become:

$$\frac{\partial l}{\partial t} = D_l \frac{\partial^2 l}{\partial x^2} - \frac{\mu_l l m}{1+l} - d_l l, \tag{4.9}$$

$$\frac{\partial m}{\partial t} = D_m \frac{\partial^2 m}{\partial x^2} - \frac{\partial}{\partial x}\Big(\chi_m m \frac{\partial p}{\partial x}\Big) - \frac{\mu_m l m}{1+l} - d_m m, \tag{4.10}$$

$$\frac{\partial p}{\partial t} = D_p \frac{\partial^2 p}{\partial x^2} - d_p p, \tag{4.11}$$

$$\frac{\partial g}{\partial t} = D_g \frac{\partial^2 g}{\partial x^2} + \sigma_g m - d_g g, \tag{4.12}$$

$$\frac{\partial s}{\partial t} = D_s \frac{\partial^2 s}{\partial x^2} - \frac{\partial}{\partial x}\Big(\chi_s s \frac{\partial g}{\partial x} + h_s \frac{\partial c}{\partial x}\Big) + \Big(1 + \frac{r_s g}{G_s + g}\Big) s(1-s) - d_s s. \tag{4.13}$$

The relevant boundary and initial conditions are:

$$\begin{aligned}
&\frac{\partial l}{\partial x}\Big|_{x=0} = -\frac{\sigma_l}{D_l}, && \frac{\partial l}{\partial x}\Big|_{x=1} = 0,\\
&\frac{\partial m}{\partial x}\Big|_{x=0} = -\frac{\sigma_m - \chi_m m \frac{\partial p}{\partial x}}{D_m}, && \frac{\partial m}{\partial x}\Big|_{x=1} = 0,\\
&\frac{\partial p}{\partial x}\Big|_{x=0} = -\frac{\sigma_p}{D_p}, && \frac{\partial p}{\partial x}\Big|_{x=1} = 0,\\
&\frac{\partial g}{\partial x}\Big|_{x=0} = 0, && \frac{\partial g}{\partial x}\Big|_{x=1} = 0,\\
&\frac{\partial s}{\partial x}\Big|_{x=0} = 0, && \frac{\partial s}{\partial x}\Big|_{x=1} = \frac{\sigma_s}{D_s},
\end{aligned} \tag{4.14}$$

with initial conditions

$$s(x,0) = 0, \quad g(x,0) = 0. \tag{4.15}$$

We focus on the equations governing the dynamics of PDGF and SMCs: namely the PDEs (4.12) and (4.13). By limiting the scope of the equations to only s and g, the objective of this chapter is to capture the main dynamics of equations (4.6) and (4.5) from the multiphase model in the simpler form of reaction-diffusion model PDEs.

Both the multiphase model of Watson *et al.* (2018) and the reaction-diffusion model of Ougrinovskaia (2011) describe the smooth muscle cell migration stage of cap formation. The multiphase model is however a more recent model; the experimental research findings used in it are more up-to-date and are reflected in the different dynamics of PDGF and the boundaries. The inclusion of different phases also allows for volume filling and exclusion in the intima. The multiphase model however is complex. Its reliance on distinct phases makes it less easily adaptable to different systems with large numbers of phases. Each additional phase introduces new mass and momentum balance equations. The reaction-diffusion model is able to include additional phases without requiring significant changes to other equations due to changes in volume filling and exclusion. This need for all phases to be accounted for in mass and momentum balance makes multiphase models less easily adaptable.

We note that the findings of the two models differ. In Ougrinovskaia (2011), the

effects of varying the chemotaxis coefficient χ_s were analysed. It was found that while χ_s had an effect on the distribution of SMCs (increasing the value of χ_s translated to greater accumulation of SMCs at the endothelial boundary), the overall distribution of SMCs throughout the intima was relatively flat. An increase in the value of χ_s by approximately 10^2 was required to produce a significant increase in the accumulation of SMCs at the endothelial boundary. It was therefore concluded that chemotaxis alone was not the only contributor to SMC migration. We note however that in this model, there is no influx of PDGF; PDGF is only expressed by macrophages. As a result, the distribution of PDGF is very flat. This means that the rate of chemotactic migration is near constant throughout the intima.

This differs from the results of Watson *et al.* (2018). As shown in 4.3.1, the PDGF profile is not uniform. The model also assumes an inward flux of PDGF at the endothelial boundary. In the multiphase model, SMC diffusion and chemotactic migration coefficients are proportional to the SMC phase pressure function $\Lambda(g)$ and $\frac{d\Lambda(g)}{g}$ respectively. The findings are explained in detail in 4.4.2; we note that a larger cap region was observed when the chemotaxis terms were increased. We recall that in Ougrinovskaia (2011), increasing the chemotaxis coefficient did lead to a larger cap region but that the distribution of SMCs throughout the intima was still relatively flat, whereas in the multiphase model, there is a clear discernible cap region. One explanation for this difference is the PDGF profile and constant chemotaxis coefficient, which leads to less migration of SMCs towards the endothelial boundary in Ougrinovskaia (2011) compared to Watson *et al.* (2018). To address this, we may propose SMC flux terms that while simpler, can be combined with the assumptions of cell movement up the PDGF gradient to reproduce the cap region shown in Watson *et al.* (2018).

The goal of this new reaction-diffusion model that we propose in this chapter is to create a model that retains the experimental validity of the multiphase model within a simpler reaction-diffusion model framework. We begin with a PDE system that models the smooth muscle cell migration stage of cap formation. We consider two equations for SMC and PDGF dynamics. Analysis of this system allows us to understand whether the model can replicate the observations of the multiphase model. If it can, the model may provide a framework for larger models with more equations and systems.

4.2 Model formulation and development

We model the smooth muscle cell migration stage by analysing SMC and PDGF dynamics in the intima, the region between the endothelium and the media. Our model represents a radial cross-section of diseased intima far from the circumferential edges of the plaque. We assume PDGF is diffusible, acts as a SMC chemoattractant and promotes SMC activation. We do not explicitly account for all the processes of cap formation but instead assume that SMC and PDGF dynamics are relevant to the initiation of cap formation. We assume that crowding has no effect on SMC and PDGF dynamics and that PDGF is unaffected by SMC density within the intima.

These dynamics are represented by two equations on a one-dimensional domain with the endothelium at $x = 0$ and the media at $x = L$ where $L = 1$. This simply describes the interface between the intima and media as displayed in Figure 4.1. The distance x is therefore the radial distance from the luminal edge of the intima towards the media.

We model on two main quantities: SMC density and PDGF concentration. We do not distinguish between different types of PDGF and focus on matrix-synthesising SMCs. Our system therefore consists of the following key variables as a function of distance x and time t:

$s(x,t)$ = density of matrix-synthesising smooth muscle cells,
$g(x,t)$ = concentration of PDGF and other SMC chemoattractants.

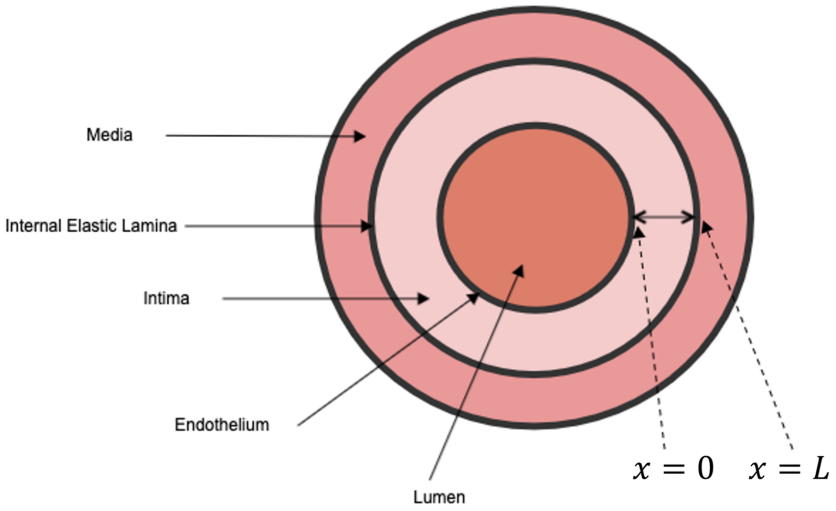

Figure 4.1: A simplified diagram of the inner arterial wall and the model's geometry.

4.2.1 Model equations

4.2.1.1 PDGF ($g(x,t)$)

Let the concentration of PDGF $g(x,t)$ be a function of time t and the radial distance x. The model equation for g is:

$$\frac{\partial g}{\partial t} = D_g \frac{\partial^2 g}{\partial x^2} - d_g g. \tag{4.16}$$

Equation (4.16) models the net rate of PDGF production. PDGF diffuses through the media with diffusion coefficient D_g, and decreases in proportion to the amount of PDGF present with a constant of proportionality d_g. There is no source term for

PDGF as we assume that PDGF is introduced at the endothelial boundary into the intima at a constant rate.

The time scales of PDGF and SMC production are different. PDGF production is estimated to be of order 10^3 seconds, while the time scale for SMC production is approximately a month. We are primarily interested in analysing SMC migration. Due to this we use the fact that the time scale of PDGF dynamics is significantly shorter than that of SMC production to set $\frac{\partial g}{\partial t} = 0$. This simplifies (4.16) to:

$$0 = D_g \frac{\partial^2 g}{\partial x^2} - d_g g. \tag{4.17}$$

4.2.1.2 Smooth muscle cells ($s(x,t)$)

The density of smooth muscle cells within the intima is modelled by:

$$\frac{\partial s}{\partial t} = D_s \frac{\partial^2 s}{\partial x^2} - \frac{\partial}{\partial x}(\chi_s s \frac{\partial g}{\partial x}) + \big(r_{s0} + \frac{r_s g}{G_s + g}\big) s(1 - \frac{s}{k}) - d_s s. \tag{4.18}$$

We assume that SMCs randomly migrate through the intima tissue with diffusion coefficient D_s. They respond chemotactically to the growth factor concentration g, where χ_s is the sensitivity of the SMCs to the chemoattractant. We note that in Watson *et al.* (2018), $\chi_s(g)$ was a nonlinear function of PDGF concentration so that cell motility was dependent on local g. Here we make a simplifying assumption and follow Ougrinovskaia (2011) in assuming that χ_s is constant and independent of g. We also assume that SMCs proliferate logistically with a mitosis rate dependent on PDGF concentration. Logistic growth is dependent on the total cell and tissue density k, while the mitosis rate is dependent on the base mitosis rate r_{s0}, the minimum mitosis rate r_s, and the Michaelis-Menten kinetic constant G_s. SMCs are assumed to die linearly at a rate d_s.

4.2.2 Boundary and initial conditions

4.2.2.1 PDGF ($g(x,t)$)

At the endothelial boundary we assume a constant influx of PDGF at rate α_g. At $x = 0$, this is represented as $J_g|_{x=0} = -\alpha_g$ where $J_g = -D_g \frac{\partial g}{\partial x}$ is the PDGF flux and $\hat{\mathbf{n}}$ is the outward unit normal. This influx is the sole source of PDGF.

At $x = 1$ we assume that there is a flux of PDGF out of the intima at the medial boundary. We require a chemical negative gradient of PDGF to drive SMC migration from the media into the intima. The medial flux of PDGF is assumed to be dependent on the concentration of PDGF at the boundary as well as the permeability σ_g at the medial boundary to PDGF. Unlike the boundary condition (4.7) in Watson *et al.* (2018), we do not assume that there is some constant notional medial PDGF concentration. The boundary condition is therefore equivalent to the

boundary condition (4.7) for $g^* = 0$. Hence at $x = 1$, $J_g|_{x=1} = -\sigma_g g$.

Therefore the boundary conditions for PDGF are:

$$\frac{\partial g}{\partial x}\Big|_{x=0} = \frac{-\alpha_g}{D_g}, \qquad \frac{\partial g}{\partial x}\Big|_{x=1} = \frac{-\sigma_g g}{D_g}. \tag{4.19}$$

4.2.2.2 Smooth muscle cells ($s(x,t)$)

Zero flux conditions are held at the endothelial boundary so that no SMCs enter the intima from the lumen. Hence at $x = 0$, we have $J_s|_{x=0} = 0$ where $J_s = -D_s\frac{\partial s}{\partial x} + \chi_s s\frac{\partial g}{\partial x}$ is the SMC flux.

We assume that SMCs enter the intima from the media, driven entirely by chemotaxis up the chemical gradient of PDGF at $x = 1$. We model this by introducing a constant s^* which represents the fixed density of SMCs in the media. We assume that this migration does not affect the medial density of SMCs. This means that at $x = 1$, $J_s|_{x=1} = \chi_s s^*\frac{\partial g}{\partial x}$.

Substituting the expressions for $\frac{\partial g}{\partial x}$ at both boundaries in the expressions for the flux of SMCs gives the boundary conditions:

$$\frac{\partial s}{\partial x}\Big|_{x=0} = \frac{-\alpha_g\chi_s s}{D_g D_s}, \qquad \frac{\partial s}{\partial x}\Big|_{x=1} = \frac{\chi_s\sigma_g g(s^* - s)}{D_s D_g}. \tag{4.20}$$

We assume a small initial intimal SMC density. This is represented as an initial condition $s(x,0) = s_0$ where s_0 represents a small spatially uniform SMC profile such that $0 < s_0 \ll 1$.

4.2.3 Non-dimensionalisation

We non-dimensionalise our model, using tildes to denote non-dimensionalised quantities. The key parameters x, t, s and g are non-dimensionalised as follows:

$$s = k\widetilde{s}\ , \quad g = g_0\widetilde{g}\ , \quad t = \tau t_0\ , \quad x = L\widetilde{x}\ ,$$

where k represents the total cell and tissue density, g_0 the characteristic PDGF concentration, t_0 the characteristic time scale of SMCs, and L the length of the domain.

The remaining model parameters are non-dimensionalised as follows:

$$\begin{aligned} d_g &= \frac{D_g \widetilde{d_g}}{L^2}\,, \quad & D_s &= \frac{L^2 \widetilde{D_s}}{t_0}\,, \quad & d_s &= \frac{\widetilde{d_s}}{t_0}\,, \quad & G_s &= \widetilde{G_s} g_0\,, \\ r &= \frac{\widetilde{r}}{t_0}\,, & \chi_s &= \frac{\widetilde{\chi_s} L^2}{t_0 g_0}\,, & r_{s0} &= \frac{\widetilde{r_{s0}}}{t_0}\,, & \widetilde{A} &= \frac{r_s}{r_{s0}}\,, \\ \alpha &= \frac{\widetilde{\alpha} D_g g_0}{L}\,, & \sigma &= \frac{\widetilde{\sigma} D_g}{L}\,. \end{aligned} \tag{4.21}$$

Dropping the tildes for clarity, the model equations (4.16) and (4.18) and boundary conditions (4.19) and (4.20) become:

$$0 = \frac{\partial^2 g}{\partial x^2} - d_g g, \tag{4.22}$$

$$\frac{\partial s}{\partial \tau} = D_s \frac{\partial^2 s}{\partial x^2} - \frac{\partial}{\partial x}(\chi_s s \frac{\partial g}{\partial x}) + r_{s0}\big(1 + \frac{Ag}{G_s + g}\big) s(1-s) - d_s s, \tag{4.23}$$

with boundary conditions

$$\begin{aligned} \frac{dg}{dx}\Big|_{x=0} &= -\alpha_g, \quad & \frac{\partial s}{\partial x}\Big|_{x=0} &= \frac{-\alpha_g \chi_s s}{D_s}, \\ \frac{dg}{dx}\Big|_{x=1} &= -\sigma_g g, \quad & \frac{\partial s}{\partial x}\Big|_{x=1} &= \frac{\chi_s \sigma_g g(s^* - s)}{D_s}. \end{aligned} \tag{4.24}$$

The initial condition for $s(x,t)$ is

$$s(x,0) = s_0, \tag{4.25}$$

where s_0 is non-dimensional.

4.2.4 Parameter values

Table 4.1: Base non-dimensionalised parameter values

Symbol	Definition	Value	Reference
D_s	Diffusion coefficient of SMC	1.0979	4.2.4.1
d_g	Rate of PDGF decay	0.075	[44]
d_s	Rate of SMC loss	0.4	[44]
n	Exponent in the SMC pressure function	1.8	[44]
κ	Reciprocal of reference PDGF concentration in SMC pressure function	5.5	[44]
G_s	Michaelis-Menten kinetic constant	1.4	[44]

Continued on next page

Table 4.1 – continued from previous page

Symbol	Definition	Value	Reference
χ_s	SMC motility coefficient	4.5952	4.2.4.1
A	Maximal factor of PDGF-stimulated increase in rate of SMC proliferation	19	[44]
r_{s0}	Baseline rate of SMC proliferation	0.02	[44]
α_g	Rate of PDGF influx from endothelium	0.55	[44]
σ_g	Permeability of IEL to PDGF	2	[44]
s_0	Initial SMC concentration	1×10^{-4}	[44]
s^*	Concentration of synthetic SMC in media	0.01	[44]

We note that our base case parameter values chosen in Table 4.2 are almost entirely equal to the base case parameters set in Table 1 of Watson *et al.* (2018). The key difference is the $\Lambda(c)$ function used in multiphase model. As explained in Section 4.2.4.1, we replace the random motion and chemotaxis rate functions with constant SMC diffusion and chemotaxis rates D_s and χ_s respectively.

4.2.4.1 SMC flux coefficients

We note that the non-dimensionalisation of most model parameters in Section 4.2.3 is the same as that of the multiphase model of Watson *et al.* (2018). This is because many of the assumptions are the same between the two models. For example, we assume the same characteristic timescale as the multiphase model to focus on SMC dynamics, recalling that we treat PDGF as time-independent because its timescale (time to reach steady state) is much shorter. Hence we set $t_0 = 2.5 \times 10^6 s$, or approximately one month.

A key difference however is the non-dimensionalisation of the rates of SMC random motion and chemotaxis, given by D_s and χ_s respectively. In the Watson *et al.* (2018), these rates are not constant but are given by functions dependent on the non-linear SMC phase pressure function $\Lambda(g)$. Specifically, the paper notes that the SMC diffusion rate is determined by $\Lambda(g)$ and the chemotaxis coefficient by $\frac{d\Lambda}{dg}$. This means that $D_s \equiv \Lambda(g)$ and $\chi_s \equiv \frac{d\Lambda}{dg}$ in the multiphase model.

We use the above equivalences to determine the values of D_s and χ_s. We note however that when the derivative terms are expanded in (4.5), D_s is equivalent to $(1-s)\Lambda(g)$. Because our objective is to align our reaction-diffusion model with the multiphase model, we address this discrepancy by following the equivalence noted in Watson *et al.* (2018). This is acceptable because the scale of s leads to $(1-s)$ being close to 1, meaning that the difference between the two equivalences is small. We

recall that our research question in this chapter is if we can create a reaction-diffusion model that is able to produce qualitatively similar results to the multiphase model. In Watson *et al.* (2018), the accumulation of SMCs near the endothelial boundary was found to be an indicator of cap formation. To match our reaction-diffusion model results with those of the multiphase model, we therefore try to demonstrate the same potential for cap formation by producing similar maximum values of s at the endothelial boundary. This means that the value of $s(0,t)$ at steady state should be similar between both models. We use this condition to determine the values of D_s and χ_s.

We observe from the multiphase model in Figure 4.3b that at steady state, SMC volume fraction is approximately $s(0,t) = 0.1995$ at the endothelial boundary. Therefore we choose the values of D_s and χ_s such that the steady state solution value of $s(x,t)$ is approximately $s(0,t) = 0.1995$ at $x = 0$ in the reaction-diffusion model (shown in Figure 4.4b). To determine these values of D_s and χ_s, we recall that their equivalent rate functions in the multiphase model are $\Lambda(g)$ and $\frac{d\Lambda}{dg}$. Because both these functions are only dependent on g, we vary g until $s(0,t) = 0.1995$. This is satisfied at approximately $g = 0.312$ which we obtain from (4.27). Evaluating $\Lambda(g)$ and $\frac{d\Lambda}{dg}$ for $g = 0.312$ returns the values of $\chi_s = 4.595$ and $D_s = 1.098$.

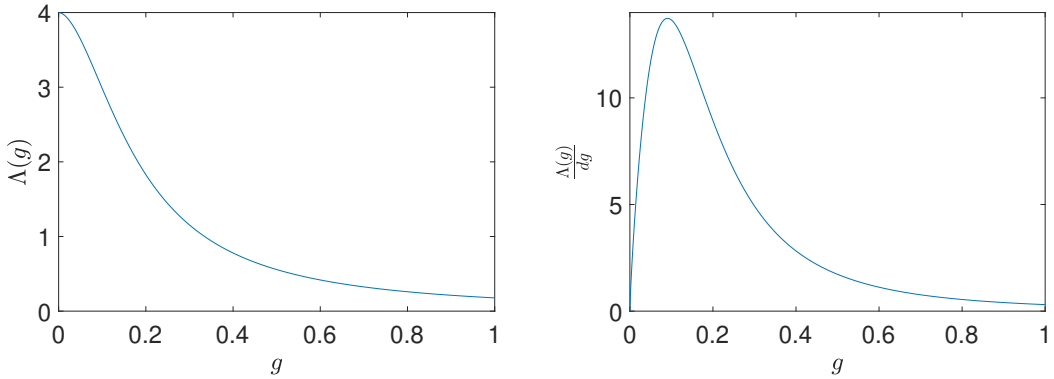

(a) (b)

Figure 4.2: (a) SMC phase pressure function $\Lambda(g)$ and (b) SMC phase pressure function derivative $\frac{d\Lambda}{dg}$ against PDGF concentration g.

4.3 Results

4.3.1 Multiphase model

The numerical solutions for the time evolution of PDGF concentration and SMC volume fraction for the multiphase model of Watson *et al.* (2018) are reproduced in Figure 4.3a and Figure 4.3b respectively. In Figure 4.3a, g decreases constantly over time until the solution profile reaches a steady state at around 15 months. The numerical result in Figure 4.3b shows SMC migrate over time from the intimal layer

(at $x = 1$) along the PDGF gradient towards the endothelium ($x = 0$). There is a clear increase in SMC accumulation at the medial boundary. The SMC distribution reaches steady state at around 15 months.

Table 4.2: Non-dimensionalised parameters used in $\Lambda(c)$ function of Watson *et al.* (2018).

Symbol	Definition	Non-dimensionalised value	Reference
χ	SMC motility coefficient	4.0	[44]
n	Exponent in SMC phase pressure function	1.8	[44]
κ	Reciprocal of reference PDGF concentration in SMC phase pressure function	5.5	[44]

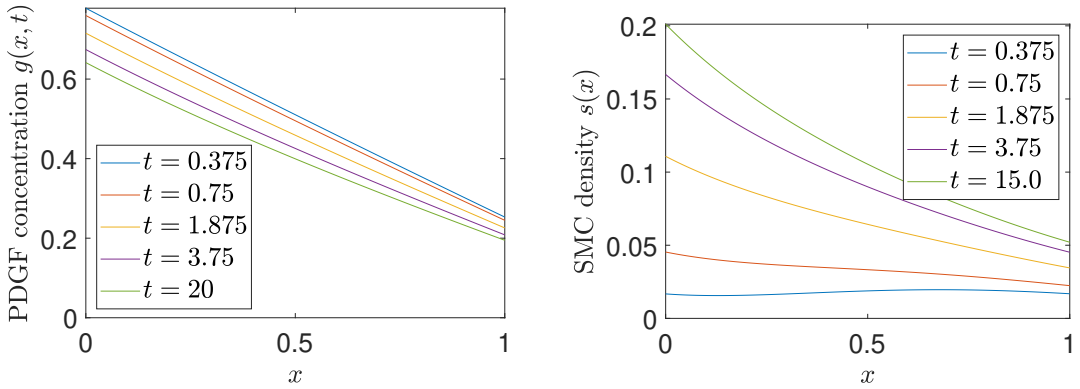

(a) (b)

Figure 4.3: Reproduced solutions of (a) PDGF concentration and (b) SMC volume fraction of Watson *et al.* (2018).

4.3.2 Reaction-diffusion model

4.3.2.1 PDGF ($g(x)$)

Equation (4.17) is solved to obtain the general solution

$$g(x) = c_1 e^{\sqrt{d_g}x} + c_2 e^{-\sqrt{d_g}x}.$$

Letting $\lambda = \sqrt{d_g}$ and noting the boundary conditions (4.19), the coefficient values are:

$$\begin{aligned} c_2 &= \frac{\alpha_g}{\lambda\left(e^{-2\lambda x}\frac{\sigma_g-\lambda}{\lambda+\sigma_g}+1\right)}, \\ c_1 &= \frac{-\alpha_g\left(e^{-2\lambda\frac{\sigma_g-\lambda}{\lambda+\sigma_g}}\right)}{\lambda\left(e^{-2\lambda\frac{\sigma_g-\lambda}{\lambda+\sigma_g}}+1\right)}. \end{aligned} \tag{4.26}$$

This gives the general solution:

$$g(x) = \frac{-\alpha_g\left(e^{-2\lambda\frac{\sigma_g-\lambda}{\lambda+\sigma_g}}\right)}{\lambda\left(e^{-2\lambda\frac{\sigma_g-\lambda}{\lambda+\sigma_g}}+1\right)}e^{\lambda x} + \frac{\alpha_g}{\lambda\left(e^{-2\lambda\frac{\sigma_g-\lambda}{\lambda+\sigma_g}}+1\right)}e^{-\lambda x}. \tag{4.27}$$

The steady state solution (4.27) displayed in Figure 4.4a has a profile that is very similar to that of the solutions in Figure 4.3a. We recall that the reaction-diffusion model assumes that PDGF exists at steady state in the intima, unlike the multiphase model which assumes that PDGF concentration changes temporally due to dependence on SMCs.

4.3.2.2 SMC ($s(x,t)$)

The solutions of s as a function of x for different times t are displayed in Figure 4.4b. We observe that SMCs enter the intima at $x = 1$ and migrate towards the endothelial boundary ($x = 0$), where the value of s is greatest. This is due to two main factors. The value of g is greatest at this boundary as PDGF enters the intima there. SMC proliferation is therefore also greatest here. Hence SMC density evolves to be greatest at $x = 0$. SMCs also migrate towards the endothelial boundary due to random motion and chemotactic flux, leading to SMCs accumulating near $x = 0$. SMC density across the domain increases over time, rising at a greater rate at the endothelial boundary. At around 17 months, the rate of SMC proliferation decreases significantly. Figure 4.4c shows that SMC density reaches steady state at approximately 22 months, which was longer than the steady state time of approximately 15 months observed in the multiphase model.

Comparisons between the profiles of g and s in Figures 4.3 and 4.4 demonstrate that the reaction-diffusion model have the same potential for cap formation as observed in the multiphase model. SMCs migrate towards the $x = 0$ boundary and proliferate over time. Their accumulation eventually slows down and the system reaches steady state. We note that these profiles resemble caps in the intima and provide a base model for the early stages of cap formation. We further test the similarity between the multiphase and reaction-diffusion models by conducting parameter sensitivity analysis in Section 4.4.

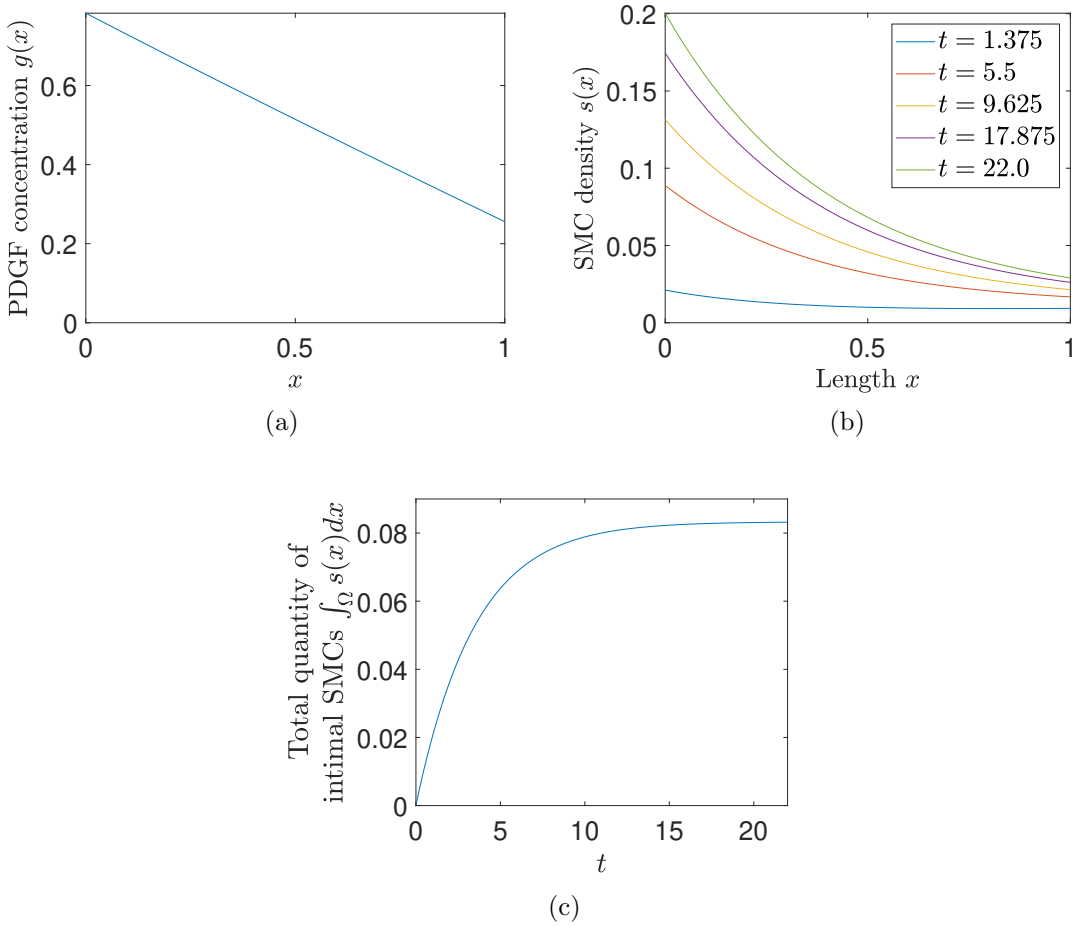

Figure 4.4: (a) Steady state solution of g, (b) solutions of s as functions of x at $t = 1.375$, 5.5, 9.625, 17.875 and 22.0, and (c) the time evolution of total intimal SMC density $\int_\Omega s(x)dx$. All plots are solved with values from Table 4.1, $D_s = 1.098$ and $\chi_s = 4.595$.

4.3.3 Steady state solution comparison

We compare the steady state solutions for g and s between the reaction-diffusion model and multiphase model in Figures 4.5a and 4.5b. We recall that the equation for the PDGF phase in the multiphase model was dependent on the SMC phase and therefore time dependent. The equation for PDGF in the reaction-diffusion model has no dependence on SMC density and is assumed to be time independent. To compare the two we take both solutions at steady state. We observe in Figure 4.5a that the spatial profiles of the two solutions are similar. Zero flux conditions are assumed for both models at the endothelial boundary ($x = 0$), while at the medial boundary ($x = 1$) the outwards flux of g is slightly greater for the reaction-diffusion model as it is proportional to PDGF concentration rather than the difference between PDGF concentration and a notional background concentration as in the multiphase model. The difference in scale is due to the effect of SMCs on PDGF dynamics in the multiphase model. Because the multiphase model assumes that SMCs uptake PDGF,

increasing SMC accumulation leads to PDGF depletion.

The comparison between the steady state solutions for SMCs of the reaction-diffusion model and multiphase model are shown in Figure 4.5b. We note that at $x = 0$, the densities/volume fractions of SMCs are equal. This is expected given our decision to choose suitable values of χ_s and D_s based on the SMC density/volume-fraction values at this boundary in the multiphase model. The spatial profiles of the two models are different however. We note that the values of χ_s and D_s of the reaction-diffusion model were chosen by evaluating $\Lambda(g)$ for a fixed value of approximately $g = 0.312$ and are constant. The diffusion and chemotaxis coefficients of the multiphase model, determined by $\Lambda(g)$ and $\frac{d\Lambda(g)}{dg}$ respectively, change spatially based on the local PDGF concentration. These changes are observed in Figures 4.2a and 4.2b. PDGF concentrations near the $x = 0$ boundary for the multiphase model as observed in Figure 4.5a are greater than the fixed value of approximately $g = 0.312$, while they are lower near the $x = 1$ boundary. The diffusion and chemotaxis coefficients of the multiphase are therefore lower than χ_s and D_s near $x = 0$ and greater near $x = 1$. As a result SMC motility will be greater for the reaction-diffusion around $x = 0$ and lower around $x = 1$. These differences in flux values result in the different profile of SMC steady state solution of the reaction-diffusion model compared to the multiphase steady state solution.

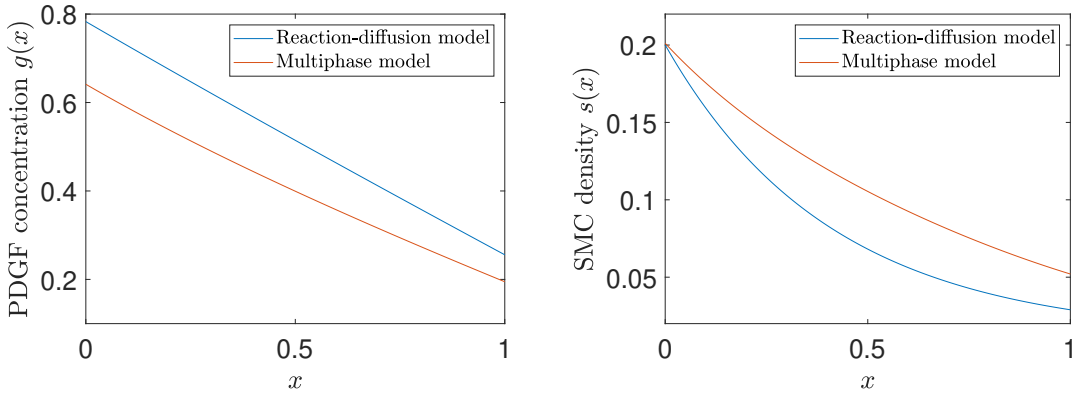

Figure 4.5: Comparisons between steady state solutions of (a) g and (b) s of reaction-diffusion model and Watson *et al.* (2018).

4.3.4 Reduced steady state solution

We reduce the model to analytically solve for a steady state solution of (4.29). We first make a number of simplifications. We linearise the system about $x = 0$ by taking the McLaurin expansion of $g(x, t)$ to $\mathcal{O}(x)$. Therefore we treat $\frac{dg}{dx}$ as a constant by taking its value at the endothelial boundary. We further simplify the Michaelis-Menten-governed proliferation term by assuming that approximating g about $x = 0$ reduces the overall proliferation term to r_{s0}. By taking the McLaurin expansion of $s(x, t)$ to $\mathcal{O}(x)$ simplifies the quadratic s in the proliferation term to

s. We recall that we linearise about $x = 0$; therefore we use boundary condition of g at this point. As a result our simplified system becomes:

$$0 = \frac{d^2 g}{dx^2} - d_g g, \tag{4.28}$$

$$\frac{\partial s}{\partial \tau} = D_s \frac{\partial^2 s}{\partial x^2} + \alpha_g \chi_s \frac{\partial s}{\partial x} + (r_{s0} - d_s)s, \tag{4.29}$$

which yields an ODE and a linear homogenous second order PDE. The boundary conditions become:

$$\frac{\partial s}{\partial x}|_{x=0} = \frac{-\alpha_g \chi_s s}{D_s}, \quad \frac{\partial s}{\partial x}|_{x=1} = \frac{\alpha_g \chi_s (s^* - s)}{D_s}. \tag{4.30}$$

We note that the gradient of $g(x)$ observed in Figure 4.4a is largely similar at the boundaries. The main difference between the reduced steady state solutions and the steady state solutions of Section 4.3.2 is therefore the reduced source and sink terms of s.

Solving for the steady state solution of (4.29) gives the general solution

$$s(x) = c_1 \exp(S_1 x) + c_2 \exp(S_2 x),$$

where S_1 and S_2 represent the conjugate real roots. From the boundary conditions (4.30), we obtain the general steady state solution coefficients:

$$c_1 = \frac{\alpha_g \chi_s s^*}{\left(s_1 + \frac{\alpha_g \chi_s}{D_s}\right)\left(\exp S_1 - \exp S_2\right)},$$
$$c_2 = \frac{\alpha_g \chi_s s^*}{\left(s_2 + \frac{\alpha_g \chi_s}{D_s}\right)\left(\exp S_2 - \exp S_1\right)}.$$

We note that the source and sink terms of both models are different, with the reduced source terms eliminating dependence on g. The flux term of the reduced model is dependent on the influx of PDGF at $x = 0$ due to the linearisation of the g about $x = 0$. We expect less overall SMC density across the domain but the profile of the solution to be similar at the $x = 0$ boundary.

From the comparison of the steady state solutions in Figure 4.6, we observe that the reduced steady state solution (4.29) is a good approximation of SMC density of the reaction-diffusion model (4.22). As expected, SMC density across the domain is lower for the reduced steady state solution though this difference appears to be of scale rather than profile. The gradient at $x = 0$ is similar to the reaction-diffusion steady state solution though the gradient at $x = 1$ is less steep.

The similarities shown in Figure 4.5b of the profiles of the reduced steady state solution and reaction-diffusion model suggests that the main contribution of PDGF to the dynamics of SMCs are the flux terms. In particular, the absence of the logistic growth term in response to PDGF appears to have a negligible effect on the SMC solution profile. These results raise questions on the impact of the logistic growth

term compared to the flux terms on cap formation, and whether they contribute to SMC dynamics more than the source term. We therefore investigate these questions in the section below by performing parameter sensitivity analysis on terms that affect the source and flux terms.

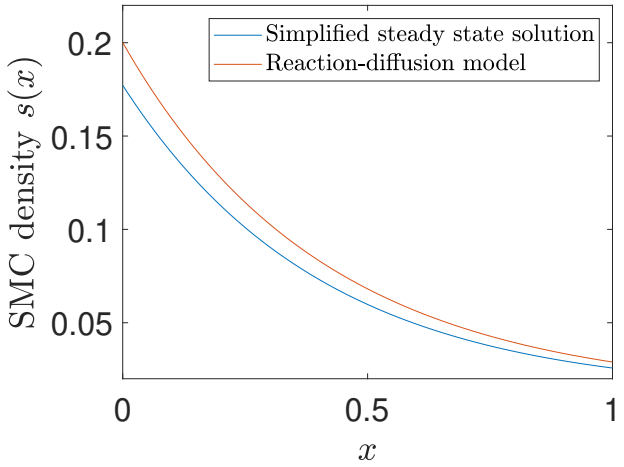

Figure 4.6: Comparison between SMC steady state solutions of reduced steady state solution and reaction-diffusion model.

4.4 Parameter sensitivity

4.4.1 r_{s0}

Following the observations in Section 4.3.4 we analyse the extent of the impact of SMC proliferation on SMC dynamics. Proliferation is dependent on three factors: the baseline proliferation rate r_{s0}, the logistic growth term in response to PDGF, and mitosis due to PDGF. We vary the baseline rate so there is no cell proliferation ($r_{s0} = 0$). Where there is no cell proliferation we expect an overall lower SMC density. We expect the impact on cell distribution to likely be greater at the $x = 0$ boundary where PDGF concentration is highest. The results in Section 4.3.4 suggest that this will have a minor effect on the gradient of the steady state solution of s.

We compare the solution of $s(x, t)$ with varying baseline rate of SMC proliferation r_{s0} against the base case steady state solution, shown in Figure 4.7a. Where there is no cell proliferation, we observe an expected overall decrease in SMC density. The decrease in SMC density is greater at the endothelial boundary where PDGF concentration is greatest as observed in Figure 4.4a. The gradient at this boundary is also lower than the base case solution, though the decrease in gradient is lower at the medial boundary ($x = 1$). These results suggest that while SMC proliferation has an effect on the overall SMC density, it does not greatly affect the profile of the solution. This suggests that the profile and greater distribution of SMCs due to migration determines the synthesis of the fibrous cap near the endothelial boundary, even without proliferation.

For comparison, the solutions of Watson *et al.* (2018) with the same varying baseline proliferation rates are shown in Figure 4.7b. While the observed SMC profile is steeper in the reaction-diffusion model, the behaviour of decreased overall SMC density, particularly near the $x = 0$ boundary, is comparable. These results lead to the observations that SMC proliferation may not be necessary for cap formation and that proliferation contributes greatest at the endothelial boundary where PDGF enters the intima from the lumen. The similarity in results and analysis between both models leads to two conclusions. We conclude that SMC proliferation may not be necessary for cap formation due to its weak contribution to the distribution of SMCs at the endothelial boundary in both models. We also conclude that the similarity between models suggests that the reaction-diffusion model captures the same dynamics as the more complex multiphase model.

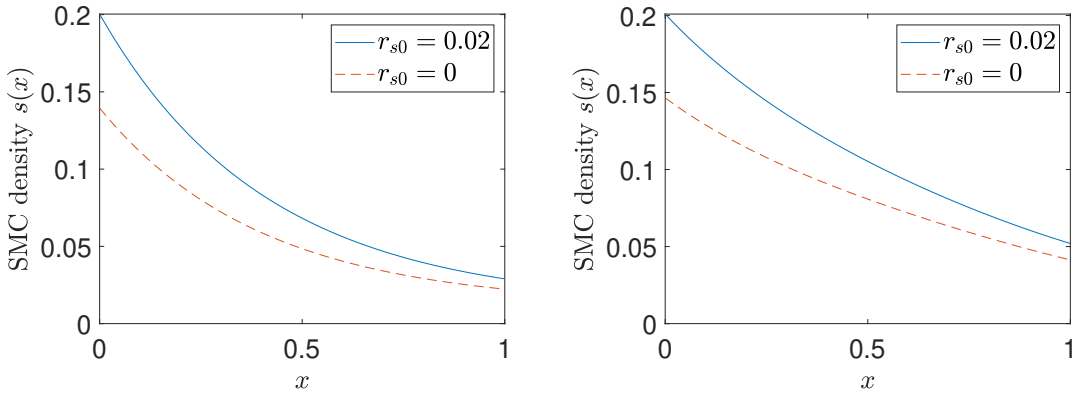

Figure 4.7: Comparisons of steady state solutions of s of (a) reaction-diffusion model and (b) Watson *et al.* (2018) with $r_{s0} = 0.0$ and 0.02 at $t = 22.0$.

4.4.2 n

In the multiphase model, the parameter n is the exponent of the SMC phase pressure function $\Lambda(g)$. Varying n has an effect on both the diffusion and chemotaxis of SMCs where the diffusion term is described by the function $\Lambda(g)$ and the chemotaxis term by $\frac{d\Lambda(g)}{dg}$. The reaction-diffusion model does not have the $\lambda(g)$ equation used in the multiphase model. To replicate the changes to n, we observe that changes in diffusion and chemotaxis due to varying n in the multiphase model correspond to changes in the reaction-diffusion diffusion and chemotaxis coefficients D_s and χ_s respectively. In Section 4.2.4.1, we obtained the corresponding values of $D_s = 1.098$ and $\chi_s = 4.595$ when $n = 1.8$ by evaluating $\Lambda(g)$ and $\frac{d\Lambda(g)}{dg}$ at a fixed value of $g = 0.312$. By following the same process, we obtain the values of $D_s = 1.4727$ and $\chi = 2.9822$ when $n = 1.0$, and $D_s = 0.7887$ and $\chi = 5.2762$ when $n = 2.6$. These values show that as n decreases, D_s increases and χ decreases; the opposite occurs when n increases. Varying n therefore changes the flux of the system to favour chemotaxis or diffusion by respectively increasing or decreasing n.

In the reaction-diffusion model, a greater value of χ_s creates a steeper gradient at both boundaries while a lower value of D_s leads to less distribution of SMCs across the domain. We therefore expect increasing n to lead to a steeper profile towards the $x = 0$ boundary. On the other hand, a lower value of χ_s creates a lower gradient at both boundaries while a greater value of D_s leads to increased distribution of SMCs across the domain. We expect decreasing n to create a flatter profile of SMC density.

We compare the solution of $s(x, t)$ with varying n with the base case steady solution ($n = 1.8$), shown in Figure 4.8a. As expected, we observe a steeper SMC profile when χ_s is greater and D_s is lower ($n = 2.6$). Similarly, we observe a flatter SMC profile when χ_s is lower and D_s is greater ($n = 1.0$). The changes in flux terms have a significant effect on the profile of s in contrast to the effect observed due to change in proliferation in Section (4.4.1).

The SMC steady state solutions of the multiphase model with the same varying n are shown in Figure 4.8b. The results are consistent with those of the reaction-diffusion model: a lower value of n corresponds to a flatter SMC profile while a higher value corresponds to a steeper SMC profile with greater cap formation at the $x = 0$ boundary than the base case. Comparing the solutions of the two models shows that the solution profiles are qualitatively similar. Both models show a significant decrease in overall SMC recruitment when $n = 1$, with the greatest decrease being at the endothelial boundary. Similarly SMC motility and chemotactic movement is greater at this boundary when $n = 2.6$, suggesting higher cap formation. A difference however is the profiles of the two solutions. We explain this by the diffusion and chemotaxis coefficients changing with respect to g as opposed to the fixed values of χ_s and D_s. As noted in Section 4.3.3, for $n = 1.8$ the diffusion and chemotaxis coefficients of the multiphase are lower than χ_s and D_s near $x = 0$ and greater near $x = 1$ such that SMC motility is greater for the reaction-diffusion around these boundaries. Figures 4.9a and 4.9b show the different values of the diffusion and chemotaxis coefficients of the multiphase model with respect to g for different values of n. Because the local PDGF concentration at the $x = 0$ boundary is greater than the fixed value $g = 0.312$ chosen in the reaction-diffusion model, the diffusion and chemotaxis coefficients are lower around this boundary. Similarly, the opposite occurs around $x = 1$.

The effect of varying n observed in both models suggests that differences in chemotaxis and diffusion have a significant impact on SMC profile. In particular, steeper gradients and increased SMC density at the endothelial boundary for increasing chemotaxis coefficients suggests that SMC motility may be important for potential cap formation near the endothelial boundary. The similarities in profile and overall SMC recruitment also demonstrate that the reaction-diffusion model is able to capture the same effects of varying diffusion and chemotaxis coefficients for s by simplifying the diffusion and chemotaxis rates.

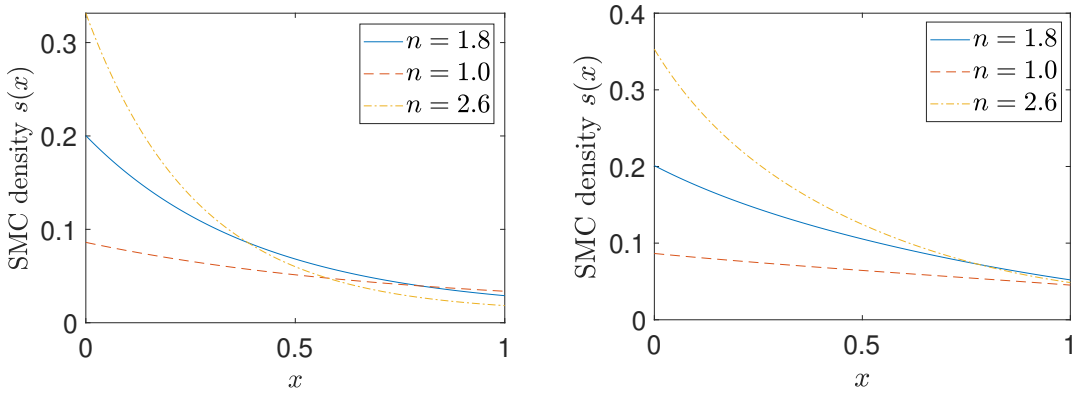

Figure 4.8: Comparisons of steady state solutions of s of (a) reaction-diffusion model and (b) Watson *et al.* (2018) for three values of n: $n = 1.0$, 1.8, and 2.6 at $t = 17.0$.

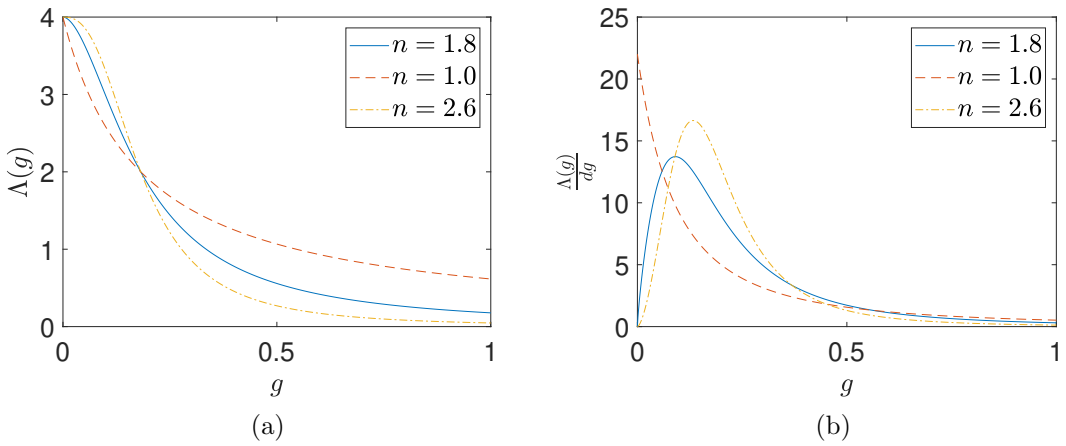

Figure 4.9: Comparisons of plots of (a) SMC phase pressure function $\Lambda(g)$ (equivalent to D_s) and (b) SMC phase pressure function derivative $\frac{d\Lambda(g)}{dg}$ (equivalent to χ_s) against PDGF concentration g for three values of n: $n = 1.0$, 1.8, and 2.6.

4.4.3 χ_s

In Section 4.4.2 the potential for cap formation was linked to the chemotaxis coefficient. When n was varied in the multiphase model, there was a corresponding change in the chemotaxis and diffusion coefficients. Recalling the flux conditions and our boundary conditions in Equation (4.24), we observe the effects of changes to s when only the chemotaxis coefficient χ_s is varied.

We expect varying χ_s to increase the gradient of s at the $x = 0$ boundary and to produce a greater cap region near this boundary due to increased cell motility. At $x = 1$ an increased χ_s corresponds to greater SMC influx from the media; we expect this to also increase the gradient of s at this boundary.

These expectations are consistent with the findings shown in Figure 4.8a. We observe that increasing χ_s leads to an overall increase in SMC recruitment and the opposite for decreasing χ_s. Importantly, a higher value of χ_s ($\chi_s = 6.5$) appears to create a larger cap at the endothelial boundary while a lower value ($\chi_s = 2.5$) leads to a low SMC profile with a negligible cap region. These results support the results in Section 4.4.2 that SMC motility may be important for cap formation. In particular, it suggests that the potential for cap formation is highly influenced by chemotaxis. Comparing these results with those in Section 4.4.1 suggests that SMC proliferation is weaker than chemotaxis and that the magnitude of the proliferation term is smaller the flux terms.

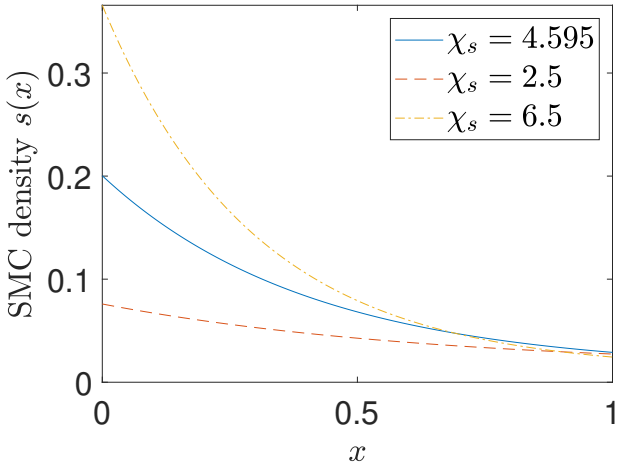

Figure 4.10: Comparisons of steady state solutions of s of reaction-diffusion model for three values of χ_s : χ_s=2.5, 4.595, and 6.5 at $t = 22.0$.

4.5 Discussion

The results of the base case solutions in 4.3.2 show the accumulation of SMCs near the endothelial boundary. This region is required for the creation of a fibrous cap: though our model does not include ECM, SMCs synthesise ECM to create a collagenous cap [38] and we therefore assume that SMC distribution may be similar to that of ECM. We also observe PDGF and its role in stimulating SMC proliferation and migration. SMC random motion and chemotactic motility are both dependent on the PDGF gradient, and changes to their rate coefficients affect the SMC distribution and density in the intima. The analysis of the chemotaxis coefficient χ_s in Section 4.4.3 shows that chemotactic migration of SMCs determines the accumulation of SMCs near the endothelial boundary, leading to the formation of a fibrous cap. The results of Section 4.4.3 showed that SMC proliferation is weaker than migration, and mainly affects SMC density and the size of the fibrous cap. The reaction-diffusion model therefore models the SMC migration stage and the cap formation dynamics.

The goal of this model was to create a reaction-diffusion model that replicated the observations of the multiphase model. In Section 4.3.2, we observed that the results

of the reaction-diffusion model were directly comparable to those of the multiphase model in Section 4.3.1. The PDGF and SMC profiles are similar and the steady state solution comparisons in Section 4.3.3 showed that the differences in magnitude and distribution between the results of the two models were minor. This was further observed in Sections 4.4.2 and 4.4.1, where we varied the same parameters analysed in Watson *et al.* (2018) and compared steady state solutions. These results therefore show that the reaction-diffusion model is directly comparable to the multiphase model.

We also note some advantages of the reaction-diffusion model framework over the multiphase model. The analysis in Section 4.3.4 showed that the model could be reduced to allow the model equation for s (4.29) to be analytically solved. This was not possible for the multiphase model due to its complexities, such as the coupling of different phases. The multiphase model also assumed complicated functions that were simplified in the reaction-diffusion model, such as the parameter sensitivity analysis of the exponent parameter n of the SMC phase pressure function $\Lambda(g)$ in Section 4.2.4.1. The phase pressure terms were simplified in the reaction-diffusion model to be constant. The comparison of the steady state solutions for different values of n between both models in Section 4.4.2 showed that the results were qualitatively similar, and that the phase pressure terms could be simplified in the reaction-diffusion model while still capturing the same general SMC dynamics observed in the multiphase model. The simplicity of the reaction-diffusion model therefore allows for analytical solutions while still producing comparable results to the more complex multiphase model.

Chapter 5

Extending the base model by modelling extra-cellular matrix and Transforming Growth Factor-β characteristics

In the previous chapter (4), we modelled the SMC migration stage in response to PDGF. We recall that SMCs migrate and proliferate within the intima, which we previously modelled as dependent only on PDGF. Within the intima, SMCs also move through the extracellular matrix (ECM) and are stimulated by growth factors such as transforming growth factor-β (TGF-β) to produce a matrix of fibrillar collagens [2]. This matrix of collagens adds to the existing ECM and results in the formation of a fibrous cap [38]. We previously assumed that SMC distribution may be similar to that of ECM, and did not directly model the formation of a fibrous cap. Our aim in this chapter is to model the formation of a fibrous cap by describing the ECM synthesis stage of atherosclerotic plaque formation. We therefore extend the previous model to include ECM and TFG-β.

The multiphase model of Watson *et al.* (2018) [44] was used as a reference model and comparison tool to build our reaction-diffusion model framework in Chapter 4. This model is extended by the multiphase model in Watson *et al.* (2020) [45], which makes it a useful reference model for our model as we extend the previous reaction-diffusion model. We note that the reaction-diffusion model in Ougrinovskaia (2011) also models the dynamics of collagen, though it does not include growth factors that stimulate collagen synthesis. The Ougrinovskaia (2011) model further includes dependence on variables that represent cells such as macrophages that are not considered in this model. This means it is not a useful reference model for this chapter. We instead refer to the multiphase model of Watson *et al.* (2020).

5.1 An extended model for cap formation: Watson *et al.* (2020)

We recall that the first multiphase model of Watson *et al.* (2018) considered two phases of SMC and other generic tissues but did not explicitly consider the formation of a fibrous cap. This is addressed in this second multiphase model of Watson *et al.* (2020) by including an intimal ECM phase. It is assumed that SMCs replace ECM with a matrix of fibrous collagens. This process of collagen synthesis is a result of SMCs stimulation by TGF-β. In the first multiphase model the diffusible growth

factor PDGF and its effects on SMCs were modelled. The second multiphase model extends this to include TGF-β as another cytokine.

We recall that the first multiphase model denoted SMC volume fraction as $s(x,t)$, the generic tissue volume fraction as $w(x,t)$ and PDGF concentration as $g(x,t)$. The newly introduced ECM volume fraction and TGF-β concentration are denoted as $\rho(x,t)$ and $T(x,t)$ respectively. As the second multiphase model is extension of the first model, a number of assumptions are maintained. There is an assumed no voids condition in the plaque so that $s+\rho+w=1$. Like PDGF, TGF-β is present only in the generic tissue phase as a diffusible growth factor. This means that $T(x,t)$ does not have any explicit volume in the model. The domain is treated as a one-dimensional cross-section of the intima, bounded by the endothelium at $x=0$ and the SMC-bearing media at $x=L$ where $L=1$.

The multiphase model is comprised of model equations for the variables s, ρ, g and T. The non-dimensionalised model equations are:

$$\begin{aligned}\frac{\partial s}{\partial t} =&\frac{\partial}{\partial x}\Big[(1-s-\rho)\frac{\partial}{\partial x}\big[s(\Lambda+\rho\psi)\big]\Big] \\ &+ r_s s(1-s-\rho)\Big[1+\frac{A_g g}{c_g+g}\Big]-\beta_s s,\end{aligned} \tag{5.1}$$

$$\begin{aligned}\frac{\partial \rho}{\partial t} =&r_s s(1-s-\rho)\Big[1+\frac{A_s T}{c_s+T}\Big]-r_d s\rho\Big[1+\frac{A_d g}{(c_d+g)(1+\sigma_d T)}\Big] \\ &-\beta_\rho\rho(1-s-\rho)\Big[\frac{1+\epsilon\sigma_\rho T}{1+\sigma_\rho T}\Big],\end{aligned} \tag{5.2}$$

$$\frac{\partial}{\partial x}\Big[(1-s-\rho)\frac{\partial g}{\partial x}\Big]=\eta_g s g(1-s-\rho)+\beta_g g(1-s-\rho), \tag{5.3}$$

$$\frac{\partial}{\partial x}\Big[(1-s-\rho)\frac{\partial T}{\partial x}\Big]=\eta_T s T(1-s-\rho)+\beta_T T(1-s-\rho). \tag{5.4}$$

Recalling that this multiphase model extends the first multiphase model, the model equation for s in (5.1) preserves some of the dynamics of SMCs from first multiphase model equation (4.5). The first differential term represents the mass balance of the three phases of s, ρ and w. In the first multiphase model, the phase pressure function in equation (4.5) ($s(\Lambda)$) described the effects of PDGF on the SMC phase. This is expanded in (5.1) to include ECM dependence. A new function $\psi(s,\rho)$ is introduced that increases with increasing s and ρ so that the phase pressure function becomes $s(\Lambda+\rho\psi)$. Expanding the first term therefore gives the nonlinear diffusion, chemotaxis and haptotaxis coefficients of s. The model equation continues to assume that SMCs undergo random motion and chemotaxis, with SMC chemotactic motility being dependent on both local PDGF concentration and its gradient. The function $\psi(s,\rho)$ introduces an additional assumption that SMCs may migrate haptotactically along ECM gradients. We note that the source and sink terms are unchanged from (4.5). This means that the model equation assumes SMCs proliferate logistically at a rate determined by g and die at a linear rate, though with dependence on the ECM phase. TGF-β does not affect SMC proliferation or death.

The presence of TGF-β is however relevant in the ECM phase. The first term in

the model equation for ρ (5.2) models ECM proliferation as saturation kinetics with dependence on TGF-β concentration. The rate of proliferation is further dependent on a proliferation rate r_s and local SMC and generic tissue volume fraction. The last two terms in the equation are sink terms. The first sink term represents ECM degradation by SMCs. This decay is assumed to be dependent on both PDGF and TGF-β concentrations and is governed by a rate r_d. The parameter A_d represents the maximal factor of PDGF-stimulated increase in rate of ECM degradation by SMCs, while σ_d represents the reciprocal of reference T for inhibition of ECM degradation by SMCs. The final sink term represents ECM degradation by other factors in the generic tissues. This degradation is assumed to be bound by a limiting function that decreases degradation monotonically with TGF-β concentration. The parameter β_ρ represents the baseline rate of ECM degradation by immune cells, while ϵ represents the maximal factor of TGF-β-stimulated decrease and $\sigma\rho$ represents the reciprocal of reference TGF-β concentration.

Unlike SMCs, the ECM phase is assumed to be fixed because collagen forms a rigid network. This means it does not diffuse or migrate. This is therefore represented by the equation for ρ having no spatial derivative terms.

Equations (5.3) and (5.4) assume that the growth factors PDGF and TGF-β are produced autocatalytically by SMCs and undergo decay. The first term of both equations represent this uptake, which is proportional to a respective uptake rate μ_g and μ_T as well as the local growth factor concentration and SMC volume fraction. The last term in each equation represents growth factor decay, which is proportional to the respective decay rates β_g and β_T.

The assumptions at the boundaries are the same as the first multiphase model. At the endothelial boundary ($x = 0$) there is a zero flux condition for SMCs. At the medial boundary ($x = 1$) it is assumed that there is a chemotactic influx of SMCs. For PDGF, it is assumed that there is an inward flux at $x = 0$ and a negative chemical gradient at $x = 1$ allowing SMCs to migrate across the medial boundary chemotactically in response to PDGF. The dynamics of TGF-β are similar to PDGF with an inward flux at $x = 0$ and a negative chemical gradient at $x = 1$. The boundary conditions are therefore:

$$\begin{aligned}
&\frac{\partial}{\partial x}\Big[s(\Lambda+\rho\psi)\Big] = 0 \text{ at } x=0, && \frac{\partial}{\partial x}\Big[s(\Lambda+\rho\psi)\Big] = \frac{d\Lambda}{dg}s_M\frac{dg}{dx} \text{ at } x=1,\\
&\frac{\partial g}{\partial x} = -\alpha_P \text{ at } x=0, && \frac{\partial g}{\partial x} = \sigma_P(P_M-g) \text{ at } x=1,\\
&\frac{\partial T}{\partial x} = -\alpha_T \text{ at } x=0, && \frac{\partial T}{\partial x} = \sigma_T(T_M-T) \text{ at } x=1,
\end{aligned} \tag{5.5}$$

with initial conditions

$$s(x,0) = s_i, \quad \rho(x,0) = \rho_i, \tag{5.6}$$

where $0 < s_i \ll 1$ and $0 < \rho_i \ll 1$.

We recall that in the first reaction-diffusion model, we adapted elements of the first multiphase model including biological assumptions and flux conditions. Our research goal with the first reaction-diffusion model was to create a model that could provide

qualitatively similar results to the more complex multiphase model of Watson *et al.* (2018). This second multiphase model extends the first model by including the ECM phase and TGF-β. In this chapter our research goal is not direct comparison with the reference model, but to instead analyse the base model's ability to be extended. We take the same approach with the second multiphase model by adapting some elements to produce a reaction-diffusion model that includes the extended phases of ECM and TGF-β.

5.2 Model formulation and development

We model the early stages of cap formation by exploring SMC, ECM, PDGF and TGF-β dynamics in the intima. Recalling this model extends the earlier reaction-diffusion model in Section 4.2.1, we maintain many of the assumptions of the earlier model. These include the spatial assumptions regarding the domain and the biological assumptions around SMCs and PDGF.

Our system consists of the key variables as a function of distance x and time t:

$$\begin{aligned} s(x,t) &= \text{density of matrix-synthesising smooth muscle cells,} \\ g(x,t) &= \text{concentration of SMC chemoattractant, such as PDGF,} \\ \rho(x,t) &= \text{density of collagenous extra cellular matrix,} \\ T(x) &= \text{concentration of TGF-}\beta. \end{aligned}$$

5.2.1 Model equations

5.2.1.1 SMC ($s(x,t)$)

The density of smooth muscle cells within the intima is modelled by:

$$\frac{\partial s}{\partial t} = D_s \frac{\partial^2 s}{\partial x^2} - \frac{\partial}{\partial x}(\chi_s s \frac{\partial g}{\partial x}) - \frac{\partial}{\partial x}\Big(h_\rho s \frac{\partial \rho}{\partial x}\Big) + (r_{s0} + \frac{r_s g}{G_s + g}) s(1-s) - d_s s. \quad (5.7)$$

We keep the assumptions held in equation (4.18) and assume that cells have random motility, chemotactic motion and undergo the same source and sink behaviour. We follow however the assumption in equation (5.1) of Watson *et al.* (2020) that SMC affinity for ECM leads to haptotactic SMC migration along ECM gradients. We assume that this SMC haptotactic migration is not dependent on a nonlinear SMC phase pressure function as in (5.1). Instead it is assumed to be linear with respect to a haptotactic coefficient h_ρ and the ECM gradient $\frac{\partial \rho}{\partial x}$.

5.2.1.2 ECM ($\rho(x,t)$)

Collagen is assumed to form a rigid network which does not diffuse or migrate. There are therefore no terms that produce spatial movement of ECM. We model the density of ECM within the intima by:

$$\frac{\partial \rho}{\partial t} = r_s s\Big[1 + \frac{A_s T}{c_s + T}\Big] - r_d s\rho\big[1 + \frac{A_d g}{(c_d + g)(1 + \gamma_d T)}\Big] - \beta_\rho \rho\Big[\frac{1 + \epsilon\gamma_\rho T}{1 + \gamma_\rho T}\Big]. \tag{5.8}$$

Recalling that the multiphase model of Watson *et al.* (2020) extends many of the assumptions of Watson *et al.* (2018), we adapt the source and sink terms from equation (5.2) of Watson *et al.* (2020). The first source term represents ECM synthesis by SMCs [2]. This is modelled as saturation kinetics, where the synthesis term is proportional to a baseline ECM production rate r_s and SMC density. This rate of ECM synthesis is also proportional to TGF-β concentration with c_s representing the half-maximal rate and A_s representing the maximal factor of TGF-β stimulated ECM proliferation. ECM production is therefore upregulated by increasing TGF-β.

The first degradation term represents ECM degradation by SMCs. We assume that this is dependent on local PDGF and TGF-β concentration, where SMC upregulation is proportional to increasing PDGF and decreasing TGF-β. This degradation is also proportional to a constant degradation term r_d. The second degradation term represents general ECM degradation. This is proportional to local ECM density and a constant rate β_ρ and a function dependent on TGF-β concentration. We design this function to decrease with increasing TGF-β concentration, where ϵ represents the minimum possible rate of TGF-β-inhibited ECM degradation and γ_ρ represents the rate at which ECM decreases with increasing TGF-β.

5.2.1.3 TGF-β ($T(x,t)$)

The concentration of TGF-β within the intima is modelled by:

$$\frac{\partial T}{\partial t} = D_T \frac{\partial^2 T}{\partial x^2} - \beta_T T. \tag{5.9}$$

TGF-β is a diffusible growth factor which we assume to diffuse at a rate D_T. We note that the same assumptions regarding time scales in the first reaction-diffusion model are true here. Like PDGF, TGF-β dynamics have a much shorter time scale than those of SMCs and ECM. We therefore set $\frac{\partial T}{\partial t} = 0$ such that:

$$0 = D_T \frac{\partial^2 T}{\partial x^2} - \beta_T T. \tag{5.10}$$

The equation for PDGF ($g(x,t)$) remains unchanged from (4.17).

5.2.2 Boundary and initial conditions

5.2.2.1 SMC ($s(x,t)$)

The assumptions in (4.20) are maintained. At $x = 0$ we assume zero flux conditions so that $J_s|_{x=1} = 0$ where $J_s = -D_s\frac{\partial s}{\partial x} + \chi_s s\frac{\partial g}{\partial x} + h_\rho s\frac{\partial \rho}{\partial x}$ is the SMC flux.

At $x = 1$ we assume there is an influx driven by the chemotactic response of SMCs in the media to the chemical gradient of PDGF. This is proportional to the constant s^* which represents the concentration of existing synthetic SMC in media. Therefore at $x = 1$, $J_s|_{x=1} = \chi_s s^*\frac{\partial g}{\partial x}$.

Substituting the expressions for $\frac{\partial g}{\partial x}$ at both boundaries in the expressions for the flux of SMCs gives the boundary conditions:

$$\left.\frac{\partial s}{\partial x}\right|_{x=0} = \frac{-\alpha_g\chi_s s}{D_g D_s} + \frac{h_\rho s}{D_s}\frac{\partial \rho}{\partial x}, \qquad \left.\frac{\partial s}{\partial x}\right|_{x=1} = \frac{\chi_s\sigma_g g(s^* - s)}{D_s D_g} + \frac{h_\rho s}{D_s}\frac{\partial \rho}{\partial x}. \tag{5.11}$$

We assume a small initial intimal SMC density. This is represented as an initial condition $s(x,0) = s_0$ where s_0 represents a small spatially uniform SMC profile such that $0 < s_0 \ll 1$.

5.2.2.2 ECM ($\rho(x,t)$)

We assume that ECM does not diffuse or migrate, so that there are no spatial derivative terms in the equation. Therefore no boundary conditions are required at either of the boundaries.

5.2.2.3 TGF-β ($T(x,t)$)

As TGF-β is a diffusible growth factor, it is assumed that there is a negative gradient in $T(x,t)$ at both boundaries. Like PDGF there is an inward flux at $x = 0$ and an outward flux at $x = 1$. The boundary conditions are therefore:

$$\left.\frac{\partial T}{\partial x}\right|_{x=0} = -\alpha_T, \qquad \left.\frac{\partial T}{\partial x}\right|_{x=1} = -\sigma_T T. \tag{5.12}$$

The boundary conditions for PDGF remain unchanged from (4.19) at $x = 0$ and $x = 1$.

5.2.3 Non-dimensionalisation

We non-dimensionalise our model, using tildes (except for t) to denote non-dimensionalised quantities. The key parameters x, t, s, g, ρ and T are non-dimensionalised as:

$$s = k\widetilde{s}, \quad g = g_0\widetilde{g}, \quad t = \tau t_0, \quad x = L\widetilde{x}, \quad \rho = \rho_0\widetilde{\rho}, \quad T = T_0\widetilde{T},$$

where k represents the total cell and tissue density, g_0 the characteristic PDGF concentration, t_0 the characteristic time value, L the length of the domain, ρ_0 the characteristic ECM density and T_0 the characteristic TGF-β concentration.

The remaining model parameters are non-dimensionalised as:

$$\begin{aligned}
d_g &= \frac{D_g\widetilde{d_g}}{L^2}\,, & D_s &= \frac{L^2\widetilde{D_s}}{t_0}\,, & d_s &= \frac{\widetilde{d_s}}{t_0}\,, & G_s &= \widetilde{G_s}g_0\,,\\
r_{s1} &= \frac{\widetilde{r_{s1}}}{t_0}\,, & \chi_s &= \frac{\widetilde{\chi_s}L^2}{t_0 g_0}\,, & r_{s0} &= \frac{\widetilde{r_{s0}}}{t_0}\,, & \widetilde{A} &= \frac{r_s}{r_{s0}}\,,\\
\alpha &= \frac{\widetilde{\alpha}D_g g_0}{L}\,, & \sigma &= \frac{\widetilde{\sigma}D_g}{L}\,, & r_d &= \frac{\widetilde{r_d}}{kt_0}\,, & &\\
r_s &= \frac{\rho_0\widetilde{r_s}}{kt_0}\,, & c_s &= T_0\widetilde{c_s}\,, & c_d &= g_0\widetilde{c_d}\,, & \gamma_d &= \frac{\widetilde{\gamma_d}}{T_0}\,,\\
\beta_T &= \frac{D_T\widetilde{\beta_T}}{L^2}\,, & \alpha_T &= \frac{D_T T_0\widetilde{\alpha_T}}{L}\,, & \sigma_T &= \frac{D_T\widetilde{\sigma_T}}{L}\,, & &\\
h_\rho &= \frac{\widetilde{h_\rho}L^2}{t_0\rho_0}\,, & \gamma_\rho &= \frac{\widetilde{\gamma_\rho}}{T_0}\,, & \beta_\rho &= \frac{\widetilde{\beta_\rho}}{t_0}\,, & &
\end{aligned}$$

Dropping the tildes for clarity, the model equations (4.17), (5.7), (5.8), (5.10), and boundary conditions (4.19), (5.11) and (5.12) become:

$$0 = \frac{d^2g}{dx^2} - d_g g, \tag{5.13}$$

$$\frac{\partial\rho}{\partial\tau} = r_s s\Big[1 + \frac{A_s T}{c_s + T}\Big] - r_d s\rho\big[1 + \frac{A_d g}{(c_d + g)(1 + \gamma_d T)}\Big] - \beta_\rho\rho\Big[\frac{1 + \epsilon\gamma_\rho T}{1 + \gamma_\rho T}\Big], \tag{5.14}$$

$$\begin{aligned}
\frac{\partial s}{\partial\tau} =& D_s\frac{\partial^2 s}{\partial x^2} - \frac{\partial}{\partial x}(\chi_s s\frac{\partial g}{\partial x}) - \frac{\partial}{\partial x}\Big(h_\rho s\frac{\partial\rho}{\partial x}\Big) + r_{s0}\Big(1 + \frac{Ag}{G_s + g}\Big)s(1 - s)\\
&- d_s s,
\end{aligned} \tag{5.15}$$

$$0 = \frac{d^2T}{dx^2} - \beta_T T, \tag{5.16}$$

with boundary conditions

$$\begin{aligned}
\left.\frac{\partial s}{\partial x}\right|_{x=0} &= \frac{-\alpha_g \chi_s s}{D_s} + \frac{h_\rho s}{D_s}\frac{\partial \rho}{\partial x}, & \left.\frac{\partial s}{\partial x}\right|_{x=1} &= \frac{\chi_s \sigma_g g(s^* - s)}{D_s} + \frac{h_\rho s}{D_s}\frac{\partial \rho}{\partial x}, \\
\left.\frac{dg}{dx}\right|_{x=0} &= -\alpha_g, & \left.\frac{dg}{dx}\right|_{x=1} &= -\sigma_g g, \\
\left.\frac{\partial T}{\partial x}\right|_{x=0} &= -\alpha_T, & \left.\frac{\partial T}{\partial x}\right|_{x=1} &= -\sigma_T T,
\end{aligned} \tag{5.17}$$

and initial condition

$$s(x, 0) = s_0, \tag{5.18}$$

where s_0 is non-dimensional.

5.2.4 Parameter values

Table 5.1: Base non-dimensionalised parameter values from [45]

Symbol	Definition	Value
d_g	Rate of PDGF decay	0.075
r_s	Baseline rate of ECM phase synthesis by SMCs	1.8
A_s	Maximal factor of PDGF-stimulated increase in rate of SMC proliferation	1.0
c_s	Exponent in SMC phase pressure function	0.3
r_d	Baseline rate of ECM degradation by SMCs	1.5
A_d	Maximal factor of PDGF-stimulated increase in rate of ECM degradation by SMCs	4.0
c_d	PDGF concentration for half-maximal increase in rate of ECM degradation by SMCs	2.5
γ_d	Reciprocal of reference TGF-β concentration for inhibition of ECM degradation by SMCs	0.5
β_ρ	Baseline rate of ECM degradation by immune cells	0.75
γ_ρ	Reciprocal of reference TGF-β concentration for inhibition of ECM degradation by immune cells	10.0
ϵ	Maximal factor of TGF-β stimulated decrease in rate of ECM degradation by immune cells	0.25

Continued on next page

Table 5.1 – continued from previous page

Symbol	Definition	Value
D_s	SMC diffusion coefficient	1.0979
χ_s	SMC motility coefficient	4.5952
h_ρ	SMC haptotaxis coefficient	2.0
r_{s0}	Baseline rate of SMC proliferation	0.02
A	Maximal factor of PDGF-stimulated increase in rate of SMC proliferation	19.0
G_s	PDGF concentration for half-maximal increase in rate of SMC proliferation	1.4
d_s	Rate of SMC loss	0.4
β_T	Rate of TGF-β decay	20.0
α_T	Rate of TGF-β influx	2.5
σ_T	Permeability of IEL to TGF-β	4.0

We note that the non-dimensionalisation of most model parameters in Section 5.2.3 is the same as that of the multiphase model of Watson *et al.* (2020). This is by choice: many of the assumptions are the same between the two models. For example, we assume the same source and sink phenomena of ECM: ECM is synthesised by SMCs but is also degraded by both SMCs and growth factors. The equations used in these source and sink terms are therefore the same between both models. We note however that the multiphase model parameters are volume fractions rather than the measures of concentration and density. This difference is exhibited in the characteristic parameter values including ρ_0 and T_0. Parameters scaled using these characteristic parameters are scaled to biologically appropriate base values.

5.2.5 Numerical analysis

5.2.5.1 Solution of $T(x)$

Solving (5.16) with respect to the boundary conditions (5.17) gives the general solution:

$$T(x) = c_1 e^{(\lambda x)} + c_2 e^{(-\lambda x)},$$

where $\lambda = \sqrt{\beta_T}$. The coefficients are:

$$c_2 = \frac{\exp\lambda\left(\alpha_T + \frac{\alpha_T^2}{\beta_T}\right)}{(\beta_T + \alpha_T)\exp\lambda + (\alpha_T - \beta_T)\exp -\lambda},$$
$$c_1 = c_2 - \frac{\alpha_T}{\beta_T}.$$

With the parameter values in Table 5.1, this gives the solution in Figure 5.1.

We recall that the assumptions of equation (4.17) are continued in this model: the solution of g is therefore the same as Figure 4.4a.

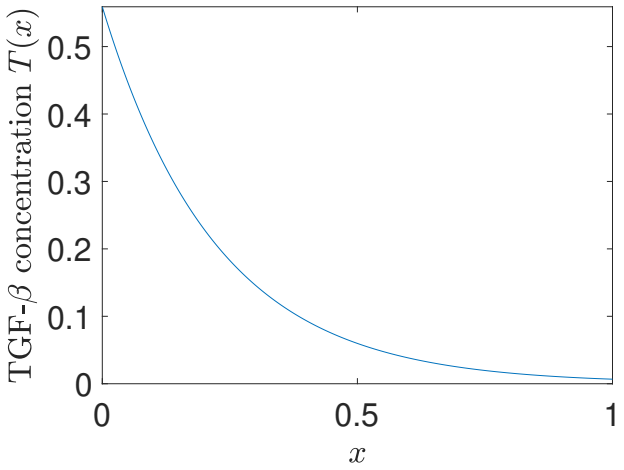

Figure 5.1: The steady state solution of T with values from Table 5.1.

5.2.6 Analytical results

The earlier multiphase model demonstrated that s approaches steady state as t increases. However our new system does not have any crowding terms nor any voids conditions that constrain ECM growth. The equation for ECM in (5.14) also has no flux terms and is space independent with zero velocity. We use this to perform simplified steady state analysis on (5.14) by fixing the values of the other model variables at steady state. Doing so allows us to ensure that ρ at steady state is bounded and behaves biologically.

We first consider PDGF and TGF-β concentrations for a certain point x^*, fixed at g^* and T^* respectively. Both g and T are time independent and are not affected by s and ρ. From these values we consider SMC density s^* also evaluated at the same point at steady state. Evaluating the model equation for ρ (5.14) at steady state where $\frac{\partial \rho}{\partial \tau} = 0$ gives the equation:

$$0 = r_s s^* \Big[1 + \frac{A_s T^*}{c_s + T^*}\Big] - r_d s^* \rho^* \big[1 + \frac{A_d g^*}{(c_d + g^*)(1 + \gamma_d T^*)}\Big] - \beta_\rho \rho^* \Big[\frac{1 + \epsilon\gamma_\rho T^*}{1 + \gamma_\rho T^*}\Big].$$

Recalling that g^* and T^* are fixed and do not change over time, we are able to simplify as constants:

$$\begin{aligned} R_s^* &= r_s \Big[1 + \frac{A_s T^*}{c_s + T^*}\Big], \\ R_d^* &= r_d \big[1 + \frac{A_d g^*}{(c_d + g^*)(1 + \gamma_d T^*)}\Big], \\ B_\rho^* &= \beta_\rho \Big[\frac{1 + \epsilon\gamma_\rho T^*}{1 + \gamma_\rho T^*}\Big], \end{aligned}$$

where R_s^*, R_d^* and B_ρ^* are positive. Our equation becomes:

$$\frac{\partial \rho^*}{\partial \tau} = R_s^* s^* - R_d^* s^* \rho^* - B_\rho^* \rho^*.$$

At steady state,

$$\begin{aligned} R_s^* s^* =& (B_\rho^* + R_d^* s*)\rho^*, \\ \implies \rho^* =& \frac{R_s^* s^*}{(B_\rho^* + R_d^* s^*)}. \end{aligned} \tag{5.19}$$

This simplified expression of ρ at steady state allows us to optimise the concentration of ρ^*. To do this, we take the first derivative of ρ^* with respect to s^*:

$$\begin{aligned} \frac{d\rho^*}{ds^*} =& R_s^*(B_\rho^* + R_d^* s^*)^{-1} \\ & - R_s^* R_d^* s^* (B_\rho^* + R_d^* s^*)^{-2}, \\ =& \frac{R_s^* B_\rho^*}{(B_\rho^* + R_d^* s^*)^2}, \end{aligned}$$

which is strictly positive for all values of s^*. We demonstrate this by solving $\frac{d\rho^*}{ds^*}$ with $T^* = 0.56$ and $g^* = 0.78$ where T^* and g^* are fixed for $x^* = 0$. Figure 5.2 shows that $\frac{d\rho^*}{ds^*}$ is strictly positive, leading to ρ^* increasing monotonically for all values of s^*.

This result of unbounded growth is unrealistic. We expect some maximal ρ^* density at a fixed point in the system which is not present in this current system. We also consider that the model has no constraints on ECM proliferation from increasing unboundedly. This is also a shortcoming of the reaction-diffusion model of Ougrinovskaia (2011), which failed to account for volume-filling in the intima over time. The multiphase model of Watson *et al.* (2020) aimed to address this problem by assuming no voids conditions. Our solution to this unconstrained proliferation is to introduce a source limiting term to the ECM source term in (5.14) so that ECM proliferation saturates over time. We describe this source limiting term in Section 5.3.2.

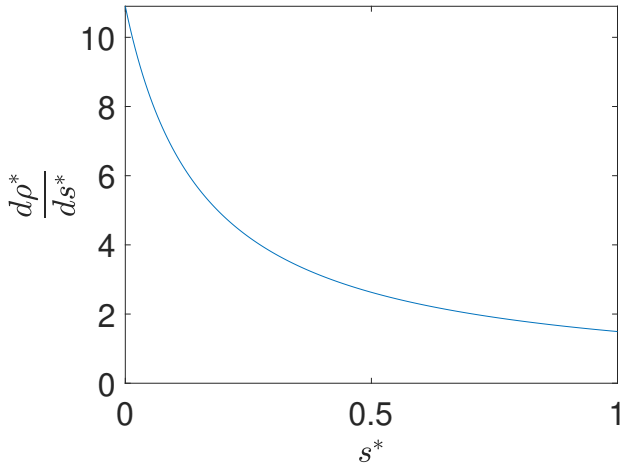

Figure 5.2: The solution of $\frac{\partial \rho^*}{\partial s^*}$ against s^* with $T^* = 0.56$ and $g^* = 0.78$.

5.2.7 Issues with h_ρ

One issue observed in early numerical simulations is that the model becomes ill-posed for large values of h_ρ. Watson *et al.* (2020) observed that the model was only well-posed within the approximate range of $0 < h_\rho < 1.0$, and noted that this ill-posedness likely arose due to the haptotaxis term becoming too large. This issue is unique to the multiphase model as the SMC flux is dependent on a coupled phase pressure equation, involving both s and ρ. We recall that the boundary conditions of s at $x = 0$ (5.5) assume zero flux. The chemotactic flux towards the endothelial boundary must therefore be matched by an opposite diffusive flux. This is an issue because both diffusion and haptotaxis are directly proportional to ρ, such that increasing ρ requires the diffusive flux to change directions to balance the zero flux condition at $x = 0$. If h_ρ becomes too large, the diffusive SMC flux sign becomes negative, which makes the problem ill-posed. Our reaction-diffusion model avoids this issue by not considering coupled phase pressure equations, with the flux terms proportional to the gradients rather than to the densities.

It is still prudent to consider a solution to potential ill-posedness due to high ρ. To do so we introduce the assumption that regions of high ECM density reduce SMC motility. We understand that ECM presence stimulates SMC haptotactic migration, with SMCs moving up the gradient of the ECM. This effect has a limit where ECM density is high. Though the SMCs still experience the adhesive effect of the ECM gradient, the highly dense ECM inhibits SMC motility. For simplicity, we only consider this effect on SMC haptotaxis and not on chemotaxis. Our solution is to make the haptotaxis coefficient a non-linear function of ρ. Noting that ECM proliferation is dependent on s and that the gradient of ECM density is likely to be highest at $x = 0$, we choose a haptotaxis coefficient function $h_\rho(\rho)$ such that it decreases monotonically with increasing ρ. We address this in Section 5.3.1.

5.3 Changes to model

We identified the issue of proliferation that is unconstrained by ECM in Section 5.2.6. We therefore address the need for a limiting function on the ECM source term that limits both SMC proliferation and ECM snythesis.

5.3.1 Haptotaxis function

The haptotaxis coefficient in (5.15) is a constant h_ρ. We recall that we introduced in Section 5.2.7 the assumption that regions of high ECM density reduce SMC motility which can be modelled with a non-linear haptotaxis coefficient function $h_\rho(\rho)$. For simplicity, we choose a haptotaxis coefficient function $h_\rho(\rho)$ that decreases monotonically with increasing ρ. One example of cell haptotaxis being modelled non-linearly with non-diffusional ECM in the literature is given by Ganesan and Lingeshwaran (2017) [21]. In this paper, a number of different non-linear haptotaxis sensitivity functions are suggested for modelling cancer cell haptotaxis. One suitable function is the logarithmic function:

$$h_\rho(\rho) = \frac{h_\rho}{1+\xi_\rho \rho},$$

where h_ρ serves as the maximum value of this function and ξ_ρ as a scaling parameter. Implementing this leads to the flux term:

$$J_s = -D_s \frac{\partial s}{\partial x} + \chi_s s \frac{\partial g}{\partial x} + \frac{h_\rho}{1+\xi_\rho \rho} s \frac{\partial \rho}{\partial x},$$

such that (5.15) becomes:

$$\begin{aligned} \frac{\partial s}{\partial \tau} =& D_s \frac{\partial^2 s}{\partial x^2} - \frac{\partial}{\partial x}(\chi_s s \frac{\partial g}{\partial x}) - \frac{\partial}{\partial x}\Big(\frac{h_\rho}{1+\xi_\rho \rho} s \frac{\partial \rho}{\partial x}\Big) \\ &+ r_{s0}\Big(1 + \frac{Ag}{G_s + g}\Big) s(1-s) - d_s s, \end{aligned} \tag{5.20}$$

and the boundary conditions accordingly change to:

$$\frac{\partial s}{\partial x}\Big|_{x=0} = \frac{-\alpha_g \chi_s s}{D_s} + \frac{h_\rho}{1+\xi_\rho \rho} \frac{s}{D_s} \frac{\partial \rho}{\partial x}, \tag{5.21}$$

$$\frac{\partial s}{\partial x}\Big|_{x=1} = \frac{\chi_s \sigma_g g(s^* - s)}{D_s} + \frac{h_\rho}{1+\xi_\rho \rho} \frac{s}{D_s} \frac{\partial \rho}{\partial x}. \tag{5.22}$$

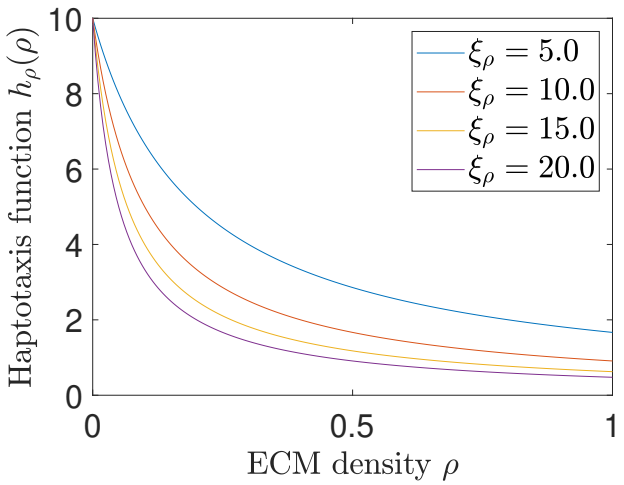

Figure 5.3: The solutions of $h_\rho(\rho) = \frac{h_\rho}{1+\xi_\rho \rho}$ with $h_\rho = 10.0$ and $\xi_\rho = 5.0$, 10.0, 15.0 and 20.0 against ρ.

Figure 5.3 shows $h_\rho(\rho)$ as a function of ρ for different values of ξ_ρ. The haptotaxis function decreases with increasing ρ, with the scaling parameter ξ_ρ determining the rate of decrease. We choose $\xi_\rho = 10.0$ as the appropriate base value for future simulations.

5.3.2 Source limiting function

The results in 5.2.6 showed that the absence of constraints on ECM growth leads to unbounded growth. The proposed solution was to introduce a limit to the source term of (5.14). We consider a limiting function $\psi(\rho)$:

$$\psi(\rho) = \frac{a^n}{a^n + \rho^n}, \tag{5.23}$$

where n is the function index and a is a scaling parameter.

As shown in Figure 5.4, the function decreases with increasing ρ and tends to zero as ρ approaches 1.0. We apply this function to the ECM synthesis term, where it operates as a nonlinear modulating factor. Therefore the dynamics of ρ become:

$$\frac{\partial \rho}{\partial \tau} = r_s \psi(\rho) s\Big[1 + \frac{A_s T}{c_s + T}\Big] - r_d s\rho\Big[1 + \frac{A_d g}{(c_d + g)(1 + \gamma_d T)}\Big] - \beta_\rho \rho\Big[\frac{1 + \epsilon\gamma_\rho T}{1 + \gamma_\rho T}\Big].$$

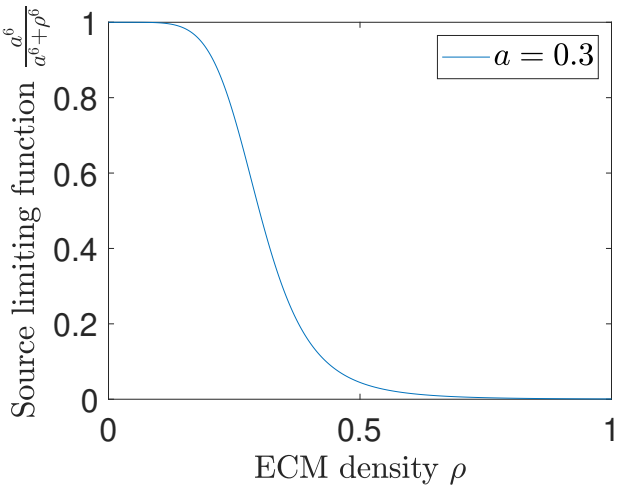

Figure 5.4: The solution of $\psi(\rho)$ over $\rho(x,t)$ with $a = 0.3$ and $n = 6$.

5.3.2.1 Analysis

We perform the same steady state analysis as in Section 5.2.6, again considering PDGF and TGF-β concentrations for a certain point x^*, fixed at g^* and T^*. From these values we consider SMC density s^* at the same point at steady state. This gives the model equation for ECM density at this fixed point ρ^*:

$$\begin{aligned}\frac{\partial \rho^*}{\partial \tau} =& r_s s^* \left(\frac{a^n}{a^n + \rho^{*n}}\right)\left[1 + \frac{A_s T^*}{c_s + T^*}\right] \\ &- r_d s^* \rho^* \left[1 + \frac{A_d g^*}{(c_d + g^*)(1 + \gamma_d T^*)}\right] - \beta_\rho \rho^* \left[\frac{1 + \epsilon\gamma_\rho T^*}{1 + \gamma_\rho T^*}\right].\end{aligned}$$

We define the constants:

$$\begin{aligned}R_s^* &= r_s\left[1 + \frac{A_s T^*}{c_s + T^*}\right], \\ R_d^* &= r_d\left[1 + \frac{A_d g^*}{(c_d + g^*)(1 + \gamma_d T^*)}\right], \\ B_\rho^* &= \beta_\rho\left[\frac{1 + \epsilon\gamma_\rho T^*}{1 + \gamma_\rho T^*}\right],\end{aligned}$$

where R_s^*, R_d^* and R_ρ^* are positive. With $\frac{\partial \rho}{\partial \tau} = 0$ at steady state our equation becomes:

$$0 = R_s^* s^* \left(\frac{a^n}{a^n + \rho^{*n}}\right) - R_d^* s^* \rho^* - B_\rho^* \rho^*. \tag{5.24}$$

For the sake of simplicity, we simplify the equation at steady state by setting the index of $\psi(\rho)$ to 1 such that:

$$\psi(\rho) = \frac{a}{a + \rho}.$$

The equation then simplifies to:

$$0 = (B_\rho^* + aR_d^* s^*)\rho^{*^2} + a(R_d^* s^* + B_\rho^*)\rho^* - aR_s^* s^*,$$

which gives the non-negative solution:

$$\rho^* = \frac{-(a^*(R_d^* s^* + B_\rho^*)) + \sqrt{(a^*(R_d^* s^* + B_\rho^*))^2 + 4(B_\rho^* + aR_d^* s^*)(a^* R_s^* s^*)}}{2(B_\rho^* + aR_d^* s^*)}. \tag{5.25}$$

Solving for $\frac{d\rho^*}{ds^*}$ gives:

$$\begin{aligned}\frac{d\rho^*}{ds^*} =& \Bigg(\Big(-a^* R_D^* + \frac{1}{2}\Big((a^*(R_d^* s^* + B_\rho^*))^2 + 4(B_\rho^* + R_d^* s^*)(a^* R_s^* s^*)\Big)^{\frac{-1}{2}} \Big) \\ & (B_\rho^* + aR_d^* s^*)\Big) - (2aR_d^* s^*)\Big((a^*(R_d^* s^* + B_\rho^*))^2 + 4(B_\rho^* + aR_d^* s^*)(a^* R_s^* s^*)\Big)^{\frac{1}{2}} \cdot \\ & \Big(2(B_\rho^* + R_d^* s^*)\Big)^{-2}.\end{aligned}$$

We choose the same steady state values as in 5.2.6, with $T^* = 0.56$ and $g^* = 0.78$. Figure 5.5 shows that $\frac{d\rho^*}{ds^*}$ is no longer strictly positive but instead becomes negative for increasing s^*.

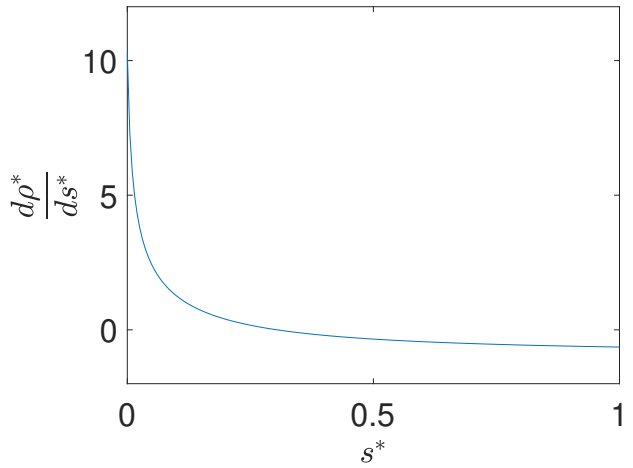

Figure 5.5: The solution of $\frac{\partial\rho^*}{\partial s^*}$ against s^* with $a = 0.3$, $T^* = 0.56$ and $g^* = 0.78$.

We obtained a general solution of ρ^* in equation (5.25) with the index $n = 1$. Increasing the index to $n = 2$ such that:

$$h(\rho) = \frac{a^2}{a^2 + \rho^2},$$

allows equation (5.24) be simplified as:

$$\rho^{*3} + a^2\rho - \frac{s^* R_s^* a^2}{R_D^* s^* + \beta_\rho^*} = 0.$$

Solving this as a depressed cubic gives the general solution with the index $n = 2$:

$$\begin{aligned}\rho^* =&(\frac{\gamma}{2} + (\frac{\gamma^2}{4} + \frac{\beta^2}{27})^{\frac{1}{2}})^{\frac{1}{3}} \\ &+ (\frac{\gamma}{2} - (\frac{\gamma^2}{4} + \frac{\beta^2}{27})^{\frac{1}{2}})^{\frac{1}{3}},\end{aligned} \tag{5.26}$$

with:

$$\beta = a \text{ and } \gamma = \frac{s^* R_s^* a^2}{R_D^* s^* + \beta_\rho^*}.$$

With the solutions of ρ^* for equations (5.19) (5.25) (5.26), we are able to observe the effect of the index n on the steady state value of ρ^*. We represent the solution (5.19) where there is no source limiting function as having index $n = 0$. This allows us to compare three solutions in Figure 5.6. The comparison shows the suppression effect of the limiting function, with the steady state solutions of ρ^* approaching a limit for $n = 1$ and 2. We also observe that this suppression effect increasing with the value of the index. We therefore choose the index value $n = 6$ for our limiting function. This ensures that the suppression effect applies even for low values of ρ. Figure 5.4 shows the solution of the limiting function $\psi(\rho)$: the function decreases rapidly for $0.2 < \rho < 0.5$.

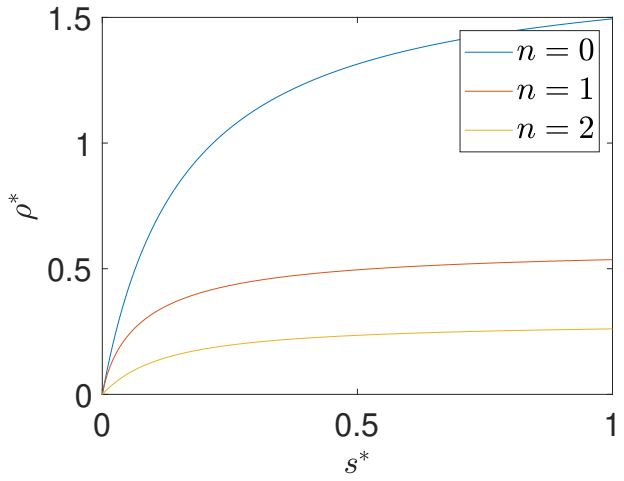

Figure 5.6: The solutions of ρ^* against s^* with $a^* = 0.3$, $T^* = 0.2$ and $g^* = 0.5$ for $n = 0$, 1 and 2.

5.3.3 Amended model

By implementing the changes outlined in subsections 5.3.1 and 5.3.2, the model equations in 5.2.3 are amended such that:

$$0 = \frac{d^2 g}{dx^2} - d_g g, \tag{5.27}$$

$$\frac{\partial \rho}{\partial \tau} = r_s s\psi(\rho)\Big[1 + \frac{A_s T}{c_s + T}\Big] - r_d s\rho\Big[1 + \frac{A_d g}{(c_d + g)(1 + \gamma_d T)}\Big] \tag{5.28}$$

$$- \beta_\rho \rho\Big[\frac{1 + \epsilon\gamma_\rho T}{1 + \gamma_\rho T}\Big], \tag{5.29}$$

$$\frac{\partial s}{\partial \tau} = D_s \frac{\partial^2 s}{\partial x^2} - \frac{\partial}{\partial x}(\chi_s s \frac{\partial g}{\partial x}) - \frac{\partial}{\partial x}\Big(h(\rho) s \frac{\partial \rho}{\partial x}\Big) + r_{s0}\Big(1 + \frac{Ag}{G_s + g}\Big) s(1 - s) \tag{5.30}$$

$$- d_s s,$$

$$0 = \frac{d^2 T}{dx^2} - \beta_T T, \tag{5.31}$$

with boundary conditions

$$\begin{aligned} \frac{\partial s}{\partial x}\Big|_{x=0} &= \frac{-\alpha_g \chi_s s}{D_s} + \frac{h(\rho) s}{D_s}\frac{\partial \rho}{\partial x}, & \frac{\partial s}{\partial x}\Big|_{x=1} &= \frac{\chi_s \sigma_g g(s^* - s)}{D_s} + \frac{h(\rho) s}{D_s}\frac{\partial \rho}{\partial x}, \\ \frac{dg}{dx}\Big|_{x=0} &= -\alpha_g, & \frac{dg}{dx}\Big|_{x=1} &= -\sigma_g g, \\ \frac{\partial T}{\partial x}\Big|_{x=0} &= -\alpha_T, & \frac{\partial T}{\partial x}\Big|_{x=1} &= -\sigma_T T, \end{aligned} \tag{5.32}$$

and initial condition

$$s(x, 0) = s_0, \tag{5.33}$$

where s_0 is non-dimensional. The non-linear haptotaxis function $h(\rho)$ is the kinetic function:

$$h(\rho) = \frac{h_\rho}{1 + \xi_\rho \rho},$$

with scaling parameter ξ_ρ. The source limiting function $\psi(\rho)$ is:

$$\psi(\rho) = \frac{a^6}{a^6 + \rho^6}.$$

The base parameter values for the newly scaled parameters h_ρ, ξ_ρ and a are in Table 5.2. These are chosen as appropriate values that provide realistic results.

Table 5.2: Amended non-dimensionalised parameter values with values from 5.3.1 and 5.3.2.

Symbol	**Definition**	**Non-dimensionalised value**
h_ρ	Haptotaxis coefficient	6.0
ξ_ρ	Scaling coefficient	10.0
a	Scaling parameter	0.3

5.4 Results

5.4.1 Base case simulation

We choose our base case parameter values from Tables 5.1 and 5.2. We recall that T and g are both time independent and their steady state solutions are shown in Figures 5.1 and 4.4a. The numerical solutions for the time evolution of s and ρ are reproduced in Figures 5.7a and 5.7b respectively.

The solution profile of s in Figure 5.7a shows that the highest accumulation of SMCs is at the endothelial boundary. This is expected given that SMC migration due to chemotaxis and haptotaxis drives SMCs towards the endothelium. We observed in Section 4.4.3 that this accumulation of SMCs is greatly affected by the chemotactic movement of SMCs up the gradient of PDGF, and that PDGF concentration is greatest near the endothelial boundary (as observed in Figure 4.4a). The effect of the introduced haptotaxis term and dependence on ρ is explored further by parameter sensitivity analysis. Figure 5.8a shows that SMC distribution reaches steady state at around 25 months. This is slightly longer than the observed steady state time of approximately 22 months in the previous model shown in Figure 4.4c.

The solutions of ρ as a function of x for different times t are shown in Figure 5.7b. Both solutions displayed in Figures 5.7a and 5.7b display greater accumulation of s and ρ near the endothelium, suggesting the formation of a cap. This ECM profile is shaped by the ECM synthesis and decay terms in equation (5.28). We recall that ECM synthesis is dependent on s and T. Noting that both s and T are greatest near the $x = 0$ boundary (Figures 5.7a and 5.1 respectively), we expect ECM synthesis to be greatest near the $x = 0$ boundary. Similarly, the second decay term in equation (5.28) decreases with increasing T so that it is lowest near the boundary $x = 0$. Figure 5.8b shows that the time to reach steady state is around 25 months, which is similar to the observed steady state time for SMCs in Figure 5.8a. This suggests the timescale of ρ is the same as that of s, which is expected given the dependence of ρ on s. It also suggests that like s, the time scale for cap formation is shorter than the time scale required to reach steady state. Intimal ECM density has already plateaued by $t = 10$, and Figure 5.7b shows that the solution of ρ at $t = 9.75$ is only marginally different to the steady state solution.

These base solutions show that with the base parameter values from Tables 5.1 and 5.2, the model equations demonstrate the initial stages of cap formation. ECM is synthesised by SMCs and growth factors and accumulates mainly around the endothelial boundary. It also undergoes general degradation and decay. The resulting profile exhibits the formation of a cap region which grows before ECM and SMC dynamics reach steady state.

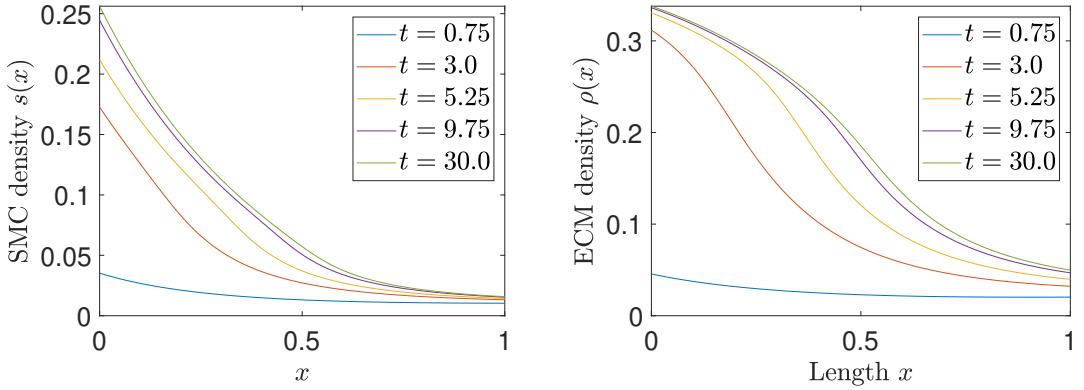

(a) (b)

Figure 5.7: Solutions of (a) s and (b) ρ as functions of x with parameter values from Tables 5.1 and 5.2 at $t = 0.75$, 3.0, 5.25, 9.75 and 30.0.

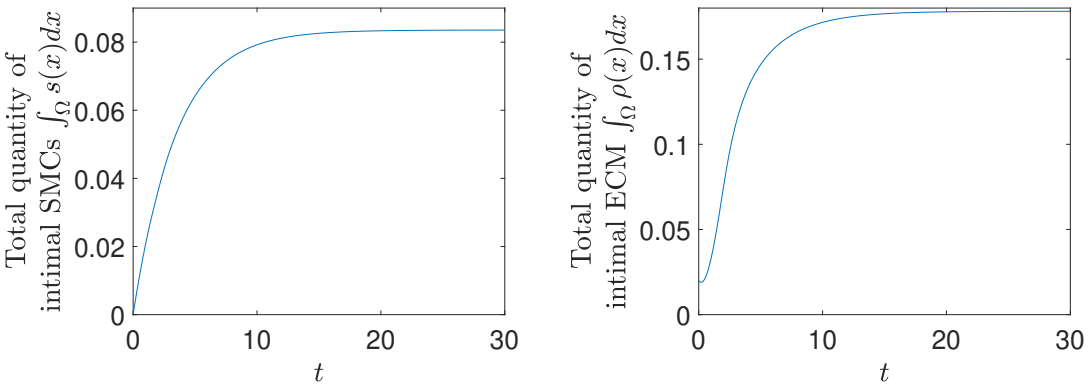

(a) (b)

Figure 5.8: Time evolutions of (a) total intimal SMC density $\int_\Omega s(x)dx$ and (b) total intimal ECM density $\int_\Omega \rho(x)dx$ with parameter values from Tables 5.1 and 5.2 from $t = 0.0$ to 30.0.

5.4.2 Parameter sensitivity

We recall that the model equations in Section 5.3.3 extend the earlier reaction-diffusion model equations of Section 4.2.3 by introducing a number of new parameters. We therefore perform parameter sensitivity analysis on three key parameters: α_T, h_ρ and α_g.

The parameter α_T determines the influx of TGF-β from the endothelium. If we set its value to zero, we can observe the effects of T on ρ. The parameter h_ρ is the haptotaxis constant coefficient that represents the haptotactic migration of s. Finally, α_g determines the influx of PDGF from the endothelium. We note that in the model equation for ρ (5.30), the first degradation term represents ECM degradation

by SMCs which is proportional to increasing g. SMC dependence on PDGF for proliferation and migration also means that the changing solution of g will affect the solution of s. This allows us to observe the effects of PDGF and SMCs on ECM dynamics.

5.4.2.1 α_T

Figure 5.9 compares the steady state solutions of T, s and ρ for $\alpha_T = 0.0$ and $\alpha_T = 2.5$. The first case ($\alpha_T = 0.0$) is when there is no influx of TGF-β from the endothelium compared to the second where the rate of TGF-β influx is the base rate from Table 5.1 ($\alpha_T = 2.5$). We observe in Figure 5.9a that when $\alpha_T = 0.0$, the absence of TGF-β influx results in zero T in the intima. The effect of this on ρ, where the equation for ECM (5.30) depends on T in its source and sink terms, is that the absence of T leads to reduced collagen at the endothelial boundary. We recall that we have assumed no spatial movement and no boundary flux conditions for ρ and that the source term in equation (5.30) is the only source of ECM. Therefore a reduction in the magnitude of the source and sink terms is expected to affect ρ, particularly in regions where there is a significant change in T when $\alpha_T = 0$. We observe this near the endothelial $x = 0$ boundary, where the change in the value of T is greatest (as shown in Figure 5.9a). This decrease was observed in Watson *et al.* (2020), where the absence of T reduced the total collagen deposition by approximately 15 percent and the average ECM volume fraction in the cap region by approximately 40 percent [45]. In Figure 5.9c, the absence of T also results in a decrease in ρ around $x = 0$. This observed decrease in ECM density is around 30 percent, which is similar to the observed 40 percent in Watson *et al.* (2020).

We observe in Figure 5.9b that the change in ρ due to the change in the value of α_T has a weak effect on the steady state solutions of s. We recall that the haptotaxis function $h_\rho(\rho)$ decreases with increasing ρ and that the term modelling the haptotaxis rate is also proportional to the ECM gradient $\frac{d\rho}{dx}$. This suggests that changes to the haptotaxis rate may have a weak effect on the dynamics of s. We contrast this to Watson *et al.* (2020) where zero influx of TGF-β was observed to lead to a small increase in s. This was due to the fact that in Watson *et al.* (2020), the influx of the two growth factors TGF-β and PDGF is mass balanced. A reduction in TGF-β influx is therefore balanced by a corresponding increase in PDGF influx. As SMC proliferation is proportional to PDGF concentration, an increasing PDGF influx lead to increasing s. This increase in s was also due to the reduction in collagen which increased SMC proliferation due to a decrease in contact inhibition. The difference in results between models is because we do not assume mass balanced growth factors in this reaction-diffusion model.

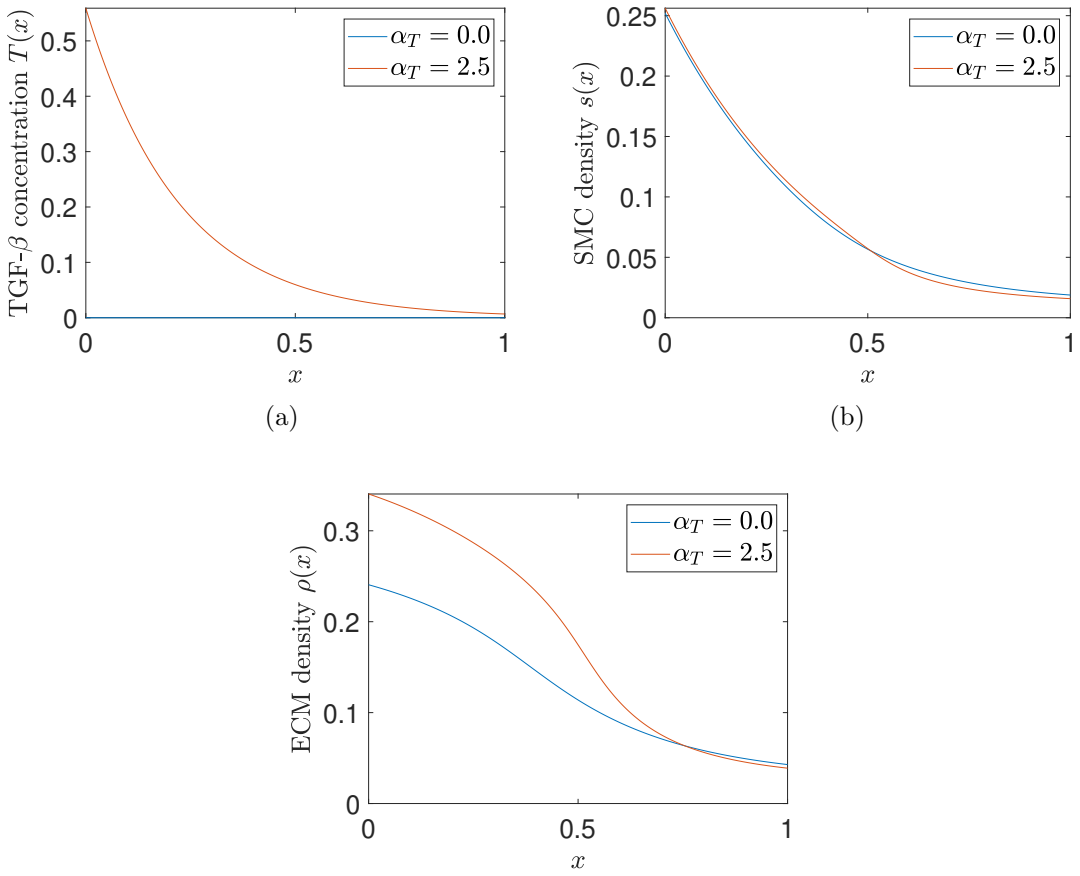

Figure 5.9: Comparisons of steady state solutions of (a) T, (b) s and (c) ρ for two values of α_T : $\alpha_T = 0.0$ and $\alpha_T = 2.5$ at $t = 30.0$.

5.4.2.2 h_ρ

In this reaction-diffusion model, the results of Section 5.4.2.1 suggest that changes to ρ have a marginal effect on s. This was attributed to a weak haptotaxis coefficient value which makes the system insensitive to changes in ρ and $\frac{d\rho}{dx}$. We therefore perform parameter sensitivity analysis on h_ρ to test this effect.

We observe in Figure 5.10a that increasing haptotaxis coefficient values correspond to greater values of s near the $x = 0$, as the greater haptotactic coefficient value increases SMC migration towards this boundary. We observe however that this changes around $x = 0.4$, where s becomes lower for greater values of h_ρ near the $x = 1$ boundary. The same change is observed in the steady state solutions of ρ in Figure 5.10b.

To explain this change, we recall that the value of g is lowest near $x = 1$ and that the solution of g is unaffected by other variables. The rate of SMC proliferation, which is dependent on g, is therefore also lowest near $x = 1$. As h_ρ and the rate of SMC haptotactic migration up the gradient of ECM is increased, the rate of SMC

proliferation near $x = 1$ is comparatively lower. SMCs therefore migrate towards $x = 0$ at a greater rate than at which they proliferate, leading to the values of s being lowest near $x = 1$.

We observe that ECM density and distribution follows that of SMC density and distribution in Figure 5.10b. The values of ρ are greatest near $x = 0$ and lowest near $x = 1$ for higher values of h_ρ, with the differences in magnitude occurring at the same regions as s. This is because ρ has zero velocity in time and its synthesis is dependent on s. These results demonstrate that changes in s are reflected in the solutions for ρ and that ECM distribution is dependent on local SMC density. We contrast this to what was observed in the parameter sensitivity analysis of α_T, where changes to ρ had a weak effect on s.

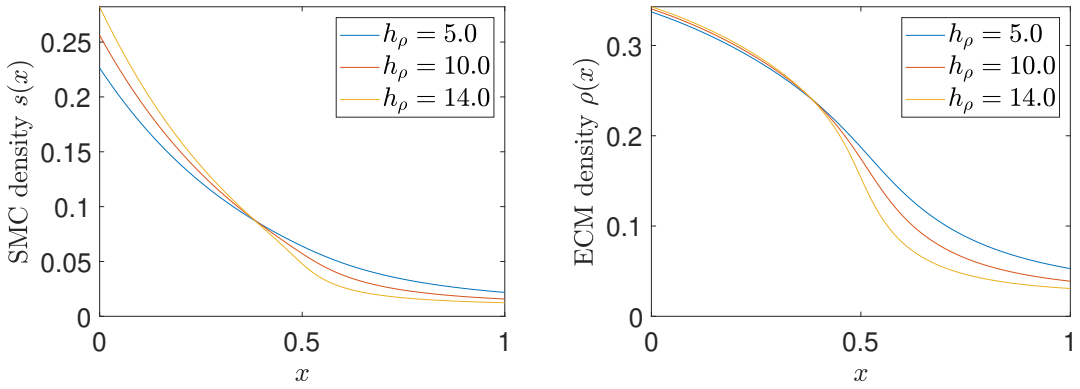

(a) (b)

Figure 5.10: Comparisons of steady state solutions of (a) s and (b) ρ for three values of h_ρ: $h_\rho = 5.0$, $h_\rho = 10.0$ and $h_\rho = 14.0$ at $t = 30.0$.

5.4.2.3 α_g

In the previous section 5.4.2.2, we observed that changes in s are reflected in the solutions of ρ. We initially observed the effects of varying the influx of TGF-β in Section 5.4.2.1. In this section we perform the same analysis on PDGF influx. SMCs are dependent on PDGF for proliferation and the chemical gradient of PDGF for chemotaxis. We recall that in Section 4.4.1, SMC proliferation was determined to have a weak contribution to SMC distribution. SMC chemotactic migration however was identified as influential to the profile of s and potential cap formation in Section 4.4.3. We therefore expect the main contribution of increasing α_g on the dynamics of s to be increasing gradients of g ($\frac{dg}{dx}$) and subsequent greater chemotactic migration of s towards the $x = 0$ boundary.

Figure 5.11b confirms these expectations with the SMC distribution close to $x = 0$ being greater for greater values of α_g. We also observe that the value of s is lower near $x = 1$ for greater values of α_g. This is because an increased PDGF influx corresponds to a greater gradient of g as observed in Figure 5.11a.

We expect changes in s to be reflected in the solutions of ρ. Figure 5.11c confirms that ECM accumulation is dependent on local SMC density. We observe that ρ is greatest close to $x = 0$ for greater values of α_g and vice versa. Within the approximate region $0 \leq x < 0.5$, the value of s is greater when $\alpha_g = 1.2$ compared to when $\alpha_g = 0.55$. The opposite holds within the region $0.5 \leq x < 1$. We observe that the value of ρ reflects this difference in the values of s for the values of α_g. ECM distribution is therefore dependent on SMC distribution. We note also that the effect of the source limiting term is also evident in the ECM profile. When $\alpha_g = 1.2$, the value of s at the $x = 0$ boundary is approximately $s(0, t) = 0.94$, which is more than three times greater than the value of value of s (approximately $s(0, t) = 0.26$ at the $x = 0$ boundary when $\alpha_g = 0.55$. The accumulation of ρ is suppressed at approximately $\rho(0, t) = 0.35$.: the source limiting term therefore imposes a restriction on the maximum value of ρ. As a result, while ECM distribution is dependent on SMC density, SMC distribution is also a critical factor to the ECM profile.

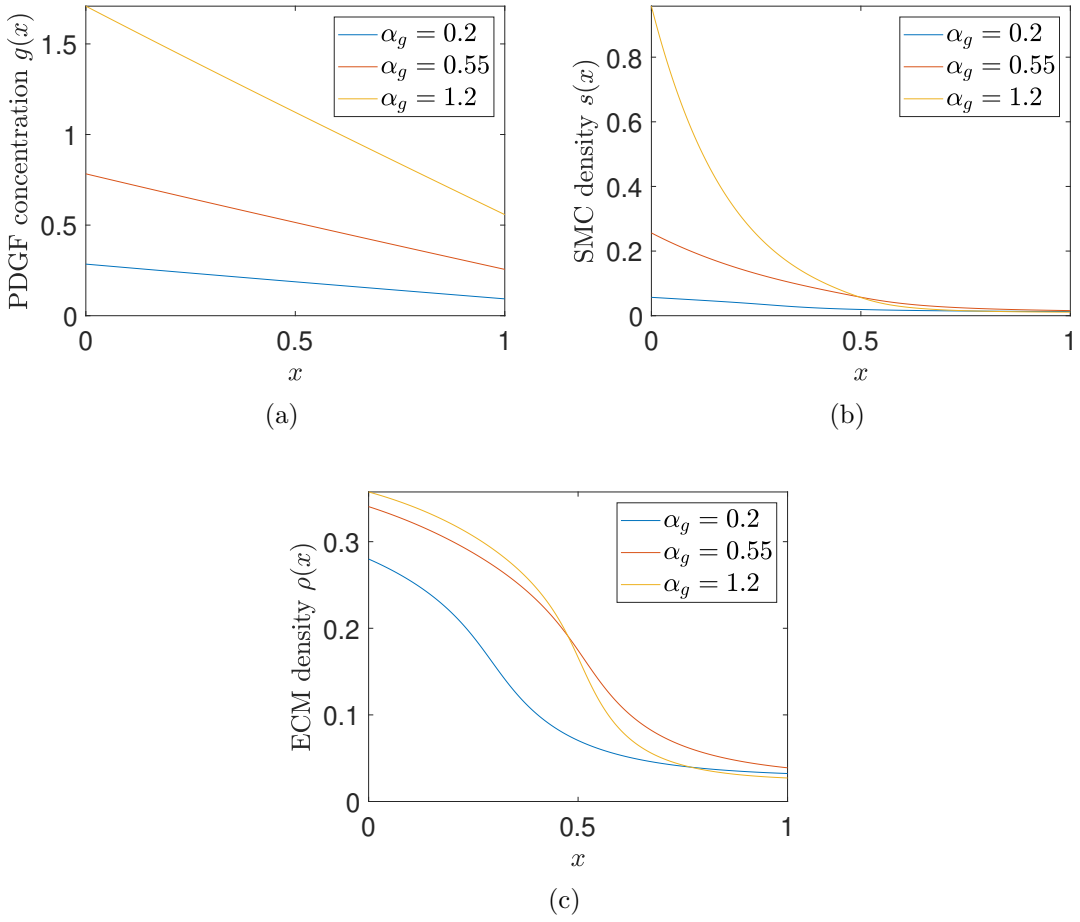

Figure 5.11: Comparisons of steady state solutions of (a) g, (b) s and (c) ρ for three values of α_g : $\alpha_g = 0.2$, $\alpha_g = 0.55$ and $\alpha_g = 1.2$ at $t = 30.0$.

5.5 Discussion

The reaction-diffusion model in this chapter represents the collagen synthesis stage of the formation of a collagenous cap. We observe from the results in Section 5.4.1 that SMCs accumulate near the endothelial boundary. Proliferation due to PDGF stimulation is greatest in this region, and SMCs migrate chemotactically and haptotactically towards this boundary. A SMC cap is therefore created near the endothelial boundary. ECM is synthesised by SMCs, which are stimulated by TGF-β [2]. The aggregation of both SMCs and TGF-β is greatest near the endothelial boundary and therefore ECM synthesis is greatest at this region. This creates a collagenous cap region near the endothelial boundary.

The dynamics of the formation of the collagenous cap region are shown in the results of parameter sensitivity analyses of α_T, h_ρ and α_g. We observe that ECM distribution is dependent on SMC distribution: SMC distribution trends are reflected in the distribution of ECM. The density of ECM however is constrained by the source limiting term, which we introduced to prevent unbounded accumulation. The rate of ECM accumulation is therefore limited by this term and is restricted to a maximum value regardless of the local SMC density. Our results in Section 5.4.2.3 suggest that for the base parameter values of Table 5.1, the magnitude of ECM density at the endothelial boundary is already quite close to this maximum value.

We observed in Section 5.4.2.1 that the solutions of ρ have a weak effect on s. Significant changes to ρ such as decreasing the value of ECM density at the endothelial boundary by around 30 percent yielded little change to s. Changing the value of the haptotaxis coefficient h_ρ in Section 5.4.2.2 resulted in some changes to s, though this also corresponded to changes in ρ. The results therefore suggest that ρ has a marginal effect on s while s has a greater effect on the dynamics of ρ.

Two main factors that contribute to cap formation were identified. The first is the presence of TGF-β. Its absence leads to a reduction in ECM density by around 30 percent around the endothelial boundary. The second is the distribution of SMCs. The results in Sections 5.4.2.2 and 5.4.2.3 show that the density and distribution of ECM are determined by those of SMCs.

We therefore conclude that a greater distribution of SMCs close to the endothelial boundary is critical to a larger fibrous cap region. SMC density affects the synthesis of ECM but the growth of this cap region saturates with increasing ECM density regardless of the local SMC density. Our model suggests that SMC density near the endothelial boundary is relevant until the maximum value of ECM density is reached.

The results of this section show that the base reaction-diffusion model described in Chapter 4 can be extended to include TGF-β and ECM dynamics. Our model adopts the assumptions from the reference models of Watson *et al.* (2018, 2020) to reflect up-to-date experimental observations: we observe the formation of a collagenous cap region near the endothelial boundary where the presence of a SMC cap stimulates ECM synthesis. As with the reference model of Watson *et al.* (2020), our base

model therefore can be extended to reflect more stages of plaque formation; our reaction-diffusion model is however computationally and analytically simpler than the multiphase model.

Chapter 6

Introducing early stages of lesion growth by modelling macrophages and modified low density lipoprotein characteristics

The two previous models addressed two intermediate stages of cap formation. The first model in Section 4.2.3 modelled the stage of SMC migration in response to PDGF. In the second model in Section 5.2.3, we extended this to include ECM and TGF-β and modelled the formation of a collagen cap region. The results of this model showed that SMC distribution had a significant effect on ECM distribution and therefore the formation of a cap region.

In this section we continue to analyse the intermediate stages of cap formation, though we introduce the early stage of lesion growth. This is the initial stage where LDL begins to enter the intima which stimulates a number of responses including monocyte differentiation into macrophages and modLDL uptake by macrophages [4]. To do so we introduce two variables representing modLDL and macrophages. We use two models for reference: the reaction-diffusion model of Ougrinovskaia (2011) [37] which analyses SMC migration during the early stages of lipid core formation, and Chalmers *et al.* (2015) [11] which focuses on modLDL, monocytes and macrophages. These two models are summarised in the next two sections. We note that variables from other stages of cap formation (including foam cells) not included in the scope of this model are excluded.

Both models begin by representing the initial stage of lesion growth by assuming that the integrity of the endothelium has failed and that LDLs penetrate the arterial wall, entering the intima through the endothelial boundary ($x = 0$). In the intima, LDLs are oxidised and become modLDLs. This presence of modLDLs trigger a number of responses. One response is the production of cytokines such as monocyte chemotactic protein 1 (MCP-1) and PDGF. These cytokines attract monocytes to migrate from the lumen and into the intima through the endothelial boundary [16,31, 36]. Monocytes differentiate into macrophages, which then consume the modLDLs [4]. We note that this uptake of modLDLs leads to macrophages converting to foam cells; we ignore this process at this stage of modelling.

The research objective is to create a reaction-diffusion model that simply describes the general progression of plaque growth. The reference models of Ougrinovskaia (2011) and Chalmers *et al.* (2015) therefore provide terms and assumptions that reflect up-to-date results from experimental data and the broader biological literature. While both are reaction-diffusion models, we note that Chalmers *et al.* (2015)

only describes the initial lesion initiation stage, while Ougrinovskaia (2011) provides a submodel for the lesion initiation stage (which is part of a larger framework).

Our objective with this model is to therefore create a reaction-diffusion model for the initial lesion initiation stage that takes the up-to-date assumptions and terms of Chalmers *et al.* (2015), while also adopting the way Ougrinovskaia (2011) integrates the lesion initiation stage into SMC and PDGF dynamics. This focus on the initial lesion initiation stage is important because unlike the stages described in the models in Chapters 4 and 5 the two phases integrated in this model (lesion initiation and SMC migration) are of significantly different timescales. We recall that an objective with our thesis model framework is that it must be extendable to include more equations and variables without adding unnecessary additional complexity. We therefore investigate the framework's ability to include a range of different timescales, and any effect they have on dynamics.

6.1 Lesion initiation and smooth muscle cell migration: Ougrinovskaia (2011)

We recall that in Section 4.1.2, we focused on the submodel of the larger reaction-diffusion model of Ougrinovskaia (2011). In that section the submodel explored the dynamics of SMC recruitment. The model in this section is a submodel of the same larger model. This means that its domain is a one dimensional slice of the intima, with $x = 0$ at the endothelial boundary and $x = L$ at the media boundary, where L is the length of the domain. The domain is defined on a one-dimensional domain $x \in [0, L]$ where $L = 1$ and time is denoted as t. The model focuses on two main stages: the recruitment of SMCs and the initial growth and influx of macrophages and modLDLs. There are four equations for the dynamics of the following respective species: modLDL concentration $l(x,t)$, macrophage density $m(x,t)$, SMC density $s(x,t)$ and PDGF concentration $g(x,t)$.

The model assumes that modLDLs diffuse through the domain with respect to diffusion coefficient D_l. They are assumed to be uptaken by both macrophages and foam cells via Michaelis-Menten dynamics at a rate proportional to the uptake rate μ_l, and to undergo linear decay with respect to the degradation term d_l.

Macrophage motility is described as driven by random motion and chemotaxis, with macrophages diffusing through the domain with respect to random motion coefficient D_m. They move chemotactically along the gradient of the macrophage chemoattractant p with respect to chemotaxis coefficient χ_m. As macrophages uptake modLDLs as described above, they are assumed to convert to foam cells at a rate proportional the rate μ_m. They also undergo apoptosis and necrosis, which are represented as a linear decay term d_m.

SMCs have no newly introduced dependence on macrophages. SMCs dynamics are therefore the same as in Section 4.1.2.

On the other hand PDGF dynamics now include a source term with macrophage dependence. PDGF-B, which is simplified as PDGF, is a chemoattractant and mitogen for SMCs [28, 36, 46]. It is also elaborated by macrophages [28, 46]: this elaboration is proportional to the local macrophage density and the rate of production of PDGF by macrophages σ_g.

The system of equations therefore become:

$$\frac{\partial l}{\partial t} = D_l \frac{\partial^2 l}{\partial x^2} - \mu_l \frac{ml}{1+l} - d_l l, \tag{6.1}$$

$$\frac{\partial m}{\partial t} = D_m \frac{\partial^2 m}{\partial x^2} - \chi_m \frac{\partial}{\partial x}\Big(m \frac{\partial p}{\partial x}\Big) - \mu_m \frac{ml}{1+l} - d_m m, \tag{6.2}$$

$$\frac{\partial g}{\partial t} = D_g \frac{\partial^2 g}{\partial x^2} + \sigma_g m - d_g g, \tag{6.3}$$

$$\frac{\partial s}{\partial t} = D_s \frac{\partial^2 s}{\partial x^2} - \chi_s \frac{\partial}{\partial x}\Big(s \frac{\partial g}{\partial x}\Big) + \Big(1 + \frac{r_s g}{G_s + g}\Big) s\Big(1 - s\Big) - d_s s. \tag{6.4}$$

At the endothelial boundary ($x = 0$), LDLs enter the intima where they oxidise to become modLDLs. The model assumes that this occurs fast enough to directly describe modLDLs influx σ_l at the $x = 0$ boundary. Macrophages and macrophage chemoattractants also enter the intima, represented as an influx σ_m and σ_p respectively at the $x = 0$ boundary. Zero flux conditions are assumed for both PDGF and SMCs.

Zero flux conditions are assumed for modLDLs, macrophages and SMCs at the medial boundary ($x = 1$). The model continues the assumption from the submodel in Section 4.1.2 that SMCs enter the intima at a rate σ_s.

The boundary conditions are therefore:

$$\begin{aligned}
&\frac{\partial l}{\partial x} = \frac{-\sigma_l}{D_l} \text{ at } x = 0, && \frac{\partial l}{\partial x} = 0 \text{ at } x = 1,\\
&\frac{\partial m}{\partial x} = -\frac{\sigma_m D_p + \chi_m m \sigma_p}{D_p D_m} \text{ at } x = 0, && \frac{\partial m}{\partial x} = 0 \text{ at } x = 1,\\
&\frac{\partial g}{\partial x} = 0 \text{ at } x = 0, && \frac{\partial g}{\partial x} = 0 \text{ at } x = 1,\\
&\frac{\partial s}{\partial x} = 0 \text{ at } x = 0, && \frac{\partial s}{\partial x} = \frac{\sigma_s}{D_s} \text{ at } x = 1.
\end{aligned} \tag{6.5}$$

6.2 Early stage plaque modelling, modLDLs and macrophages: Chalmers *et al.* (2015)

Like the submodel outlined in the prior section, the model of Chalmers *et al.* (2015) focuses on the initial lesion initiation stage. The domain is also the same as the submodel with a bounded domain Ω representing the region of the intima between the lumen and media. $x \in \Omega$ denotes position within the intima, with the $x = 0$ boundary representing the interface between the lumen and the intima and the $x = 1$ boundary representing the interface between the media and the intima. Time is denoted as t. The model does not however include the later stages of SMC and PDGF growth and influx. To explain the model, we focus on macrophages and modLDLs and disregard the other species. Macrophage density and modLDL concentration is denoted by $m(x,t)$ and $l(x,t)$ respectively.

For modLDL, the assumptions are the same as in Ougrinovskaia (2011). They diffuse, are uptaken by both macrophages and foam cells and undergo linear decay.

Macrophages are also assumed to undergo random motion and chemotaxis. In this model however, macrophages move chemotactically in response to both modLDL and macrophage chemoattractant such as MCP-1. This is simplified as moving chemotactically along the gradient of modLDL. Aside from this difference, macrophages dynamics in the intima are assumed to be the same as in Ougrinovskaia (2011). They uptake modLDLs and undergo apoptosis and necrosis, the two sink terms being expressed consistently with Ougrinovskaia (2011).

The equations are therefore:

$$\frac{\partial l}{\partial t} = D_l \frac{\partial^2 l}{\partial x^2} - \mu_l \frac{ml}{1+l} - d_l l, \tag{6.6}$$

$$\frac{\partial m}{\partial t} = D_m \frac{\partial^2 m}{\partial x^2} - \chi_m \frac{\partial}{\partial x}\Big(m \frac{\partial l}{\partial x}\Big) - \mu_m \frac{ml}{1+l} - d_m m. \tag{6.7}$$

The assumptions for the behaviour of modLDL at the boundaries are the same as (6.5), with an influx of σ_l at $x = 0$. The flux of macrophages at $x = 0$ is however not assumed to be constant as in (6.5). It is instead proportional to the function $\psi(p,q) = (1 + A_0 q)(p - p_0)H(p - p_0)$, where p and q are variables for the concentration of chemoattractants and ES cytokines respectively. The value of this function changes step-wise, with P_0 representing the interstitial concentration of chemoattractant. Increased macrophage chemoattractant and ES cytokine concentration therefore leads to increased macrophage migration into the intima.

Both LDLs and macrophages are assumed to have zero flux at the $x = 1$ boundary.

The boundary conditions become:

$$\begin{aligned} &\frac{\partial l}{\partial x} = -\sigma_l \text{ at } x = 0, && \frac{\partial l}{\partial x} = 0 \text{ at } x = 1, \\ &D_m \frac{\partial m}{\partial x} - \chi_m m \frac{\partial l}{\partial x} = -\sigma_m \psi(p, q) \text{ at } x = 0, && D_m \frac{\partial m}{\partial x} = \chi_m m \frac{\partial l}{\partial x} \text{ at } x = 1. \end{aligned} \tag{6.8}$$

Both models share a number of assumptions. The assumptions towards modLDL dynamics are the same: that modLDLs diffuse, are uptaken by macrophages and undergo linear decay. There is a constant influx of modLDLs (denoted in both models at rate σ_l) at the $x = 0$ boundary and zero flux conditions at the $x = 1$ boundary. Macrophages are also assumed to undergo random motion and chemotaxis, though the chemotactic concentration gradient differs between the models with Chalmers *et al.* (2015) using the gradient of modLDL. Both models assume macrophages uptake modLDLs and undergo apoptosis and necrosis. We note however that this macrophage uptake is due to its conversion to foam cells and that foam cells are disregarded in our current model.

The similarities between both models provide a foundation of agreed assumptions. These shared assumptions are used as a useful reference for the formulation of our reaction-diffusion model in the next section. The scope of this section's model however is limited to four key species: modLDLs, macrophages, SMCs and PDGF.

6.3 Model formulation and development

We model both the initial lesion initiation stage and the prior stage of SMC migration from the first reaction-diffusion submodel (Section 4.2). This is therefore an extension of the first model of Chapter 4. It maintains the spatial assumptions in Section 4.2 regarding the domain. We note that the model does not address ECM and is limited to the following key variables as a function of distance x and time t:

$$\begin{aligned} g(x,t) &= \text{concentration of SMC chemoattractant, such as PDGF,} \\ s(x,t) &= \text{density of matrix-synthesising smooth muscle cells,} \\ l(x) &= \text{concentration of modLDL,} \\ m(x,t) &= \text{density of macrophages.} \end{aligned}$$

6.3.1 Model equations

6.3.1.1 PDGF ($g(x,t)$)

The assumptions held in equation (4.17) are continued in this system: that PDGF diffuses through the media and decays, and that its timescale (a month) is significantly shorter than that of SMC production. We however introduce a source term with macrophage dependence. In the Ougrinovskaia (2011) submodel outlined in

Section 6.1, this source term was due to PDGF-B (a variant of PDGF). PDGF-B is a chemoattractant and mitogen for SMCs that is elaborated by macrophages [28,46]. The source term is therefore proportional to the local macrophage density and the rate of production of PDGF by macrophages μ_g. The model equation is:

$$0 = D_g \frac{d^2 g}{dx^2} - d_g g + \mu_g m. \tag{6.9}$$

6.3.1.2 SMC ($s(x,t)$)

The density of smooth muscle cells within the intima is modelled by:

$$\frac{\partial s}{\partial \tau} = D_s \frac{\partial^2 s}{\partial x^2} - \frac{\partial}{\partial x}\Big(\chi_s s \frac{\partial g}{\partial x}\Big) + r_g\Big(1 + \frac{Ag}{G_s + g}\Big)s(1 - \frac{s}{k}) - d_s s - d_{sm} s m. \tag{6.10}$$

We maintain the assumptions held in equation (4.18) around random motility, chemotaxis, and the source and sink terms. We additionally assume that SMCs undergo apoptosis (cell death) in response to increased cytokines [36]. While cytokines are disregarded in our model, ES cytokines such as IFN-γ are produced by macrophages consuming modLDL [36]. We therefore assume that IFN-γ presence is proportional to macrophage density, meaning that the apoptosis term is proportional to the local macrophage density and the death term d_{sm}.

6.3.1.3 ModLDL ($l(x,t)$)

We assume that modLDLs diffuse through the intima with diffusion coefficient D_l. They are uptaken by macrophages, the rate of this uptake having an upper limit. We model this by a saturating function with respect to modLDL concentration. In our equation, this is represented by a Michaelis–Menten-type function. We also assume that modLDLs experience loss generally, which is represented by a linear decay term d_l. The model equation is:

$$\frac{\partial l}{\partial \tau} = D_l \frac{\partial^2 l}{\partial x^2} - \frac{\mu_l l m}{\gamma_l + l} - d_l l. \tag{6.11}$$

6.3.1.4 Macrophages ($m(x,t)$)

Within the intima, macrophages randomly move with the random movement coefficient D_m. We assume they move chemotactically along the gradient of modLDLs with chemotactic coefficient χ_m. We note that the same assumptions of macrophage flux within the intima as Chalmers *et al.* (2015) are used in this equation. However, both Ougrinovskaia (2011) and Chalmers *et al.* (2015) assumed macrophage uptake due to conversion to foam cells. We do not include this macrophage conversion term as foam cells are not in the scope of this model. Finally, we assume general loss and cell death of macrophages which is modelled by a death term with rate d_m. We

model the density of macrophages within the intima by:

$$\frac{\partial m}{\partial \tau} = D_m \frac{\partial^2 m}{\partial x^2} - \frac{\partial}{\partial x}\Big(\chi_m m \frac{\partial l}{\partial x}\Big) - d_m m. \tag{6.12}$$

6.3.2 Boundary and initial conditions

6.3.2.1 ModLDL ($l(x,t)$)

We first note that in our model, we do not differentiate between LDL and modLDL. This is because LDLs become modified by oxidants to form modLDLs after entering the intima, which we assume to occur extremely quickly. Therefore the influx of non-modLDLs is modelled as an influx of modLDLs. This influx at the $x = 0$ boundary is constant at rate α_l. This is represented as $J_l|_{x=0} = \alpha_l$ where $J_l = -D_l \frac{\partial l}{\partial x}$ is the modLDL flux.

At $x = 1$ we assume zero flux conditions. This is represented as $J_l|_{x=1} = 0$. Therefore the boundary conditions are:

$$\frac{\partial l}{\partial x}\Big|_{x=0} = \frac{-\alpha_l}{D_l}, \qquad \frac{\partial l}{\partial x}\Big|_{x=1} = 0. \tag{6.13}$$

We assume that initially, modLDLs exist at steady state in the intima and that this steady state has been reached with very low macrophage presence. This is to simulate the very early stages of lesion initiation, when significant monocyte recruitment has not occurred and modLDL exists *in vivo* [15, 41]. We therefore describe $l(0,t)$ as the steady state solution of $l(x,t)$ (6.11) when $m(x,0) = 0$. The steady state equation for $l(x,0)$ simplifies to:

$$D_l \frac{\partial^2 l}{\partial x^2} - d_l l = 0,$$

which is solved with the boundary conditions (6.13) to give the steady state solution:

$$l(x,0) = \Big(\frac{-\alpha_l}{D_l \gamma} + \frac{\frac{\alpha_l}{D_l \gamma}}{1 - \frac{\exp(-\gamma)}{\exp(\gamma)}}\Big)\exp(\gamma x) + \Big(\frac{\frac{\alpha_l}{D_l \gamma}}{1 - \frac{\exp(-\gamma)}{\exp(\gamma)}}\Big)\exp(-\gamma x), \tag{6.14}$$

with $\gamma = \sqrt{\frac{d_l}{D_l}}$. The profile of equation (6.14) is Figure 6.1. We note that this profile appears to be approximately constant: later results show that the solution profile of l is flat.

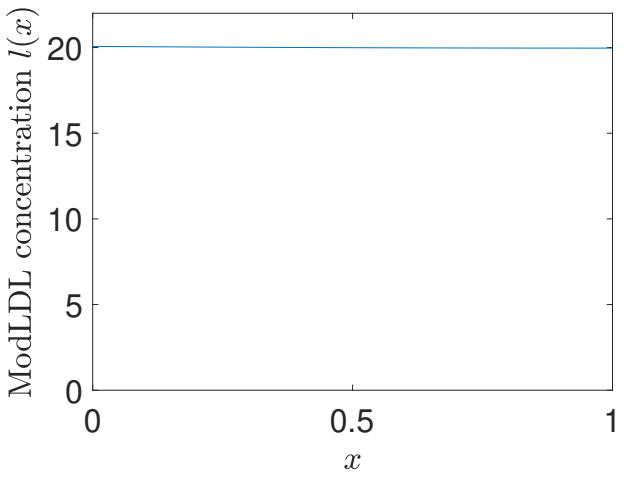

Figure 6.1: The initial condition solution of $l(x, 0)$ which is the steady state solution of $l(x, t)$ when $m(x, t) = 0$.

6.3.2.2 Macrophages ($m(x, t)$)

We first note that in our model, we do not differentiate between monocytes and macrophages. Monocytes rapidly differentiate into macrophages when they leave the bloodstream and enter the intima [4]. As a result we represent the influx of monocytes into the intima as an influx of macrophages. We first assume this is proportional to a rate α_m and m. We however introduce the assumption that this influx is saturated at high concentrations of modLDL. This is to simulate the saturation of the production of monocyte chemoattractants such as MCP-1. These chemoattractants are triggered at the endothelium by modLDL presence, resulting in monocytes entering the intima [16, 31, 36]. They are not however in the scope of this model. We therefore simulate this by assuming the influx to be saturated at high concentrations of l which is represented by a Michaelis–Menten-type function $\frac{l}{\gamma+l}$. At $x = 0$, this is represented as $J_m|_{x=0} = \frac{\alpha_m l m}{\gamma+l}$ where $J_m = -D_m \frac{\partial m}{\partial x} + \chi_m m \frac{\partial l}{\partial x}$ is the macrophage flux into the intima.

At $x = 1$ we assume zero flux conditions. This is represented as $J_m|_{x=1} = 0$. Using the boundary conditions of l (6.13) to substitute the value of $\frac{\partial l}{\partial x}$ at both boundaries, the boundary conditions of m are:

$$\left.\frac{\partial m}{\partial x}\right|_{x=0} = \frac{-\frac{\alpha_m l m}{\gamma+l} D_l - \chi_m m \alpha_l}{D_m D_l}, \qquad \left.\frac{\partial m}{\partial x}\right|_{x=1} = 0. \tag{6.15}$$

We assume there is an initial distribution of macrophages in the intima, with the majority accumulated at the endothelial boundary. This distribution simulates the early stage of monocyte recruitment by describing a small initial influx of macrophages from the lumen at the endothelial layer. We model this with a half-Gaussian function:

$$m(x, 0) = \frac{m_0 \sqrt{2}}{\sigma \pi} \exp\Big(- \frac{x^2}{2\sigma^2} \Big), \tag{6.16}$$

with $m_0 = 1.0 \times 10^{-4}$ and $\sigma = 0.05$. The profile of this initial condition $m(x, 0)$ is shown in Figure 6.2.

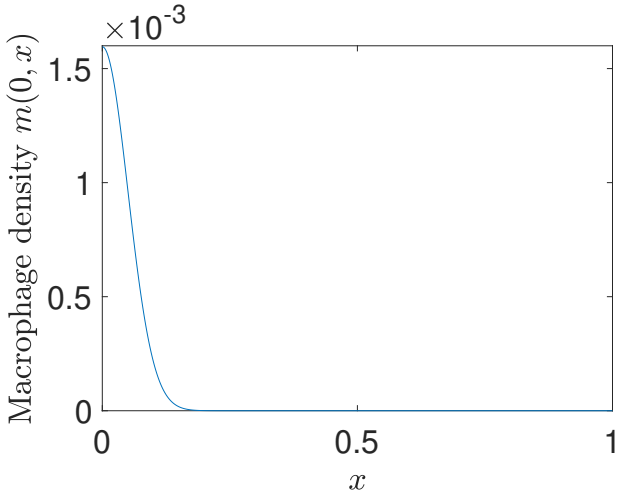

Figure 6.2: The initial condition of $m(x, 0)$ where $m(x, 0)$ is the half-Gaussian function given in (6.16) with $m_0 = 1.0 \times 10^{-4}$ and $\sigma = 0.05$.

The boundary conditions for PDGF and SMCs at $x = 0$ and $x = 1$ remain unchanged from (4.19) and (5.11). We continue to assume a small initial intimal SMC density, represented by the initial condition $s(x, 0) = s_0$ where $0 < s_0 \ll 1$.

6.3.3 Non-dimensionalisation

We non-dimensionalise our model, using tildes (except for t) to denote non-dimensionalised quantities. Setting $s = k\widetilde{s}$, $g = g_0\widetilde{g}$, $l = \gamma_l\widetilde{l}$, $t = t_0\tau$ and $x = L\widetilde{x}$, we non-

dimensionalise the remaining variables as:

$$
\begin{aligned}
&d_g = \frac{\widetilde{d_g} D_g}{L^2} \ , \qquad \mu_g = \frac{\widetilde{\mu_g} D_g}{L^2} \ , \qquad \alpha_g = \frac{\widetilde{\alpha} D_g g_0}{L} \ , \\
&\sigma_g = \frac{\widetilde{\sigma} D_g}{L} \ , \\
&D_s = \frac{L^2 \widetilde{D_s}}{t_0} \ , \qquad d_s = \frac{\widetilde{d_s}}{t_0} \ , \qquad G_s = \widetilde{G_s} g_0 \ , \\
&\chi_s = \frac{\widetilde{\chi_s} L^2}{t_0 g_0} \ , \qquad r_{s0} = \frac{\widetilde{r_{s0}}}{t_0} \ , \qquad \widetilde{A} = \frac{r_s}{r_{s0}} \ , \\
&d_{sm} = \frac{\widetilde{d_{sm}}}{t_0} \ , \\
&D_m = \frac{L^2 \widetilde{D_m}}{t_0} \ , \quad \chi_m = \frac{L^2 \widetilde{\chi_m}}{t_0 \gamma_l} \ , \quad d_m = \frac{\widetilde{d_m}}{t_0} \ , \\
&\mu_l = \frac{\gamma_l \widetilde{\mu_l}}{t_0} \ , \qquad \mu_m = \frac{\widetilde{\mu_m}}{t_0} \ , \\
&D_l = \frac{L^2 \widetilde{D_l}}{t_0} \ , \qquad d_l = \frac{\widetilde{d_l}}{t_0} \ , \qquad \alpha_m = \frac{\widetilde{\alpha_m} L}{t_0} \ , \\
&\alpha_l = \frac{\widetilde{\alpha_l} L \gamma_l}{t_0} \ .
\end{aligned}
\tag{6.17}
$$

Dropping the tildes for clarity, the model equations (6.9), (6.10), (6.11), (6.12), and boundary conditions (4.19), (5.11), (6.13) and (6.15) become:

$$
0 = \frac{d^2 g}{dx^2} - d_g g + \mu_g m, \tag{6.18}
$$

$$
\frac{\partial s}{\partial \tau} = D_s \frac{\partial^2 s}{\partial x^2} - \frac{\partial}{\partial x}\Big(\chi_s s \frac{\partial g}{\partial x}\Big) + r_g (1 + \frac{Ag}{G_s + g}\Big) s(1 - \frac{s}{k}) - d_s s - d_{sm} s m, \tag{6.19}
$$

$$
\frac{\partial m}{\partial \tau} = D_m \frac{\partial^2 m}{\partial x^2} - \frac{\partial}{\partial x}\Big(\chi_m m \frac{\partial l}{\partial x}\Big) - d_m m, \tag{6.20}
$$

$$
\frac{\partial l}{\partial \tau} = D_l \frac{\partial^2 l}{\partial x^2} - \frac{\mu_l l m}{\gamma_l + l} - d_l l, \tag{6.21}
$$

with boundary conditions

$$\begin{aligned}
&\frac{\partial m}{\partial x}\Big|_{x=0} = \frac{\frac{-\alpha_m D_l l m}{\gamma + l} - \chi_m m \alpha_l}{D_m D_l}, && \frac{\partial m}{\partial x}\Big|_{x=1} = 0, \\
&\frac{\partial l}{\partial x}\Big|_{x=0} = \frac{-\alpha_l}{D_l} && \frac{\partial l}{\partial x}\Big|_{x=1} = 0 \\
&\frac{dg}{dx}\Big|_{x=0} = \frac{-\alpha_g}{D_g}, && \frac{dg}{dx}\Big|_{x=1} = \frac{-\sigma_g g}{D_g}, \\
&\frac{\partial s}{\partial x}\Big|_{x=0} = \frac{-\alpha_g \chi_s s}{D_g D_s} && \frac{\partial s}{\partial x}\Big|_{x=1} = \frac{\chi_s \sigma_g g(s^* - s)}{D_g D_s}.
\end{aligned} \tag{6.22}$$

and initial conditions

$$s(x,0) = s_0, \tag{6.23}$$

$$l(x,0) = \Big(\frac{-\alpha_l}{D_l \gamma} + \frac{\frac{\alpha_l}{D_l \gamma}}{1 - \frac{\exp(-\gamma)}{\exp(\gamma)}}\Big)\exp(\gamma x) + \Big(\frac{\frac{\alpha_l}{D_l \gamma}}{1 - \frac{\exp(-\gamma)}{\exp(\gamma)}}\Big)\exp(-\gamma x), \tag{6.24}$$

$$m(x,0) = \frac{m_0\sqrt{2}}{\sigma\pi}\exp\Big(-\frac{x^2}{2\sigma^2}\Big), \tag{6.25}$$

where s_0 is non-dimensional, $m_0 = 1.0 \times 10^{-4}$, $\sigma = 0.05$ and $\gamma = \sqrt{\frac{d_l}{D_l}}$.

6.3.4 Parameter values

Table 6.1: Base non-dimensionalised parameter values

Symbol	Definition	Value	Reference
d_g	Rate of PDGF decay	0.075	[44]
μ_g	Rate of production of PDGF by macrophages	10^1	6.3.4.1
D_s	Diffusion coefficient of SMC	1.0979	4.2.4.1
χ_s	SMC motility coefficient	4.5952	4.2.4.1
r_g	Baseline rate of SMC proliferation	0.02	[44]
d_s	Rate of SMC decay	0.4	[44]
d_{sm}	Rate of SMC apoptosis	0.2	6.3.4.1
G_s	Michaelis-Menten kinetic constant	1.4	[44]
A	Maximal factor of PDGF-stimulated increase in rate of SMC proliferation	19	[44]
α_g	Rate of PDGF influx from endothelium	0.55	[44]
σ_g	Permeability of IEL to PDGF	2	[44]
s_0	Initial SMC concentration	1×10^{-4}	[44]
s^*	Concentration of synthetic SMC in media	0.01	[44]
D_m	Diffusion coefficient of macrophages	10^{-1}	[11]
χ_m	Macrophage motility coefficient	10^{-1}	[11]
μ_m	Rate of macrophage conversion	10^2	[11]
d_m	Rate of macrophage decay	10^{-1}	[11]
D_l	Diffusion coefficient of LDLs	10^3	[11]
μ_l	Rate of LDL uptake by macrophages	10^5	[11]
d_l	Rate of LDL decay	10^1	[11]
α_l	Rate of LDL influx from endothelium	2×10^2	6.3.4.1
α_m	Rate of macrophage influx from endothelium	6×10^{-1}	6.3.4.1

6.3.4.1 Parameter value justification

The non-dimensionalisation of the model parameters in Section 6.3.3 is the same as Chalmers *et al.* (2015) for the parameters: μ_l, D_m, d_m, χ_m, d_l, α_l and α_m. We note however that the characteristic timescale t_0 from Chalmers *et al.* (2015) is 19 days, which is approximately half of the characteristic timescale of our system (approximately $t_0 = 1$ month). The parameter values of Chalmers *et al.* (2015) are however approximate and are estimated using order of magnitude assumptions. We therefore rescale the base parameter values from Chalmers *et al.* (2015): the difference between the timescales (and therefore non-dimensionalised values) is the order of approximately two.

The model in Chalmers *et al.* (2015) however has no base values of α_l and α_m and instead takes different values of the two parameters. Values of α_l are taken between 1.0×10^2 and 7.0×10^2 while values of α_m are taken between 5.0×10^{-1} and 8.0×10^{-1}. We therefore choose appropriate intermediate values: we set $\alpha_l = 2 \times 10^2$ and $\alpha_m = 6 \times 10^{-1}$

The model equations for g and s also introduce the parameters μ_g and d_{sm}. We note that the analogous term for μ_g in Ougrinovskaia (2011) is σ_g, which is rescaled rather than non-dimensionalised and its value is estimated based on reasonable results and model sensitivity. We apply the same approach and set $\mu_g = 10^1$ due to the scale of m. The parameter d_{sm} also has an analogous term in Ougrinovskaia (2011). Based on the rescaling used in Ougrinovskaia (2011), we can estimate the value of d_{sm}. We therefore set $d_{sm} = 0.2$.

6.4 Results

We recall that that the timescales of m and l, taken from Chalmers *et al.* (2015), are shorter than s. The results from Chalmers *et al.* (2015) show that m and l approach steady state before $t = 4$, as opposed to approximately $t = 22$. We therefore expect m and l to reach steady state quicker than g and s in our model. This is expected because the stages of lesion initiation and SMC migration are different, with the latter being a later, intermediate stage of plaque formation.

We contrast this to the reaction-diffusion model of the previous chapter 5, where the model equations for s and ρ were determined in Section 5.4.1 to have the same timescales. We recall that the reference models of Watson *et al.* (2018, 2020) and Chalmers *et al.* (2015) only consider distinct phases with different timescales: for example, Watson *et al.* (2018, 2020) does not model lipids with SMCs. This integration of phases with different timescales therefore departs from the approach taken in our reference models. The effect of this difference on the results of the model is therefore worth investigating. We aim to understand if there is a significant difference in results between separating the phases with different timescales, and integrating them.

To query the effect of this difference in timescales, we begin by solving the model equations simultaneously with values from Table 5.1. We observe any differences in dynamics by solving the equations for the SMC migration stage (equations for g and s) after the equations for the lesion initiation stage (equations for m and l) have reached steady state, and compare the results between the two types of solutions.

6.4.0.1 Base case simulation

We choose our base case parameter values from Table 6.1. We begin with the time evolutions of the solutions of l and m in Figures 6.4a and 6.4b respectively.

Figure 6.3b shows that the solution profile of m is not linear, with the greatest macrophage density being near the endothelial boundary as macrophages randomly move through the intima. Over time the value of m near $x = 0$ decreases while the distribution of m across the domain increases. We recall that there is an influx of macrophages into the intima at $x = 0$ and that macrophages move chemotactically along the gradient of l. Figure 6.4b shows that the intimal macrophage density increases rapidly over approximately half a month and decreases to reach steady state at approximately $t = 2.1$. This is similar to the results from Chalmers *et al.* (2015) which show m and l approaching steady state before $t = 4$.

We observe in Figure 6.3a that the solution profile of l decreases from the initial condition steady state solution ((6.14) shown in Figure 6.1) over time. The solution profiles of l are almost constant at each time. The total amount of intimal modLDL as a function of time in Figure 6.4a shows that l decreases rapidly over about half a month, and then increases to reach steady state at a slower rate. We recall that the initial condition for l (6.14) is the steady state solution of (6.21) with zero m. We therefore expect the rapid decrease in l as there is an initial non-zero macrophage density (6.16) which m increases from. We also expect the time taken to reach steady state to be the same for m and l due to the dependence of (6.21) on m. The time to reach steady state is approximately 2.1 months for both l and m.

The equation for g in (6.18) introduces a source term which is proportional to rate μ_g and dependent on m. Figure 6.3c shows that the effect of this term is small: there is a small difference between the solutions of g at $t = 0.04$ and at steady state $t = 25.0$. As m remains positive over time, g increases over time. Due to the dependence on m, this change occurs on the same timescale as m and l. We choose this base value of μ_g ($\mu_g = 10.0$) due to our observations in Section 6.4.1.2 that show that the dynamics of g are sensitive to changes in μ_g above the base value of $\mu_g = 10.0$.

The equation for s in (6.19) describes the effect of PDGF on the dynamics of s through chemotaxis and SMC proliferation. We recall that the results from Section 4.4.3 showed that SMC proliferation has a weak effect on SMC dynamics, and that the dynamics of s are more sensitive to changes in the chemotaxis term as observed in Section 5.4.2.3. The results in Figure 6.3c however show minor changes in g and $\frac{dg}{dx}$ over time. Because the changes to g and $\frac{dg}{dx}$ are small, we expect the effect of μ_g and the introduction of m dependence on g to have a small effect on the dynamics of s. We therefore compare these solutions with the solutions of s from the reaction-diffusion model without m in Figures 4.4b and 4.4c. Comparing Figures 6.3d and 4.4b shows that the maximum value of s at $x = 0$ increases by a small amount when m is introduced to the system. The difference in steady state time is also minor, with the time to reach steady state in Figure 6.4c being about $t = 24$ compared to the time to reach steady state of about $t = 22$ in Figure 4.4c.

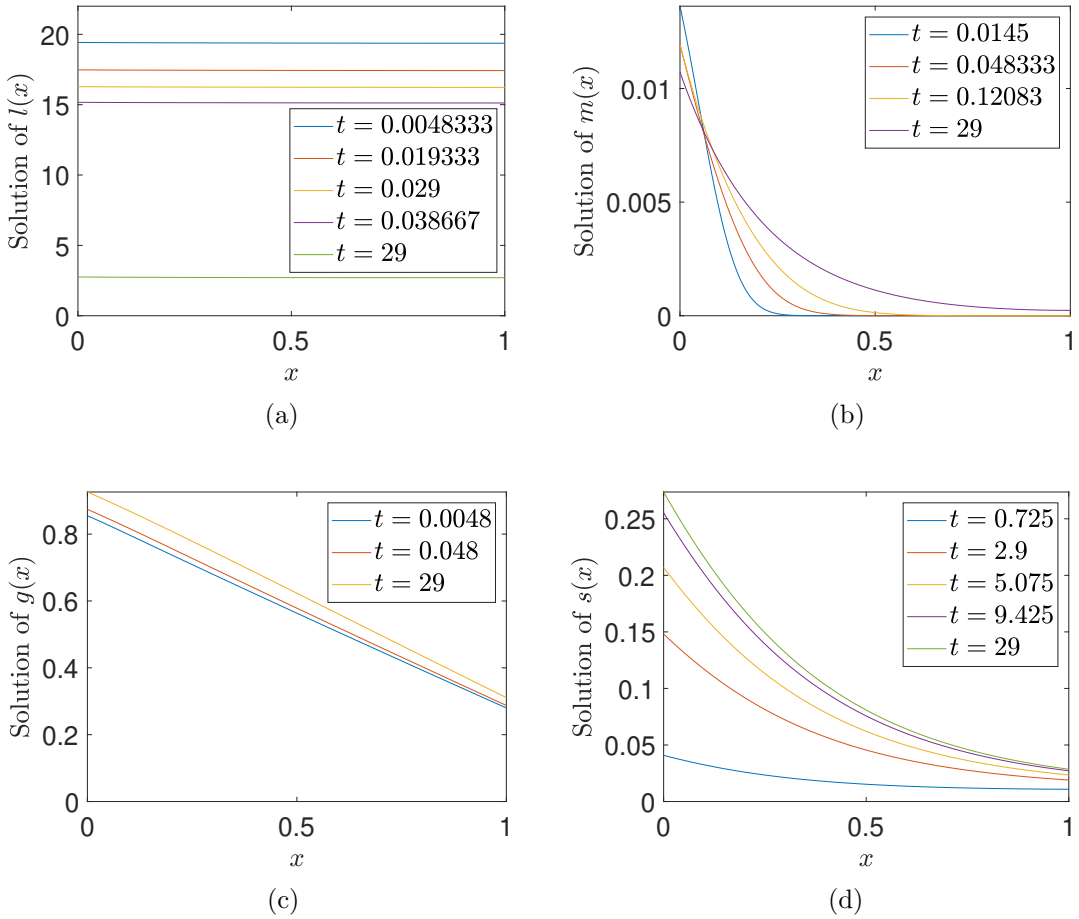

Figure 6.3: Solutions of (a) l, (b) m, (c) g and (d) s as functions of x with parameter values from Table 6.1 at times t from $t = 0.0$ to 29.0.

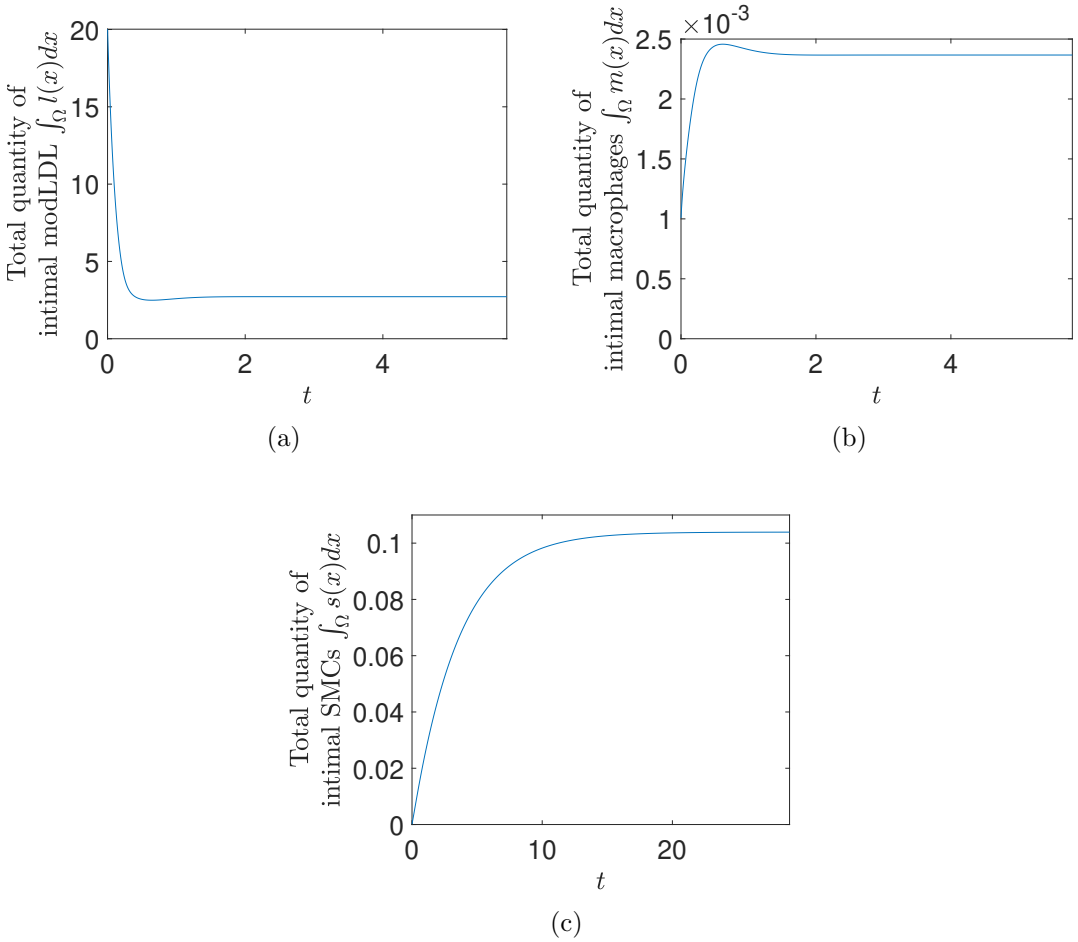

Figure 6.4: Time evolutions of the total quantity of (a) intimal modLDL $\int_\Omega l(x)dx$, (b) intimal macrophages $\int_\Omega m(x)dx$, and (c) intimal SMCs $\int_\Omega s(x)dx$ with parameter values from Table 6.1 from $t = 0.0$ to 29.0

6.4.0.2 Staggered solutions

We recall that the timescales of m and l are shorter than the timescale of the evolution of s. As observed in Figures 6.4a and 6.4b, m and l approach steady state at approximately $t = 2.1$ which is shorter than the observed time taken for s to reach steady state in Figure 6.4c (approximately $t = 22$). This is because the stage of lesion initiation is the initial stage where LDL begins to enter the intima. SMC migration is a later, intermediate stage of plaque formation.

We query if our reaction-diffusion model can accommodate coupled equations with significantly different timescales. In the previous section 6.4.0.1 we solved all equations simultaneously, which we refer to as "simultaneous solutions". In this section we solve the equations for the SMC migration stage (equations for g and s) after the equations for the lesion initiation stage (equations for m and l) have reached steady state, and compare the results between the two sections to observe any changes in dynamics. We refer to solutions of g and s obtained after shorter timescale equations have reached steady state as "staggered solutions".

We compare both simultaneous and staggered solutions solved with values from Table 5.1 with a view to analyse at three main times: the time taken for the whole system to reach steady state, the time taken to reach steady state for equations m and l, and the time taken to reach steady state for equations g and s. We recall that for staggered solutions, the equations for m and l are solved to steady state first, after which the equations for g and s are solved. Because m and l have no dependence on g or s, there is no difference in their solutions whether they are solved simultaneously or otherwise. Therefore for staggered solutions, the time taken for s to reach steady state is the difference between the time taken for the whole system to reach steady state and the time taken to reach steady state for equations m and l. We note that for simultaneous solutions, the time taken for the whole system to reach steady state is equivalent to the time taken for s to reach steady state. We can therefore compare the times taken for s to reach steady state: if the times are similar, then this suggests that the equations for s approach steady state at approximately the same time for both simultaneous and staggered solutions. We also compare the total quantity of intimal SMCs in both solutions to analyse any differences in dynamics: if the two are similar, then we will be able to conclude that there is negligible difference in time taken to reach steady state and dynamics between the simultaneous and staggered solutions.

Figures 6.5a, 6.5b and 6.5c compare simultaneous and staggered solutions with different values of α_m. For the staggered solution, the equations for g and s are solved starting from the times when the equations for m and l reach steady state as observed in Section 6.4.1.1. Due to the dependence of g on m, we expect g to either operate in the same timescale of m (when solved simultaneously) or to not change over time (when solved after m has reached steady state). We observe that in all three figures, the maximum values of the the total quantity of intimal SMCs for both simultaneous and staggered solutions are equal.

We also compare the times taken for the whole system to reach steady state between the simultaneous and staggered solutions. For the base value of α_m ($\alpha_m = 6.0 \times 10^{-1}$), we recall that the time to reach steady state of s for the simultaneous solutions is approximately $t = 24$ in Figure 6.4c. The steady state time for the staggered solutions with the same parameter values is approximately $t = 26$ in Figure 6.5a, and the time to reach steady state of equations m and l is approximately $t = 2.1$ in Figure 6.5a. Given that the equation for s is solved for the staggered system starting at $t = 2.1$, the time to reach steady state of the equation of s for the staggered solution is therefore the difference between the time taken for the whole system to reach steady state and the time to reach steady state for equations m and l. We observe that this time is approximately $t = 26 - 2.1 = 23.9$, which is very similar to the time to reach steady state of s for the simultaneous solutions ($t = 24$). This result suggests that there is no difference in the dynamics of s between the staggered and simultaneous solutions when solved with the base parameter values.

This analyses is continued for the solutions for $\alpha_m = 2.0$ and 8.0×10^{-1}. In Figure 6.5b for $\alpha_m = 2.0$, the steady state time of the staggered solutions is approximately $t = 26$. The time to reach steady state for the simultaneous equations with the same parameter values is approximately $t = 24$ and the time to reach steady state of equations m and l is approximately $t = 1.5$. The time to reach steady state of the

equation of s for the staggered solution is therefore approximately $t = 26 - 1.5 = 24.5$, which is very similar to the time to reach steady state of s for the simultaneous solutions ($t = 24$). Similarly in Figure 6.5b for $\alpha_m = 8.0 \times 10^{-2}$, the steady state time of the staggered solution is approximately $t = 26$. The time to reach steady state for the simultaneous equations with the same parameter values is approximately $t = 24$ and the time to reach steady state of equations m and l is approximately $t = 2.5$. The time to reach steady state of the equation for s for the staggered solution ($t = 26 - 2.5 = 23.5$) is therefore very similar to the time taken for the whole system to reach steady state of the simultaneous equations ($t = 24$).

The results show that across the three values of α_m, the time to reach steady state of the equation for s for the staggered solution is very similar to the time to reach steady state of the simultaneous equations. We also observe that in all three figures, the maximum values of the the total quantity of intimal SMCs for both simultaneous and staggered solutions are equal. This suggests that there is little difference in dynamics whether equations are solved simultaneously or staggered. We therefore solve the equations simultaneously for the remainder of the model analyses.

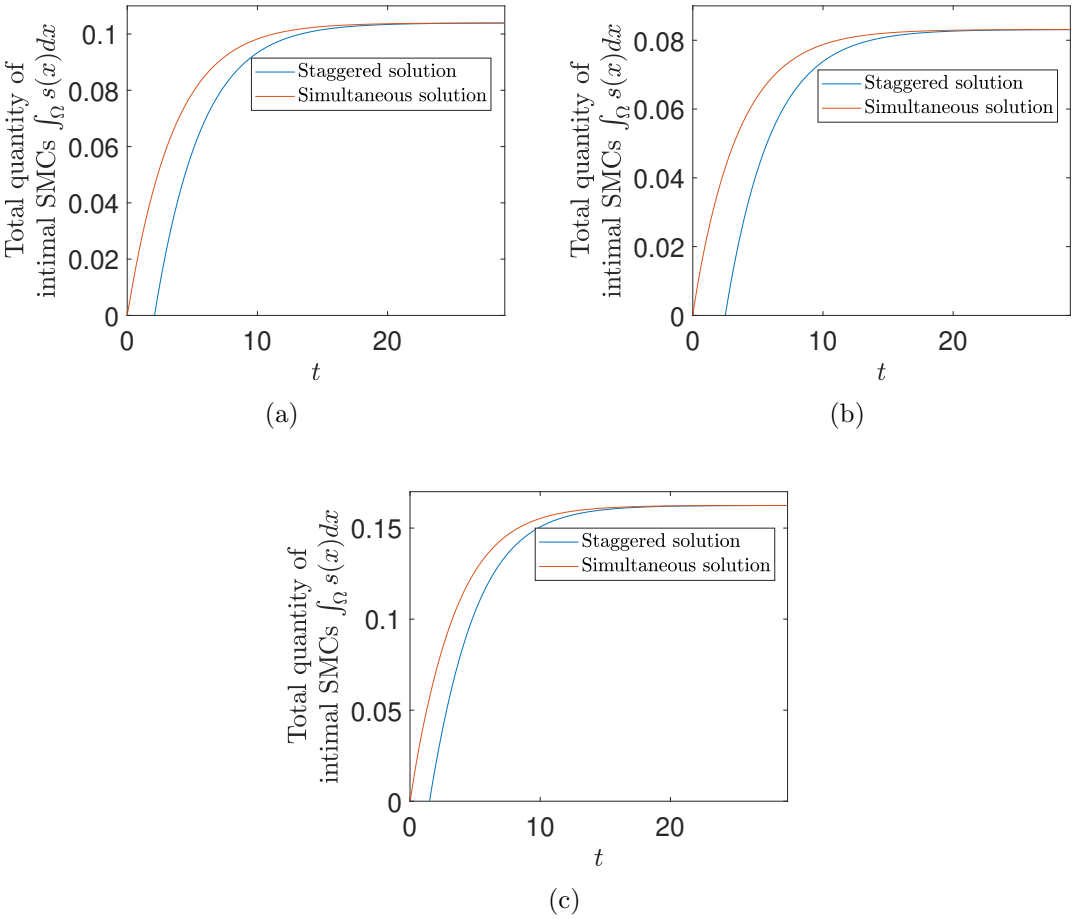

Figure 6.5: Comparisons of time evolutions of the total quantity of intimal SMCs $\int_\Omega s(x)dx$ between simultaneous and staggered solutions for three values of α_m : (a) $\alpha_m = 6.0 \times 10^{-1}$, (b) $\alpha_m = 8.0 \times 10^{-2}$, and (c) $\alpha_m = 2.0$ from $t = 0.0$ to 29.0. Staggered equations are solved starting from the steady state times of m and l, which is (a) $t = 2.1$, (b) $t = 2.5$, and (c) $t = 1.5$.

6.4.1 Parameter sensitivity

The model equations in Section 6.3.3 introduce equations for m (6.20) and l (6.21), which include new dependencies in the equations for g (6.18) and s (6.19). We therefore perform parameter sensitivity analysis on four key parameters: α_m, μ_g, d_{sm} and χ_m.

We recall that α_m is the rate of macrophage influx into the intima: we therefore expect changing α_m to affect the dynamics of m. Both g and s are affected by m due to two parameters: μ_g and d_{sm}. For g, PDGF is produced by macrophages proportional to rate μ_g and m, while for s we assume that SMC undergoes apoptosis proportionally to the rate d_{sm} and m.

The parameter μ_g is based on the introduced assumption that PDGF is elaborated by macrophages. We therefore analyse the effects of varying μ_g. In Section 6.4.0.1 we observed that the base value of μ_g resulted in a small change in g. This suggests that our equations are not highly sensitive to changes in μ_g.

The equation for s (6.19) has dependencies on m due to SMC apoptosis. We assume SMC apoptosis is proportional to m and the rate of SMC apoptosis d_{sm}. We therefore analyse the direct effects of m on the dynamics of s by changing d_{sm}. We recall that changes in g affect the dynamics of s due to the dependence on g and $\frac{\partial g}{\partial x}$ by the chemotaxis and proliferation terms in (6.19) and the boundary conditions (6.22). This means that the dynamics of m have an effect on s directly due to the SMC apoptosis term, and indirectly due to its effect on g and the chemotaxis and proliferation terms of s. To understand the relative scale and effect of the parameters μ_g and d_{sm} on the dynamics of s, we compare the effects of the parameters.

The parameter sensitivity analysis of χ_s in the first reaction-diffusion model (Section 4.4.3) showed the significant effect of the chemotaxis parameter of the dynamics of s. In equation (6.20) we assume that macrophages migrate chemotactically in response to the gradient of l at a rate proportional to the chemotaxis parameter χ_m. We therefore analyse the sensitivity of the dynamics of m and the rest of the equations to changes in χ_m.

6.4.1.1 α_m

Figure 6.6b compares the steady state solutions of m by using three values of α_m: $\alpha_m = 8.0 \times 10^{-2}$, 6.0×10^{-1} and 2.0. We note that $\alpha_m = 6.0 \times 10^{-1}$ is the base value in Table 6.1. The other values of α_m are chosen due to their difference in scale by approximately 10^1 from the base value.

We observe in Figure 6.6b that the value of α_m affects the magnitude and spatial distribution of the steady state solution of m. For the base value of $\alpha_m = 6.0 \times 10^{-1}$, the steady state solution is non-zero and m is greatest near the $x = 0$ boundary. When α_m is low ($\alpha_m = 8.0 \times 10^{-2}$), m decreases rapidly from the initial condition value to near zero m. The time evolution of $\int_\Omega m(x)dx$ in Figure 6.7a shows this

change over time. These results show that for low values of α_m, there is insufficient macrophage influx to overcome the loss of macrophages due to death. These dynamics change when α_m is greater than the base value ($\alpha_m = 2.0$). Figure 6.6b shows that m at steady state for this value of α_m is greater than for the base steady state solution ($\alpha_m = 6.0 \times 10^{-1}$). This is expected due to the increase in the influx of macrophages and therefore total macrophages in the intima.

We recall in (6.21) that macrophages uptake modLDL at rate μ_l with dependence on m and l: changes to m affect the dynamics of l through this uptake term. When α_m is low ($\alpha_m = 8.0 \times 10^{-2}$), m decreases to near zero. The absence of m therefore removes the effect of this uptake term from the dynamics of l, meaning that there is no modLDL loss. As observed in Figures 6.6c and 6.7b, this corresponds to more modLDL in the intima. When α_m is greater than the base value ($\alpha_m = 2.0$), we observed greater m due to the higher rate of macrophage influx. The effect of the macrophage uptake of modLDL is therefore greater and we therefore expect less magnitude and spatial distribution of l: Figure 6.6c shows that the magnitude and spatial distribution of the steady state solution of l is indeed lower than observed for the base value steady state solution (when $\alpha_m = 6.0 \times 10^{-1}$). Figure 6.7b demonstrates the effect of the increased rate of modLDL uptake by macrophages on modLDL, as the total quantity of intimal modLDL $\int_\Omega l(x)dx$ decreases at a greater rate than for the base value of α_m.

Changes in m affect the dynamics of g in (6.18) due to the rate of production of PDGF by macrophages, which is proportional to rate μ_g and m. We therefore expect greater m to increase this production term, leading to greater g. Figure 6.6a confirms this, with greater values of α_m leading to a larger steady state solution of g and the opposite for lower values of α_m. The results also show a larger gradient of g near the $x = 0$ boundary.

We recall that g affects the dynamics of s in (6.19) due to dependence on PDGF for proliferation and chemotaxis, which are dependent on g and $\frac{\partial g}{\partial x}$ respectively. As observed in Section 5.4.2.3, more PDGF in the intima corresponds to more SMCs. We note that the dynamics of s in (6.19) include a term for SMC death due to apoptosis, proportional to apoptosis rate d_{sm} and m. There are therefore two ways by which macrophages affect the dynamics of s: SMC migration and proliferation, which we expect to increase when α_m is increased due to greater values of g and $\frac{\partial g}{\partial x}$; and SMC death, which we also expect to increase when α_m is increased. The effect of increasing values of α_m on the dynamics of s is shown in Figures 6.6c and 6.7c, as we observe that the magnitude and spatial distribution of the steady state solutions of s increase with greater values of α_m. This suggests that the effect of the apoptosis term is low, and that the effects of chemotaxis and proliferation dominate.

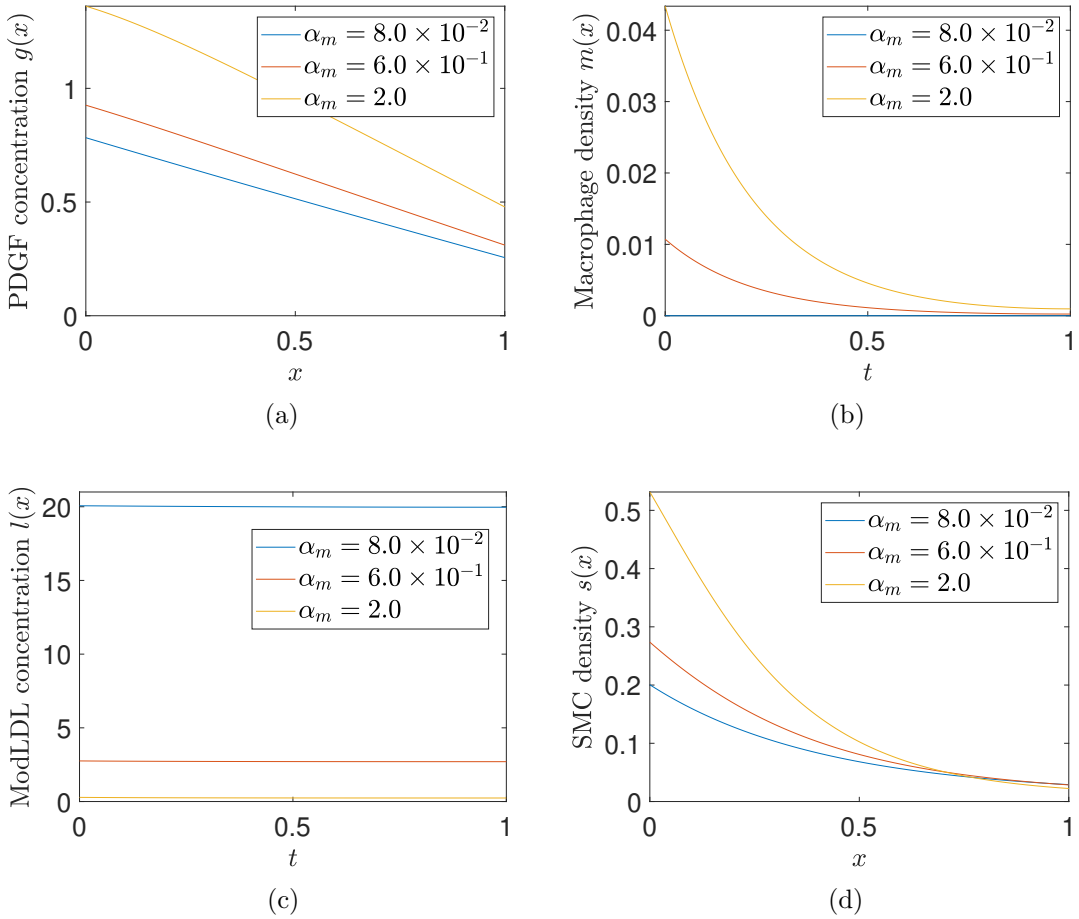

Figure 6.6: Comparisons of steady state solutions of (a) g, (b) m, (c) l and (d) s for three values of α_m : $\alpha_m = 8.0 \times 10^{-2}$, 6.0×10^{-1} and 2.0 at $t = 29.0$.

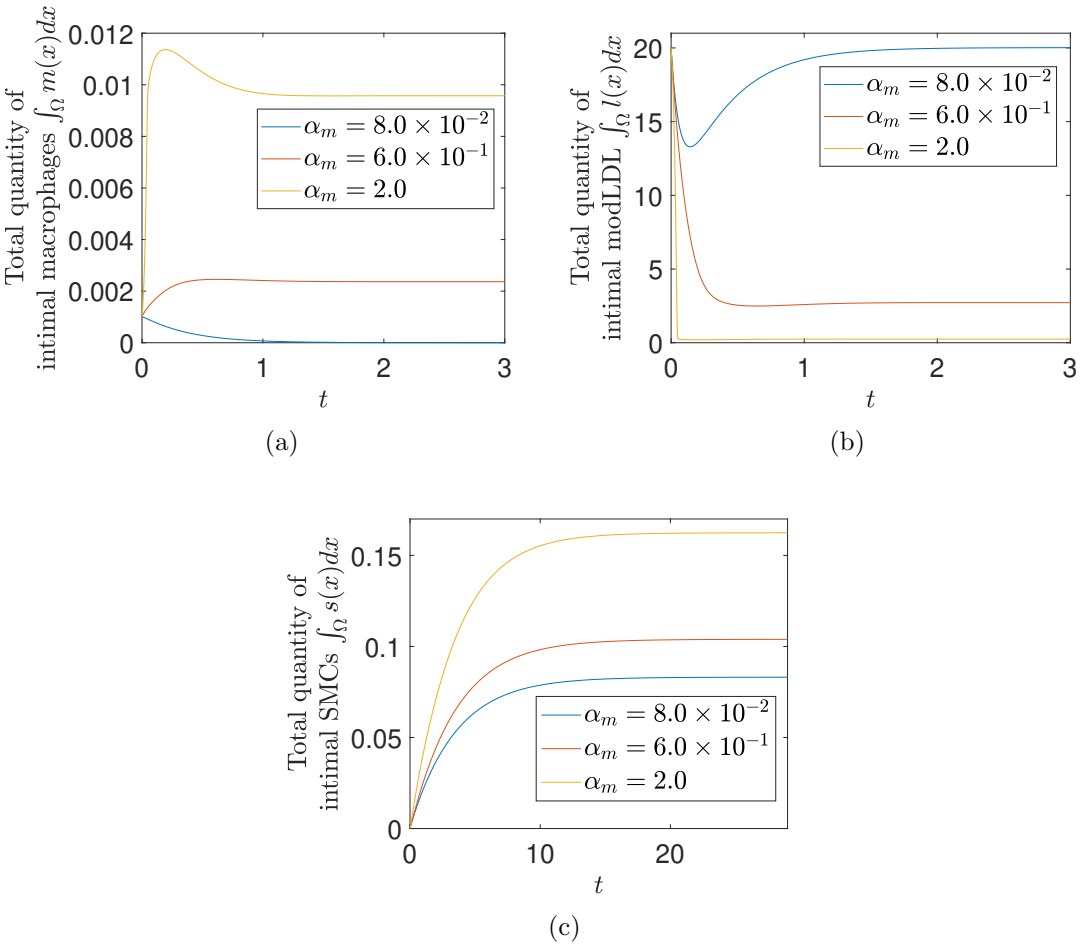

Figure 6.7: Comparisons of time evolutions of the total quantity of (a) intimal macrophages $\int_\Omega m(x)dx$, (b) intimal modLDL $\int_\Omega l(x)dx$, and (c) intimal SMCs $\int_\Omega s(x)dx$ for three values of α_m : $\alpha_m = 8.0 \times 10^{-2}$, 6.0×10^{-1} and 2.0 from $t = 0.0$ to 29.0.

6.4.1.2 μ_g and d_{sm}

As explained in Section 6.4.1.1, there are two ways by which macrophages affect the dynamics of s: SMC migration and proliferation, and SMC death. The first is due to the PDGF production term, which is dependent on m and the production rate μ_g. The second is due to the the SMC loss due to SMC apoptosis term, which we assume to be proportional to m and rate d_{sm}. We observed in Section 6.4.1.1 that greater values of m due to increasing α_m lead to increased s. This suggested that the effect of the apoptosis term is smaller than the chemotaxis, influx and proliferation terms. We therefore analyse this by comparing the effects of two parameters: μ_g and d_{sm}.

Figures 6.8a and 6.8b show the steady state solutions of g and s respectively for varying values of μ_g, while Figure 6.8c shows the time evolution of the intimal SMC density for those values. We note that the base values from Table 6.1 are $\mu_g = 10.0$ and $d_{sm} = 0.2$. When μ_g is increased from the base value by a factor of 10

($\mu_g = 100.0$), the changes in the steady state solutions of g and s are greater than when μ_g is increased from zero to the base values. This suggests that the dynamics of g are more sensitive to μ_g for values larger than the base value, and that an increase from the base value by a factor of 10 can create significant changes in the dynamics of g and s.

We directly compare these results to those in Figures 6.9a and 6.9b which show the steady state solution of s and the time evolution of the intimal SMC density of varying values of d_{sm}. We compare the base value ($d_{sm} = 0.2$) with an increase by a factor of 10 ($d_{sm} = 2.0$). The results from these figures show that increasing the value of d_{sm} to 2.0 leads to a smaller steady state solution of s and less intimal SMC density at steady state, though this difference is minor. This suggests that for values of d_{sm} in this range, the parameter's effect on s is small. As the parameter only affects s, there are no changes to the solutions of the other variables.

We therefore query the relative effects of both μ_g and d_{sm} given that both rates are proportional to m. To do so we compare the steady state solution of s for the base values of μ_g and d_{sm} to the solution when both μ_g and d_{sm} are increased. If we increase μ_g to $\mu_g = 100.0$ (increased from the base value by a factor of 10), we observe an increase in g in Figure 6.10a. Based on earlier results we expect this to result in increased s due to the chemotaxis and proliferation terms.

To understand the scale of change to the values of d_{sm} required to counteract the effect of the increased value of μ_g, we increase the value of d_{sm} to $d_{sm} = 40.0$ (increased from the base value by a factor of 200). Figures 6.10b and 6.10c show that when $d_{sm} = 40.0$ and $\mu_g = 100.0$ the steady state solution of s and the intimal SMC density is similar to those of the base values of d_{sm} and μ_g. To achieve this a much larger increase of d_{sm} from the base value was required compared to the increase of μ_g. This shows that for the base values of μ_g and d_{sm}, the effect of the SMC apoptosis term on the dynamics of s is weaker than the chemotaxis and prolferation terms. The effects of m on the dynamics of s are therefore mainly through the PDGF production term μ_g and changes to the g. These reflect the importance of PDGF on SMC dynamics due to SMC chemotaxis and proliferation.

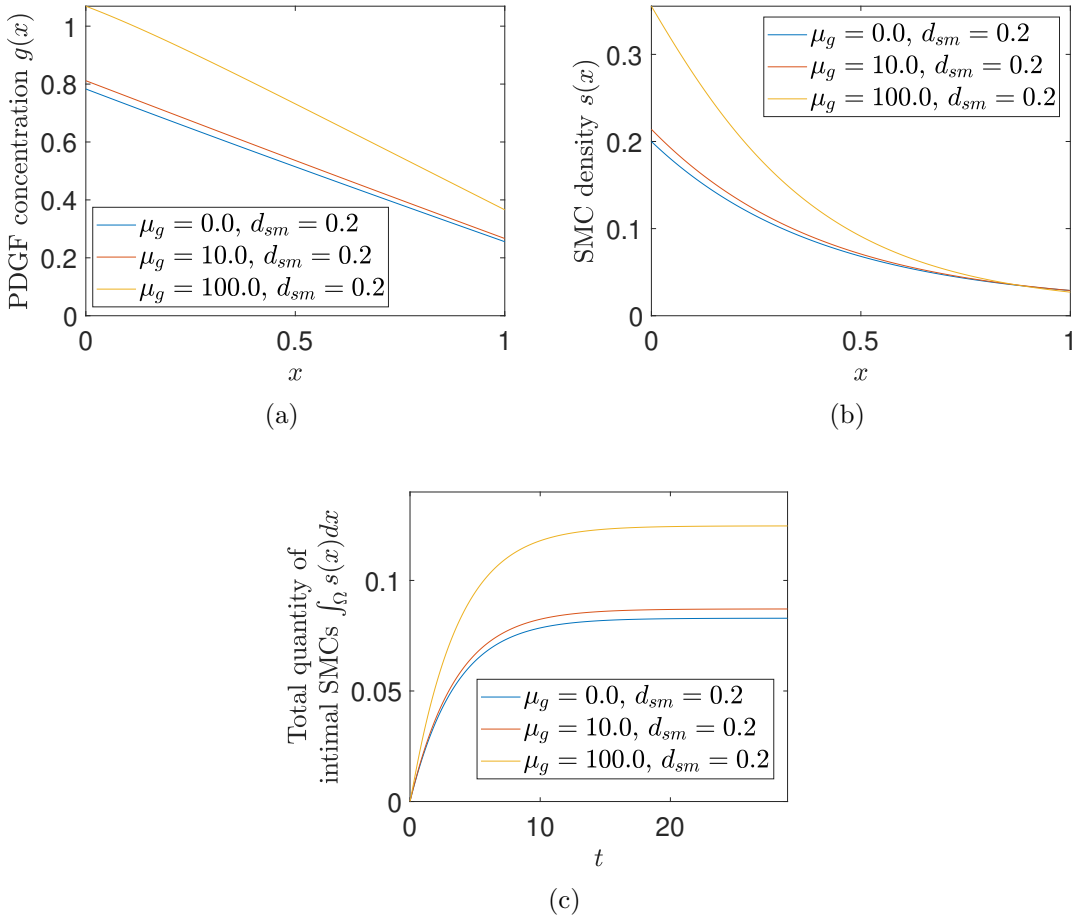

Figure 6.8: Comparisons of steady state solutions of (a) g and (b) s at $t = 29.0$, and (c) the time evolution of the total quantity of intimal SMCs $\int_\Omega s(x)dx$ from $t = 0.0$ to 29.0, with three values of μ_g: $\mu_g = 0.0$, 10.0 and 100.0 and $d_{sm} = 0.2$.

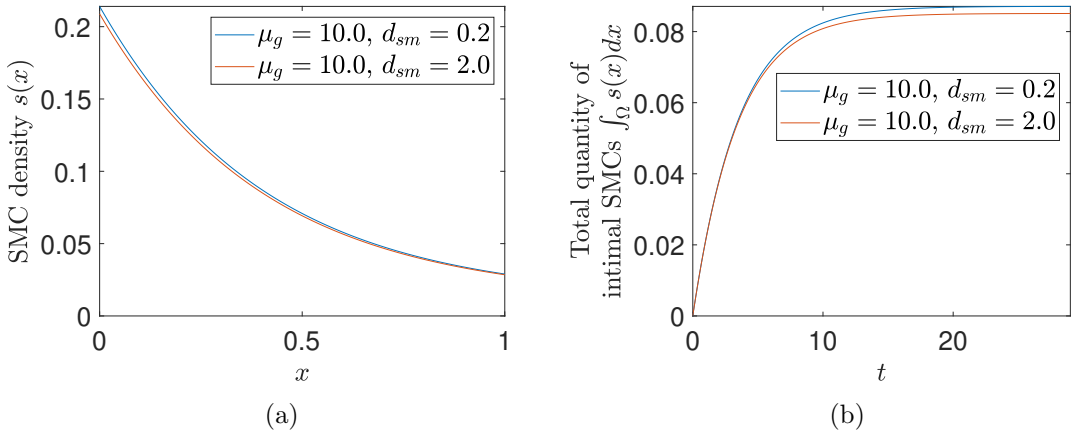

Figure 6.9: Comparisons of steady state solution of (a) s at $t = 29.0$, and (b) the time evolution of the total quantity of intimal SMCs $\int_\Omega s(x)dx$ from $t = 0.0$ to 29.0, with two values of d_{sm}: $d_{sm} = 0.2$ and 2.0 and $\mu_g = 10.0$.

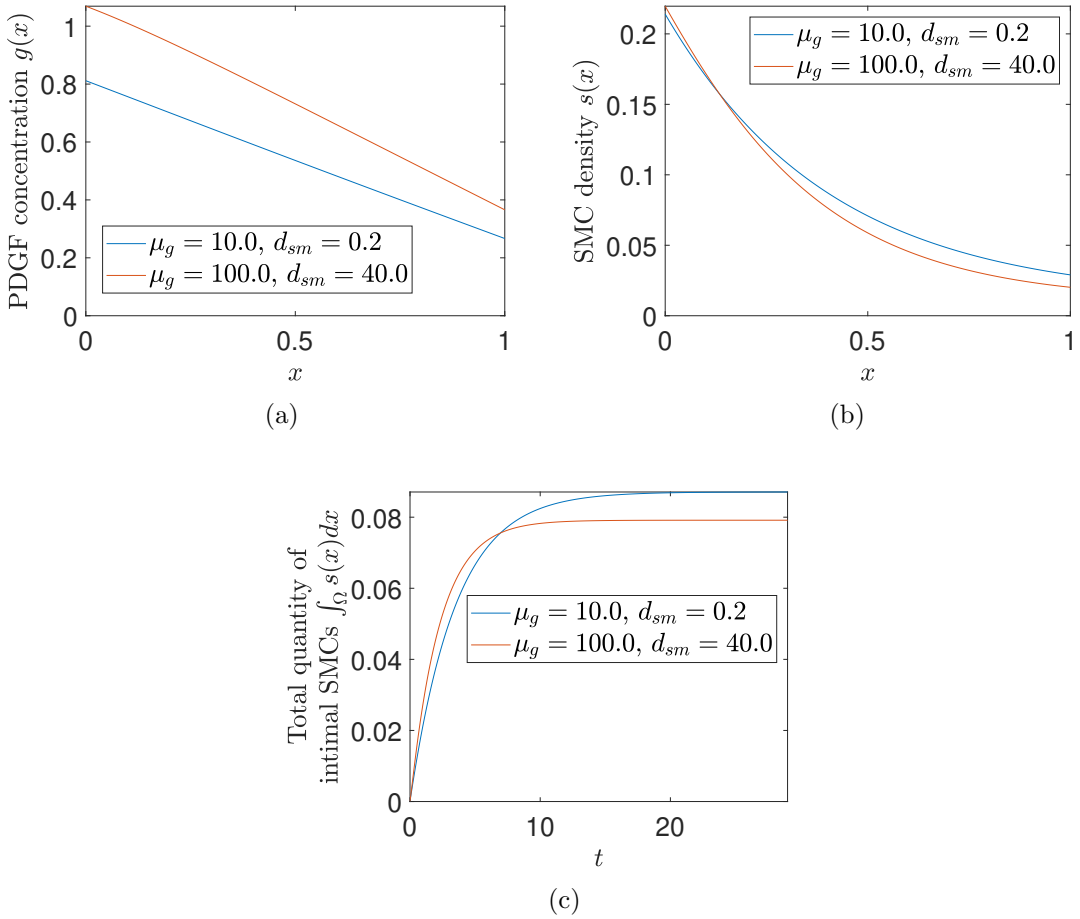

Figure 6.10: Comparisons of steady state solutions of (a) g and (b) s at $t = 29.0$, and (c) the time evolution of the total quantity of intimal SMCs $\int_\Omega s(x)dx$ from $t = 0.0$ to 29.0, with the base values of μ_g and d_{sm} from Table 6.1 and the values $\mu_g = 100.0$ and $d_{sm} = 40.0$

6.4.1.3 χ_m

The analyses in Sections 6.4.1.1 and 6.4.1.2 explained the two ways m affect the dynamics of s: indirectly through its effect on g and $\frac{\partial g}{\partial x}$, and directly through the SMC apotosis term. Section 6.4.1.1 focused on the effects of the rate of macrophage influx α_m on the dynamics of m; another key parameter we expect to affect m is the macrophage chemotaxis coefficient χ_m. We assume in equation (6.12) that macrophages move chemotactically along the gradient of modLDLs at a rate proportional to chemotactic coefficient χ_m. This means that we expect varying χ_m to affect the movement of macrophages towards the $x = 0$ boundary and the amount and distribution of macrophages in the intima. We also expect the gradient of m to change near the $x = 0$ boundary as the boundary condition (6.15) is affected by χ_m. Due to the effect of m on the dynamics of s, changes in χ_m affect g and s, particularly near the $x = 0$ boundary. We solve the model with three values of χ_m: $\chi_m = 0.0$, 1.0 and 10.0.

Figure 6.11b shows the steady state solutions of m for the three values of χ_m. Recalling the base value of $\chi_m = 0.1$, we observe that increasing χ_m leads to a greater distribution of m near the $x = 0$ boundary as the chemotactic movement of macrophages towards $x = 0$ becomes greater. A greater value of χ_m also leads to a more rapid recruitment of macrophages which produces a greater negative gradient of m at the $x = 0$ boundary. This increase leads to greater overall m as shown in Figure 6.12b where the intimal macrophage density increases with increasing χ_m. The results also show that the base value of χ_m, taken from the values in Chalmers *et al.* (2015), has a minor effect on m. This is evident in the small difference in steady state solutions of m between the values $\chi_m = 0.0$ and $\chi_m = 1.0$, as the base value ($\chi_m = 0.1$) lies between them.

Because macrophages uptake modLDL in equation 6.21, greater m leads to greater modLDL loss and therefore lower l. This is observed in Figures 6.11a and 6.12a, where the scale of the steady state solutions and intimal concentrations of l are inversely proportional to the scale of m.

The rate of PDGF production by macrophages is linearly proportional to m. Increasing χ_m, which we observe to increase the amount of macrophages in the intima, leads to greater PDGF production and therefore increasing g. This was observed in the results of both Sections 6.4.1.1 and 6.4.1.2: we observe the same dynamics in Figure 6.11c. The steady state solutions of g show greater g and $\frac{\partial g}{\partial x}$ near the $x = 0$ boundary. We expect the analyses of the effects of m on the dynamics of g and s from both Sections 6.4.1.1 and 6.4.1.2 to hold: the greater values of g and $\frac{\partial g}{\partial x}$ near the $x = 0$ boundary result in increased accumulation of s near the $x = 0$ boundary due to SMC proliferation and chemotaxis. We observe these dynamics in Figures 6.11d and 6.12c.

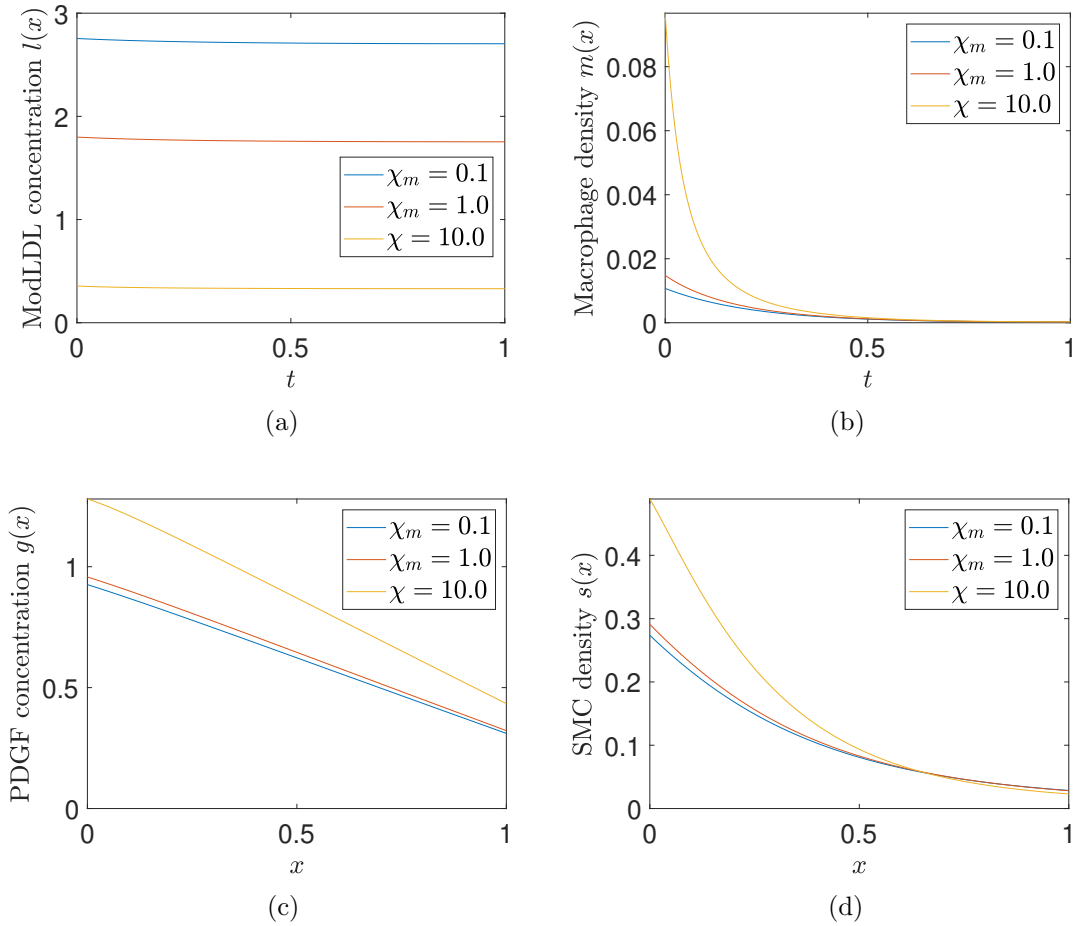

Figure 6.11: Comparisons of steady state solutions of (a) l, (b) m, (c) g and (d) s with three values of χ_m : $\chi_m = 0.1$, 1.0 and 10.0 at $t = 29.0$.

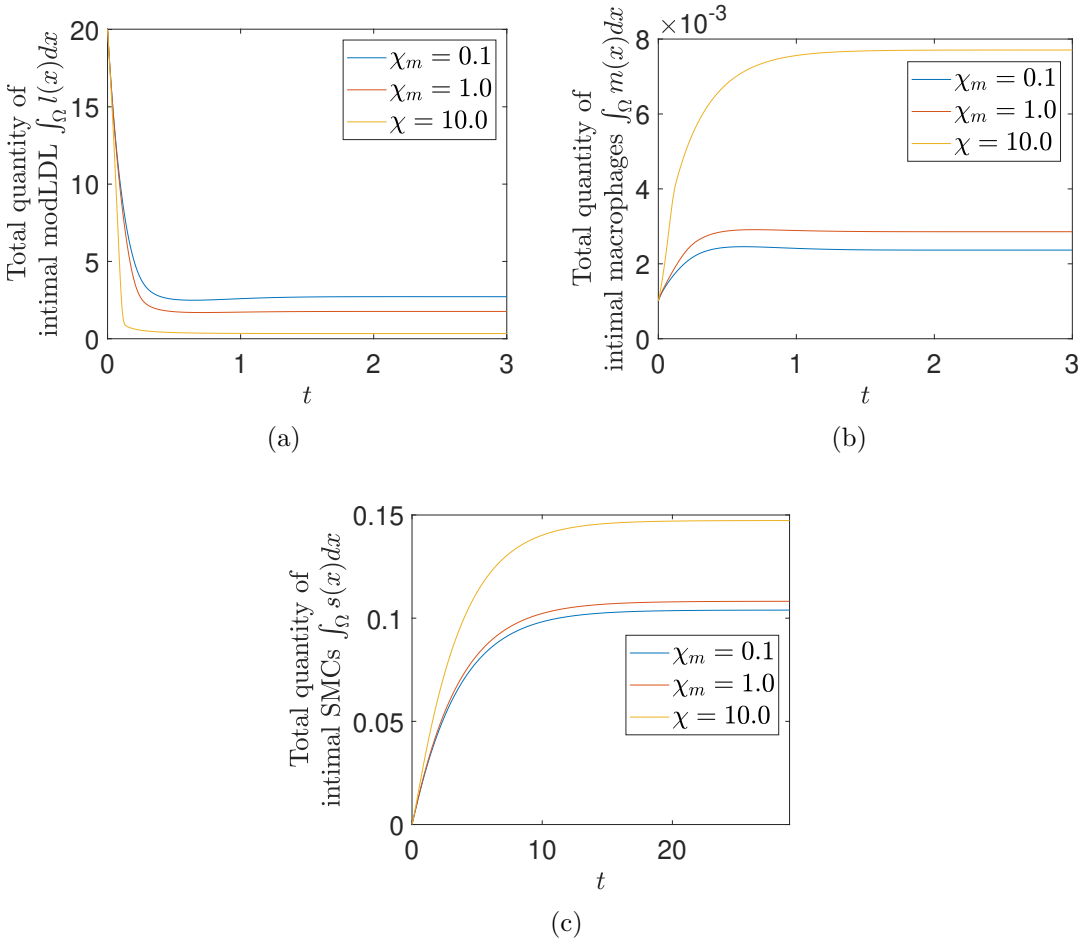

Figure 6.12: Comparisons of time evolutions of the total quantity of (a) intimal modLDL $\int_\Omega l(x)dx$, (b) intimal macrophages $\int_\Omega m(x)dx$, and (c) intimal SMCs $\int_\Omega s(x)dx$ with three values of χ_m : $\chi_m = 0.1$, 1.0 and 10.0 from $t = 0.0$ to 29.0.

6.5 Discussion

The results of the parameter sensitivity analyses in Sections 6.4.1.1, 6.4.1.2 and 6.4.1.3 demonstrate a number of factors in the dynamics of two different stages of cap formation. By varying parameters that affect the dynamics of macrophages such as α_m and χ_m, the results of Sections 6.4.1.1 and 6.4.1.3 showed that increasing macrophage density corresponds to increasing modLDL uptake and therefore lower modLDL concentration in the intima. The time evolutions of the total quantity of macrophages and modLDL also showed that the timescales of m and l remained short and that changes to the time to steady state due to varying parameters were small. modelling the two stages of lesion initiation and SMC migration together, despite the difference in timescale between the two stages, did not create any issues.

The results also showed that the dynamics of PDGF and SMCs were affected by macrophages. This was due to two factors. The first factor was the effect of macrophages on PDGF due to macrophages elaborating PDGF at a linear pro-

duction rate μ_g. Increasing macrophage density therefore leads to an increase in the magnitude of the PDGF production term, producing more PDGF in the intima. This in turn leads to SMC proliferation increasing because the mitosis rate depends on PDGF concentrations. We note that both macrophage density and PDGF production are greatest near the endothelial boundary. SMC proliferation therefore increases near this boundary, although we note that the aggregation of SMCs was already greatest near this boundary. Changes in the dynamics of PDGF, and therefore the magnitude of its concentration and gradient, affect SMCs through the chemotaxis and proliferation terms.

The second factor that affected the dynamics of SMCs was the effect of macrophages on SMCs directly due to SMC apoptosis, which is proportional to macrophage density and rate d_{sm}. Section 6.4.1.2 compared the relative strength of both μ_g and d_{sm} on SMCs and showed that a greater change in scale from the base value was required for d_{sm} to have a balancing effect on a smaller change in scale for μ_g. This demonstrated that the effect of SMC apoptosis on SMC dynamics is weak.

Our model suggests that the main contribution of macrophages to PDGF and SMC dynamics is the elaboration of PDGF by macrophages. By affecting PDGF concentration in the intima, macrophages can indirectly stimulate the proliferation of SMCs and contribute to the SMC profile and a fibrous cap.

We therefore explore the thesis objective of modelling stages of plaque formation by extending the base reaction-diffusion model. We specifically take parameter values and model assumptions from Chalmers *et al.* (2015) to reflect up-to-date experimental observations on lesion growth and cap formation. The results above demonstrate that our reaction-diffusion model captures the dynamics of modLDL, macrophages, SMCs and PDGF.

Chapter 7

Integrating prior models to model three key stages of cap formation

7.1 Integrating three stages: smooth muscle cell migration, collagen synthesis, and lesion initiation

We recall the first three models in Chapters 4, 5 and 6. In Chapter 4, we proposed a reaction-diffusion model that described the SMC migration stage by considering two equations for SMC and PDGF dynamics. This reaction-diffusion model was intended to adopt the more up-to-date biological assumptions of the multiphase model of Watson *et al.* (2018) [44] while providing the simpler reaction-diffusion framework employed in Ougrinovskaia (2011) [37]. The analyses of the first reaction-diffusion model demonstrated that the reaction-diffusion model was comparable to the multiphase model in capturing SMC and PDGF dynamics. The reaction-diffusion model was therefore used as a framework for subsequent models.

The second reaction-diffusion model in Chapter 5 built off the reaction-diffusion model of Chapter 4. In that model, we expanded the scope of the reaction-diffusion model framework of Chapter 4 to include the collagen synthesis stage of cap formation. This was because the multiphase model in Watson *et al.* (2020) [45] extended the first multiphase model of Watson *et al.* (2018) by including SMC stimulation by TGF-β and the movement of SMCs through the ECM. This meant additional equations for ECM and TGF-β. The first reaction-diffusion model of Chapter 4 used the first multiphase model of Watson *et al.* (2018) as a reference model; the second reaction-diffusion model therefore used the multiphase model in Watson *et al.* (2020) as a reference model. As a result, two equations for TGF-β and ECM were introduced in addition to the equations for SMC and PDGF dynamics. To account for the absence of volume filling and constraints on SMC proliferation and ECM synthesis, we made two changes to the equations for SMCs and ECM. The first was a nonlinear haptotaxis coefficient function to limit unconstrained SMC migration towards the endothelial boundary. The second was a source limiting function on ECM synthesis. To analyse the model, analyses were performed on the model equations of the second reaction-diffusion model. We note that we performed parameter sensitivity analyses on the same parameters analysed in Watson *et al.* (2020). The results of these analyses demonstrated that the second reaction-diffusion model was comparable to the second multiphase model in capturing key aspects of the dynamics of PDGF, SMCs, ECM and TGF-β. This showed two things: that the base reaction-diffusion model framework from Chapter 4, which was extended in Chapter 5, could be extended to capture the same general dynamics as the more complex

multiphase model in Watson *et al.* (2020), and that SMC distribution near the endothelial boundary was critical to size of a fibrous cap region.

The results of Chapters 4 and 5 affirmed the validity of the reaction-diffusion model framework in its ability to be extended and its capture of key dynamics analysed in Watson *et al.* (2018) and Watson *et al.* (2020). This allowed us to depart from using the research of Watson *et al.* (2018) and Watson *et al.* (2020) in Chapter 6. The reaction-diffusion model in Chapter 6 therefore used the models in Ougrinovskaia (2011) and Chalmers *et al.* (2015) [11] as references to model the lesion initiation stage of cap formation. We note that the aim of this third reaction-diffusion model was to understand the scope and ability of the framework to include more stages of cap formation. As a result, two equations for modLDL and macrophages were introduced in addition to the equations for SMC and PDGF dynamics. These equations introduced a number of changes from the prior two reaction-diffusion models and adopted some different assumptions to the reference models of Ougrinovskaia (2011) and Chalmers *et al.* (2015). An example of a change from the earlier reaction-diffusion models of Chapters 4 and 5 was the shorter timescale for the equations for the lesion initiation stage compared to those of the SMC migration and collagen synthesis stages. The analyses of the model equations showed that the shorter timescale for the model equations for modLDL and macrophages did not affect the general dynamics of SMCs and PDGF. The steady state times of SMCs were not significantly changed and the magnitude and distribution of the steady state solution of SMCs were unchanged whether the model equations were solved simultaneously or after the shorter timescale equations had reached steady state. Parameter sensitivity analyses was also conducted on the parameters related to the introduced equations of modLDL and macrophages and their interdependence with the equations for PDGF and SMCs. This analyses demonstrated that the reaction-diffusion model captured the dynamics of modLDL, macrophages, SMCs and PDGF. Importantly it captured the dynamics of the early stage of cap formation and demonstrated that the reaction-diffusion model framework could accommodate stages of different timescales.

7.2 Model formulation and development

The aim of the model presented here is to combine the three reaction-diffusion models of Chapters 4, 5 and 6 to provide a continuous depiction of early lesion initiation to the intermediate stage of collagen synthesis. These reaction-diffusion models only modelled up to two stages of cap formation: we aim to model all three previously modelled stages. This means that we no longer rely on reference models and instead focus on integrating and expanding the model equations from the prior three reaction-diffusion models. The model therefore introduces new interdependencies as well as assumptions to capture more biological phenomena. As a result, we aim to have a model that can model an increasing number of stages without significant complexity and issues.

7.2.1 Model equations

7.2.1.1 Macrophages ($m(x,t)$)

The model equation for m holds the same base assumptions as (6.12). It assumes that macrophages move randomly and move chemotactically along the gradient of modLDLs. It also assumes general loss and cell death of macrophages which is modelled by a linear decay term with decay rate d_m.

We note that previous model equations for m did not consider any cell crowding effects in the intima. In the third reaction-diffusion model, the model equation for ρ (5.8) cell crowding was simulated by a source limiting function that constrained ECM synthesis when ECM density exceeded some maximum carrying capacity. In this model equation, we seek to represent spatial crowding between SMCs and macrophages by introducing a new assumption: that SMCs constrain macrophage spatial dispersion. We assume that macrophages are less motile than SMCs and are therefore displaced by SMCs. To simulate this we assume that macrophages move down the gradient of s at a rate governed by the taxis coefficient χ_{ms}. This tactic response to smooth muscle cells describes the inhibition of macrophage migration where there is a high density of SMCs. We therefore model macrophage density within the intima by:

$$\frac{\partial m}{\partial \tau} = D_m \frac{\partial^2 m}{\partial x^2} - \frac{\partial}{\partial x}\Big(\chi_m m \frac{\partial l}{\partial x} - \chi_{ms} m \frac{\partial s}{\partial x}\Big) - d_m m. \tag{7.1}$$

7.2.1.2 ECM ($\rho(x,t)$)

We assume that ECM dynamics are explicitly space-independent and model the density of ECM within the intima by:

$$\begin{aligned}\frac{\partial \rho}{\partial \tau} =& r_s s \psi(\rho)\Big[1 + \frac{A_s T}{c_s + T}\Big] - r_d s \rho\Big[1 + \frac{A_d g}{(c_d + g)(1 + \gamma_d T)}\Big] \\ &- \beta_\rho(m)\rho\Big[\frac{1 + \epsilon\gamma_\rho T}{1 + \gamma_\rho T}\Big].\end{aligned} \tag{7.2}$$

We continue to use the base assumptions of equation (5.8): the first source term describes ECM synthesis by SMCs which is proportional to a baseline ECM production rate r_s, local SMC density, the source limiting function $\psi(\rho)$, and a kinetic growth term dependent on T with c_s representing the half-maximal rate and A_s representing the maximal factor of TGF-β stimulated ECM proliferation. The first degradation term represents ECM degradation by SMCs, which is dependent on s, g and T. This degradation is proportional to a constant degradation term r_d.

We note that the second degradation term represents general ECM degradation, which in equation (5.8) was assumed to be proportional to ρ, the constant rate β_ρ and a function of T. This general ECM degradation includes degradation due to MMPs such as MMP-9, which are expressed by macrophages [3,24,38]. We therefore

modify this degradation term to be a function of m. The solution profile of m in Figure 6.3b shows that the distribution of m is greatest near the $x = 0$ boundary and decreases across the domain towards the $x = 1$ boundary. The degradation term cannot be linearly proportional to m as low values of m will make this term negligible, but we also expect the effect of the term to increase with m. Because the degradation term describes general degradation (including degradation unrelated to macrophage-expressed MMPs), the function must be non-zero when $m(x,t) = 0$. We therefore consider the increasing non-linear degradation rate function $\beta_\rho(m)$:

$$\beta_\rho(m) = \beta_\rho(1 + \epsilon_\rho m)^2, \tag{7.3}$$

where β_ρ is the baseline rate of ECM degradation by immune cells and ϵ_ρ is the scaling parameter. We choose this quadratic function because it is an increasing function of m but increases at a lower rate at low macrophage density than for high macrophage density. The function is also simple and provides reasonable values for the expected range of values of m (approximately of order 10^{-2}).

As shown in Figure 7.1, the function increases with increasing m from the baseline value of β_ρ.

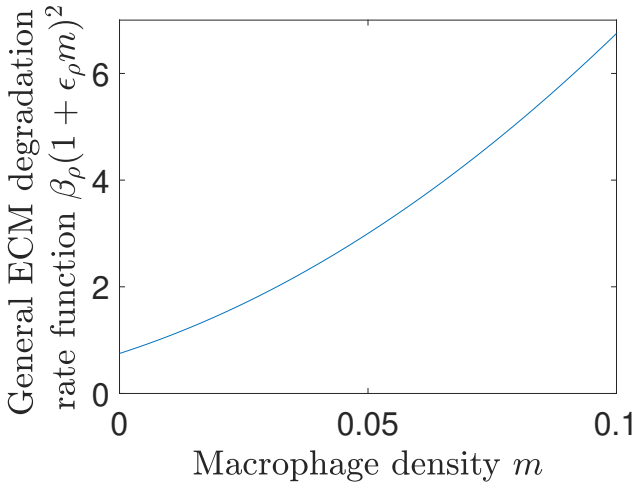

Figure 7.1: The solution of $\beta_\rho(m)$ over $m(x,t)$ with $\beta_\rho = 0.75$ and $\epsilon_\rho = 20.0$.

The equations for PDGF ($g(x,t)$), SMCs ($s(x,t)$), TGF-β ($T(x,t)$) and modLDL ($l(x,t)$) remain unchanged from (6.9), (6.10), (5.10) and (6.11) respectively.

7.2.2 Boundary and initial conditions

7.2.2.1 Macrophages ($m(x,t)$)

In equation (7.1), we assumed that macrophage flux is comprised of a random motion component and a component due to the chemotactic response to modLDL and

SMCs. Random motion is assumed to be proportional to the diffusion coefficient D_m, while the chemotactic movement along the gradient of modLDL and tactic movement down the gradient of SMCs are proportional to coefficients χ_m and χ_{ms} respectively. The flux term J_m is therefore:

$$J_m = -D_m \frac{\partial m}{\partial x} + m\Big(\chi_m \frac{\partial l}{\partial x} - \chi_{ms} \frac{\partial s}{\partial x}\Big). \tag{7.4}$$

We continue the same assumptions towards flux conditions at the $x = 0$ and $x = 1$ boundaries as previous model boundary conditions (6.15). This means that at $x = 0$, we assume an influx rate proportional to α_m and m that is saturated at high concentrations of modLDL. At $x = 0$, this is represented as $J_m|_{x=0} = \frac{\alpha_m l m}{\gamma + l}$ where $J_m = -D_m \frac{\partial m}{\partial x} + \chi_m m \frac{\partial l}{\partial x} - \chi_{ms} m \frac{\partial s}{\partial x}$ is the macrophage flux into the intima.

We assume zero flux conditions at $x = 1$. This is represented as $J_m|_{x=1} = 0$. The boundary conditions of m are therefore:

$$\frac{\partial m}{\partial x}\Big|_{x=0} = \frac{\frac{-\alpha_m l m}{1+l} + m\Big(\chi_m \frac{\partial l}{\partial x} - \chi_{sm} \frac{\partial s}{\partial x}\Big)}{D_m}, \qquad \frac{\partial m}{\partial x}\Big|_{x=1} = 0. \tag{7.5}$$

The initial condition of m is unchanged from (6.16). The profile of this initial condition $m(x, 0)$ is shown in Figure 6.2.

The boundary conditions for PDGF, SMCs, TGF-β and modLDL at $x = 0$ and $x = 1$ remain unchanged from (4.19), (5.11), (5.12) and (6.13) respectively. The initial conditions for $s(x, 0)$ and $l(x, 0)$ (described in (6.14)) are also unchanged.

7.2.3 Non-dimensionalisation

We non-dimensionalise our model, using tildes (except for t) to denote non-dimensionalised quantities. The key parameters x, t, m, l, s, g, ρ and T are non-dimensionalised as:

$$t = \tau t_0, \quad x = L\widetilde{x}, \quad l = \gamma_l \widetilde{l}, \quad m = m_0 \widetilde{m}, \quad s = k\widetilde{s}, \quad g = g_0 \widetilde{g},$$
$$\rho = \rho_0 \widetilde{\rho}, \quad T = T_0 \widetilde{T},$$

where t_0 represents the characteristic time value, L the length of the domain, γ_l the saturation rate of modified LDL consumption, m_0 the characteristic macrophage density, k the total cell and tissue density, g_0 the characteristic PDGF concentration, ρ_0 the characteristic ECM density and T_0 the characteristic TGF-β concentration.

The remaining model parameters are non-dimensionalised as:

$$
\begin{aligned}
&d_g = \frac{\widetilde{d_g} D_g}{L^2}\ , && \mu_g = \frac{\widetilde{\mu_g} g_0 D_g}{L^2 m_0}\ , && \alpha_g = \frac{\widetilde{\alpha} D_g g_0}{L}\ , && \sigma_g = \frac{\widetilde{\sigma} D_g}{L}\ ,\\
&D_s = \frac{L^2 \widetilde{D_s}}{t_0}\ , && d_s = \frac{\widetilde{d_s}}{t_0}\ , && G_s = \widetilde{G_s} g_0\ , && \chi_s = \frac{\widetilde{\chi_s} L^2}{t_0 g_0}\ ,\\
&r_{s0} = \frac{\widetilde{r_{s0}}}{t_0}\ , && \widetilde{A} = \frac{r_s}{r_{s0}}\ , && h_\rho = \frac{\widetilde{h_\rho} L^2}{t_0 \rho_0}\ , && \xi = \frac{\widetilde{\xi}}{\rho_0}\ ,\\
&d_{sm} = \frac{\widetilde{d_{sm}}}{t_0}\ , && && && \\
&D_m = \frac{L^2 \widetilde{D_m}}{t_0}\ , && \chi_m = \frac{L^2 \widetilde{\chi_m}}{t_0 \gamma_l}\ , && \chi_{ms} = \frac{\widetilde{\chi_{ms}} L^2}{t_0 k}\ , && d_m = \frac{\widetilde{d_m}}{t_0}\ ,\\
&D_l = \frac{L^2 \widetilde{D_l}}{t_0}\ , && d_l = \frac{\widetilde{d_l}}{t_0}\ , && \alpha_m = \frac{\widetilde{\alpha_m} L}{t_0}\ , && \alpha_l = \frac{\widetilde{\alpha_l} L \gamma_l}{t_0}\ ,\\
&\mu_l = \frac{\gamma_l \widetilde{\mu_l}}{t_0}\ , && && && \\
&r_s = \frac{\rho_0 \widetilde{r_s}}{k T_0}\ , && c_s = T_0 \widetilde{c_s}\ , && c_d = g_0 \widetilde{c_d}\ , && \gamma_d = \frac{\widetilde{\gamma_d}}{T_0}\ ,\\
&r_d = \frac{\widetilde{r_d}}{T_0}\ , && \gamma_\rho = \frac{\widetilde{\gamma_r h o}}{T_0}\ , && \beta_\rho = \frac{\widetilde{\beta_\rho}}{m_0 t_0}\ , && \\
&\beta_T = \frac{D_T \widetilde{\beta_T}}{L^2}\ , && \alpha_T = \frac{D_T T_0 \widetilde{\alpha_T}}{L}\ , && \sigma_T = \frac{D_T \widetilde{\sigma_T}}{L}. &&
\end{aligned}
\tag{7.6}
$$

Dropping the tildes for clarity, the model equations (6.11), (7.1), (7.2), (5.10), (6.9) and (6.10) and boundary conditions (6.13), (7.5), (5.12), (4.19) and (5.11) become:

$$\frac{\partial l}{\partial \tau} = D_l \frac{\partial^2 l}{\partial x^2} - \frac{\mu_l l m}{1+l} - d_l l, \tag{7.7}$$

$$\frac{\partial m}{\partial \tau} = D_m \frac{\partial^2 m}{\partial x^2} - \frac{\partial}{\partial x}\Big(\chi_m m \frac{\partial l}{\partial x} - \chi_{sm} m \frac{\partial s}{\partial x}\Big) - d_m m, \tag{7.8}$$

$$0 = \frac{d^2 g}{dx^2} - d_g g + \mu_g m, \tag{7.9}$$

$$
\begin{aligned}
\frac{\partial s}{\partial \tau} =& D_s \frac{\partial^2 s}{\partial x^2} - \frac{\partial}{\partial x}\Big(\chi_s s \frac{\partial g}{\partial x} + h_\rho(\rho) s \frac{\partial \rho}{\partial x}\Big) + r_{s0}\Big(1 + \frac{A g}{G_s + g}\Big) s(1-s) \\
&- d_s s - d_{sm} s m,
\end{aligned}
\tag{7.10}
$$

$$\begin{aligned}\frac{\partial \rho}{\partial \tau} =& r_s s\psi(\rho(x))\Big[1+\frac{A_s T}{c_s+T}\Big] - r_d s\rho\Big[1+\frac{A_d g}{(c_d+g)(1+\gamma_d T)}\Big] \\ &- \beta_\rho(m)\rho\Big[\frac{1+\epsilon\gamma_\rho T}{1+\gamma_\rho T}\Big],\end{aligned} \tag{7.11}$$

$$0 = \frac{d^2T}{dx^2} - \beta_T T, \tag{7.12}$$

with boundary conditions:

$$\begin{aligned}
&\frac{\partial m}{\partial x}\Big|_{x=0} = \frac{\frac{-\alpha_m l m}{1+l} + m\Big(\chi_m\frac{\partial l}{\partial x} - \chi_{sm}\frac{\partial s}{\partial x}\Big)}{D_m}, && \frac{\partial m}{\partial x}\Big|_{x=1} = 0,\\
&\frac{\partial l}{\partial x}\Big|_{x=0} = \frac{-\alpha_l}{D_l}, && \frac{\partial l}{\partial x}\Big|_{x=1} = 0,\\
&\frac{dg}{dx}\Big|_{x=0} = -\alpha_g, && \frac{dg}{dx}\Big|_{x=1} = -\sigma_g g,\\
&\frac{\partial s}{\partial x}\Big|_{x=0} = \frac{-\alpha_g\chi_s s}{D_s} + \frac{h_\rho}{1+\xi_\rho\rho}\frac{s}{D_s}\frac{\partial \rho}{\partial x}, && \frac{\partial s}{\partial x}\Big|_{x=1} = \frac{\chi_s\sigma_g g(s^*-s)}{D_s} + \frac{h_\rho}{1+\xi_\rho\rho}\frac{s}{D_s}\frac{\partial \rho}{\partial x},\\
&\frac{\partial T}{\partial x}\Big|_{x=0} = -\alpha_T, && \frac{\partial T}{\partial x}\Big|_{x=1} = -\sigma_T T,
\end{aligned} \tag{7.13}$$

and initial conditions:

$$s(x,0) = s_0, \tag{7.14}$$

$$l(x,0) = \Big(\frac{-\alpha_l}{D_l\gamma} + \frac{\frac{\alpha_l}{D_l\gamma}}{1-\frac{\exp(-\gamma)}{\exp(\gamma)}}\Big)\exp(\gamma x) + \Big(\frac{\frac{\alpha_l}{D_l\gamma}}{1-\frac{\exp(-\gamma)}{\exp(\gamma)}}\Big)\exp(-\gamma x), \tag{7.15}$$

$$m(x,0) = \frac{m_0\sqrt{2}}{\sigma\pi}\exp\Big(-\frac{x^2}{2\sigma^2}\Big), \tag{7.16}$$

where s_0 is non-dimensional, $m_0 = 1.0\times10^{-4}$, $\sigma = 0.05$ and $\gamma = \sqrt{\frac{d_l}{D_l}}$. The non-linear haptotaxis function $h(\rho)$ is the kinetic function:

$$h(\rho) = \frac{h_\rho}{1+\xi_\rho\rho},$$

with scaling parameter ξ_ρ. The source limiting function $\psi(\rho)$ is:

$$\psi(\rho) = \frac{a^6}{a^6+\rho^6},$$

where $a = 0.3$. The general ECM degradation rate function $\beta_\rho(m)$ is:

$$\beta_\rho(m) = \beta_\rho(1+\epsilon_\rho m)^2, \tag{7.17}$$

where β_ρ is the baseline rate of ECM degradation by immune cells and ϵ_ρ is the scaling parameter.

7.2.4 Parameter values

Table 7.1: Base non-dimensionalised parameter values

Symbol	Definition	Value	Reference
d_g	Rate of PDGF decay	0.075	6.1
μ_g	Rate of production of PDGF by macrophages	10^1	6.1
D_s	Diffusion coefficient of SMC	1.0979	6.1
χ_s	SMC motility coefficient	4.5952	6.1
h_ρ	SMC haptotaxis coefficient	2.0	
r_{s0}	Baseline rate of SMC proliferation	0.02	6.1
d_s	Rate of SMC decay	0.4	6.1
d_{sm}	Rate of SMC apoptosis	0.2	6.3.4.1
G_s	Michaelis-Menten kinetic constant	1.4	6.1
A_s	Maximal factor of PDGF-stimulated increase in rate of SMC proliferation	19	6.1
α_g	Rate of PDGF influx from endothelium	0.55	6.1
σ_g	Permeability of IEL to PDGF	2	6.1
s_0	Initial SMC concentration	1×10^{-4}	6.1
s^*	Concentration of synthetic SMC in media	0.01	6.1
D_m	Diffusion coefficient of macrophages	10^{-1}	6.1
χ_m	Macrophage motility coefficient	10^{-1}	6.1
χ_{ms}	Macrophage dispersion constraint due to cell crowding motility coefficient	0.5	7.2.4.1
μ_m	Rate of macrophage conversion	10^2	6.1
d_m	Rate of macrophage decay	10^{-1}	6.1
D_l	Diffusion coefficient of LDLs	10^3	6.1
μ_l	Rate of LDL uptake by macrophages	10^5	6.1
d_l	Rate of LDL decay	10^1	6.1
α_l	Rate of LDL influx from endothelium	2×10^2	6.3.4.1
α_m	Rate of macrophage influx from endothelium	0.9	7.2.4.1
d_g	Rate of PDGF decay	0.075	6.1
r_s	Baseline rate of ECM phase synthesis by SMCs	1.8	5.1
c_s	Exponent in SMC phase pressure function	0.3	5.1
r_d	Baseline rate of ECM degradation by SMCs	1.5	5.1
A_d	Maximal factor of PDGF-stimulated increase in rate of ECM degradation by SMCs	4.0	5.1

Continued on next page

Table 7.1 – continued from previous page

Symbol	Definition	Value	Reference
c_d	PDGF concentration for half-maximal increase in rate of ECM degradation by SMCs	2.5	5.1
γ_d	Reciprocal of reference TGF-β concentration for inhibition of ECM degradation by SMCs	0.5	5.1
β_ρ	Baseline rate of ECM degradation by immune cells	0.75	7.2.4.1
ϵ_ρ	Scaling parameter of general ECM degradation rate function $\beta_\rho(m)$	20.0	7.2.4.1
γ_ρ	Reciprocal of reference TGF-β concentration for inhibition of ECM degradation by immune cells	10.0	5.1
ϵ	Maximal factor of TGF-β stimulated decrease in rate of ECM degradation by immune cells	0.25	5.1
β_T	Rate of TGF-β decay	20.0	5.1
α_T	Rate of TGF-β influx	2.5	5.1
σ_T	Permeability of IEL to TGF-β	4.0	5.1

7.2.4.1 Parameter value justification

The parameter values of the reaction-diffusion model are mostly unchanged from the three prior reaction-diffusion models due to the same non-dimensionalisation of parameters. There are three main exceptions to this: ϵ_ρ, α_m, and χ_{ms}.

The parameter ϵ_ρ is the scaling parameter of general ECM degradation rate function (7.3): we assumed in the model equation for ρ (7.2) that the general ECM degradation term was additionally proportional to m. The base case solution profile of m in Figure 6.3b from the reaction-diffusion model in Chapter 6 showed that the distribution of m increases near the $x = 0$ boundary, with the maximum value of $m(0, t)$ at steady state being approximately $m(0, t) = 0.018$. The value of $\beta_\rho(m)$ should reasonably increase with m yet be sufficiently small to keep macrophage growth at the same order of magnitude as the general ECM degradation term. The value of ϵ_ρ is therefore set to $\epsilon_\rho = 20.0$.

The parameter χ_{ms} is a newly introduced parameter which represents the chemotactic coefficient used in (7.1) to describe the constraint on macrophage dispersion due to cell crowding. As this is a newly introduced term with no equivalent in the previous models, we choose a value for the term that is reasonable. We therefore set the base value of χ_{ms} as $\chi_{ms} = 0.5$. We note that some numerical issues were faced when $\chi_{ms} > 2.0$.

The effect of χ_{ms} reduces macrophage migration due to competition for space between macrophages and smooth muscle cells. As a result there is lower macrophage density near the $x = 0$ boundary where SMC distribution is greatest. The effect of the general loss and cell death term for macrophages in (7.1), which is proportional to decay rate d_m and m, is weaker where the value of m is lower. We observed in the base case solution for m in Section 6.4.0.1 that the distribution of macrophages is greatest near the $x = 0$ boundary. This means that the effect of this general loss and cell death term is greatest near the $x = 0$ boundary. The rate of influx of macrophages must therefore be sufficient to replace the macrophages that have died. The previous base value of α_m in Chapter 6 was $\alpha_m = 6.0 \times 10^{-1}$; due to the effect of χ_{ms} on the dynamics of m, we increase this value to $\alpha_m = 9.0 \times 10^{-1}$.

7.3 Results

7.3.0.1 Base case simulation

The solutions of the model equations (7.7), (7.8), (7.9), (7.10) and (7.11) are solved with the parameter values from Table 7.1. To show the effect of the new parameters χ_{ms} and ϵ_ρ, a comparison steady state solution is plotted against the steady state solutions of the model variables where the values of the new parameters are set to zero.

The model equation for m (7.8) expands the previous model equation (6.12) by assuming that macrophages compete for space with SMCs. This competition is described by a constraint-taxis term for macrophage dispersion that assumes macrophages move away from the SMC gradient at a rate proportional to the taxis coefficient χ_{ms}. With $\chi_{ms} = 0.5$, $\alpha_m = 0.9$ and all other parameter values the same as those used in the base case of the third reaction-diffusion model (Section 6.4.0.1), the solutions of m as a function of x are shown in Figure 7.2a. Macrophages are most highly aggregated near the $x = 0$ boundary and macrophage density decreases in the intima over time. These are the same general dynamics of m observed in the base case results of the third reaction-diffusion model (Section 6.4.0.1). Figure 7.3a compares the steady state solution of m where $\chi_{ms} = 0.5$ and $\epsilon_\rho = 20.0$ to a comparison steady state solution where χ_{ms} and ϵ_ρ equal zero. We observe that when macrophages compete with SMCs for space, the aggregation of macrophages decreases near $x = 0$. As shown in Figure 7.2d, SMC density is greatest near $x = 0$ and therefore macrophage density decreases in this region. This decrease in the endothelial macrophage density is approximately 40% from $m(0, t) = 0.018$ to $m(0, t) = 0.011$.

There are no changed assumptions or parameter values for the model equation for l (7.7) from the third reaction-diffusion model (6.11). The modLDL profile shown in Figure 7.2b is near constant, and the solutions of l as a function of x at increasing times show that l increases over time. These same dynamics were observed in Section 6.4.0.1. The steady state solutions of l in Figure 7.3b show that l is greater when $\chi_{ms} = 0.5$ and $\epsilon_\rho = 20.0$. This is because m is lower for non-zero values of χ_{ms}, leading to lower modLDL uptake by macrophages.

The PDGF profile shown in Figure 7.2c shows the solutions of g as a function of x at two times: the first near the beginning time value and the second at $t = 29.0$. The model equation for g (7.9) and parameter values are unchanged from the third reaction-diffusion model. The effect of non-zero ϵ_ρ and χ_{ms} on the dynamics of g is shown in Figure 7.3c. PDGF production increases proportionally to macrophage density at rate μ_g. The decrease in macrophage density near the $x = 0$ boundary due to the cell crowding term at the rate governed by the chemotaxis coefficient χ_{ms} means that PDGF production is lower when χ_{ms} is non-zero. We observe that the difference in g between the two solutions in 7.3c is minor.

The model equation for s (7.10) combines the model equations for s of the second and third reaction-diffusion models (5.7) and (6.10). The dynamics of s therefore include haptotactic SMC migration along EMC gradients ($h_\rho(\rho)s\frac{\partial \rho}{\partial x}$) and apoptosis ($d_{sm}sm$). The parameter values are the same as in (5.7) and (6.10). The SMC profiles of the solutions of s as a function of x in Figure 7.2d show that s increases in the intima over time and that the density of SMCs is highest near the $x = 0$ boundary. This general SMC profile is the same as those observed in previous models. We perform the comparison of the steady state solution of s between base and zero values of ϵ_ρ and χ_{ms} in Figure 7.3d. We observe that due to the decrease in macrophage density near the $x = 0$ boundary due to the cell crowding term, the PDGF concentration in the intima is lower than when $\chi_{ms} = 0$. SMC proliferation, which is stimulated by PDGF, is therefore lower, leading to decreased SMC density near the $x = 0$ boundary.

The model equation for ρ (7.11) expands the model of the second reaction-diffusion model (5.8) by introducing macrophage dependency in the general ECM degradation term. The term is assumed to be proportional to ρ, the non-linear rate function $\beta_\rho(m)$ and a function dependent on T. As explained in Section 7.2.4.1, the value of the scaling parameter ϵ_ρ used in $\beta_\rho(m)$ was set to $\epsilon_\rho = 20.0$ to yield appropriate results. The ECM profile for the solution of ρ as a function of x in Figure 7.2e shows that over time, ECM increases and accumulates largely near the $x = 0$ boundary. This suggests the formation of a cap, which we also observed in the base ECM profile of the second reaction-diffusion model (Figure 5.7b). The solution comparisons of ρ in Figure 7.3e show the effect of both χ_{ms} and ϵ_ρ on the dynamics of ρ. We note that because cell crowding leads to decreased macrophage density and therefore decreased SMC density, the rate of ECM synthesis is smaller. This leads to decreased ECM density in regions where SMC density is lower. The non-linear rate function $\beta_\rho(m)$ is a function of m that increases monotonically with m as observed in Figure 7.1. As macrophage density is non-zero, the scale of the ECM degradation term is therefore greater for all non-zero values of ϵ_ρ. These two factors lead to a decrease in ECM density when $\chi_{ms} = 0.5$ and $\epsilon_\rho = 20.0$, though these new elements do not change the distribution of ECM and the formation of a cap around the $x = 0$ boundary.

The base case results therefore show that the general dynamics of the model variables observed in previous reaction-diffusion models are continued to be observed in this combined model. The reaction-diffusion model is therefore able to integrate and expand the previous model equations. Three main changes were made: increasing the value of α_m, introducing macrophage dependence to the non-linear rate function $\beta_\rho(m)$, and introducing a constraint term for macrophage dispersion due to cell

crowding at rate χ_{ms}. The steady state solution comparison figures showed effects of the above changes to the dynamics of the model variables. To understand the relative contribution of these changes, we perform parameter sensitivity analysis on three key parameters: α_m, χ_{ms} and ϵ_ρ.

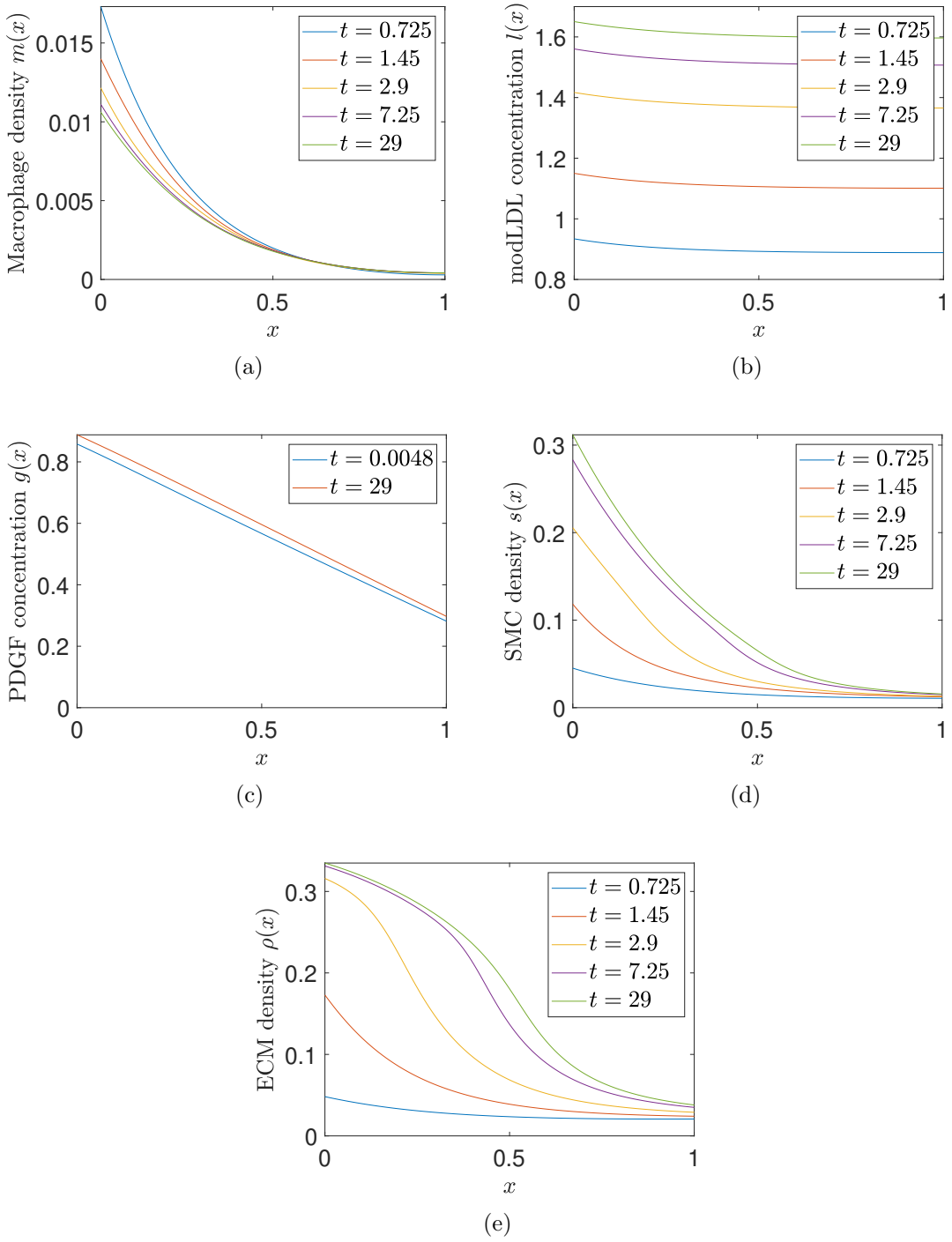

Figure 7.2: Solutions of (a) m, (b) l, (c) g, (d) s and (e) ρ as functions of x with parameter values from Table 7.1 at times t from $t = 0.0$ to 29.0.

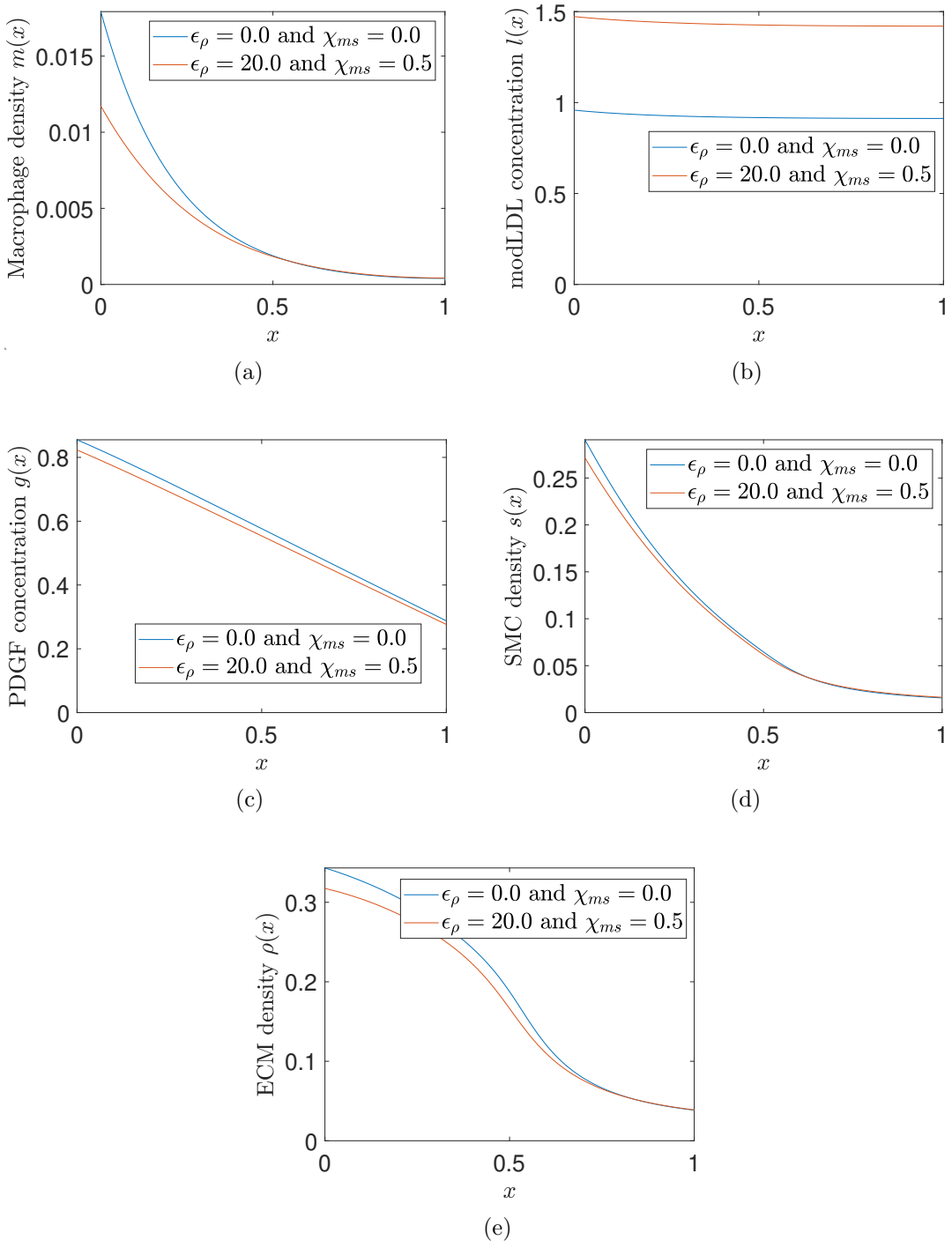

Figure 7.3: Comparisons of steady state solutions of (a) m, (b) l, (c) g, (d) s and (e) ρ for parameter values $\epsilon_\rho = 0.0$ and $\chi_{ms} = 0.0$, and $\epsilon_\rho = 20.0$ and $\chi_{ms} = 0.5$ at $t = 29.0$.

7.3.1 Parameter sensitivity

We perform parameter sensitivity analysis on three key parameters: α_m, χ_{ms} and β_ρ. A key consideration in the analysis is the effect of these parameters on cap

formation. In the analysis in Section 5.4.2, SMC distribution and density were identified as being critical to a larger fibrous cap region. With the introduction of m to the dynamics of ρ, we analyse the effects of macrophages on the formation of a cap region.

7.3.1.1 α_m

In the third reaction-diffusion model, the rate of macrophage influx into the intima α_m was determined to affect the density and spatial distribution of macrophages in the intima (Section 6.4.1.1). This is also observed in our integrated reaction-diffusion model in the macrophage steady state solution profiles in Figure 7.4a. When $\alpha_m = 0.4$, the influx of macrophages is insufficient to overcome two factors: the loss of macrophages due to decay and the constraint on macrophage dispersion due to space competition with SMCs. The value of m therefore decreases to near zero in the intima. For sufficiently high values of α_m such as our base case value $\alpha_m = 1.0$, we observe macrophages distributed in the intima with the greatest distribution near the $x = 0$ boundary. When α_m is increased to $\alpha_m = 2.0$, the increased macrophage influx lead to greater m near the $x = 0$ boundary than the value for the base value of α_m as the rate of macrophage influx at the boundary is greater.

The modLDL profile of the steady state solutions of l in Figure 7.4a shows that for increasing values of α_m, the steady state solution of l decreases.

There are no changes in parameter values from (6.9) in the model equation for g (7.9). Figure 7.4d shows that for increasing values of α_m, the magnitude of g increases in the intima due to increased PDGF production.

The dynamics of s in equation (7.10) are dependent on g and $\frac{\partial g}{\partial x}$ for proliferation and chemotaxis of SMCs at the $x = 1$ boundary in (7.13). They are also dependent on m due to the apoptosis decay term proportional to apoptosis rate d_{sm} and m. Figure 7.4b shows that the magnitude and spatial distribution of the steady state solutions of s increase with greater values of α_m.

The general loss term for ECM in the model equation for ρ (7.2) is proportional to the non-linear degradation rate function $\beta_\rho(m)$, ρ and a function dependent on T. We recall that in the results of the second reaction-diffusion model (Section 5.4.2.3), the distribution of s was observed to determine the distribution of ρ. The ECM profile of the steady solutions of ρ in Figure 7.4e shows that this no longer holds. When the value of α_m is increased, we observe that the value of ρ near the $x = 0$ boundary decreases. The value of ρ is greater in the approximate region $0.2 < x < 0.9$ when $\alpha_m = 0.9$ compared to when $\alpha_m = 0.4$, and there is a negligible difference in the value of ρ in that region when $\alpha_m = 0.9$ compared to when $\alpha_m = 2.0$. We note that Figure 7.4b show that the steady state solutions of s increase with greater values of α_m; the values of ρ do not increase proportionally.

This is due to the general loss term. The values of m, and therefore the effect of the general loss term, are greatest near the $x = 0$ boundary as shown in Figure 7.4a.

The synthesis of ECM due to SMCs in (7.2) is insufficient to overcome the effect of the general loss term. The synthesis term is also constrained by the source limiting function (5.23) and is therefore weaker when ρ is greater than approximately $\rho > 0.1$. This changes as the value of m decreases away from the $x = 0$ boundary, resulting in greater values of ρ in the approximate region $0.2 < x < 0.9$. In the approximate region $0.9 < x \leq 1.0$ however, the value of s is very similar for the three values of α_m in Figure 7.4b while the values of m are greater for larger values of α_m in Figure 7.4a. The effect of the synthesis term is therefore similar for all three solutions of ρ but the effect of the general loss term increases as α_m increases. The change in the total quantity of intimal ECM for the three values of α_m is shown in Figure 7.5: while the total quantity of intimal ECM is larger when $\alpha_m = 0.9$ compared to when $\alpha_m = 0.4$, it is also larger compared to when $\alpha_m = 2.0$.

These results suggest that too many macrophages may lead to a reduction in ρ in the intima as the general loss term becomes more dominant than the synthesis term. This suggests that increasing the rate of macrophage influx, which we observed to lead to more SMCs in the intima, does not necessarily lead to more ECM. We note however that all three solutions demonstrate the formation of an ECM cap region near $x = 0$. Therefore macrophages stimulate PDGF production, which in turn drives SMC proliferation and leads to SMCs accumulate near the endothelial boundary. ECM also accumulate near the boundary but at a decreased rate, not only due to the cell crowding simulated by the source limiting function, but also due to the presence of macrophages near this boundary which degrade ECM.

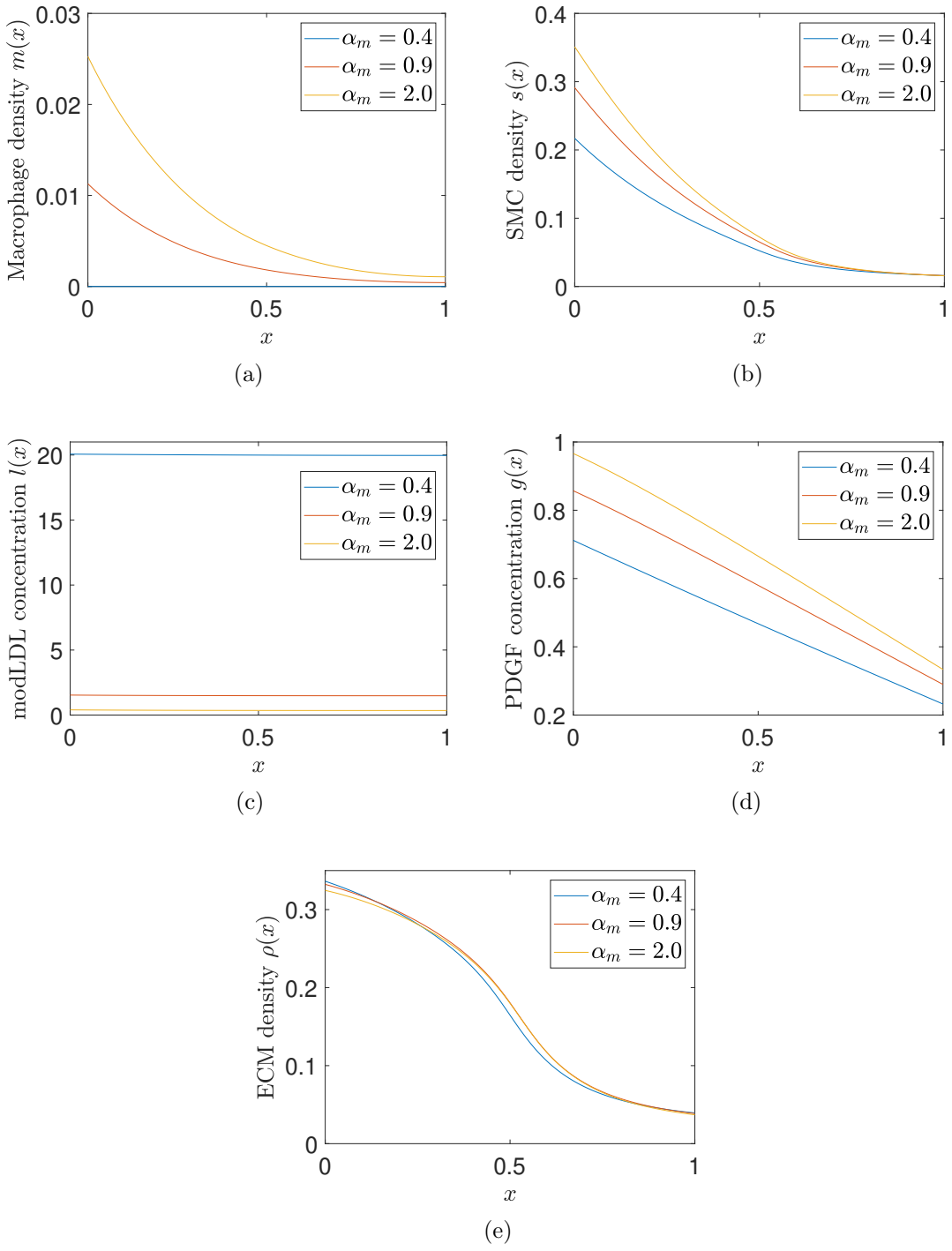

Figure 7.4: Comparisons of steady state solutions of (a) m, (b) s, (c) l, (d) g and (e) ρ for three values of α_m : $\alpha_m = 0.4$, 0.9 and 2.0 at $t = 29.0$.

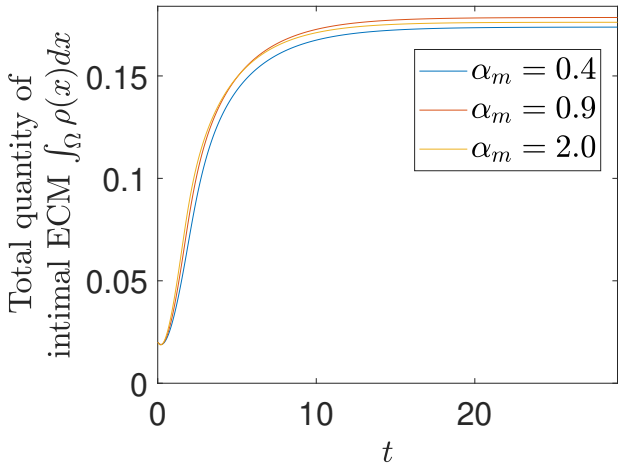

Figure 7.5: Time evolution of the total quantity of intimal macrophages $\int_\Omega m(x)dx$ with three values of α_m : $\alpha_m = 0.4$, 0.9 and 2.0 from $t = 0.0$ to 29.0.

7.3.1.2 χ_{ms}

Figure 7.7a shows the steady state solutions of m for three different values of χ_{ms}. Because macrophages compete with SMCs for space, their distribution decreases near $x = 0$ where SMC density is greatest because the effect of the cell crowding term increases. Increasing values of χ_{ms} therefore increases the effect of the cell crowding term and leads to lower m near the $x = 0$ boundary. We note that the effect of χ_{ms} on the distribution of macrophages is limited to regions of high SMC density, and that from the approximate region $0.6 < x < 1.0$, macrophage density is equal. We contrast this to the effect of varying α_m observed in Section 7.3.1.1, where increasing α_m lead to greater macrophage density across the domain.

As χ_{ms} increases, the gradient of m at $x = 0$ becomes smaller as shown in the steady state solution of m when $\chi_{ms} = 0.9$ (Figure 7.7a). For larger values of χ_{ms} the gradient approached zero at values (Figure 7.6 shows the steady state solution of m for $\chi_{ms} = 1.9$) and macrophage density becomes very low. For values of $\chi_{ms} > 2.0$, we observed issues with the numerical scheme, which may be due to numerical instability as the sign of the gradient changed. Investigation of this issue was beyond the scope of the thesis. The results nonetheless demonstrate that increasing values of χ_{ms} increases the effect of the cell crowding term and leads to lower m near the $x = 0$ boundary.

Figure 7.7b shows that increasing values of χ_{ms} lead to greater values of modLDL concentration.

The changes in the spatial distribution of macrophages near the $x = 0$ boundary affect the PDGF production by macrophages term in the model equation for g (7.9). Figure 7.7c shows lesser PDGF concentration as χ_{ms} increases due to decreasing macrophage density near $x = 0$. We note that the difference in PDGF concentration between the steady state solutions is small.

The decrease in PDGF concentration as χ_{ms} increases leads to decreased SMC proliferation. In the results of the third reaction-diffusion model (Section 6.4.1.2), we determined that changes to macrophage density have a weak direct effect on SMC density, and that changes to PDGF concentration have a more important effect on SMC dynamics due to proliferation and chemotactic movement. SMC density in the intima is therefore lower as shown in Figure 7.7d. The minor differences in s between the solutions is due to the small differences in g observed in Figure 7.7c.

The ECM steady state solutions in Figure 7.7e show minor changes to the ECM profile. ECM aggregation remains greatest at the $x = 0$ boundary showing a cap region. Near $x = 0$ (in the approximate $0 \leq x < 0.2$ region), we observe greater ECM density for larger values of χ_{ms}. This is because the rate of ECM proliferation remains similar for the three values of χ_{ms} due to the minor differences in s observed in Figure 7.7d, while the effect of the ECM degradation term decreases due to lower macrophage density observed near $x = 0$ in Figure 7.7a. Beyond the approximate $0 \leq x < 0.2$ region, we observe that the differences ECM density between the solutions are marginal as differences in macrophage density and the effect of the ECM degradation term become smaller. The scale of the differences in the ECM steady state solution shows that changes to χ_{ms} have a weak effect on the dynamics of ρ, and that changes to macrophage density alone have a minor effect on ECM density.

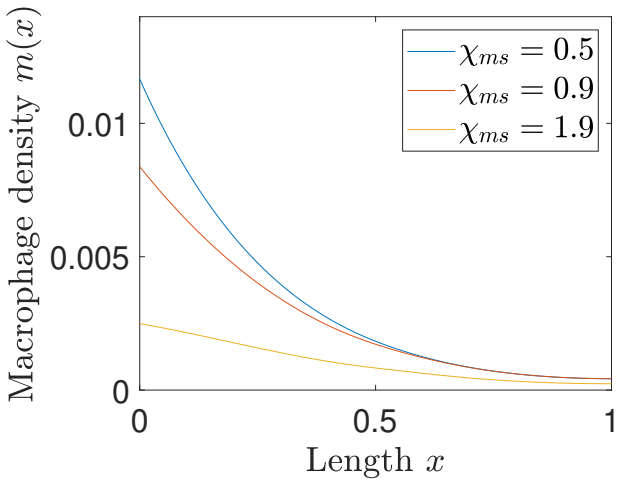

Figure 7.6: Comparisons of steady state solutions of m for three values of χ_{ms} : $\chi_{ms} = 0.5$, 0.9 and 1.9 at $t = 29.0$.

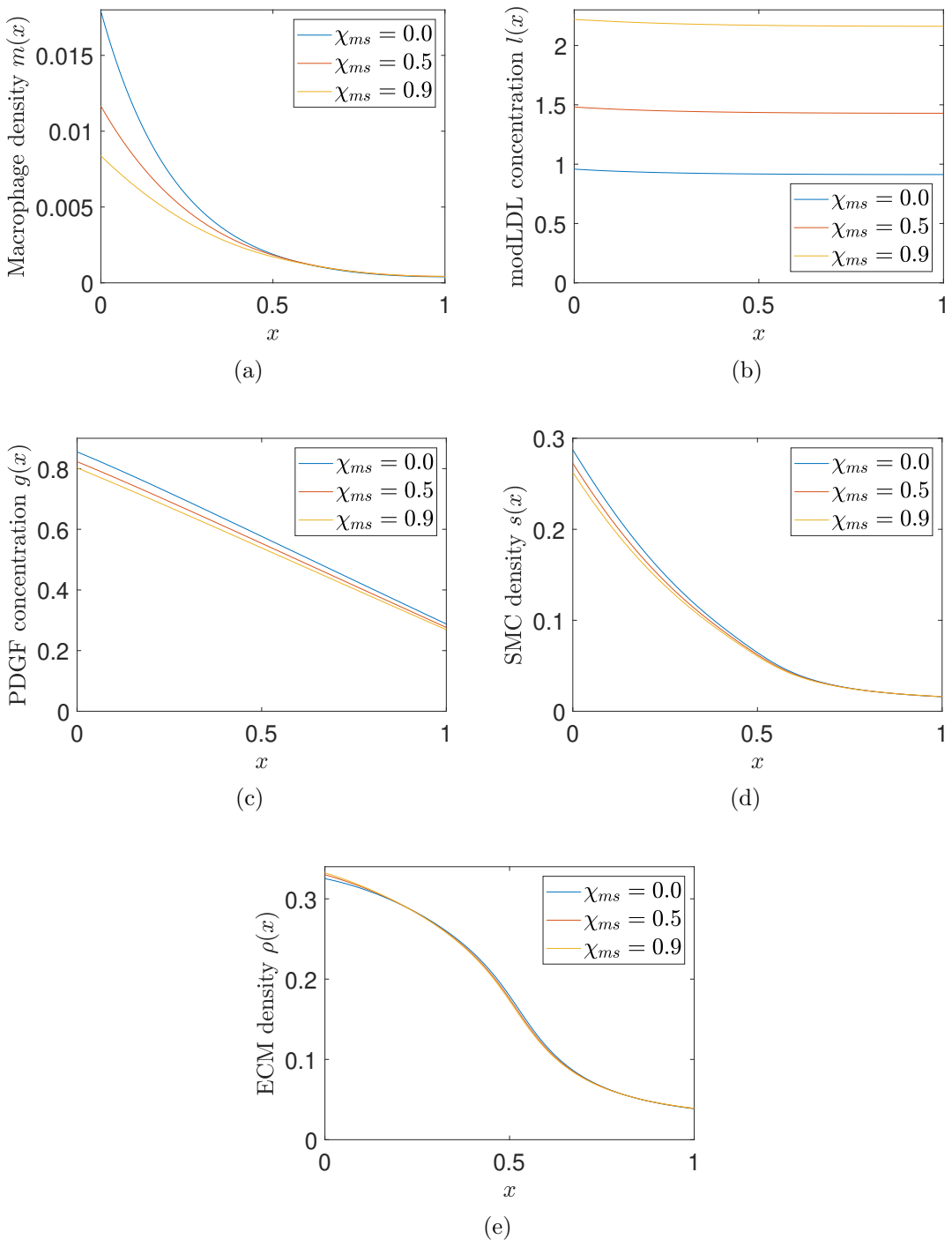

Figure 7.7: Comparisons of steady state solutions of (a) m, (b) l, (c) g, (d) s and (e) ρ for three values of χ_{ms} : $\chi_{ms} = 0.0$, 0.5 and 0.9 at $t = 29.0$.

7.3.1.3 ϵ_ρ

We have already observed the effects of changes to macrophage density on the general ECM degradation term (7.2) in Sections 7.3.1.1 and 7.3.1.2. The scaling parameter ϵ_ρ affects the strength of the general ECM degradation term. Our parameter analysis

of h_ρ in the second reaction-diffusion model (Section 5.4.2.2) showed that changes to ρ have a weak effect on the dynamics of s. Changes to s and m due to varying ϵ_ρ are therefore minimal, so we focus on the dynamics of ρ. Figure 7.8 shows the steady state solutions of ρ when ϵ_ρ is varied. We observe that when ϵ_ρ is increased, ECM density decreases. This decrease is greatest near the $x = 0$ boundary because macrophage density is highest around $x = 0$ and the effect of the degradation term decreases by order 2 as macrophage density decreases. The ECM profile is preserved when ϵ_ρ changes however, with the greatest aggregation of ECM near the $x = 0$ forming a cap region.

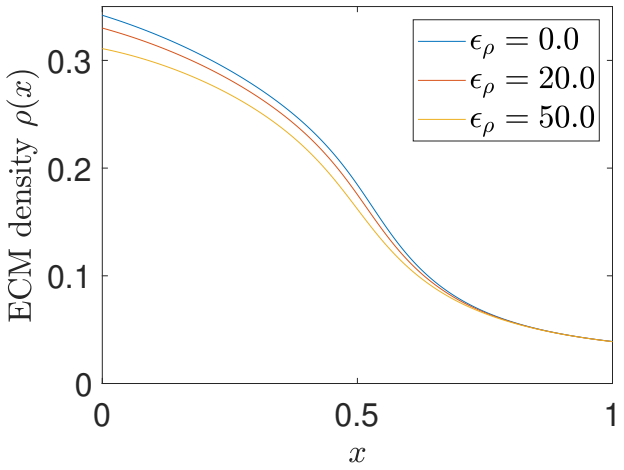

Figure 7.8: The steady state solutions of ρ with three values of ϵ_ρ : $\epsilon_\rho = 0.0$, 20.0 and 50.0 at $t = 29.0$.

7.4 Discussion

In this model we aimed to combine the three previous reaction-diffusion models and model all three stages of cap formation: lesion initiation, SMC migration and collagen synthesis. This allows us to provide a continuous depiction of early lesion initiation to the intermediate stage of collagen synthesis. To accurately represent these stages, the model must therefore reflect the base dynamics of the model variables analysed in the previous models. We retained the same non-dimensionalisation (Section 7.2.3) and parameter values (Section 7.3.1) that were used in the previous reaction-diffusion models, with exceptions to this being parameters that were changed in value to accommodate new assumptions and parameters.

The results of the base case solution in Section 7.3.0.1 showed that for all model variables, the base dynamics observed in the base case solutions of the previous reaction-diffusion models (Sections 5.4.1 and 6.4.0.1) were continued to be observed in the combined reaction-diffusion model. For example, we consider the model variables in the lesion initiation and SMC migration stage. An increase in macrophage density led to a corresponding decrease in modLDL concentration due to increased modLDL uptake, and an increase in PDGF concentration due to more PDGF being

produced by macrophages in total. This increase in PDGF concentration in the intima corresponded to an increase in SMC proliferation and chemotactic movement. The solution profiles of SMCs show that the aggregation of SMCs is greatest near the endothelial boundary, forming a fibrous cap as required. These dynamics, and the profiles of the model variable solutions, are consistent with those observed in the base case results (Section 6.5) for the third reaction-diffusion model.

The new assumption of the model in this chapter was that SMCs constrain macrophage spatial dispersion due to cell crowding. We observed in the parameter sensitivity analysis of χ_{ms} (Section 7.3.1.2) that when the taxis term χ_{ms} was non-zero, macrophage aggregation decreased in regions of high SCM density (near the endothelial boundary). The rate of macrophage influx α_m was increased to accommodate the reduction in macrophage density due to crowding by SMCs. The macrophage solution profiles however show that macrophage aggregation remains greatest near the $x = 0$ boundary which is consistent with the profile observed in Section 6.4.0.1.

We amended the model equation for ρ by introducing macrophage density dependence to the ECM degradation term in the collagen synthesis stage. The analysis of ECM solution profiles in Sections 7.3.0.1 and 7.3.1 showed that while the macrophage dependence introduces new dynamics, the general pattern of ECM aggregation near the endothelial boundary and the formation of a cap region are preserved. We recall that the parameter sensitivity analysis of α_g in the second reaction-diffusion model (Section 5.4.2.3) showed that the distribution of s was critical to determining the distribution of ρ. This was shown to no longer hold in this integrated reaction-diffusion model (Section 7.3.1.1). While greater macrophage density stimulated further PDGF production and therefore SMC proliferation which led to increased ECM synthesis, greater macrophage density also increased ECM general degradation. The total quantity of intimal ECM increased with increasing macrophage density up to a certain point, after which it fell as the ECM degradation term became dominant. Our model therefore suggests that while macrophage density is another factor in SMC proliferation and ECM synthesis, high macrophage density may lead to a reduction in overall ECM as loss becomes greater than synthesis. The parameter sensitivity analysis of ϵ_ρ demonstrated this by showing how increasing the value of ϵ_ρ increased the effect of the general degradation term, leading to a reduction in ECM density. We note however that the ECM solution profiles in our results all show the highest aggregation of ECM near the $x = 0$ boundary, forming a cap region. The parameter analysis of χ_{ms} and ϵ_ρ showed that the ECM cap region is maintained as these parameters vary, though the extent of their effects on the dynamics of ρ differ. These results are significant because they show that the model can be extended to include new assumptions and dependencies yet retain the core dynamic of ECM cap formation.

Changes to the model equations for the stages of cap formation demonstrate key dynamics observed in the previous models: the model reflects up-to-date assumptions and observations from the reference models. We concluded in the previous two reaction-diffusion models (Sections 5.5 and 6.5) that the base reaction-diffusion model framework can be extended to include new assumptions and dependencies. The results of this integrated reaction-diffusion model in this chapter confirm these conclusions and continue the thesis objective of creating an extendable reaction-

diffusion model by showing that the model can combine a number of different effects without changing its key dynamics.

Chapter 8

Describing late stage plaque formation by modelling foam cells and debris characteristics

The previous four reaction-diffusion models described three main stages of cap formation: lesion initiation, SMC migration and collagen synthesis. In the previous chapter 7, the reaction-diffusion model was identified as being able to model an increasing number of stages without significant complexity and issues. We therefore extend the model to consider the final stage: the formation of the necrotic lesion core. Our interest in the other three stages of cap formation was the dynamics involved in the process of cap formation; the main interest in this stage is the necrotic core's position in the intima and its effects on plaque rupture.

We assume that macrophages uptake modLDL within the intima, and that macrophages that have consumed a large amount of modLDL will become classified as macrophage foam cells. Foam cells retain some of the same characteristics as macrophages, such as MMP expression, but are assumed to be larger and less motile and to stop consuming modLDL. These foam cells accumulate in the intima, forming a lesion core. The foam cells die and break down to form dead cells and debris. This breakdown releases the internalised lipids, forming an extra-cellular lipid pool. As a result, the lesion core, comprised of macrophage foam cells, extra-cellular lipids and debris, becomes a necrotic core. This necrotic core is formed under the fibrous cap of ECM and SMCs.

The aim of this model is to therefore model the necrotic core formation stage, and capture all four main stages of plaque formation. We analyse the dynamics of foam cells and debris in the formation of the necrotic lesion core as well as the effects of newly-introduced interdependencies.

8.1 Necrotic core formation: two different reference models (Chalmers *et al.* (2017) and Ougrinovskaia (2011))

To model the necrotic core formation stage, we review two reference models: Chalmers *et al.* (2017) [10] and Ougrinovskaia (2011) [37]. We compare assumptions and terms used to model the mechanisms of the creation of the lesion and necrotic core.

8.1.1 Foam cell generation and macrophage uptake of modLDL: Chalmers *et al.* (2017)

The model of Chalmers *et al.* (2017) describes the necrotic core formation stage by considering a lesion core that does not contain necrotic tissue such as debris. We focus on three main variables of the model: modLDL, macrophages and foam cells. We note that Chalmers' model also considers HDL and its anti-inflammatory properties, which is beyond the scope of our current model. ModLDL concentration, macrophage density and foam cell density is denoted by $l(x,t)$, $m(x,t)$ and $N(x,t)$ respectively. Though this model is distinct from the earlier model of Chalmers *et al.* (2015) [11], a number of assumptions are shared between the two models. These include the flux boundary conditions and the functions used to describe modLDL uptake by macrophages.

ModLDL is assumed to diffuse through the intima. It is consumed by macrophages at a rate proportional to modLDL concentration and macrophage density. This consumption is assumed to saturate for high levels of modLDL concentration and is modelled as a Michaelis-Menten kinetic function. ModLDL also undergo chemical decay, which is modelled by a linear term. These assumptions are captured in the three terms on the right hand side of the model equation for l:

$$\frac{\partial l}{\partial t} = D_l \frac{\partial^2 l}{\partial x^2} - \mu_l \frac{ml}{1+l} - d_l l. \tag{8.1}$$

Macrophages are assumed to undergo random motion and chemotactic migration, moving chemotactically up the gradient of modLDL. This is described in the first two right hand side terms of (8.2). Macrophages consume modLDL and convert to foam cells at a rate proportional to consumption rate μ_m, local macrophage density and a saturating Michaelis-Menten kinetic function with respect to modLDL concentration. Because the model considers HDL and its anti-inflammatory effects, it assumes that foam cells convert back to macrophages due to HDL facilitating reverse cholesterol transport (RCT) from foam cells. This is assumed to be proportional to the rate that HDL removes lipid from foam cells, which is given by the proportion Θ of foam cells, the local foam cell density and a saturating Michaelis-Menten kinetic function with respect to HDL concentration. Finally, macrophages are assumed to die linearly. These assumptions give the last three terms on the right hand side of the model equation for m:

$$\frac{\partial m}{\partial t} = D_m \frac{\partial^2 m}{\partial x^2} - \chi_m \frac{\partial}{\partial x}\left(m \frac{\partial l}{\partial x}\right) - \mu_m \frac{ml}{1+l} + \Theta \nu_N \frac{hN}{\kappa + h} - d_m m. \tag{8.2}$$

Foam cells are assumed to undergo random motion. The rate of foam cell production is the same as the rate of macrophage loss in (8.2) due to macrophage conversion. They are assumed to revert to macrophages at the same rate of foam cell conversion due to RCT described in (8.2). The model equation for N is therefore:

$$\frac{\partial N}{\partial t} = D_N \frac{\partial^2 N}{\partial x^2} + \mu_m \frac{ml}{1+l} - \Theta \nu_N \frac{hN}{\kappa + h}. \tag{8.3}$$

The flux boundary conditions for macrophages and modLDL are the same as those (6.2) in Chalmers *et al.* (2015). At $x = 0$, modLDL influx is assumed to be constant and macrophage influx is proportional to a Heaviside function $H(p - P_0)$ where P_0 is the concentration of monocyte chemoattractant in the lumen of the artery. ModLDL influx is therefore assumed to stop once the monocyte chemoattractant concentration at the endothelial boundary reaches, or surpasses, that of P_0. Zero flux boundary conditions are assumed at $x = 1$ for both macrophages and modLDL. For foam cells, zero flux boundary conditions are assumed at both boundaries. The boundary conditions are therefore:

$$\begin{aligned} &\frac{\partial l}{\partial x} = -\sigma_l \text{ at } x = 0, && \frac{\partial l}{\partial x} = 0 \text{ at } x = 1, \\ &D_m \frac{\partial m}{\partial x} - \chi_m m \frac{\partial l}{\partial x} = -\sigma_m H(p - P_0) \text{ at } x = 0, && D_m \frac{\partial m}{\partial x} = \chi_m m \frac{\partial l}{\partial x} \text{ at } x = 1, \\ &\frac{\partial N}{\partial x} = 0 \text{ at } x = 0, && \frac{\partial N}{\partial x} = 0 \text{ at } x = 1. \end{aligned} \tag{8.4}$$

The key points of interest in these equations are therefore the term describing macrophage conversion and the zero flux boundary conditions for foam cells. We compare these assumptions with those held in the model equations of Ougrinovskaia (2011) in the next section.

8.1.2 Lesion initiation and smooth muscle cell migration: Ougrinovskaia (2011)

The reaction-diffusion model of Ougrinovskaia (2011) which is described in Section 4.1.2 of this thesis includes a submodel that describe the formation of the fibrous cap over an extra-cellular lipid pool core. From the equations of that submodel, we focus on the model equations for the following variables: modLDL concentration $l(x, t)$, macrophage density $m(x, t)$, collagen density $c(x, t)$, foam cell density $N(x, t)$ and debris density $d(x, t)$. These model equations have many of the same assumptions as the model equations described in that section.

ModLDL are assumed to diffuse through the domain, and are uptaken by macrophages via Michaelis-Menten dynamics at a rate proportional to the uptake rate μ_l and undergo linear decay. We note that the uptake term is modelled in the same manner (8.1) as in Chalmers *et al.* (2017). The model equation for l is therefore:

$$\frac{\partial l}{\partial t} = D_l \frac{\partial^2 l}{\partial x^2} - \left(\frac{\mu_l l m}{1 + l}\right) - d_l l. \tag{8.5}$$

Macrophages undergo random motion and chemotaxis, moving chemotactically along the gradient of the macrophage chemoattractant p with respect to chemotaxis coefficient χ_m. Due to the consumption of modLDL, macrophages convert to foam cells at a rate proportional to the consumption rate μ_m, local macrophage density and a saturating Michaelis-Menten kinetic function with respect to modLDL concentra-

tion. We note that this term is also described in the same manner as the model equation for macrophage density (8.2) in Chalmers *et al.* (2017). Macrophages are also assumed to undergo apoptosis and necrosis, which is assumed to be linearly proportional to macrophage density. The model equation for m is therefore:

$$\frac{\partial m}{\partial t} = D_m \frac{\partial^2 m}{\partial x^2} - \chi_m \Big(\chi_m m \frac{\partial p}{\partial x} \Big) - \Big(\frac{\mu_m l m}{1 + l} \Big) - d_m m. \tag{8.6}$$

In our reaction-diffusion model, we describe the collagenous cap by modelling the dynamics of plaque ECM. The reaction-diffusion model of Ougrinovskaia (2011) instead models the dynamics of collagen in the ECM. Collagen is assumed to be immotile and synthesised by SMCs that are activated by PDGF. This is modelled in the first right-hand side term of (8.7) by a function of SMC density ($s(x,t)$), collagen density and PDGF concentration ($g(x,t)$). The final right-hand side term describes the degradation of collagens by collagen-degrading MMPs [3, 24, 38]. We note that this is proportional to macrophage density. This is because in this model, foam cells are assumed to remain a macrophage cell type and therefore exhibit some of the same behaviours, including secreting collagen-degrading MMPs. The model equation for c is:

$$\frac{\partial c}{\partial t} = \Big(\frac{k_c l s}{R_c^2 + c^2} \Big) - d_c (m + N) c. \tag{8.7}$$

Foam cells are assumed to move randomly in the intima, though unlike the model equation for foam cell density (8.3) in the model of Chalmers *et al.* (2017), they are also assumed to be displaced by SCMs and macrophages. This is because foam cells are assumed to be larger and less motile due to consuming modLDL, meaning that SMCs and macrophages are able to physically displace them. Their displacement is therefore assumed to move them away from regions of high SMC and macrophage concentration, which is modelled as the second and third terms on the right-hand side of equation (8.8). In the second last right-hand side term, the production of foam cells is assumed to be due to the uptake of modLDL by macrophages and foam cells. We note that this foam cell production term is different to that in (8.3), where foam cell production was assumed to be due to the conversion of macrophages uptaking modLDL only. In this model equation, foam cell density is assumed to increase as foam cells continue to consume modLDL and foam cell volume increases. The rate of foam cell production is therefore assumed to be proportional to a saturating Michaelis-Menten kinetic function with respect to modLDL concentration and both macrophage and foam cell density. The final right-hand side term describes the linear death of foam cells. The model equation for N is therefore:

$$\frac{\partial N}{\partial t} = D_N \frac{\partial^2 N}{\partial x^2} + \rho_S \frac{\partial}{\partial x}(N \frac{\partial s}{\partial x}) + \rho_N \frac{\partial}{\partial x}(N \frac{\partial m}{\partial x}) + \Big(\frac{\mu_l l (m + N)}{1 + l} \Big) - d_N N. \tag{8.8}$$

Debris is assumed to be the direct product of foam cell death. It is assumed to be immotile, and has no other sources of production and is not removed from the system. The model equation for d is therefore:

$$\frac{\partial d}{\partial t} = d_N N. \tag{8.9}$$

Zero flux boundary conditions are assumed at both boundaries for foam cells. Collagen and debris are assumed to be immotile. The boundary conditions are therefore:

$$\begin{aligned} &\frac{\partial l}{\partial x} = \frac{-\sigma_l}{D_l} \text{ at } x = 0, && \frac{\partial l}{\partial x} = 0 \text{ at } x = 1, \\ &\frac{\partial m}{\partial x} = -\frac{\sigma_m D_p + \chi_m m \sigma_p}{D_p D_m} \text{ at } x = 0, && \frac{\partial m}{\partial x} = 0 \text{ at } x = 1, \\ &\frac{\partial N}{\partial x} = 0 \text{ at } x = 0, && \frac{\partial N}{\partial x} = 0 \text{ at } x = 1. \end{aligned} \tag{8.10}$$

Both Ougrinovskaia (2011) and Chalmers *et al.* (2017) assume that foam cells are produced by macrophages uptaking modLDL and converting. They also assume zero flux boundary conditions at both boundaries for foam cells. We note three key differences between the two models. The first is the rate of foam cell production, which is assumed to be proportional to macrophage density in Chalmers *et al.* (2017) and both macrophage and foam cell density in Ougrinovskaia (2011). In our reaction-diffusion model, we adopt the simpler assumption in Chalmers *et al.* (2017) and do not assume that the uptake of modLDL by foam cells increases foam cell density. The second difference is that foam cells are assumed to be displaced by SMCs and macrophages in Ougrinovskaia (2011). We use this assumption in our reaction-diffusion model. This is because the displacement terms allow us to propose effects that SMCs and macrophages may have on the spatial distribution of foam cells. They also potentially produce more realistic distributions of necrotic cores deeper in the intima, away from the endothelium. We finally note that the model of Ougrinovskaia (2011) included collagen, which is assumed to be degraded by both macrophages and foam cells. We adopt this assumption, and change the ECM degradation term in our model equations to reflect the expression of MMPs by foam cells.

8.2 Model formulation and development

8.2.1 Model equations

8.2.1.1 Foam cells ($N(x,t)$)

Foam cells are macrophages which have ingested modLDL and acquired a significant amount of internalised lipid [4]. We assume they behave like other cells, including SMCs and macrophages. We assume that foam cells move randomly through the intima with the random movement coefficient D_N but are also less motile than SMCs or macrophages and are displaced by them. We model this by assuming that foam cells move away from regions of high SMC and macrophage density. This movement down the gradient of SMC and macrophage density is assumed to be at a rate governed by the coefficient χ_{sN} and χ_{mN} respectively. Foam cells are the result of macrophages consuming modLDL which we model by a saturating function of modLDL concentration and macrophage density governed by the parameter μ_m. The saturating kinetics are represented by a Michaelis–Menten-type function. We

assume that foam cells die linearly at rate d_N. We therefore model foam cell density within the intima by:

$$\frac{\partial N}{\partial \tau} = D_N \frac{\partial^2 N}{\partial x^2} + \frac{\partial}{\partial x}\Big(N\chi_{mN}\frac{\partial m}{\partial x} + N\chi_{sN}\frac{\partial s}{\partial x}\Big) + \frac{\mu_m l m}{\gamma_l + l} - d_N N. \tag{8.11}$$

8.2.1.2 Debris ($d(x,t)$)

Debris is created by the death and decay of foam cells, leading to a lipid-rich necrotic core, or equivalently an extra-cellular lipid pool core [3]. This core is not motile and we assume that debris does not move. We further assume that debris dynamics do not affect other variables. We therefore model debris density within the intima by:

$$\frac{\partial d}{\partial \tau} = d_N N. \tag{8.12}$$

8.2.1.3 Macrophages ($m(x,t)$)

The model equation for m in this chapter is an extension of the previous chapter's model equation (7.1). It assumes that macrophages move randomly, move chemotactically along the gradient of modLDLs and are displaced by SMCs. Macrophages experience general loss and cell death which is modelled by a linear death rate d_m.

Macrophages uptake modLDL to convert into foam cells. We model this as proportional to a saturating function with respect to modLDL concentration and macrophage density and at a rate μ_m. This term is the foam cell source term in (8.11). As explained in Section 2.5, macrophage-like trans-differentiated SMCs uptake modLDL to create foam cells [3,4,25]. Our model does not distinguish between macrophages of different origins. We therefore describe this uptake of modLDL by macrophage-like cells as part of the general uptake of modLDL by macrophages.

We model macrophage density within the intima by:

$$\frac{\partial m}{\partial \tau} = D_m \frac{\partial^2 m}{\partial x^2} - \frac{\partial}{\partial x}\Big(\chi_m m\frac{\partial l}{\partial x} - \chi_{ms} m\frac{\partial s}{\partial x}\Big) - \frac{\mu_m l m}{\gamma_l + l} - d_m m. \tag{8.13}$$

8.2.1.4 ECM ($\rho(x,t)$)

The model equation for ρ in this chapter is an extension of (7.2). We recall that foam cells are the result of macrophages uptaking modLDL; they are therefore still a macrophage cell type and express MMPs [3, 24, 38]. The degradation of ECM due to MMPs was included in the general ECM degradation term, which was modified in (7.2) to be proportional to the non-linear degradation rate function $\beta_\rho(m)$. This degradation rate function is modified to include foam cell dependence:

$$\beta_\rho(m, N) = \beta_\rho(1 + \epsilon_{\rho m} m + \epsilon_{\rho N} N)^2, \tag{8.14}$$

where β_ρ is the baseline rate of ECM degradation by immune cells and $\epsilon_{\rho m}$ and $\epsilon_{\rho N}$ are scaling parameters that represent the relative contributions of macrophages and foam cells to ECM degradation from the production of MMPs.

We therefore model the density of ECM within the intima by:

$$\begin{aligned}\frac{\partial \rho}{\partial \tau} =& r_s s\psi(\rho)\Big[1+\frac{A_s T}{c_s+T}\Big] - r_d s\rho\Big[1+\frac{A_d g}{(c_d+g)(1+\gamma_d T)}\Big] \\ &- \beta_\rho(m,N)\rho\Big[\frac{1+\epsilon\gamma_\rho T}{1+\gamma_\rho T}\Big].\end{aligned} \tag{8.15}$$

The first term describes the synthesis of ECM by SMCs proportionally to a baseline ECM production rate r_s, s, the source limiting function $\psi(\rho)$, and a kinetic growth term dependent on T with c_s representing the half-maximal rate and A_s representing the maximal factor of TGF-β stimulated ECM proliferation. The second term assumes that ECM is degraded by SMCs, which is modelled by a function dependent on s, g and T and proportional to a constant degradation term r_d. The last term represents the general degradation of ECM, which includes the degradation of ECM due to MMPs.

The equations for PDGF ($g(x,t)$), SMCs ($s(x,t)$), TGF-β ($T(x,t)$) and modLDL ($l(x,t)$) remain unchanged from (6.9), (6.10), (5.10) and (6.11) respectively.

8.2.2 Boundary and initial conditions

8.2.2.1 Foam cells ($N(x,t)$)

Foam cells move randomly through the intima with the random movement coefficient D_N. They are displaced by SMCs and macrophage, moving down the gradient of SMCs and macrophages at a rate governed by the coefficient χ_{sN} and χ_{mN} respectively. The foam cell flux is therefore:

$$J_N = -D_N\frac{\partial N}{\partial x} - N\Big(\chi_{sN}\frac{\partial s}{\partial x}+\chi_{mN}\frac{\partial m}{\partial x}\Big). \tag{8.16}$$

We assume that foam cells are unable to permeate the endothelial and medial boundary, which we describe as zero flux conditions at both $x=0$ and $x=1$. The boundary conditions are therefore:

$$\frac{\partial N}{\partial x}\Big|_{x=0} = -N\Big(\chi_{sN}\frac{\partial s}{\partial x}+\chi_{mN}\frac{\partial m}{\partial x}\Big), \quad \frac{\partial N}{\partial x}\Big|_{x=1} = -N\Big(\chi_{sN}\frac{\partial s}{\partial x}+\chi_{mN}\frac{\partial m}{\partial x}\Big). \tag{8.17}$$

We assume there are no foam cells in the intima before the onset of cap fibrosis. The initial condition is therefore zero: $N(x,0)=0$.

8.2.2.2 Debris ($d(x,t)$)

We assume no spatial movement for debris and no flux. No boundary conditions are required for $d(x,t)$. We assume that $d(x,0) = 0$.

The boundary conditions for PDGF, SMCs, TGF-β, modLDL and macrophages at $x = 0$ and $x = 1$ remain unchanged from (4.19), (5.11), (5.12), (6.13) and (7.5) respectively. The initial conditions for $s(x,0)$, $l(x,0)$ (described in (6.14)) and $m(x,0)$ (described in (6.16)) are also unchanged.

8.2.3 Non-dimensionalisation

We non-dimensionalise our model, using tildes (except for t) to denote non-dimensionalised quantities. The key parameters x, t, m, l, s, g, ρ and T are non-dimensionalised as:

$$t = \tau t_0, \quad x = L\widetilde{x}, \quad l = \gamma_l \widetilde{l}, \quad m = m_0 \widetilde{m}, \quad s = k\widetilde{s}, \quad g = g_0 \widetilde{g},$$
$$\rho = \rho_0 \widetilde{\rho}, \quad T = T_0 \widetilde{T}, \quad N = N_0 \widetilde{N}, \quad d = d_0 \widetilde{d},$$

where t_0 represents the characteristic time value, L the length of the domain, γ_l the saturation rate of modified LDL consumption, m_0 the characteristic macrophage density, k the total cell and tissue density, g_0 the characteristic PDGF concentration, ρ_0 the characteristic ECM density, T_0 the characteristic TGF-β concentration, N_0 the characteristic foam cell density, and d_0 the characteristic debris density.

The remaining model parameters are non-dimensionalised as:

$$
\begin{aligned}
&d_g = \frac{\widetilde{d}_g D_g}{L^2}\ , && \mu_g = \frac{\widetilde{\mu}_g g_0 D_g}{L^2 m_0}\ , && \alpha_g = \frac{\widetilde{\alpha} D_g g_0}{L}\ , && \sigma_g = \frac{\widetilde{\sigma} D_g}{L}\ ,\\
&D_s = \frac{L^2 \widetilde{D_s}}{t_0}\ , && d_s = \frac{\widetilde{d}_s}{t_0}\ , && G_s = \widetilde{G_s} g_0\ , && \chi_s = \frac{\widetilde{\chi_s} L^2}{t_0 g_0}\ ,\\
&r_{s0} = \frac{\widetilde{r_{s0}}}{t_0}\ , && \widetilde{A} = \frac{r_s}{r_{s0}}\ , && h_\rho = \frac{\widetilde{h_\rho} L^2}{t_0 \rho_0}\ , && \xi = \frac{\widetilde{\xi}}{\rho_0}\ ,\\
&d_{sm} = \frac{\widetilde{d_{sm}}}{t_0}\ , &&&&&&\\
&D_m = \frac{L^2 \widetilde{D_m}}{t_0}\ , && \chi_m = \frac{L^2 \widetilde{\chi_m}}{t_0 \gamma_l}\ , && \chi_{ms} = \frac{\widetilde{\chi_{ms}} L^2}{t_0 k}\ , && d_m = \frac{\widetilde{d_m}}{t_0}\ ,\\
&D_l = \frac{L^2 \widetilde{D_l}}{t_0}\ , && d_l = \frac{\widetilde{d}_l}{t_0}\ , && \alpha_m = \frac{\widetilde{\alpha_m} L}{t_0}\ , && \alpha_l = \frac{\widetilde{\alpha}_l L \gamma_l}{t_0}\ ,\\
&\mu_l = \frac{\gamma_l \widetilde{\mu}_l}{t_0}\ , &&&&&&\\
&r_s = \frac{\rho_0 \widetilde{r_s}}{k T_0}\ , && c_s = T_0 \widetilde{c_s}\ , && c_d = g_0 \widetilde{c_d}\ , && \gamma_d = \frac{\widetilde{\gamma_d}}{T_0}\ ,\\
&r_d = \frac{\widetilde{r_d}}{T_0}\ , && \gamma_\rho = \frac{\widetilde{\gamma_r h o}}{T_0}\ , && \beta_\rho = \frac{\widetilde{\beta_\rho}}{m_0 t_0}\ , &&\\
&\beta_T = \frac{D_T \widetilde{\beta_T}}{L^2}\ , && \alpha_T = \frac{D_T T_0 \widetilde{\alpha_T}}{L}\ , && \sigma_T = \frac{D_T \widetilde{\sigma_T}}{L} &&\\
&D_m = \frac{L^2 \widetilde{D_m}}{t_0}\ , && \chi_{mN} = \frac{L^2 \widetilde{\chi_{mN}}}{t_0 m_0}\ , && \chi_{sN} = \frac{\widetilde{\chi_{sN}} L^2}{t_0 k}\ , && \mu_m = \frac{\gamma_l \widetilde{\mu_m}}{t_0}\ ,\\
&d_N = \frac{\widetilde{d_N}}{t_0}\ , && \epsilon_{sN} = \frac{\widetilde{\epsilon_{sN}}}{N_0}\ , && \epsilon_{mN} = \frac{\widetilde{\epsilon_{mN}}}{m_0}\ . &&
\end{aligned}
\tag{8.18}
$$

Dropping the tildes for clarity, the model equations (6.11), (8.13), (8.15), (5.10), (6.9), (6.10), (8.11) and (8.12), and boundary conditions (6.13), (7.5), (5.12), (4.19), (5.11) and (8.17) become:

$$\frac{\partial l}{\partial \tau} = D_l \frac{\partial^2 l}{\partial x^2} - \frac{\mu_l l m}{1+l} - d_l l, \tag{8.19}$$

$$\frac{\partial m}{\partial \tau} = D_m \frac{\partial^2 m}{\partial x^2} - \frac{\partial}{\partial x}\Big(\chi_m m \frac{\partial l}{\partial x} - \chi_{sm} m \frac{\partial s}{\partial x}\Big) - d_m m, \tag{8.20}$$

$$0 = \frac{d^2 g}{dx^2} - d_g g + \mu_g m, \tag{8.21}$$

$$\begin{aligned}\frac{\partial s}{\partial \tau} =& D_s\frac{\partial^2 s}{\partial x^2} - \frac{\partial}{\partial x}\Big(\chi_s s\frac{\partial g}{\partial x} + h_\rho(\rho)s\frac{\partial \rho}{\partial x}\Big) + r_{s0}(1+\frac{Ag}{G_s+g})s(1-s) \\ & - d_s s - d_{sm}sm,\end{aligned} \tag{8.22}$$

$$\begin{aligned}\frac{\partial \rho}{\partial \tau} =& r_s s\psi(\rho(x))\Big[1+\frac{A_s T}{c_s+T}\Big] - r_d s\rho\Big[1+\frac{A_d g}{(c_d+g)(1+\gamma_d T)}\Big] \\ & - \beta_\rho(m,N)\rho\Big[\frac{1+\epsilon\gamma_\rho T}{1+\gamma_\rho T}\Big],\end{aligned} \tag{8.23}$$

$$0 = \frac{d^2T}{dx^2} - \beta_T T, \tag{8.24}$$

$$\frac{\partial N}{\partial \tau} = D_N\frac{\partial^2 N}{\partial x^2} + \frac{\partial}{\partial x}\Big(N\chi_{mN}\frac{\partial m}{\partial x} + N\chi_{sN}\frac{\partial s}{\partial x}\Big) + \frac{\mu_m l m}{\gamma_l + l} - d_N N, \tag{8.25}$$

$$\frac{\partial d}{\partial \tau} = d_N N. \tag{8.26}$$

with boundary conditions:

$$\begin{aligned}
&\frac{\partial m}{\partial x}\Big|_{x=0} = \frac{\frac{-\alpha_m l m}{1+l} + m\Big(\chi_m\frac{\partial l}{\partial x} - \chi_{sm}\frac{\partial s}{\partial x}\Big)}{D_m}, && \frac{\partial m}{\partial x}\Big|_{x=1} = 0,\\
&\frac{\partial l}{\partial x}\Big|_{x=0} = \frac{-\alpha_l}{D_l}, && \frac{\partial l}{\partial x}\Big|_{x=1} = 0,\\
&\frac{dg}{dx}\Big|_{x=0} = -\alpha_g, && \frac{dg}{dx}\Big|_{x=1} = -\sigma_g g,\\
&\frac{\partial s}{\partial x}\Big|_{x=0} = \frac{-\alpha_g\chi_s s}{D_s} + \frac{h_\rho}{1+\xi_\rho\rho}\frac{s}{D_s}\frac{\partial \rho}{\partial x}, && \frac{\partial s}{\partial x}\Big|_{x=1} = \frac{\chi_s\sigma_g g(s^*-s)}{D_s} + \frac{h_\rho}{1+\xi_\rho\rho}\frac{s}{D_s}\frac{\partial \rho}{\partial x},\\
&\frac{\partial N}{\partial x}\Big|_{x=0} = -N\Big(\chi_{sN}\frac{\partial s}{\partial x} + \chi_{mN}\frac{\partial m}{\partial x}\Big), && \frac{\partial N}{\partial x}\Big|_{x=1} = -N\Big(\chi_{sN}\frac{\partial s}{\partial x} + \chi_{mN}\frac{\partial m}{\partial x}\Big),\\
&\frac{\partial T}{\partial x}\Big|_{x=0} = -\alpha_T, && \frac{\partial T}{\partial x}\Big|_{x=1} = -\sigma_T T,
\end{aligned} \tag{8.27}$$

and initial conditions:

$$s(x,0) = s_0, \tag{8.28}$$

$$l(x,0) = \Big(\frac{-\alpha_l}{D_l\gamma} + \frac{\frac{\alpha_l}{D_l\gamma}}{1-\exp(-2\gamma)}\Big)\exp(\gamma x) + \Big(\frac{\frac{\alpha_l}{D_l\gamma}}{1-\exp(-2\gamma)}\Big)\exp(-\gamma x), \tag{8.29}$$

$$m(x,0) = \frac{m_0\sqrt{2}}{\sigma\pi}\exp\Big(-\frac{x^2}{2\sigma^2}\Big), \tag{8.30}$$

$$N(x,0) = 0, \tag{8.31}$$

$$d(x,0) = 0, \tag{8.32}$$

where s_0 is non-dimensional, $m_0 = 1.0\times10^{-4}$, $\sigma = 0.05$ and $\gamma = \sqrt{\frac{d_l}{D_l}}$. The

non-linear haptotaxis function $h(\rho)$ is the kinetic function:

$$h(\rho) = \frac{h_\rho}{1 + \xi_\rho \rho},$$

with scaling parameter ξ_ρ. The source limiting function $\psi(\rho)$ is:

$$\psi(\rho) = \frac{a^6}{a^6 + \rho^6}.$$

where $a = 0.3$. The general ECM degradation rate function $\beta_\rho(m, N)$ is:

$$\beta_\rho(m) = \beta_\rho(1 + \epsilon_{\rho m} m + \epsilon_{\rho N} N)^2, \tag{8.33}$$

where β_ρ is the baseline rate of ECM degradation by immune cells and $\epsilon_{\rho m}$ and $\epsilon_{\rho N}$ are scaling parameters.

8.2.4 Parameter values

Table 8.1: Base non-dimensionalised parameter values

Symbol	Definition	Value	Reference
d_g	Rate of PDGF decay	0.075	6.1
μ_g	Rate of production of PDGF by macrophages	10^1	6.1
D_s	Diffusion coefficient of SMC	1.0979	6.1
χ_s	SMC motility coefficient	4.5952	6.1
h_ρ	SMC haptotaxis coefficient	2.0	
r_{s0}	Baseline rate of SMC proliferation	0.02	6.1
d_s	Rate of SMC decay	0.4	6.1
d_{sm}	Rate of SMC apoptosis	0.2	6.3.4.1
G_s	Michaelis-Menten kinetic constant	1.4	6.1
A_s	Maximal factor of PDGF-stimulated increase in rate of SMC proliferation	19	6.1
α_g	Rate of PDGF influx from endothelium	0.55	6.1
σ_g	Permeability of IEL to PDGF	2	6.1
s_0	Initial SMC concentration	1×10^{-4}	6.1
s^*	Concentration of synthetic SMC in media	0.01	6.1
D_m	Diffusion coefficient of macrophages	10^{-1}	6.1
χ_m	Macrophage motility coefficient	10^{-1}	6.1
χ_{ms}	Macrophage dispersion constraint due to cell crowding motility coefficient	0.5	7.2.4.1
μ_m	Rate of macrophage conversion	10^1	8.2.4.1
d_m	Rate of macrophage decay	10^{-1}	6.1

Continued on next page

Table 8.1 – continued from previous page

Symbol	Definition	Value	Reference
D_l	Diffusion coefficient of LDLs	10^3	6.1
μ_l	Rate of LDL uptake by macrophages	10^5	6.1
d_l	Rate of LDL decay	10^1	6.1
α_l	Rate of LDL influx from endothelium	2×10^2	6.3.4.1
α_m	Rate of macrophage influx from endothelium	1.2	8.2.4.1
d_g	Rate of PDGF decay	0.075	6.1
r_s	Baseline rate of ECM phase synthesis by SMCs	1.8	5.1
c_s	Exponent in SMC phase pressure function	0.3	5.1
r_d	Baseline rate of ECM degradation by SMCs	1.5	5.1
A_d	Maximal factor of PDGF-stimulated increase in rate of ECM degradation by SMCs	4.0	5.1
c_d	PDGF concentration for half-maximal increase in rate of ECM degradation by SMCs	2.5	5.1
γ_d	Reciprocal of reference TGF-β concentration for inhibition of ECM degradation by SMCs	0.5	5.1
β_ρ	Baseline rate of ECM degradation by immune cells	0.75	7.2.4.1
$\epsilon_{\rho m}$	Scaling parameter for m of general ECM degradation rate function $\beta_\rho(m, N)$	20.0	7.2.4.1
$\epsilon_{\rho N}$	Scaling parameter for N of general ECM degradation rate function $\beta_\rho(m, N)$	20.0	8.2.4.1
γ_ρ	Reciprocal of reference TGF-β concentration for inhibition of ECM degradation by immune cells	10.0	5.1
ϵ	Maximal factor of TGF-β stimulated decrease in rate of ECM degradation by immune cells	0.25	5.1
β_T	Rate of TGF-β decay	20.0	5.1
α_T	Rate of TGF-β influx	2.5	5.1
σ_T	Permeability of IEL to TGF-β	4.0	5.1
D_N	Diffusion coefficient of foam cells	10^{-1}	8.2.4.1
χ_{sN}	Foam cell displacement by SMCs coefficient	10^{-1}	8.2.4.1
χ_{mN}	Foam cell displacement by macrophages coefficient	1.0	8.2.4.1

Continued on next page

Table 8.1 – continued from previous page

Symbol	Definition	Value	Reference
d_N	Rate of foam cell decay and debris production	2.5	8.2.4.1

8.2.4.1 Parameter value justification

The reaction-diffusion model introduces six new parameters: D_N, χ_{sN}, χ_{mN}, μ_m, d_N and $\epsilon_{\rho N}$. The remaining parameter values are mostly unchanged from the previous model (Section 7.2.3) except for α_m.

The parameter value of α_m is increased due to the assumption in the model equation for m (8.13) that macrophages convert into foam cells proportional to rate μ_m, Macrophages are therefore lost to conversion and cell death. The rate of macrophage influx is therefore increased to prevent macrophages density decreasing to unreasonably low values. The value of α_m is increased from the base value of $\alpha_m = 0.9$ in the previous reaction-diffusion model (Section 7.2.4.1) to $\alpha_m = 1.2$.

We note that the non-dimensionalisation and assumptions of the model equations for N and d differ from those in Chalmers *et al.* (2017) and Ougrinovskaia (2011). The parameter values used in those models are therefore not applicable. The values are instead chosen to maintain reasonable amounts of macrophages, ECM, foam cells and debris in the intima. We set $D_N = 10^{-1}$, $\chi_{sN} = 10^1$, $\chi_{mN} = 10^0$, $\mu_m = 10^1$, $d_N = 2.5$ and $\epsilon_{\rho N} = 20.0$.

8.3 Results

8.3.1 Base case simulation

The solutions of the model equations (8.19), (8.20), (8.21), (8.22) and (8.23) are solved with the parameter values from Table 8.1. We recall that the model equations represent the four stages of cap formation: lesion initiation, SMC migration, collagen synthesis and the necrotic core formation.

The model equation for m (8.20) is an extension of the previous chapter's equation for m (7.1). The assumptions held in (7.1) are continued in this model. Figure 8.1a shows that the pattern of macrophage dispersion is very similar to that observed in Figure 7.2a. Macrophage density increases over time, with the greatest aggregation of macrophages being near the endothelial boundary ($x = 0$). We note however that this model introduces the assumption that macrophages ingest modLDL and convert to foam cells, which is modelled in (8.13) by a saturating function of modLDL concentration and macrophage density governed by the parameter μ_m. The effect of this term is shown in Figure 8.2, where the steady state solution of m with $\mu_m = 10.0$ is compared against the steady state solution where $\mu_m = 0.0$. The

conversion of macrophages to foam cells leads to lower macrophage density across the intima, though the foam cell conversion term does not change the macrophage profile. The results therefore show that macrophages enter the intima at the endothelial boundary. They move randomly, migrate chemotactically up the modLDL gradient towards the endothelial boundary, and are displaced from regions of high SMC density due to cell crowding. These dynamics lead to macrophages accumulating near the endothelial boundary. In addition to undergoing decay, macrophages also convert to foam cells in the intima, leading to a decrease in macrophage density.

The solutions of N as a function of x at increasing times in Figure 8.1b show that foam cells rapidly form in the intima. The initial condition for N is $N(x,0) = 0$ and there is no influx of foam cells; the solution of N at $t = 1.45$ is greater than the solutions at later times. Foam cell density therefore rapidly increases then decreases over time until the solution of N reaches steady state. This decrease in foam cell density is due the decay of foam cells which is described linearly at rate d_N and the decrease in macrophage density over time. Foam cells are created by the conversion of macrophages to foam cells at the rate μ_m in the model equation for m (8.13). The macrophage profile in Figure 8.1a shows that macrophage density is greatest near the endothelial boundary meaning that macrophage conversion is greatest in this region. The foam cell profile in Figure 8.1b however shows that the local maximum is not at $x = 0$. This is due to the foam cell displacement terms in (8.13) which describe the displacement of foam cells from regions of high SMC and macrophage density at taxis rates χ_{sN} and χ_{sN} respectively. The SMC and macrophage profiles in Figures 8.1g and 8.1a show that SMC and macrophage density is greatest near the endothelial boundary. Foam cells are therefore displaced from this region and instead reach their maximum density at approximately $x = 0.2$. These results show that the creation of foam cells is dependent on macrophage density, though foam cell density is also affected by the displacement of foam cells near the endothelial boundary.

Debris is formed due to the death of foam cells. As described in the model equation for N (8.11), the death rate of foam cells is linearly proportional to d_N and foam cell density. The rate of debris production in the model equation for d (8.12) is equal to this death rate. The initial condition for d is $d(x,0) = 0$ and there is no influx of foam cells. Debris therefore accumulate in the intima over time until the profile is proportional to that of foam cells. The profiles of the steady state solutions of d and N at $t = 29.0$ in Figures 8.1c and 8.1b are qualitatively the same.

The model equation for ρ (8.15) is the same as the previous model's equation for ρ (7.2) except for the general ECM degradation term. The general ECM degradation term is proportional to the non-linear rate function $\beta_\rho(m, N)$, which was modified to be a function of foam cell density in (8.14) such that the effect of the term increases with foam cell density. Foam cell density is greatest in the region (near $x = 0.2$) shown in Figure 8.1b. We note that this region is different to the local maximum of m, which is at the endothelial boundary. The effect of this general ECM degradation term on the dynamics of ρ is shown in Figure 8.3, where ECM density decreases due to the increased degradation of ECM by both macrophage and foam cell expressed MMPs. With all other terms the same as the model equation for ρ (7.2) in the previous chapter's reaction-diffusion model, the ECM profile in Figure 8.1d shows

that the greatest aggregation of ECM is near the endothelial boundary. We therefore continue to observe a cap region near the endothelial boundary.

There are no changed assumptions or parameter values for the model equation for l (8.19), g (8.21) and s (8.22) from the model equations from the previous chapter's reaction-diffusion model. We therefore expect dynamics to be the same as those observed in 7.3.0.1. Figure 8.1e shows the solutions of l as a function of x at increasing times. The modLDL profile remains near constant, and modLDL concentration increases over time as macrophage density decreases and modLDL uptake is reduced. ModLDL therefore diffuses through the intima and is consumed by macrophages until the dynamics reach steady state. Figure 8.1f shows the solutions of g as a function of x at two times. PDGF concentration increases over time, with PDGF production being linearly proportional to macrophage density. The solutions of s as a function of x in Figure 8.1e show that SMC density increases over time. SMCs move randomly in the intima, also moving chemotactically along the gradient of PDGF and haptotactically along the gradient of ECM. This migration drives them towards the endothelial boundary. Their proliferation rate also depends on PDGF concentration which is greatest near the endothelial boundary. SMCs also continue to undergo cell death and cytokine-stimulated apoptosis [36]. SMC density is greatest near the endothelial boundary as shown in the SMC profiles in Figure 8.1e, which display the distribution required for the formation of a fibrous collagenous cap. We note that these dynamics are the same as those observed in the previous reaction-diffusion model (Section 7.3.0.1). Because the model equations for l, g and s are unchanged, the dynamics displayed in the results are also unchanged.

For the model equations that are unchanged from the previous reaction-diffusion model, the base case results show that the general dynamics of the model variables are very similar to those observed in Section 7.3.0.1. This is demonstrated in the solutions of l, g and s. The model equations for m, N, d and ρ however include new assumptions and changed parameter values. Macrophages are now assumed to convert to foam cells by consuming modLDL, meaning that the influx of macrophages must be increased to compensate for this loss. The macrophage profile however remains similar to that observed in the previous reaction-diffusion model, with the aggregation of macrophages being greatest near the endothelial boundary. The degradation of ECM due to MMPs is also assumed to be affected by foam cells, which as macrophage-like cells still express MMPs [3,24,38]. The ECM profile however shows that the formation of a collagenous cap near the endothelial boundary is not affected by the change. The reaction-diffusion model therefore maintains the general dynamics of the lesion initiation, SMC migration and collagen synthesis stages of cap formation.

The necrotic core formation stage is modelled by the inclusion of foam cells and debris. Foam cells are assumed to be the result of macrophages ingesting modLDLs, and are displaced by SMCs and macrophages. Debris is formed from dying foam cells, and is produced at a rate linearly proportional to foam cell density. This dependence on foam cell density results in the debris profile being similar to that of foam cells. To understand the effects of the parameters in the model equations for N and d, we perform parameter sensitivity analysis on certain parameters in the next section.

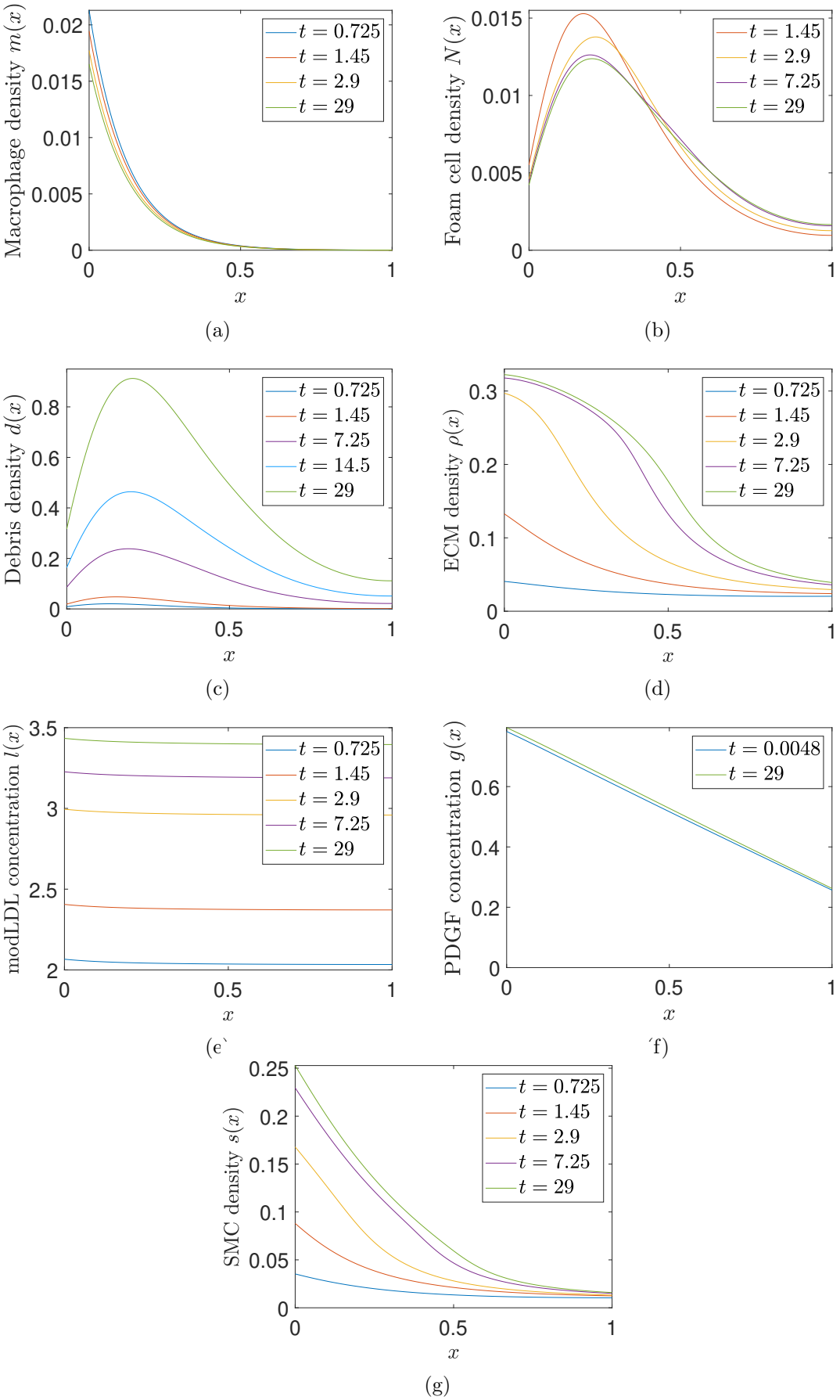

Figure 8.1: Solutions of (a) m, (a) m, (b) N, (c) d, (d) ρ, (e) l, (f) g and (g) s as functions of x with parameter values from Table 8.1 at times t from $t = 0.0$ to 29.0.

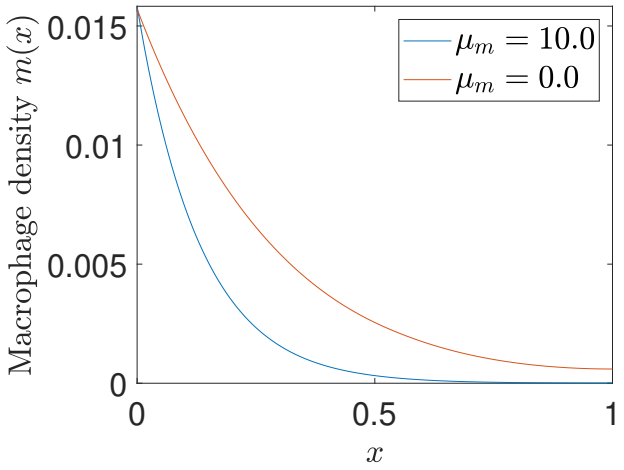

Figure 8.2: The steady state solution of m as a function of x with parameter values $\mu_m = 10.0$, and $\mu_m = 0.0$ at $t = 29.0$.

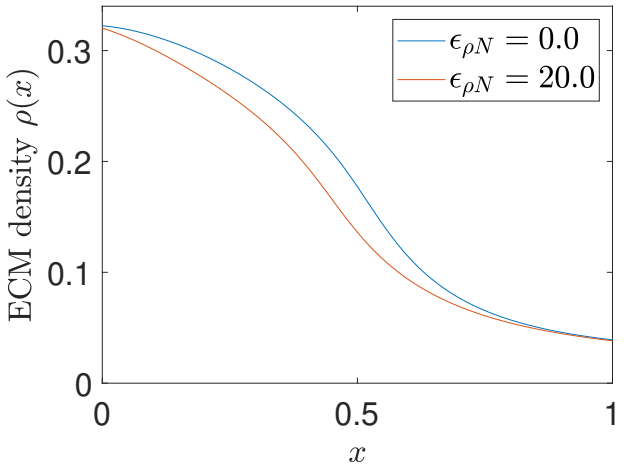

Figure 8.3: The steady state solution of ρ as a function of x with parameter values $\epsilon_{\rho N} = 20.0$, and $\epsilon_{\rho N} = 0.0$ at $t = 29.0$.

8.3.2 Parameter sensitivity

In Section 8.2.3 we introduced equations for N and d which included dependencies on m and ρ. We therefore perform parameter sensitivity analysis on three new parameters: χ_{sN}, χ_{mN} and μ_m, which govern these new terms.

The parameters χ_{sN} and χ_{mN} are the taxis rates that affect the displacement of foam cells by SMCs and macrophages respectively. We therefore analyse the effects of χ_{sN} and χ_{mN} on the magnitude and distribution of N.

The parameter μ_m is the rate at which macrophages uptake modLDL to convert into foam cells. Because the creation of foam cells is dependent on this parameter, we

analyse its effects on foam cell density. The parameter sensitivity analyses of these parameters provide us an understanding of the dynamics of necrotic core formation.

8.3.2.1 χ_{mN} and χ_{sN}

The parameters χ_{mN} and χ_{sN} govern the taxis rates at which foam cells are displaced by macrophages and SMCs respectively. Foam cells are assumed to move away from regions of high macrophage and SMC density.

Figure 8.4a shows the steady state solutions of N with three values of χ_{mN}. Macrophage density is greatest near the endothelial boundary as shown in Figure 8.1a; the displacement of foam cells by macrophages is therefore greatest near this boundary. There is a moderate change to the position of the local maxima of the steady state solutions. This is due to the macrophage profile which decreases sharply with macrophage density being very low in the approximate region $x > 0.2$. The effect of the term describing the displacement of foam cells by macrophages is moderate in this approximate region relative to the changes to the value of χ_{mN} (changed by a factor of approximately ten).

The debris profile of the steady state solutions in Figure 8.4b shows that the profile is very similar to that of foam cells in Figure 8.4a. This result is expected because the formation of debris is linearly proportional to foam cell density and the foam cell decay rate d_N.

Figure 8.5a shows the steady state solutions of N with three values of χ_{sN}. We observe that as the value of χ_{sN} increases, the region in the intima where the aggregation of foam cells is greatest moves further from the endothelial boundary. The local foam density maximum value also decreases as the value of χ_{sN} increases, but foam cell density deeper in the intima beyond the point of local maximum also increases. Increasing the parameter value of χ_{sN} increases the displacement of foam cells down the SMC gradient, leading to the local maximum of foam cell density being further from the endothelial boundary. The decrease in the local foam cell density maximum value is due to the SMC profile. SMC density is greatest near the endothelial boundary and decreases along the intima as shown in Figure 8.1g. The displacement of foam cells therefore decreases along the intima, leading to a smaller local foam cell density maximum value the further foam cells become displaced.

When the value of χ_{sN} is large, such as when $\chi_{sN} = 3.0$, we observe two potential regions of local foam cell density maxima. The local foam cell density maximum value in the intimal region is near approximately $x = 0.5$ due to the displacement of foam cells from regions of high SMC density. The other potential local maxima of the approximate region $0.2 < x < 0.4$ occurs at approximately $x = 0.3$. This is due to the displacement of foam cells by macrophages. The macrophage profile and rapid decrease in macrophage density past the endothelial boundary to near zero beyond approximately $x = 0.4$ (shown in Figure 8.1a) lead to the effect of the displacement χ_{mN} taxis term being weaker than that of χ_{sN}. We note that the changes to the values of χ_{sN} in Figure 8.5a are approximately of a factor of 3, compared to the changes to the values of χ_{sN} in Figure 8.5a being approximately of a factor 10. It

is clear that the dynamics of foam cell displacement are more sensitive to changes to χ_{sN}.

Analysis of the effects of χ_{mN} and χ_{sN} on the location and scale of these peaks is beyond the scope of this thesis, but is worth exploring in future work.

These results suggest that the region of greatest foam cell aggregation is affected by χ_{sN} and χ_{mN}, with greater values of χ_{sN} and χ_{mN} driving foam cells away from the endothelial boundary and deeper into the intima. Changes to the regions of greatest foam cell aggregation are more sensitive to changes to the term describing the displacement of foam cells by SMCs. The aggregation and density of debris is dependent on foam cells and are very similar to those of foam cells.

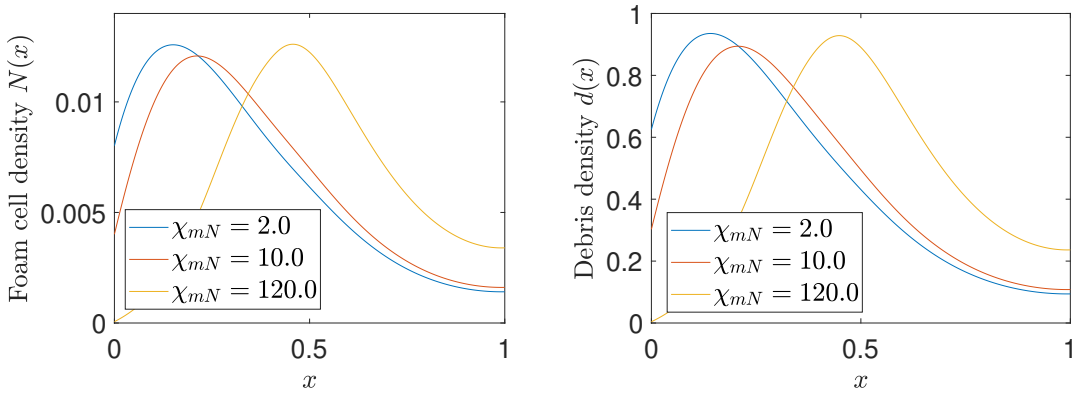

(a) (b)

Figure 8.4: Comparisons of steady state solutions of (a) N and (b) d for three values of χ_{mN} : $\chi_{mN} = 2.0$, 10.0 and 120.0 at $t = 29.0$.

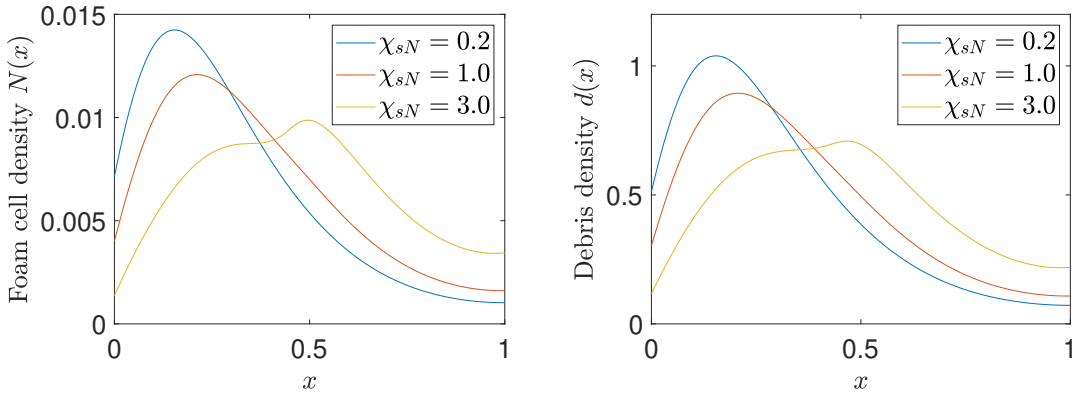

(a) (b)

Figure 8.5: Comparisons of steady state solutions of (a) N and (b) d for three values of χ_{sN} : $\chi_{sN} = 0.2$, 1.0 and 3.0 at $t = 29.0$.

8.3.2.2 μ_m

We assume in the model equations for m (8.13) and N (8.11) that macrophages consume modLDL and become foam cells. This conversion is modelled as being proportional to the conversion rate μ_m, the local macrophage density, and a saturating function with respect to modLDL concentration. In the model equation for m (8.13), the conversion term is a sink term while it is a source term in the model equation for N (8.11). We observe in Figure 8.6a that increasing values of μ_m lead to decreasing macrophage density in the intima as more macrophages become foam cells. When the rate of this conversion is very high, such as when $\mu_m = 15.0$ in Figure 8.6a, the conversion term dominates macrophage influx at the endothelial boundary, leading to very low macrophage density in the intima.

The steady state solutions of N in Figure 8.6b show that for three values of μ_m ($\mu_m = 6.0$, 10.0 and 12.0), increasing the value of μ_m corresponds to greater foam cell density. We also observe that the local maxima moves closer to the endothelial boundary. This is because macrophage density is greatest near the endothelial boundary meaning that the conversion rate is also greatest near this boundary. For the largest value of μ_m ($\mu_m = 15.0$) in Figure 8.6b however, the foam cell density in the intima is lower than that for the smaller values of μ_m. As observed in Figure 8.6a, this is because macrophage density is very low for this value of μ_m as the rate of macrophage conversion dominates the rate of macrophage influx. Because the conversion term is proportional to the local macrophage density, the rate of macrophage conversion is very low despite the large value of μ_m. Macrophages therefore become foam cells so quickly that they cannot contribute to the recruitment of more macrophages via the boundary conditions. We also note that the region of highest foam cell aggregation moves closer to the endothelial boundary as μ_m increases, even when local macrophage density is low for large values of μ_m. This is because macrophage density is greatest near the endothelial boundary. For very large values of μ_m, macrophages are not able to proliferate beyond the endothelial boundary where they enter the intima. The spatial distribution of foam cells is therefore affected by the value of μ_m.

As observed in Section 8.3.2.1, the spatial distribution of debris is dependent on that of foam cells. Figure 8.6c shows that the debris profile is qualitatively similar to that of foam cells in Figure 8.6b.

The results show that when the rate of macrophages converting to foam cells increases, macrophage density decreases. The rate of foam cell creation is equal to this rate of macrophage conversion, which is proportional to μ_m and local macrophage density. Foam cell density therefore does not necessarily increase as the value of μ_m increases: if the value of μ_m is too high, macrophages convert into foam cells at a rate that prevents macrophages from migrating through the intima, leading to low densities of local macrophages except near the endothelial boundary. Because macrophages aggregate near the endothelial boundary and the rate of macrophage conversion is proportional to local macrophage density, the region of greatest foam cell aggregation becomes closer to the endothelial boundary as the value of μ_m increases.

We note that this switch in behaviour observed in N and d as μ_m increases could be analysed further through bifurcation theory or phase diagrams. This analysis is beyond the scope of this thesis, but is worth exploring in future work.

Foam cell and debris dynamics are therefore dependent on macrophage density due to the dependence of foam cell production on macrophage density. To accommodate the increase of the rate of macrophage conversion, macrophage influx must be increased. We analyse the effects of increasing the influx of macrophages and the rate of macrophage conversion on foam cell density, and observe its effects on necrotic core dynamics. Because both foam cells and macrophages degrade ECM and the collagenous cap at the endothelial boundary, we also analyse the effects of macrophage influx and macrophage conversion on cap formation dynamics.

Figure 8.7a compares the steady state solutions of m for different values of α_m and μ_m. The blue curve is the steady state solution of m with all base parameter values from Table 8.1 ($\alpha_m = 1.2$ and $\mu_m = 10.0$). The green curve is the steady state solution of m with the parameter values of values α_m and μ_m increased to $\alpha_m = 3.0$ and $\mu_m = 20.0$. The influx of macrophages is large enough to accommodate the increased macrophage conversion rate and results in greater macrophage density across the intima in the green curve compared to the base parameter value solution (the blue curve).

This increased macrophage density and macrophage conversion rate lead to increased foam cell density for the steady state solution of N with parameter values $\alpha_m = 3.0$ and $\mu_m = 20.0$ in Figure 8.7b. The local maximum foam cell density value is greater for the steady state solution of N with the increased parameter values of α_m and μ_m compared to the base solution, and the local maximum region is also further from the endothelial boundary due to crowding because of the increased concentration of macrophages near the boundary. Due to the linear dependence of the rate of debris production on foam cell density, the debris profile with the increased parameter values of α_m and μ_m in Figure 8.6c is the same as the foam cell profile. The necrotic core therefore becomes larger and is simultaneously deeper in the intima as the rate of macrophage conversion and macrophage influx is increased.

The effect of this larger necrotic core on the ECM and collagenous cap is shown in Figure 8.7d. Macrophages and foam cells are assumed to express MMPs that degrade the ECM; the rate of general ECM degradation in the model equation for ρ (8.15) is proportional to a function of both macrophage and foam cell density. Increased macrophage and foam cell density therefore increases the rate of ECM degradation. Our parameter sensitivity analysis of the macrophage scaling parameter ϵ_ρ in the general degradation rate function (Section 7.3.1.3) in the fourth reaction-diffusion model showed that due the aggregation of macrophages at the endothelial boundary and increased ECM degradation, high macrophage density leads to a decrease in ECM density near the endothelial boundary.

Foam cells however are distributed away from the endothelial boundary. This means that the degradation of the ECM is not isolated to regions near the endothelial boundary. The ECM profile in Figure 8.3 showed that foam cells degrade the ECM further towards the centre of the intima. Increasing the contributions of

macrophages and foam cells to the degradation of ECM therefore leads to a decreases in ECM density across the intima as observed in Figure 8.7d. Biologically, this can understood as the degrading and weakening of the fibrous collagenous cap. A degraded fibrous cap may lead to plaque rupture due to the decreased integrity of the plaque [4, 33, 35].

We observe, when the rate of macrophage influx and macrophage conversion to foam cells is increased, a larger necrotic core and diminished fibrous collagenous cap form in the intima. We recall that in Section 5.4.2.3 we observed SMC distribution having a critical role in the size and distribution of the collagenous cap. By varying only μ_m and α_m, we simulate a system where there is sufficient PDGF influx and SMC proliferation. The results therefore suggest that even when ECM growth is not low, an increase in macrophage density and a larger necrotic core may lead to the degradation of the collagenous cap at the endothelial boundary. The role of SMCs in helping to maintain a collagenous cap is therefore critical; this collagenous cap may be degraded and weakened by excessive macrophages and foam cells.

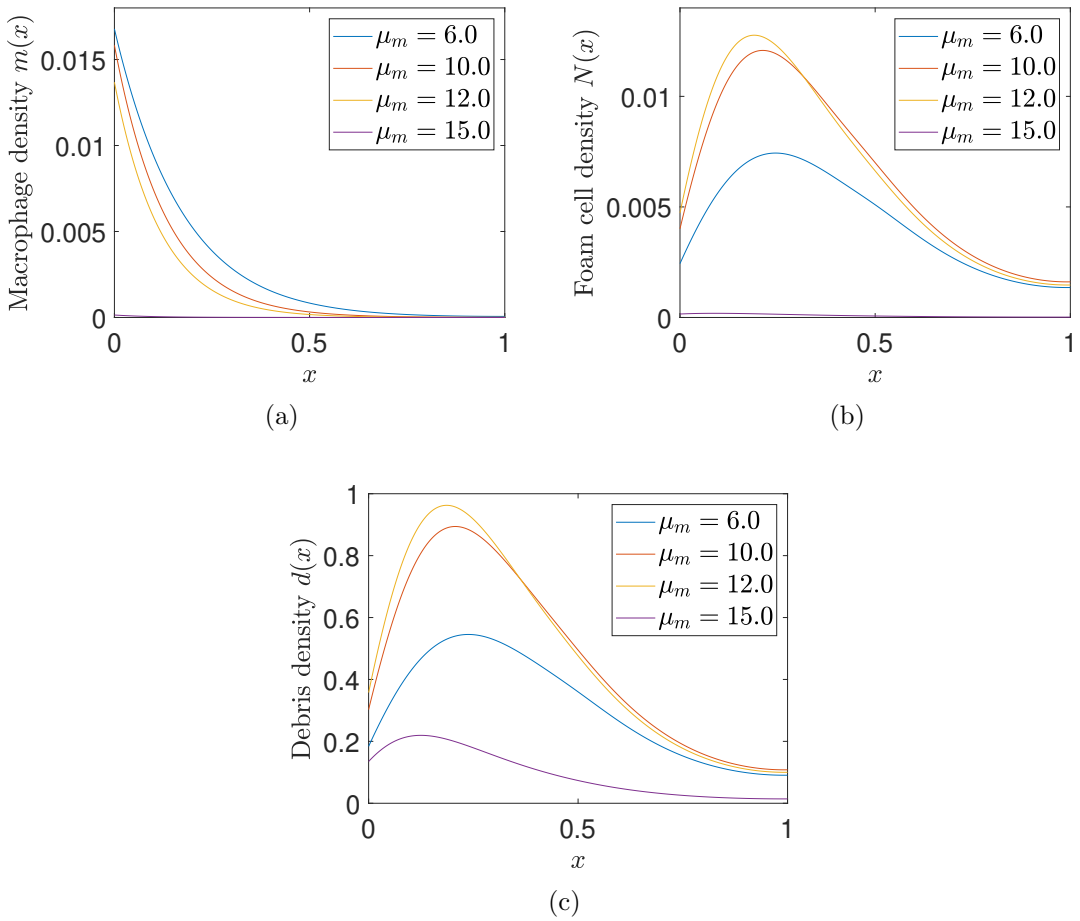

Figure 8.6: Comparisons of steady state solutions of (a) m, (a) N and (b) d for four values of μ_m : $\mu_m = 6.0$, 10.0, 12.0 and 15.0 at $t = 29.0$.

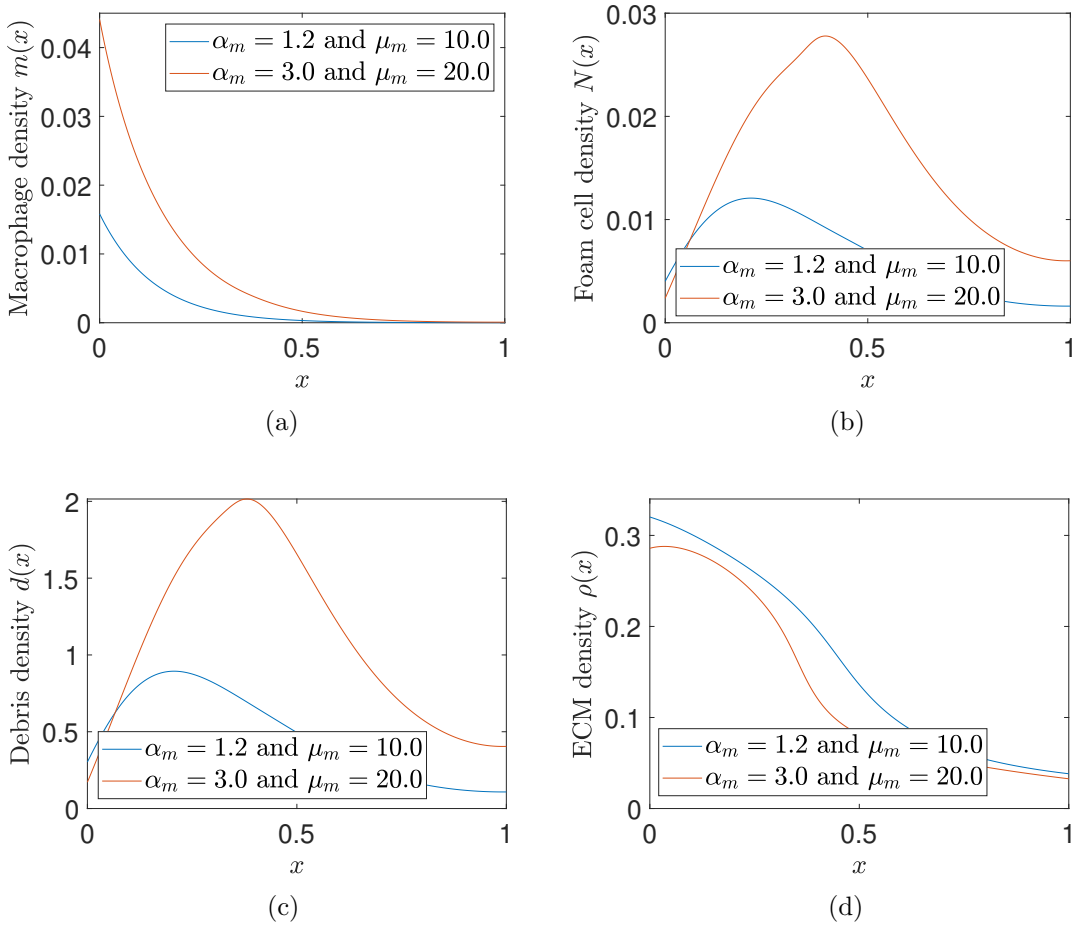

Figure 8.7: Comparisons of steady state solutions of (a) m, (b) N, (c) d and (d) ρ with the base values of α_m and μ_m from Table 8.1 and the values $\alpha_m = 3.0$ and $\mu_m = 20.0$ at $t = 29.0$.

8.4 Discussion

This reaction-diffusion model describes the four main stages of cap formation: lesion initiation, SMC migration, collagen synthesis and necrotic core formation. The results of the base case solutions in Section 8.3.1 showed that the basic dynamics of the first three stages of cap formation (lesion initiation, SMC migration, collagen synthesis) are demonstrated in our model.

Our results showed the initiation of lesions in the intima due to the influx of modLDL and macrophages at the endothelial boundary. Macrophages in the intima stimulated the production of PDGF, leading to the proliferation of SMCs. SMCs entered the intima from the lumen, migrating by random motion and chemotaxis and haptotaxis towards the endothelial boundary. The migration of SMCs led to the aggregation of SMCs at the endothelial boundary, forming the SMC distribution needed for a fibrous cap. ECM synthesis by SMCs, which is stimulated by TGF-β, and ECM degradation due to macrophage-expressed MMPs led to ECM being mainly

aggregated near the endothelial boundary. We note that macrophage foam cells are assumed to express MMPs that degrade ECM and that their introduction to the dynamics of ECM led to the decrease in ECM density away from the endothelial boundary. These dynamics created a collagenous cap at the endothelial boundary. The results therefore describe the key dynamics of the first three stages of atherosclerotic plaque formation by describing the formation of a fibrous collagenous ECM cap near the endothelial boundary.

The fourth and final stage of plaque formation is the necrotic core formation stage. We assume that macrophages do not enter the intima as foam cells and that foam cells are unable to cross the endothelial and medial boundaries. They are instead converted from macrophages when macrophages consume modLDL, and are displaced by SMCs and macrophages proportionally to the taxis coefficients χ_{sN} and χ_{sN} respectively. We observed that when the effect of displacement was made stronger by increasing the values of these coefficients, foam cells aggregation occurred further away from the endothelial boundary. Because we assume no influx of foam cells nor any existing initial foam cells in the intima, the production of foam cells is dependent on the rate of macrophage conversion to foam cells. The effect of this was that increasing this conversion rate generally led to an increase in foam cell density and a corresponding decrease in macrophage density. This remained the case until the rate of macrophage loss due to foam cell conversion was large enough to dominate the influx of macrophages at the endothelial boundary, which in turn limited the migration of macrophages through the intima. The result was an overall decrease in macrophage density in the intima. This is because the rate of macrophage conversion to foam cells is proportional to the local macrophage density, meaning that foam cell production decreased despite a greater rate of macrophage conversion. The results therefore suggest that the rate of macrophage conversion, macrophage density and foam cell motility are significant factors in the way that the presence of foam cells affects plaque growth.

The results showed that the spatial distribution of debris was very similar to that of foam cells. The rate of production of debris is modelled as equal to the rate of foam cell death, which is linearly proportional to local foam cell density. We recall that foam cells, extra-cellular lipids (which we did not consider), and debris form the necrotic core. The reaction-diffusion model therefore describes a collagenous cap near the endothelial boundary and a necrotic core deeper in the intima. The dynamics of the necrotic core, including its spatial characteristics, are dependent on foam cells which in turn are affected by macrophages.

Macrophages and the necrotic core are also shown to have an effect on the stability of the fibrous collagenous cap. We observed in Section 8.3.2.2 that due to macrophages and foam cells degrading ECM, the size of the cap can decrease when macrophage and foam cell density is large. When the influx of macrophages and the rate of macrophage conversion to foam cells is increased, the necrotic core increases and the rate of ECM degradation increases across the intima. This is because foam cells are distributed deeper in the intima rather than primarily accumulating at the endothelial boundary like macrophages. The decrease in the size of the collagenous cap suggests that the cap can become smaller and weakened, leaving it vulnerable to rupture [4, 33, 35].

We recall that our thesis objective is to create reaction-diffusion framework that can be extended to model key stages of atherosclerotic plaque dynamics. The reaction-diffusion model therefore shows how macrophages, first incorporated in the modelling of lesion initiation, influence the later necrotic core formation stage which affects cap dynamics depicted in the collagen synthesis stage. The four main stages of cap formation are finally represented in this model, maintaining the key dynamics observed in earlier reaction-diffusion models while describing the necrotic core formation stage and its effects on collagen synthesis.

Chapter 9

Discussion and Conclusion

The results of each of the five submodels are discussed in their respective chapter discussion sections (4.5, 5.5, 6.5, 7.4 and 8.4). In this section we summarise how these results capture four key stages of atherosclerotic plaque formation: lesion initiation, SMC migration, collagen synthesis, and necrotic core formation. We seek a model that captures current understandings of the mechanisms of atherosclerosis while being simple and extendable without introducing additional complexity. We therefore compare the model results to the reference models used in this paper: Watson *et al.* (2018, 2020) [44, 45], Ougrinovskaia (2011) [37], and Chalmers *et al.* (2015, 2017) [10, 11].

9.1 Lesion initiation

The initiation of lesions in the intima is described in the reaction-diffusion models of Chapters 6, 7 and 8. We recall that atherosclerosis is initiated by the deposition of lipids in the intima, and that LDLs pass through the endothelium and accumulate in the intima [4, 23, 38]. LDLs then become modified, undergoing oxidation [4, 33]. In our model, the movement of LDLs through the endothelium into the intima is modelled as an influx of LDLs at the endothelial boundary at a constant rate. We assume that these LDLs oxidise immediately, and therefore treat the influx of non-modLDLs as the same as that of modLDLs. In response to the inflammatory effect of modLDLs, endothelial cells express adhesion molecules that promote the adhesion of monocytes [16, 31, 36]. These monocytes differentiate into macrophages in the intima [4]. We assume that this differentiation occurs immediately and model the adhesion of monocytes as the influx of macrophages into the intima.

In the intima, modLDL is a chemoattractant and we model macrophages as moving chemotactically up the gradient of modLDL. Macrophages uptake modLDL which we model as a saturating function with respect to modLDL concentration. The uptake of modLDL by macrophage-like trans-differentiated SMCs that create foam cells [3, 4, 25] is not directly modelled as our model does not distinguish between macrophages of different origins. We instead assume the uptake of modLDL by macrophage-like cells is part of the general uptake of modLDL by macrophages. The conversion of macrophages to foam cells is modelled as proportional to the rate of lipid uptake by macrophages. We assume that foam cell production is only due to the conversion of macrophages to foam cells.

Our results in Sections 6.4.0.1 and 7.3.0.1 show that the timescales of modLDL, macrophage and foam cell dynamics are short, which reflects the short initial stage at which these processes occur in the formation of atherosclerotic plaques. ModLDLs

migrate through the endothelial boundary and diffuse in the intima where they are rapidly consumed by macrophages. Macrophages are shown to accumulate at the endothelial boundary, with macrophage density being highest near this region.

In our model, lesions are assumed to be comprised of lipid-laden foam cells. The formation of lesions is therefore dependent on foam cells which are produced by the conversion of modLDL-consuming macrophages to foam cells. The parameter sensitivity analysis in Section 8.3.2.2 shows that high macrophage density leads to high foam cell density. If the rate of this conversion is too high however, macrophages become foam cells so quickly that they cannot contribute to the recruitment of more macrophages. This leads to macrophage density in the intima becoming low, which reduces foam cell density. Foam cell density is therefore shown to be dependent on macrophage density. Our model therefore suggests that the early initiation and later formation of lesions is significantly driven by inflammatory processes that affect the presence of macrophages in the intima.

9.2 Smooth muscle cell migration

The inflammatory processes created by the presence of modLDL and macrophages in the intima stimulate de-differentiated SMCs to migrate from the media through the internal elastic lamina into the intima [4]. SMCs are modelled as migrating from the medial boundary into the intima, where they migrate and proliferate. We do not differentiate between phenotypes and only consider vascular SMCs that are collagen-synthesising. PDGF, expressed by macrophages and endothelial cells, is a strong chemoattractant to SMCs [39]. We assume that PDGF enter the intima via influx at the endothelial boundary.

In the intima, the de-differentiation of SMCs is stimulated by growth factors including PDGF, and undergo clonal expansion [28, 39]. We model this proliferation of SMCs in the intima using a logistic growth function of PDGF concentration. PDGF acts as a chemoattractant for SMCs which respond chemotactically to migrate into the intima [36, 39]. This is modelled as SMCs moving chemotactically up the gradient of PDGF. The expression of PDGF by macrophages is modelled as a source term in the model equation for PDGF. SMCs undergo ES cytokine-stimulated apoptosis [36]; these cytokines are produced by macrophages. We model this apoptosis by assuming that the rate of apoptosis is proportional to macrophage density. The presence of SMCs in the intima means that SMCs, macrophages and foam cells occupy space in the intima, though macrophages are less motile than SMCs and foam cells are less motile than both macrophages and SMCs. We assume that they compete for space and that less motile cells are displaced by their more motile competitors. This is modelled as the tactic movement of macrophages down the gradient of SMCs, and the tactic movement of foam cells down the gradients of SMCs and macrophages.

Our results in Sections 4.3.2 and 6.4.0.1 show that SMC proliferation and migration is dependent on PDGF concentration. We recall that PDGF concentration is af-

fected by macrophages due to their expression of PDGF. PDGF concentration and macrophage density is greatest near the endothelial boundary, resulting in increased SMC proliferation and migration. We observe SMC accumulation to be greatest near this boundary. When comparing the effects of PDGF and macrophages on SMCs, the results of Section 6.4.1.2 suggests that the effect of SMC proliferation, which is stimulated by PDGF, is greater than that of SMC apoptosis. The main contribution of macrophages on SMC dynamics is therefore through their effect on PDGF concentration (which SMC migration is driven by) rather than directly through SMC apoptosis. The implications of these dynamics on cap stability are explained in the next section.

9.3 Collagen synthesis

De-differentiated SMCs in the intima secrete ECM proteins which remodel the intimal ECM [2]. The synthesis of these secreted ECM proteins is stimulated by TGF-β [22, 34]. This synthesis is modelled as a rate function dependent on SMC and TGF-β density. The rate function is assumed to saturate with respect to ECM density as unconstrained ECM proliferation is unrealistic. ECM is degraded by a number of factors including MMPs, which contribute to the lysis of ECM [3, 24, 38]. MMPs are secreted by plaque SMCs, macrophages and foam cells. This is modelled as two sink terms that are proportional to SMC density, and macrophage and foam cell density respectively.

We assume that SMCs have an affinity for the ECM. This means that SMCs contract towards regions of high ECM density. We model this as SMCs migrating haptotactically up the gradient of ECM.

The results in Sections 5.4.1 and 7.3.0.1 show that the synthesis of ECM is dependent on SMCs and TGF-β. The accumulation of SMCs near the endothelial boundary leads to ECM density being greatest near this region, and local TGF-β concentration influences the magnitude of ECM density. The magnitude and spatial distribution of ECM creates a cap region near the endothelial boundary. We note that models such as Watson *et al.* (2020) assume that SMC dynamics determine ECM dynamics. Our results in Section 7.3.1.1 however show that this does not hold where there is a high presence of macrophages in the intima. In the earlier stage of SMC migration, we observed that macrophages express PDGF and therefore increase SMC proliferation, leading to increased ECM synthesis. Macrophages however degrade ECM and also create foam cells by uptaking modLDL. Because foam cells degrade ECM, high macrophage density in the intima leads to increased ECM degradation due to MMP expression. The size of the fibrous cap therefore becomes larger as more SMCs proliferate in the intima, but decreases as inflammatory processes increase macrophage and foam cell presence in the intima.

9.4 Necrotic core formation

As the lesion core under the fibrous cap develops, foam cells undergo cell death and create debris. Their accumulation forms a necrotic core in the plaque. Our model assumes that the rate of debris creation is linearly proportional to foam cell density.

The results in Section 8.3.1 show that the size and profile of the necrotic core is influenced by macrophages and foam cells. We assume that SMCs that change phenotype to become macrophage-like convert into foam cells after uptaking modLDL [3, 4, 25]. Because our model variables do not differentiate between phenotypes, the creation of foam cells from macrophage-like SMCs is included in the creation of foam cells from macrophages. As explained in Section 9.1, foam cell density is dependent on macrophage density, and a large amount of macrophages in the intima corresponds to a large lesion core. Due to the corresponding large amount of debris situated in the same region as foam cells, this translates to a large necrotic core. The displacement of foam cells by macrophages and SMCs result in foam cells and debris aggregating away from the endothelial boundary to where macrophage and SMC density is least. The position of the necrotic core is therefore deeper in the intima than the fibrous cap which lies near the endothelial boundary.

We recall that inflammatory responses in the intima due to the presence of modLDL lead to the recruitment of monocytes, which differentiate into macrophages [4]. The results in Section 9.3 show that high macrophage density degrades the fibrous cap, while the results in Section 8.3.2.2 show that high macrophage density leads to a larger necrotic core. High macrophage presence in the plaque therefore leads to the degradation of the fibrous cap and the increase of the necrotic core. Plaque rupture occurs when the integrity of the plaque breaks down and debris is released into the bloodstream [4, 33, 35]. Our results therefore suggest that significant inflammation may lead to plaque rupture due to the degradation of the fibrous cap and the increase of the necrotic core.

9.5 Comparison with multiphase models of Watson *et al.* (2018, 2020)

An aim of our research is to reproduce some of the observations of the multiphase models of Watson *et al.* (2018, 2020) by using simpler reaction-diffusion models. In Chapter 4 we aimed to simulate key cap formation dynamics of Watson *et al.* (2018) as similarly as possible with our reaction-diffusion submodel. Our results in Section 4.3.2 compared the solutions of PDGF concentration and SMC density and showed that we were able to achieve qualitatively similar solutions of PDGF concentration and SMC density. We performed parameter sensitivity analysis on the same parameters analysed in Watson *et al.* (2018) and found that the qualitative differences in solutions between the two models were minor. We also simplified the non-linear SMC phase pressure functions using constant flux coefficients and observed that SMC dynamics were qualitatively similar between the two models.

These results showed us that the key aspects of a two-species multiphase model could still be demonstrated in a simpler reaction-diffusion model.

In Chapter 5 we used the multiphase model of Watson *et al.* (2020) as a reference model to model the collagen synthesis stage. The assumptions adopted from the multiphase model are those for the dynamics of ECM synthesis and degradation, SMC haptotactic migration, and TGF-β growth. We note that the increase of model species in this multiphase model required mass and momentum balancing, whereas our reaction-diffusion model did not require these complex considerations. The multiphase model assumed that the rate of ECM proliferation is dependent on TGF-β concentration. We adopted this assumption in our source term for ECM density, though we added a source limiting term to limit ECM growth. The model also assumed that ECM is degraded by SMC and non-SMC phases. Our model adopted qualitatively similar terms in the model equation for ECM density. The rate of SMC haptotactic migration in the multiphase model is modelled as a non-linear function of SMC and ECM volume fraction that decreases as SMC and ECM volume fraction become sufficiently large. We note that this was to address an issue with possible ill-posedness due to diffusive SMC flux becoming negative, which could occur when the gradient of ECM became too large and SMC haptotactic flux dominated. While we do not have this issue in our model, our proposed solution was to use a decreasing haptotactic coefficient function so that the rate of haptotactic flux decreases for high values of ECM density. Our simpler reaction-diffusion submodel was therefore able to adopt a number of key assumptions from the more complex multiphase model. The simplicity of the reaction-diffusion submodels make the model framework more easily extendable.

We note however that the multiphase models have features that our model lacks. Because our model simplifies a number of the dynamics modelled in these multiphase models, they lack some detail and complexity. An example is the absence of phase mass and momentum balancing and no-voids conditions in our reaction-diffusion model, which means that our model must introduce terms to simulate these terms. In the multiphase model of Watson *et al.* (2018), no-voids conditions are imposed on the SMC and non-SMC phases which ensures that the total mass in the volume is constant. To simulate volume-filling in our reaction-diffusion, we instead introduced source limiting constraints to impose an appropriate limit on ECM synthesis.

9.6 Comparison with Ougrinovskaia (2011)

The reaction-diffusion model of Ougrinovskaia was used as a reference model for our reaction-diffusion model. An attractive feature of Ougrinovskaia (2011) was the use of submodels, which we adopted in our model. The submodels of Ougrinovskaia (2011) described the following stages of atherosclerotic plaque formation: lesion initiation, early lipid pool core formation, SMC migration, fibrous cap formation, and atheroma formation. These stages are described generally by the submodels of our reaction-diffusion model.

We note that key differences between our reaction-diffusion model and that of Ougrinovskaia (2011) led to differences in some of our results. In Ougrinovskaia (2011), zero initial conditions are assumed for modLDL and macrophages. Our model instead assumes that there are existing modLDL and macrophages in the intima to simulate a more realistic picture of the intima before the onset of inflammation. Ougrinovskaia (2011) assumes that ECM or collagen is only degraded by macrophages and foam cells. We include the degradation of ECM due to MMP expression by SMCs and the effect of TGF-β on this MMP expression. Ougrinovskaia (2011) further assumes that foam cells continue to uptake modLDL, which differs from our assumption that foam cells in our model are saturated and can no longer uptake modLDL. These differences lead to different numerical results between the two models. We note however that both models conclude that inflammation and immune responses are the main drivers of plaque rupture.

Despite the differences between the two models, the reaction-diffusion model of Ougrinovskaia (2011) is an important reference for our reaction-diffusion model. This is due to its use of submodels and relative ease in extension and simplicity relative to more complex models, which align with our aim of creating a model that captures current understandings of the mechanisms of atherosclerosis while being simple and extendable without introducing additional complexity.

9.7 Comparison with Chalmers *et al.* (2015, 2017)

In Chapters 6 and 7 we used the reaction-diffusion models of Chalmers *et al.* (2015, 2017) as references for our submodels. Our submodels adopted similar assumptions and non-dimensionalisation as these reaction-diffusion models. An example is the assumption in Chalmers *et al.* (2017) that foam cells do not uptake modLDL (which we adopted), compared to the assumption in Ougrinovskaia (2011) that they do. Our results for the solutions of modLDL and macrophage density are qualitatively similar to those observed in Chalmers *et al.* (2015, 2017).

We note however that the models include ES cytokines, HDL and monocyte chemoattractants as model species. These models extend beyond the scope of our model to describe the mechanisms of RCT and its modulating effect on macrophages. The qualitative similarity of our reaction-diffusion submodels to the models of Chalmers *et al.* (2015, 2017) is therefore limited to the model equations for modLDL and macrophages.

9.8 Future directions

Our reaction-diffusion model we modelled four key stages of atherosclerotic plaque formation: lesion initiation, SMC migration, collagen synthesis, and necrotic core formation. Other models, such as Friedman *et al.* (2015) [20], Younes *et al.* (2021) [47], and Chalmers *et al.* (2015, 2017) model the modulating effect of HDL on plaque

formation. HDL inhibits the oxidation of LDL which leads to less modLDL entering the intima, and facilitates RCT from foam cells which revert to macrophages [3,8,15]. RCT is therefore a mechanism for a reduction in the necrotic core. This may cause the plaque to regress. Our model results show that by using submodels, we are able to include stages relatively easily. Extending the existing model to include this stage is probably feasible.

A number of simplifications made in our model reduce the accuracy and detail of our results. An example is our simplification of phenotype-switching, which is observed in SMCs and macrophages. As explained in Section 2.3, SMCs can undergo trans-differentiation into macrophage-like cells, which can uptake modLDL to create foam cells [4]. This is significant as up to 50% of foam cells are estimated to be SMC-derived [3]. In our model, we simplify this change in phenotype by increasing the rate of influx of macrophages into the intima. Macrophages can also change phenotype to produce cytokines which promote SMC apoptosis [3, 36]. We do not differentiate between phenotypes in our model and generalise our macrophage species to include all phenotypes. Models such as Cobbold *et al.* (2002) [36] distinguish between numerous different types of cells and chemoattractants. Given our model's relative ease and simplicity in introducing new species, increasing the accuracy and details of our description of the mechanisms of plaque formation should be a feasible extension of our research.

Another cost of our model's simplicity is the fixed intima. In our model, we assume a fixed one-dimensional domain that represents the intima with stationary boundary conditions. The advantage of this fixed domain is that we are able to perform relatively simple numerical and analytical analysis. A fixed domain is also biologically reasonable when SMC and ECM densities are not too large. For later stages of the atherosclerotic plaque formation however, the intima distends and grows [3, 4]. To more accurately model plaque formation, it requires the assumption of a moving boundary. We also note that our domain is defined as the region of the intima between its luminal edge and media. Expanding the domain past the intima could allow us to model important phenomena such as SMC phenotype-switching: we recall that quiescent SMCs adopt a de-differentiated phenotype in the media [25]. These complex extensions of the models are beyond the scope of this research as our aim was to create a relatively simple reaction-diffusion model.

We note some research areas unexplored in this thesis that could form future work. The first is the numerical issues with the solution of m observed in Section 7.3.1.1 for large values of χ_{ms} ($\chi_{ms} > 2.0$). We noted that our results still demonstrated the general effect of χ_{ms} on macrophage dynamics; analysis on the cause of the numerical issue could provide insights on the effects of a change in the sign of m at the endothelial boundary on the system. Another potential research area is analysis on the location and scale of local maxima in foam cell and debris density. As observed in Section 8.3.2.1, the parameters χ_{mN} and χ_{sN} appeared to affect the distribution of foam cell and debris. Steady state analysis of their distribution could provide further insight into the influence of χ_{mN} and χ_{sN}. Our results also warrant further analyses on the change in the foam cell dynamics as the value of μ_m increases. We observed in Section 8.3.2.2 that up to a certain value of μ_m, foam cell density increases with the rate of macrophage conversion. If the value of μ_m is too high

however, macrophages convert into foam cells at a rate that prevents macrophages from migrating through the intima, which leads to low values of macrophage and foam cell density. This switch in behaviour may be analysed mathematically using bifurcation theory or phase diagrams. Bifurcation analysis on a number of other parameters, such as r_s due to the importance of SMC distribution to the ECM profile, could provide deeper insights into their effect on plaque dynamics. This could be extended to suggest plaque rupture criteria and potential therapies.

9.9 Conclusion

Our research shows that reaction-diffusion models for different stages of plaque development or combinations of stages are relatively simple and extendable without introducing additional complexity or issues. When synthesised, they are able present a simplified complete picture of atherosclerotic plaque formation. They should continue to be considered as a powerful tool in atherosclerosis modelling alongside more complicated model formulations.

List of commonly used terms

ECM Extracellular matrix, a network of macromolecules mainly consisting of collagen that is remodelled into a protective fibrous cap;

IFN-γ Interferon-γ, a cytokine that affects collagen synthesis and apoptosis;

IL-10 Interleukin-10, an anti-inflammatory cytokine that affects collagen synthesis and apoptosis;

MCP-1 Monocyte Chemoattractant Protein-1, a chemoattractant that stimulates monocyte migration;

MMP Matrix metalloproteinase, the main enzymes in collagen degradation.

modLDL Modified low density lipoproteins, oxidised LDLs that are uptaken by macrophages;

PDGF Platelet-derived growth factor, a growth factor that drives SMC dedifferentiation, proliferation, and migration;

SMC Smooth muscle cells, these cells migrate from the media into the intima form a cap;

TGF-β Transforming Growth Factors-β, a growth factor involved in collagen synthesis;

Appendix A

Method of Lines

To solve the differential equations in our models, we use the numerical method of the method of lines. The method of lines is a finite differencing scheme that replaces the spatial derivatives in a partial differential equation with algebraic approximations. These approximations allow us to discretise in one spatial dimension, which reduces the partial differential equation system into a system of ordinary differential equations which depend on time only. We can solve this system of ODEs using standard numerical integration routines.

We choose this method for a few reasons. We note that stability is a concern in all numerical schemes, and that identifying and fixing issues quickly and easily is a priority. Inbuilt PDE solvers such as `pdepe`, while reliable and widely used, can suffer from stability issues when there are significant differences in scale between flux terms. This is a concern because our model systems include a number of partial differential equations which introduce multiple potential sources of instability. Algebraically discretising partial differential equations in one spatial dimension allows us to address instability by choosing appropriate stable spatial discretisation schemes. We can then rely on time integrators based on stability regions. Choosing our own appropriate stable spatial discretisation schemes also gives us greater control over spatial discretisation, as opposed to relying on a blackbox inbuilt PDE solver.

Another reason for choosing the method of lines is its relative simplicity and ease of use. While consideration must be given to analysing the spatial discretisation scheme, the time derivative component is left to an inbuilt time integrator. This makes the method both computationally and analytically simple, and offers an appropriate degree of accuracy. This differs from more accurate yet complex numerical methods that involve bespoke discretisation schemes in both space and time. There are, however some problems with the method of lines: the method has stability issues with purely elliptic partial differential equations and requires initial conditions for all functions. We are able to work around these problems because none of our model equations are purely elliptic, and we are able to use trivial initial conditions. This relative simplicity and ease of use therefore makes the method of lines more attractive for our models than other more complex schemes despite their potential for greater accuracy and stability.

A.1 Spatial discretisation

We recall that the method of lines involves algebraically discretising partial differential equations in one dimension, and then using time integrators for the time dimension. The spatial domain is discretised into a grid with equal width subinter-

vals. Our approach is to discretise the source terms in the equations at each grid point. The flux terms are discretised with an appropriate discretisation scheme at the interior grid points, and the boundary flux terms are imposed at grid points at either end of the spatial domain.

Consider an arbitrary function $f(t) = f(x,t)$ on a spatial domain $x \in [0,1]$ divided into n equal subintervals with grid points $x_i = i\Delta x$. By taking the interior grid points, a partial differential equation can be expressed as the matrix ordinary differential equation:

$$\frac{d\hat{f}}{dt} = \mathcal{A}\hat{f} + g(\hat{f}), \tag{A.1}$$

where $\hat{f}$ represents the vector of grid values for the function evaluated for $n+1$ grid points ($f(x_i,t) = f_i$ with x_i for $i = 0,1,...,n$). The operator $\mathcal{A}$ represents the derivative operator which specifies the discretisation of the spatial derivative terms, and $g(\hat{f})$ represents the matrix of discretised source terms.

In the derivative operator $\mathcal{A}$, the equation flux terms are discretised using central differencing at the interior grid points. This means that for a given flux term J_f, the flux at x_i is evaluating using the adjacent half-grid points:

$$\frac{\partial}{\partial x} J_{f_i} = \frac{1}{\Delta x}\Big(J_{f_{i+\frac{1}{2}}} - J_{f_{i-\frac{1}{2}}}\Big). \tag{A.2}$$

Recalling that we discretise the flux term J_f using central differencing and take half-points, the first order derivative terms at the half-points become:

$$\frac{\partial f_{i+\frac{1}{2}}}{\partial x_{i+\frac{1}{2}}} = \frac{1}{\Delta x}\Big(f_{i+1} - f_i\Big). \tag{A.3}$$

To evaluate second order derivative terms, we use the relation (A.2) to obtain the expression:

$$\frac{d^2 f_i}{dx_i^2} = \frac{1}{\Delta x}\Big(\frac{\partial f_{i+\frac{1}{2}}}{\partial x_{i+\frac{1}{2}}} - \frac{\partial f_{i-\frac{1}{2}}}{\partial x_{i-\frac{1}{2}}}\Big). \tag{A.4}$$

The non-derivative terms are evaluated at the half-points by taking the average of the adjacent half-points:

$$f_{i+\frac{1}{2}} = \frac{1}{2}\Big(f_{i+1} - f_i\Big). \tag{A.5}$$

There is no need to evaluate the source terms at the half-points. We evaluate the values of f in the matrix of discretised source terms $g(\hat{f})$ at each interior grid point.

The boundary condition flux terms are solved differently. The derivatives at the boundary $x_0 = 0$ and $x_n = 1$ are discretised using second-order forward and back-

ward differencing respectively:

$$\frac{df_0}{dx_0} = \frac{4f_1 - f_2 - 3f_0}{2\Delta x}, \tag{A.6}$$

$$\frac{df_n}{dx_n} = \frac{-4f_{n-1} + f_{n-2} + 3f_n}{2\Delta x}. \tag{A.7}$$

Given that we know the values of the interior grid points, we can solve for the boundary values f_0 and f_n. We therefore express these differential algebraic equations (DAEs) as a vector γ_f, where the boundary values f_0 and f_n are expressed as DAEs.

This yields the system of ODEs:

$$\dot{\hat{f}} = \mathcal{A}\hat{f} + \gamma_f + g(\hat{f}), \tag{A.8}$$

We are able to integrate these ODEs using the Matlab routine `ode45`: this routine's inbuilt scheme uses pairs of explicit Runge-Kutta formulas of order 4 and 5. We note that this explicit method has conditional stability. The solver is able to address this in some situations by adaptively changing its time-step sizes. We note that have not performed stability analysis such as CFL condition or Neumann stability analysis for our spatial discretisation. Our highly coupled systems make this analysis difficult. We instead rely on chosing the appropriate spatial step sizes and the adaptive time-stepping of `ode45`.

Bibliography

[1] O. Adebayo and A. M. Adeoye. *Atherosclerosis: A Journey around the Terminology*, chapter 5. IntechOpen, Rijeka, 2020.

[2] E. Adiguzel, P. J. Ahmad, C. Franco, and M. P. Bendeck. Collagens in the progression and complications of atherosclerosis. *Vasc. Med. Rev.*, 14(1):73–89, 2009.

[3] G. L. Basatemur, H. F. Jørgensen, M. C. H. Clarke, M. R. Bennett, and Z. Mallat. Vascular smooth muscle cells in atherosclerosis. *Nat. Rev. Cardiol*, 16:727–744, 2019.

[4] J. L.M. Bjorkegren and A. J. Lusi. Atherosclerosis: Recent developments. *Cell*, 185(10):1630–1645, 2022.

[5] Y. V. Bobryshev, E. A. Ivanova, D. A. Chistiakov, N. G. Nikiforov, and A. N. Orekhov. Macrophages and their role in atherosclerosis: Pathophysiology and transcriptome analysis. *Biomed Res. Int.*, 2016:9582430, 2016.

[6] M. S. Brown, J. L. Goldstein, M. Krieger, and R. G. Anderson Y. K. Ho. Reversible accumulation of cholesteryl esters in macrophages incubated with acetylated lipoproteins. *JCB*, 82(3):597–613, 1979.

[7] H. M. Byrne and M. R. Owen. A new interpretation of the keller-segel model based on multiphase modelling. *J. Math. Biol.*, 49:604–626, 2004.

[8] Tardy C, Goffinet M, Boubekeur N, Ackermann R, Bluteau A Sy G, Cholez G, Keyserling C, Lalwani N, Paolini JF, Dasseux J-L, Barbaras R, and Baron R. Cer-001, a hdl-mimetic, stimulates the reverse lipid transport and atherosclerosis regression in high cholesterol diet-fed ldl-receptor deficient mice. *Atherosclerosis*, 232:110–118, 2014.

[9] V. Calvez, A. Ebde, N. Meunier, and A. Raoult. Mathematical modelling of the atherosclerotic plaque formation. *ESAIM: Proc.*, 29:1–12, 2009.

[10] A. D. Chalmers, C. A. Bursill, and M. R. Myerscough. Nonlinear dynamics of early atherosclerotic plaque formation may determine the efficacy of high density lipoproteins (hdl) in plaque regression. *PLoS One*, 12:e0187674–1–e0187674–23, 2017.

[11] A. D. Chalmers, A. Cohen, C. A. Bursill, and M. R. Myerscough. Bifurcation and dynamics in a mathematical model of early atherosclerosis: How acute inflammation drives lesion development. *J. Math. Biol.*, 71:1451–1480, 2015.

[12] K. L. Chambers, M. G. Watson, and M. R. Myerscough. A lipid-structured model of atherosclerotic plaque macrophages with lipid-dependent kinetics. *Bull. Math. Biol.*, 85(9):85, 2002.

[13] J. Chappell, J. L. Harman, V. M. Narasimhan, H. Yu, K. Foote, B. D. Simons, M. R. Bennett, and H. F. Jørgensen. Extensive proliferation of a subset of

differentiated, yet plastic, medial vascular smooth muscle cells contributes to neointimal formation in mouse injury and atherosclerosis models. *Circ. Res.*, 119:1313–1323, 2016.

[14] C. A. Cobbold, J. A. Sherratt, and S. R. J. Maxwell. Lipoprotein oxidation and its significance for atherosclerosis: a mathematical approach. *Bull. Math. Biol.*, 64(1):65–95, 2002.

[15] D. A. Cox and M. L. Cohen. Effects of oxidised low-density lipoprotein on vascular contraction and relaxation: clinical and pharmacological implications in atherosclerosis. *Pharmacol. Rev.*, 48:3–19, 1996.

[16] S. D. Cushing, J. A. Berliner, A. J. Valente, M. C. Territo, M. Navab, F. Parhami, R. Gerrity, C. J. Schwartz, and A. M. Fogelman. Minimally modified low density lipoprotein induces monocyte chemotactic protein 1 in human endothelial cells and smooth muscle cells. *PNAS*, 87(13):5134–5138, 1990.

[17] A. C. Doran, N. Meller, and C. A. McNamara. Role of smooth muscle cells in the initiation and early progression of atherosclerosis. *ATVB*, 28(5):812–819, Feb 2008.

[18] E. E. Eriksson. Intravital microscopy on atherosclerosis in apolipoprotein e-deficient mice establishes microvessels as major entry pathways for leukocytes to advanced lesions. *Circulation*, 124(19):2129–2138, Nov 2011.

[19] H. Z. Ford, H. M. Byrne, and M. R. Myerscough. A lipid-structured model for macrophage populations in atherosclerotic plaques. *J. Theor. Biol.*, 479(1):48–63, 2019.

[20] A. Friedman and W. Hao. A mathematical model of atherosclerosis with reverse cholesterol transport and associated risk factors. *Bull. Math. Biol.*, 77(5):758–781, 2015.

[21] S. Ganesana and S. Lingeshwaran. A biophysical model of tumor invasion. *Commun. Nonlinear Sci. Numer. Simul.*, 46:135–152, 2017.

[22] G. K. Hansson and P. Libby. Molecular bases of the acute coronary syndromes. *Circulation*, 91(11):2844–2850, 1995.

[23] G. K. Hansson and P. Libby. The immune response in atherosclerosis: a double-edged sword. *Nat. Immunol.*, 6:508–519, 2006.

[24] G. K. Hansson, P. Libby, and I. Tabas. Inflammation and plaque vulnerability. *J. Intern. Med.*, 278:483–493, 2015.

[25] J. Harman and H. Jørgensen. The role of smooth muscle cells in plaque stability: Therapeutic targeting potential. *Br. J. Pharmacol.*, 176(19):3741–3753, June 2019.

[26] M.E. Hubbard and H.M. Byrne. Multiphase modelling of vascular tumour growth in two spatial dimensions. *J. Theor. Biol.*, 316:70–89, 2013.

[27] K. Jacobsen, M. B. Lund, J. Shim, S. Gunnersen, E.-M. Fuchtbauer, M. Kjolby, L. Carramolino, and J. F. Bentzon. Diverse cellular architecture of atherosclerotic plaque derives from clonal expansion of a few medial smcs. *JCI Insight*, 2:e95890, 2017.

[28] A. Yurdagul Jr. Crosstalk between macrophages and vascular smooth muscle cells in atherosclerotic plaque stability. *ATVB*, 42(4):372–380, April 2019.

[29] J. F. Keaney, D. I. Simon, and J. E. Freedman. Vitamin e and vascular homeostasis: implications for atherosclerosis. *FASEB J.*, 13:965–976, 1999.

[30] N. E. Khatib, S. Génieys, and V. Volpert. Atherosclerosis initiation modeled as an inflammatory process. *MMNP*, 2(2):126–141, 2007.

[31] R. Kraemer. Regulation of cell migration in atherosclerosis. *Curr. Atheroscler. Rep.*, 2:445–452, 2000.

[32] G. Lemon, J. R. King, H. M. Byrne, O. E. Jensen, and K. M. Shakeshef. Mathematical modelling of engineered tissue growth using a multiphase porous flow mixture theory. *J. Math. Biol.*, 52:571–594, 2006.

[33] A. J. Lusis. Atherosclerosis. *Nature*, 407(6801):233–241, 2000.

[34] E. Lutgens, M. Gijbels, M. Smook, P. Heeringa, P. Gotwals, V. E. Koteliansky, and M. J. A. P. Daemen. Transforming growth factor-β mediates balance between inflammation and fibrosis during plaque progression. *Arterioscler. Thromb. Vasc. Biol.*, 22:975–982, 2002.

[35] J. M. Mann and M. J. Davies. Vulnerable plaque: Relation of characteristics to degree of stenosis in human coronary arteries. *Circulation*, 94(5):928–931, 1996.

[36] A. C. Newby and A. B. Zaltsman. Fibrous cap formation or destruction — the critical importance of vascular smooth muscle cell proliferation, migration and matrix formation. *Cardiovasc. Res.*, 41(2):345–360, Feb 1999.

[37] A. Ougrinovskaia. *Mathematical Models of Atherosclerosis*. Phd. thesis, University of Sydney, 2011.

[38] M. Rafieian-Kopaei, M. Setorki, M. Doudi, A. Baradaran, and H. Nasri. Atherosclerosis: Process, indicators, risk factors and new hopes. *Int. J. Prev. Med.*, 5(8):927 – 946, 2014.

[39] H. Sano, T. Sudo, M. Yokode, T. Murayama, H. Kataoka, N. Takakura, S. Nishikawa, S. Nishikawa, and T. Kita. Functional blockade of platelet-derived growth factor receptor-β but not of receptor-α prevents vascular smooth muscle cell accumulation in fibrous cap lesions in apolipoprotein e–deficient mice. *Circulation*, 103(24):2955–2960, Jun 2001.

[40] A. H. Schulick, A. J. Taylor, W. Zuo, and D. A. Dichek. Overexpression of transforming growth factor beta1 in arterial endothelium causes hyperplasia, apoptosis, and cartilaginous metaplasia. *PNAS*, 95(12):6983–6988, Jun 1998.

[41] D. Steinberg, S. Parthasarathy, T. E. Carew, J. C. Khoo, and J. L. Witztum. Beyond cholesterol: Modifications of low-density lipoprotein than increase its atherogenicity. *New Eng. J. Med.*, 320:915–924, 1989.

[42] R. Stocker. The ambivalence of vitamin e in atherogenesis. *Trends Biochem. Sci.*, 24:219–223, 1999.

[43] M. P. Thon, H. Z. Ford, M. W. Gee, and M. R. Myerscough. A quantitative model of early atherosclerotic plaques parameterized using in vitro experiments. *Bull. Math. Biol.*, 80:175–214, 2018.

[44] M. G. Watson, H. M. Byrne, C. Macaskill, and M. R. Myerscough. A two-phase model of early fibrous cap formation in atherosclerosis. *J. Theor. Biol.*, 456:123–136, 2018.

[45] M. G. Watson, H. M. Byrne, C. Macaskill, and M. R. Myerscough. A multiphase model of growth factor-regulated atherosclerotic cap formation. *J. Math. Biol.*, 81:725–767, 2020.

[46] P. Xiang, V. Blanchard, and G. A. Francis. Smooth muscle cell—macrophage interactions leading to foam cell formation in atherosclerosis: Location, location, location. *Front. Physiol.*, 13, June 2022.

[47] G. A. Younes and N. E. Khatib. Mathematical modeling of atherogenesis: Atheroprotective role of hdl. *J. Theor. Biol.*, 529:126–141, 2021.